

Microstructure and Electrochemical Performance of Fully Ceramic Composite Anodes for SOFCs

Harald Schlegl



University of
St Andrews

This thesis is submitted for the degree of PhD

at the

University of St Andrews

October 2014

1. Candidate's declarations:

I, Harald Schlegl hereby certify that this thesis, which is approximately 41500 words in length, has been written by me, and that it is the record of work carried out by me, or principally by myself in collaboration with others as acknowledged, and that it has not been submitted in any previous application for a higher degree.

I was admitted as a research student in October 2009 and as a candidate for the degree of PhD in September 2010; the higher study for which this is a record was carried out in the University of St Andrews between 2009 and 2013.

Date signature of candidate

2. Supervisor's declaration:

I hereby certify that the candidate has fulfilled the conditions of the Resolution and Regulations appropriate for the degree of PhD in the University of St Andrews and that the candidate is qualified to submit this thesis in application for that degree.

Date signature of supervisor

3. Permission for publication:

In submitting this thesis to the University of St Andrews I understand that I am giving permission for it to be made available for use in accordance with the regulations of the University Library for the time being in force, subject to any copyright vested in the work not being affected thereby. I also understand that the title and the abstract will be published, and that a copy of the work may be made and supplied to any bona fide library or research worker, that my thesis will be electronically accessible for personal or research use unless exempt by award of an embargo as requested below, and that the library has the right to migrate my thesis into new electronic forms as required to ensure continued access to the thesis. I have obtained any third-party copyright permissions that may be required in order to allow such access and migration, or have requested the appropriate embargo below.

The following is an agreed request by candidate and supervisor regarding the publication of this thesis:

PRINTED COPY

Embargo on all or part of print copy for a period of 1 year on the following ground:

- Publication would preclude future publication

ELECTRONIC COPY

Embargo on all or part of electronic copy for a period of 1 year on the following ground:

- Publication would preclude future publication

Date signature of candidate signature of supervisor

Acknowledgements

Firstly I would like to express my gratitude to my supervisor Professor John T.S. Irvine for paying me for a hobby, lots of good advice, trust in my abilities and patience with my failures. My thanks also go to all members of the JTSl group for being the best colleagues I could wish for. Namely I want to mention my mentor Professor Jung Hyun Kim for helping me in the starting phase of my PhD in a patient and friendly manner, when I needed a lot of time and advice, and Dr. Paul Connor for helping me in the final phase of my PhD in a patient and friendly manner, when I still needed a lot of time and advice. Dr. Dragos Neagu was of valuable help discussing the chemistry and structure of perovskites and Dr. Abul Kalam Azad a guide in the miraculous world of structure, X-ray diffraction and refinement. Thank you very much to both of you. I also feel obliged to Mrs. Julie Nairn, Mr. Ross Blackley and Mr. George Anthony for their generous help with many different aspects of the daily work during the work for my PhD.

As well as being lucky enough to work in St. Andrews for almost four years, I got lucky again and was presented with the opportunity to work for six weeks in Philadelphia at the University of Pennsylvania. My gratitude again goes to Professor John T.S. Irvine for organising the money for this adventure, and to Professor Raymond Gorte, Professor John Vohs and Mr. Anthony Sky Yu for a friendly welcome, help, advice and new insights.

On a more private level I want to thank my lovely girlfriend Claire for her love and understanding, and my parents Herbert and Elfi for their love and emotional support and also their financial help whenever I needed it. My brothers Herbert, Roland and Emerich and my friends Isabella, Angelika, Babsi and Ernestine visited me during my time at St. Andrews and brought a little bit of Austria to Scotland, thank you for that.

For the permanent stupid grin on my face during the last five years, for the constant annoying answer "very, very well" to every question "how are you?" which was in fact truthful reporting and not just positive thinking, I feel you are all responsible. Danke.

Harald

Abstract

Solid Oxide Fuel Cells could play a key role in energy systems of the future because they can directly convert the chemical energy of fuels into electrical energy in a reliable and energy efficient way. The choice of materials for the components of fuel cells is crucial for the achievement of the high performance and the low price necessary to establish fuel cell technology in the energy market. Current state of the art anodes consisting of nickel and yttria stabilised zirconia (Ni/YSZ) offer good electrochemical performance but suffer from limitations like carbon deposition, redox instability and sulphur poisoning.

This thesis explores the properties of composite fully ceramic anodes consisting of a skeleton of yttria stabilised zirconia (YSZ) or cerium gadolinium oxide (CGO) and a perovskite phase based on B-site doped lanthanum strontium titanate. The perovskite phase was fabricated in situ inside the pores of the skeleton material by the infiltration of an aqueous precursor and subsequent firing (impregnation method). Material characterisation of the composite anodes was carried out by X-ray diffraction and the microstructure investigated by electron microscope techniques. The electrochemical performance was tested by IV-curves and impedance spectroscopy. Particularly the investigation of the connection between the microstructure of the impregnated anodes and their electrochemical performance is a main objective of this work.

The electrochemical performance of cells with a CGO skeleton and an impregnated lanthanum strontium titanate phase was found to be inferior compared to cells with a YSZ skeleton, even if the ionic conductivity of CGO is known to be higher than the ionic conductivity of YSZ. The difference was assigned to mass transport problems tightly connected to the different microstructure of the composite anodes.

A significant improvement of the performance could be achieved by the utilisation of A-site deficient perovskites as impregnated phase in a YSZ skeleton. Cells with composite anodes of YSZ and $\text{La}_{0.4}\text{Sr}_{0.4}\text{Ti}_{0.94}\text{Mn}_{0.06}\text{O}_{3-\delta}$ show power densities of 156.2 mW/cm^2 at a measuring temperature of $750 \text{ }^\circ\text{C}$ compared to 58.5 mW/cm^2 measured in a similar cell with A-site stoichiometric LSTM, both cells having an electrolyte thickness of around $60 \text{ }\mu\text{m}$. The superiority of the performance of anodes with A-site deficient perovskites is mainly due to a lower ohmic resistance of only $0.5 \text{ }\Omega\cdot\text{cm}^2$, indicating better conductivity of the composite with A-site deficient perovskites. The investigation of the microstructure of composite anodes with A-site deficient perovskites showed the decoration of the surface with nanoparticles after reduction. These nanoparticles originate from exsolution of ions from the B-site of the perovskite and can't be found in A-site stoichiometric perovskites.

The influence of fabrication parameters like firing temperature of the skeleton, firing temperature after impregnation or vacuum impregnation on the microstructure and electrochemical performance of the composite anodes was studied. Particularly the increase of the firing temperature of the skeleton from $1400 \text{ }^\circ\text{C}$ to $1500 \text{ }^\circ\text{C}$ resulted in an impressive improvement of total cell resistance and maximal power density.

Contents

1. Introduction	5
1.1. The importance of renewable energy	5
1.2. Energy storage.....	9
1.3. The role of electrolysers and fuel cells	10
1.4. Types of fuel cells	12
1.5. Fuel Cell Design	15
1.6. Efficiency of fuel cells	17
1.6.1. Thermodynamic efficiency	17
1.6.2. Current efficiency	20
1.6.3. Voltage efficiency	21
1.7. SOFC materials	24
1.7.1. Interconnect materials	24
1.7.2. Electrolyte materials.....	25
1.7.3. Electrode materials	27
1.7.3.1. Composite electrodes.....	28
1.7.3.2. Microstructure of composite electrodes	29
1.7.3.3. Cathode materials	30
1.7.3.4. Anode materials	31
1.7.3.4.1. State of the art SOFC anodes.....	32
1.7.3.4.2. Alternative SOFC anodes	33
1.7.3.4.3. Fully ceramic SOFC anodes.....	34
1.7.3.4.4. Catalysts for SOFC anodes	35
1.7.3.5. Impregnation method	36
1.7.4. Perovskite oxides for SOFCs.....	38
2. Experimental Methods and Techniques	48
2.1. Preparation of thin button cells	48
2.1.1. Fabrication of the skeleton	49
2.1.1.1. Slurry preparation for tape casting	50
2.1.1.2. The tape casting process	51
2.1.1.3. Arrangement and lamination of the green tapes	53
2.1.1.4. Firing of the skeleton.....	54
2.1.2. Impregnation of the skeleton	55
2.1.2.1. Preparation of the impregnation liquids	55

2.1.2.2. The impregnation process	56
2.1.2.3. Firing of the impregnated oxides	57
2.1.2. Impregnation with the catalyst	58
2.1.3. Current collection	59
2.2. Sample characterisation	60
2.2.1. X-ray diffraction (XRD)	60
2.2.2. Scanning electron microscopy (SEM)	63
2.2.2.1. Secondary electron imaging (SEI)	66
2.2.2.2. Backscattered electron spectroscopy (BES)	67
2.2.2.3. Energy dispersive X-ray spectroscopy (EDS or EDX)	69
2.2.2.4. Sample preparation	70
2.2.2.4. Instrumentation	71
2.3. Electrochemical fuel cell testing	72
2.3.1. IV curves	72
2.3.1.1. Activation polarisation	74
2.3.1.2. Ohmic resistance	76
2.3.1.3. Concentration polarisation	77
2.3.1.4. IV curves from experimental data	78
3. Microstructure and performance of LSTM in skeletons of YSZ and CGO	91
3.1. Comparison of YSZ/LSTM and CGO/LSTM anodes	91
3.1.1. XRD analysis of the composite anodes	93
3.1.2. Comparison of the microstructure	94
3.1.3. Electrochemical performance of the single cells	96
3.1.4. Theory of the interaction of Mn with YSZ	104
3.1.5. Conclusions	105
3.2. Microstructural studies of composite anodes	106
3.2.1. Microstructure of the skeletons of the composite anodes	106
3.2.1.1. Skeletons of pure YSZ and CGO	106
3.2.1.2. Skeletons of YSZ with impregnated CGO	107
3.2.1.3. Skeletons of CGO with impregnated YSZ	111
3.2.2. Microstructure of composite SOFC anodes impregnated with titanates	112
3.2.3. Changes of the microstructure of composite SOFC anodes upon reduction	114
3.2.4. Development of the microstructure of composite SOFC anodes	118
3.2.5. Microstructure of composite anodes with a mixed material skeleton of YSZ and CGO	120
3.2.6. Conclusions	123
3.3. Improvement of the performance of cells with CGO/LSTM composite anodes	124
3.3.1. LSTM4646 and LSTM4682	124

3.3.2. Catalytic effects	129
3.3.3. Effects of the cathode porosity	134
3.3.4. Conclusions	138
4. Composite SOFC anodes with YSZ and A-site deficient titanates.....	141
4.1. Composite anodes with LST44	142
4.1.1. Microstructure of composite anodes with A-site deficient perovskites.....	143
4.1.2. Oxidized and reduced forms of composite anodes with A-site deficient perovskites	145
4.1.3. Electrochemical performance	150
4.1.4. Conclusions	151
4.2. B-site substitution of A-site deficient titanates	152
4.2.1. Microstructure of B-site substituted perovskites	152
4.2.2. Phase investigation of B-site substituted titanates	158
4.2.3. Electrochemical performance	161
4.2.4. Conclusions	163
4.3. Comparison with stoichiometric titanates	165
4.3.1. Differences in the microstructure	166
4.3.2. Differences in the electrochemical performance	168
4.3.3. Conclusions	169
4.4. The influence of a CGO coating on the YSZ skeleton	170
4.4.1. Microstructure of composite anodes with a CGO layer.....	173
4.4.2. Electrochemical performance of composite anodes with a CGO layer	176
4.4.3. Conclusions	179
4.5. The influence of the calcination temperature on the composite anodes.....	180
4.5.1. Temperature related differences in the XRDs	181
4.5.2. Influence on the microstructure	184
4.5.3. Conclusions	187
4.6. Cell fabrication using the vacuum impregnation method	189
4.6.1. Evaluation of the weight gain per cycle	190
4.6.2. Comparison of the microstructure.....	191
4.6.3. Comparison of the electrochemical performance	192
4.6.4. Conclusions	194
4.7. Different cell fabrication with a higher skeleton firing temperature	194
4.7.1. Differences in the fabrication	195
4.7.2. Differences in the microstructure	196
4.7.3. Differences in the electrochemical performance	198
4.7.4. Conclusions	201
5. Conclusions	204

Glossary of used acronyms

CGO	general cerium gadolinium oxide
CGO91	cerium gadolinium oxide of the composition $\text{Ce}_{0.9}\text{Gd}_{0.1}\text{O}_{1.95}$
LSF	general lanthanum strontium ferrate
LSF82	lanthanum strontium ferrate $\text{La}_{0.8}\text{Sr}_{0.2}\text{FeO}_{2.9}$
LSM	general lanthanum strontium manganate
LSM82	lanthanum strontium manganate $\text{La}_{0.8}\text{Sr}_{0.2}\text{MnO}_{2.9}$
LST	general lanthanum strontium titanate
LST44	A-site deficient lanthanum strontium titanate $\text{La}_{0.4}\text{Sr}_{0.4}\text{TiO}_3$
LST46	lanthanum strontium titanate $\text{La}_{0.4}\text{Sr}_{0.6}\text{TiO}_{3.2}$
LSTM	general lanthanum strontium titanate manganate
LSTM4646	lanthanum strontium titanate manganate $\text{La}_{0.4}\text{Sr}_{0.6}\text{Ti}_{0.4}\text{Mn}_{0.6}\text{O}_{3-\delta}$
LSTM4664	lanthanum strontium titanate manganate $\text{La}_{0.4}\text{Sr}_{0.6}\text{Ti}_{0.6}\text{Mn}_{0.4}\text{O}_{3-\delta}$
LSTM4682	lanthanum strontium titanate manganate $\text{La}_{0.4}\text{Sr}_{0.6}\text{Ti}_{0.8}\text{Mn}_{0.2}\text{O}_{3-\delta}$
LST44Mn6	lanthanum strontium titanate manganate $\text{La}_{0.4}\text{Sr}_{0.4}\text{Mn}_{0.06}\text{Ti}_{0.94}\text{O}_{3-\gamma}$
YSZ	general yttrium stabilised zirconia, zirconium yttrium oxide
8YSZ	yttrium stabilised zirconia of the composition $(\text{ZrO}_2)_{0.92}(\text{Y}_2\text{O}_3)_{0.08}$
SEM	secondary electron microscope
FE-SEM	field emission secondary electron microscope
EDS	energy dispersive spectroscopy
EDAX	energy dispersive X-ray analysis
BS	backscattered (electron imaging)
EIS	electrochemical impedance spectroscopy

1. Introduction

1.1. The importance of renewable energy

Worldwide around 12 billion tons oil equivalent (12000 Mtoe) of energy are consumed every year [1] [2]. On average every human being uses a yearly amount of 1.6 tons oil equivalent, around 67000 MJ or around 19000 kWh, with striking differences between the developing and the developed nations [3]. To meet these demands various sources of primary energy are available.

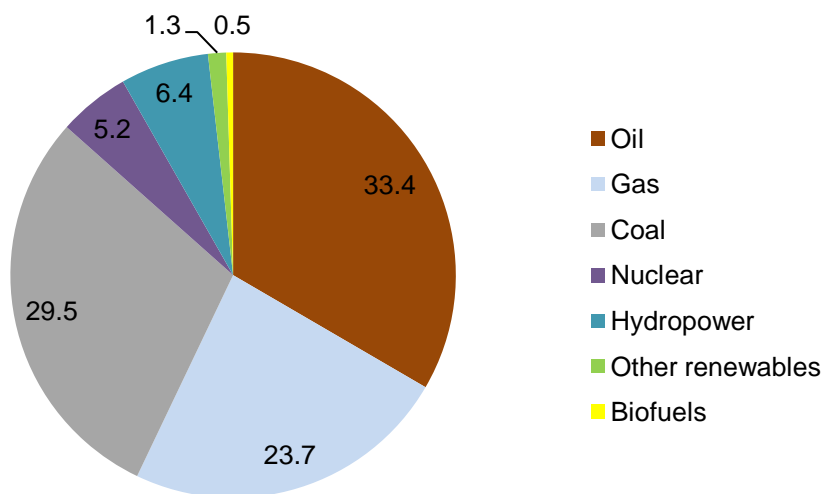


Figure 1.1: World energy consumption by source in % [1]

Fossil fuels like oil, gas and coal currently provide around 87% of the world's consumed energy. The contribution of renewable fuels like hydroelectric energy, wind energy, tidal energy, wave power, solar energy, biomass, geothermal energy and biofuels is still quite small with around 8% (2010).

The energy economy based on fossil fuels is unsustainable in at least two ways. The resources used now have been generated over millions of years and they are limited. Even if the projections differ in when cheap oil, gas and coal will no longer be available [4] [5], they all agree that this will happen eventually. The rising prices for fossil fuels witnessed in the past several years might indicate the supplies falling short of the demands already. Secondly the burning of fossil fuels provides a problem with its end product, carbon dioxide. An atmosphere with an increasing concentration of this gas absorbs more of the heat radiation from the planetary surface, a phenomenon commonly known as the greenhouse effect. The greenhouse effect already does considerably change the climate on earth, increasing average temperatures and causing extreme weather conditions [6]. Most experts agree that in the future more problems are to be expected related to the partial melt of the polar caps and rise of sea level [7].

Next to measures helping the consumers to save energy, the use of renewable fuels instead of fossil fuels seems an attractive alternative to the current energy policy. However, there are some problems connected to the use of renewable energy which have to be tackled. The implementation prices are still high and cause long payback times [8]. There are concerns that a rise in the production of biofuels might increase the prices of basic foods like corn, making it impossible to afford for the poorest part of the population [9]. Wind and solar energy are unpredictable and unreliable in most parts of the world, and also suffer from intermittency, meaning that at some times there is a lot of energy production, at other times little or none. There is a need of cheap and energy efficient ways to store the energy produced in times of excess and release it in times of shortage to make these power sources more reliable.

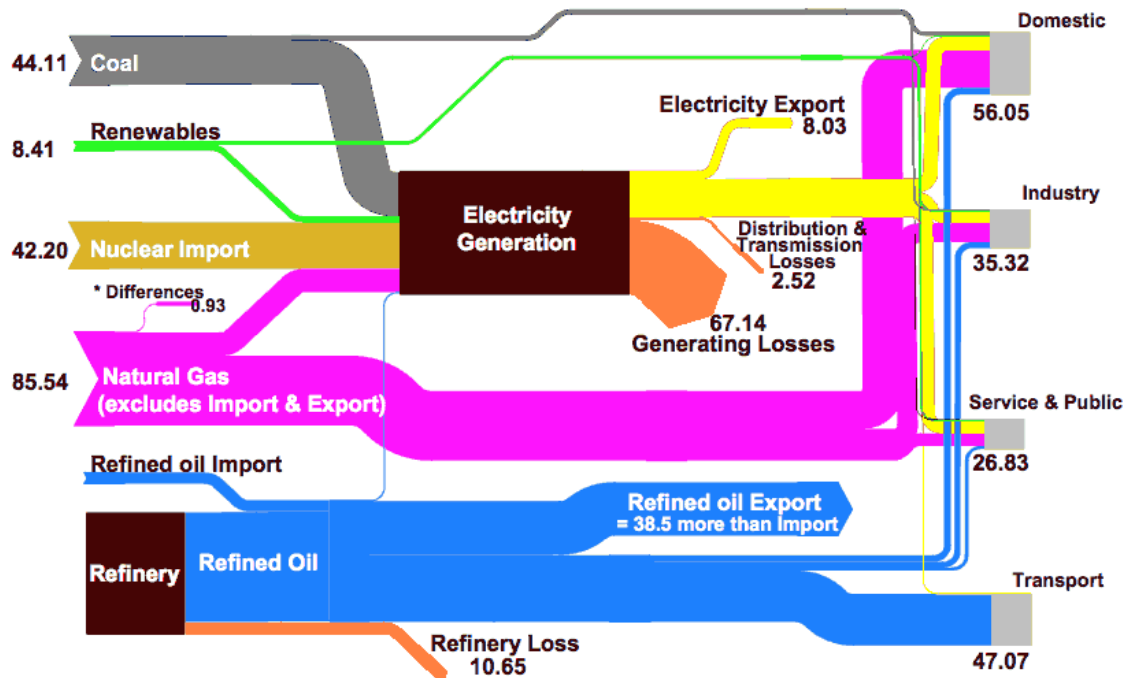


Figure 1.2: Summary of Energy Flows in Scotland in TWh (2002), figure from [10]

Primary energy sources like natural gas, crude oil, coal or renewable energy can be transformed to more convenient forms of energy like electricity. Figure 1.2 is an overview of energy flows in Scotland 2002 [10]. It shows that end users like households, industry and the public sector use a mix of primary energy and electricity. The energy consumed in households, for example, predominantly consists of the primary energy source natural gas and electricity.

Electrical energy is very convenient to use and an essential part of the computer and information society of today. However, it can only be used by a consumer connected to the grid or to batteries, which causes some limitations if electricity is used in the transportation sector. Figure 1.2 indicates that electrical energy is produced out of primary energy with a very poor efficiency, actually only one third of the primary energy invested into electricity production ends up as useful electrical energy in the grid.

Figure 1.2 also shows that at present fossil fuels and nuclear energy are used to generate electricity. The part of electricity produced by renewable energy sources is small, but steadily increased over the last few years, and is expected to increase even more in the future [11]. Transforming mechanical and chemical energy into electrical energy as well as transforming excess electrical energy into the chemical energy of fuels, both as efficiently as possible, will be one of the key tasks of a sustainable energy policy. The chemical fuels, produced by excess electricity in times when the supply of sun or wind energy exceeds the electricity demand, can be stored and used for transport or to level out the intermittencies of the renewable energy production.

A possible future vision for a sustainable energy policy could be based on many decentralised energy centres where energy is produced from renewable sources. All of these energy centres could be connected by an electrical grid and each of them could be equipped with facilities to transform electrical energy into chemical energy and vice versa.

1.2. Energy storage

Since most of the renewable energy sources produce energy intermittently, it is important that the electrical energy produced by them can be stored in times of excess production and released in times of limited production. Electrical energy cannot simply be stored in the grid, it has to either be transformed to other kinds of energy or stored as electrical energy for instance in a capacitor or a supercapacitor [12].

The most commonly used technique is to use the electrical energy to pump water to an increased height and store the energy in the form of gravitational energy [13]. To release the stored energy the water flows down and moves a turbine. Other mechanical ways of storing the electrical energy are to compress air [14] or to accelerate a flywheel [15].

Chemical ways of storing electrical energy include the reversible transformation of chemicals in batteries [16] or redox flow batteries [17] and the use of electricity for the production of fuels. The most basic fuel is hydrogen, which can be produced by simply splitting water using electrical energy in an electrolyser. The main problem of hydrogen as a fuel is its very low volumetric energy density. To overcome this problem hydrogen can be compressed or even liquefied using pressure and very low temperature. However, both of these methods demand additional energy lowering the efficiency of the use of hydrogen as energy carrier [18]. Hydrogen also can be subject to chemical or electrochemical reactions, it bonds to other elements creating fuels like hydrocarbons[19] or ammonia [20], which have higher volumetric densities due to the fact that they are liquids or at least can be liquefied much easier than hydrogen.

1.3. The role of electrolysers and fuel cells

The main part of electrical energy produced today is produced by burning fuels in heat engines. The heat of the burning fuel is used to create steam from water, which runs a turbine connected with an electrical generator.

The transformation of the chemical energy of the fuel to electrical energy can also be done in a different, more direct way, in a device called fuel cell. In a fuel cell the fuel is oxidised in an electrochemical reaction while at a different place oxygen is reduced to oxide ions. The flow of electrons from the place of the oxidation of the fuel to the place where oxygen is reduced directly generates the electrical energy next to residual heat. Water is created as a by-product. The main reason for the use of a fuel cell instead of a heat engine to produce electricity out of a fuel, is the higher efficiency of the transformation process [21], the same amount of fuel can create more electrical energy when it is converted in a fuel cell.

A very similar device can be used in the opposite direction. Electrical energy is used to force electrons to move in the opposite direction, reducing the protons of water to hydrogen or other fuels and oxidising the oxide ions to oxygen. This device is called an electrolyser. A reversible fuel cell is a device that can work both ways, as a fuel cell and as an electrolyser.

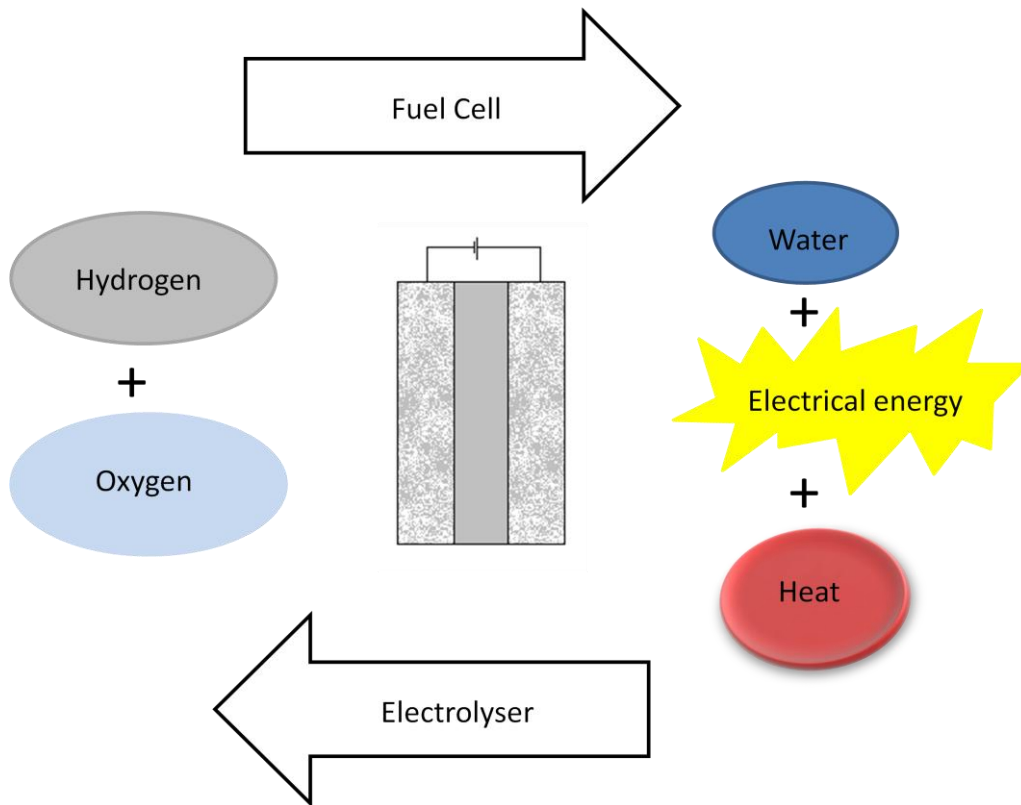


Figure 1.3: Fuel Cells and Electrolysers

1.4. Types of fuel cells

Generally every fuel cell consists of four parts. The two electrodes anode and cathode are separated by the electrolyte, and the interconnect connects the single cells with each other and with an outer circuit. At the anode the continuously fed fuel is oxidised and free electrons are generated. These electrons move through the interconnect and the outer circuit to the cathode, where oxygen is reduced to oxide ions. The electrolyte either conducts anions from the cathode to the anode or cations from the anode to the cathode.

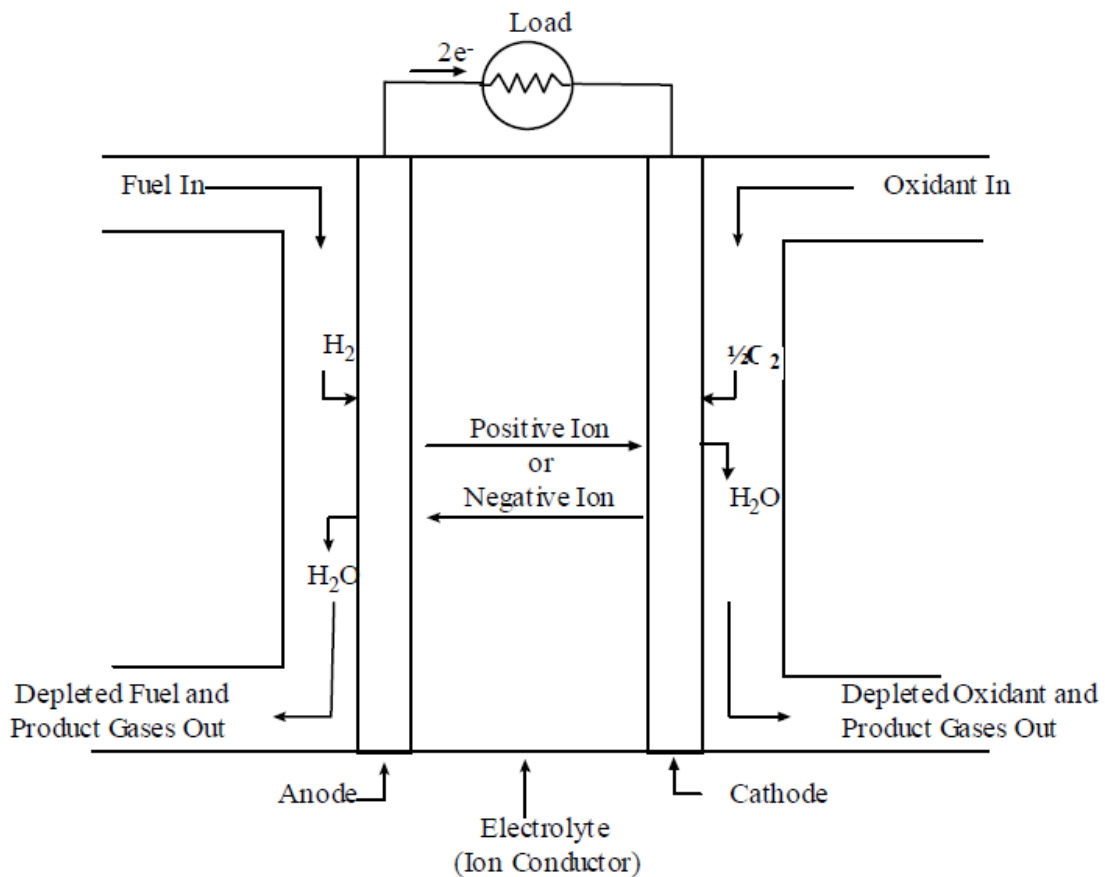


Figure 1.4: Schematic drawing of an individual fuel cell, image from [22]

Fuel cells differ in the fuels used, the material of the electrolyte, the type of the charge carrying ions and the operating temperature. Most commonly fuel cells are classified by the material of their electrolytes.

Fuel Cell Type	Polymer Electrolyte Membrane (PEM)	Alkaline (AFC)	Phosphoric Acid (PAFC)	Molten Carbonate (MCFC)	Solid Oxide (SOFC)
Common Electrolyte	perfluoro sulfonic acid	aqueous KOH solution in a matrix	phosphoric acid in a matrix	solution of carbonates of Li, Na, K in a matrix	yttria stabilised zirconia
Operating Temperature	50 - 100 °C typically 80 °C	90 - 100 °C	150 - 200 °C	600 - 700 °C	700 - 1000 °C
Typical Stack Size	<1 – 100 kW	10 – 100 kW	400 kW 100 kW module	300 kW – 3 MW 300 kW module	1 kW – 2 MW
Efficiency	60% transportation 35% stationary	60%	40%	45 - 50%	60%
Applications	-backup power -portable power -distributed generation -transportation	-military -space	- distributed generation	-electric utility -distributed generation	-auxiliary power -electric utility -distributed generation
Advantages	-low temperature -quick start up	-cathode reaction faster in alkaline electrolyte leads to higher performance -low cost components	-higher T enables CHP -Increased tolerance to fuel impurities	-high efficiency -fuel flexibility -can use a variety of catalysts -suitable for CHP	-high efficiency -fuel flexibility -can use a variety of catalysts -suitable for CHP&CHHP -solid electrolyte
Disadvantages	-expensive catalysts -sensitive to fuel impurities -low T waste heat	-sensitive to CO ₂ in fuel and air -electrolyte management	-Pt catalyst -long start up time -low current and power	-high T corrosion and breakdown of cell components -long start up time -low power density	-high T corrosion and breakdown of cell components -high T operation requires long start up time and limits

Figure 1.5: Comparison of different types of fuel cells [23]

Solid Oxide Fuel Cells (SOFCs) are defined by their ceramic electrolytes conducting O^{2-} ions from the cathode to the anode, or in the case of proton conductive SOFCs, conducting H^+ ions from the anode to the cathode of the fuel cell. Their operation temperature is the highest of all types of fuel cells. This high operation temperature is responsible for the advantages as well as for the disadvantages of SOFCs compared to other types of fuel cells. At temperatures of 700 °C and above a lot of hydrocarbon fuels can be used without an external reformer and complicated fuel processing. The efficiency is high and can even be increased by using the hot exhaust gases of the fuel cell for heating or cooling purposes, or even to run a gas turbine. Combined heat and power (CHP) systems of that kind can provide efficiencies of over 60%, far more than conventional electricity generation systems [24]. The negative aspects of the high operating temperature are long start up and cool down times and problems with the chemical and mechanical stability of the materials used in SOFCs. High temperature fuel cells are more suitable for continuous energy production than for machines like cars, which have to be turned on and off regularly.

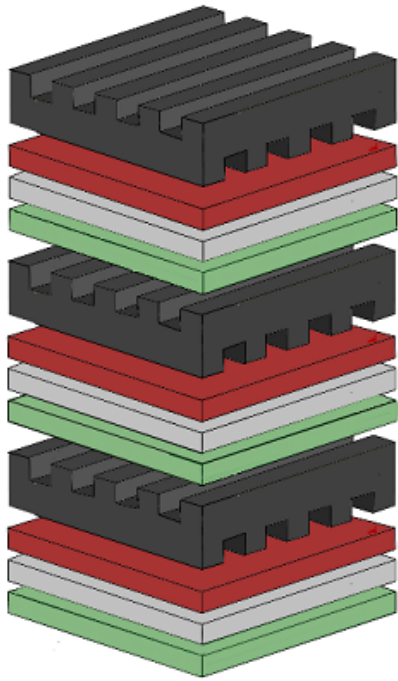
1.5. Fuel Cell Design

Due to the fact that all the components in a SOFC are solid, principally there are no restrictions about the geometrical design of its general components electrodes, electrolyte and interconnect. However, most SOFCs are either configured as flat planes (planar SOFC) or rolled tubes (tubular SOFC). As an alternative design also a double spiral configuration was patented in St. Andrews (SOFC roll).

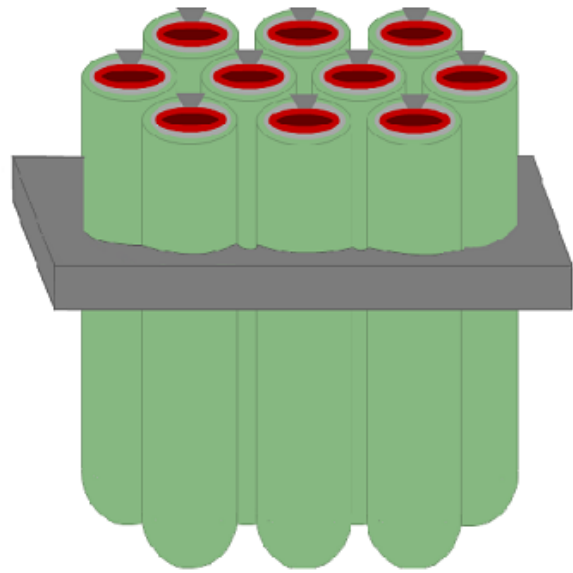


Figure 1.6: different designs of SOFCs: a) planar, b) tubular, c) SOFC roll. The red layers represent the cathodes, the green layers the anodes, the light grey layers the electrolytes and the dark grey parts the interconnect.

For most practical applications the voltage and power of one single fuel cell is not sufficient, so many of them have to be combined. The possibility to combine any number of single cells in a modular way, allowing to tailor the fuel cell system to the needs of the application, is one of the advantages of fuel cells.



d)



e)

Figure 1.7.: Fuel cell stacks: d) planar fuel cell stack, e) tubular fuel cell stack

1.6. Efficiency of fuel cells

The chemical energy stored in fuel and oxygen can be quantified by the enthalpy difference of the products and the reactants of the cell reaction ΔH . After transforming the chemical energy in a fuel cell only a part of ΔH is available as electrical energy. The ratio of the amount of useful energy put out by the fuel cell to the amount of chemical energy put in via the fuel is called efficiency. The overall efficiency of the fuel cell can be split into a product of different efficiencies related to the different losses of available energy during the conversion process.

$$\epsilon_{F.C.} = \epsilon_T \cdot \epsilon_J \cdot \epsilon_V$$

$\epsilon_{F.C.}$... total efficiency of the fuel cell

ϵ_T ... thermodynamic efficiency

ϵ_J ... current efficiency

ϵ_V ... voltage efficiency

Equation 1.1.: total efficiency of a fuel cell as the product of different efficiencies

1.6.1. Thermodynamic efficiency

All of the losses of available energy in the conversion process are related to thermodynamics. Some are impossible to avoid even under ideal conditions, which, for a fuel cell would mean operation at OCV, with no electrical current flowing through the electrodes. Under these ideal conditions the cell reaction

would be reversible and at equilibrium, but not supplying any usable power to the environment. Thermodynamic efficiency is often used to compare fuel cells to heating engines, pointing out that, at least at low temperatures, fuel cells are more efficient than heat engines.

The production of electricity in heat engines is limited by the thermal loss of the heat of the exhaust gases. Therefore the efficiency of a heat engine, even under ideal conditions, can never exceed the Carnot efficiency.

$$\epsilon_T = 1 - \frac{T_C}{T_H}$$

ϵ_T ... thermodynamic efficiency

T_C ... absolute temperature at the engine exhaust [K]

T_H ... absolute temperature at the engine inlet [K]

Equation 1.2: Carnot efficiency of heat engines

The efficiency of electrical energy production by fuel cells will also suffer from losses related to thermodynamics. Even under ideal circumstances the efficiency of a fuel cell can never be higher than the ratio of the change of free energy to the change of enthalpy during the cell reaction.

$$\epsilon_T = \frac{\Delta G}{\Delta H} = 1 - \frac{T \cdot \Delta S}{\Delta H}$$

ϵ_T ... thermodynamic efficiency of a fuel cell

ΔG ... free energy of the cell reaction [J·mol⁻¹]

ΔH ... enthalpy of the cell reaction [J·mol⁻¹]

ΔS ... entropy of the cell reaction [J·mol⁻¹·K⁻¹]

T ... absolute temperature [K]

Equation 1.3: Maximum theoretical efficiency of fuel cells

A comparison of the maximal theoretical efficiency of heat engines and fuel cells at different temperatures shows that the maximal efficiency of heat engines increases with increasing temperature, the maximum efficiency of fuel cells decreases with increasing temperature. Figure 1.4. shows the graphs of the theoretical efficiencies of a fuel cell and a heat engine versus temperature.

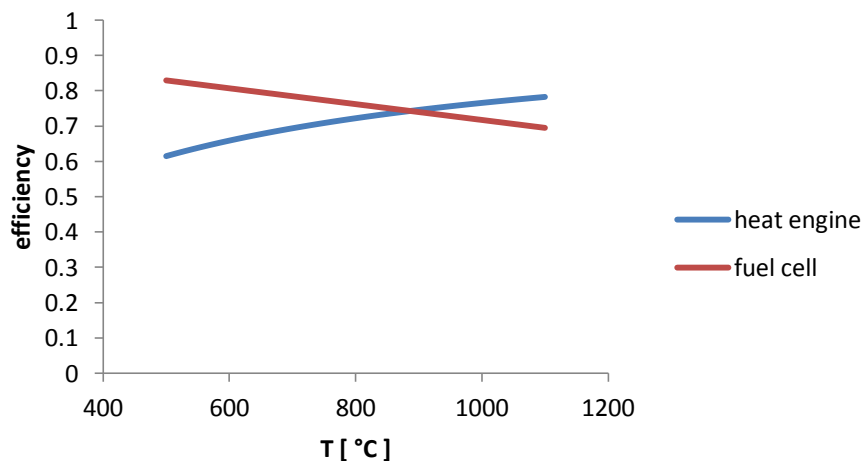


Figure 1.8: Temperature dependent thermodynamic efficiency of a fuel cell and a steam engine with an exhaust temperature of 25 °C

1.6.2. Current efficiency

The current efficiency can be expressed as the fuel utilization energy. It is the ratio of the amount of current which would be produced if all the fuel supplied would be oxidized to the amount of current which is actually produced.

$$\epsilon_J = \frac{i}{i_F}$$

ϵ_J ... current efficiency

i ... current produced [A]

i_F ... current produced at 100% fuel utilisation according to Faraday's law [A]

Equation 1.4: current efficiency

The current which should be produced at a certain molar flow rate of fuel can be calculated by Faraday's law.

$$i_F = z \cdot F \cdot \frac{dn}{dt}$$

i_F ... theoretically produced current [A]

z ... amount of electrons produced from one equivalent cell reaction

F ... Faraday constant ~ 96485 [C·mol⁻¹]

dn/dt ... molar flow of fuel [mol·s⁻¹]

Equation 1.5: current produced at a certain fuel flow if 100% of the fuel is utilized

1.6.3. Voltage efficiency

The thermodynamic efficiency described in chapter 1.6.2 deals with inevitable losses occurring even if the fuel cell does not produce power. As soon as current is drawn from the fuel cell additional losses have to be considered. The reversible cell potential is reduced because internal resistances of the fuel cell, working against the movement of the electrons, have to be overcome.

$$E_{\text{rev}} = E_0 - \frac{R \cdot T}{z \cdot F} \cdot \ln \prod_k P_k^{\nu_k}$$

E_{rev} ... reversible cell potential [V]

ΔG ... standard free energy change of the cell reaction at T [Jmol⁻¹]

z ... electrons produced from one equivalent cell reaction

F ... Faraday constant (~ 96485) [Cmol⁻¹]

R ... universal gas constant (~ 8.31) [JK⁻¹mol⁻¹]

T ... absolute temperature [K]

$\prod_k P_k^{\nu_k}$... reaction quotient

Equation 1.6: reversible cell potential

The voltage drop whenever electrical energy is drawn from the fuel cell is due to a combination of activation polarisation, ohmic polarisation and mass transport polarisation. The contribution of each of these polarisations to the total cell voltage loss depends on the amount of current drawn from the fuel cell. Polarisation curves (IV curves) are useful performance indicators for fuel cells and show in their different parts the effects of activation polarisation, ohmic polarisation and concentration polarisation. These polarisations are described in more detail in the section about polarisation curves in chapter 2.3.1.

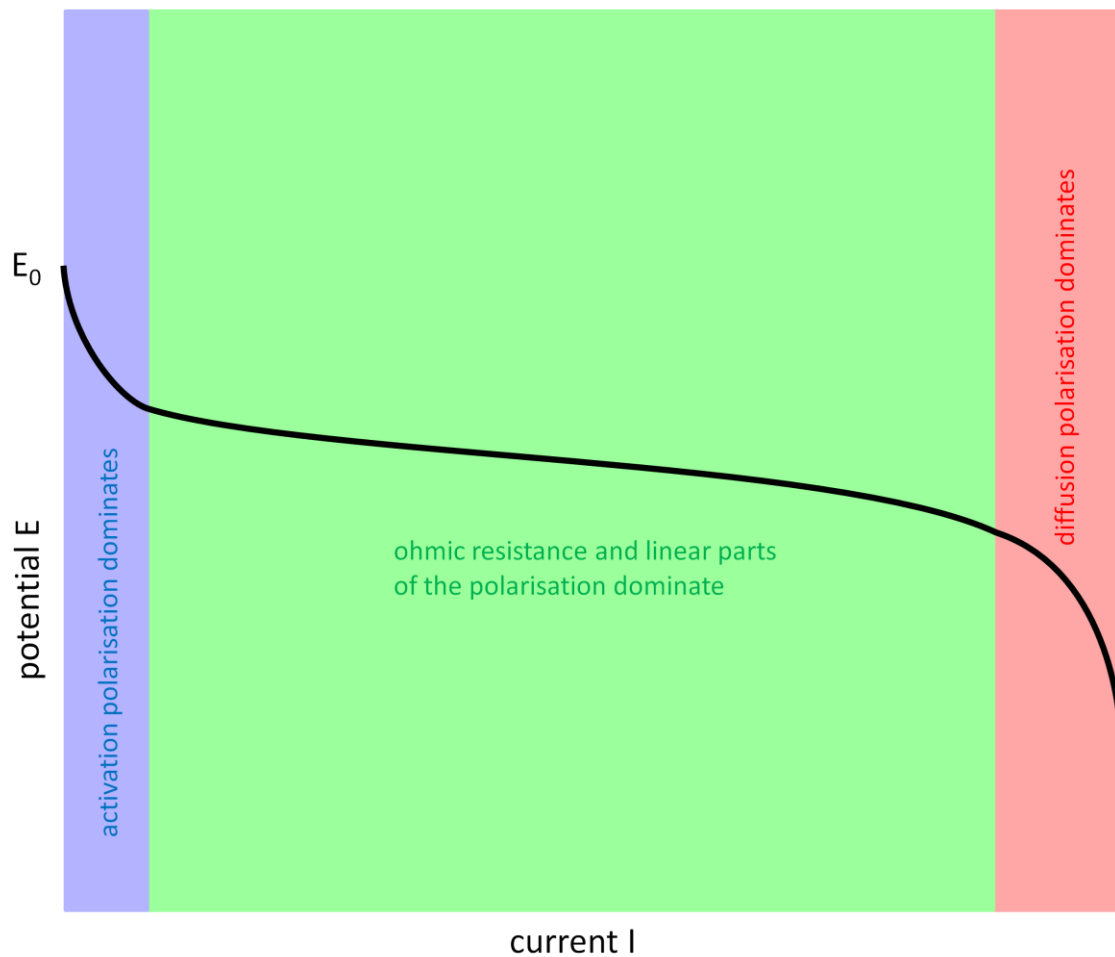


Figure 1.9: An idealised polarisation curve shows in its different parts the domination of different polarisations

Unlike the thermodynamic efficiency, the voltage efficiency can be influenced by the choice of materials for the different parts of the fuel cell. Materials providing better ionic and electronic conductivity can reduce the ohmic polarisation of the fuel cell, the choice of suitable catalysts can reduce the activation polarisation and the porosity and microstructure of the electrodes can influence the concentration polarisation.

The current efficiency and the voltage efficiency are clearly not independent from each other, but connected by fuel utilisation. A high fuel utilisation means that the current efficiency is high, but might lead to a low voltage efficiency because of diffusion limitations. To judge the performance of a fuel cell under certain conditions it will always be favourable to have a look at the overall efficiency.

1.7. SOFC materials

The choice of materials for the fuel cell components is particularly challenging for SOFCs, because of the high operating temperatures. At temperatures of 700 °C to 1000 °C in highly reducing and oxidising environments the danger of corrosion and unwanted reactions between the different materials of the fuel cell is potentially very high. The thermal expansion coefficients of the different materials also have to be reasonably similar to avoid mechanical stress and fractures during heat up and cool down phases.

1.7.1. Interconnect materials

The interconnect in fuel cells provides the contact between the single cells and also typically distributes fuel and oxidant to the anode and the cathode side of the fuel cells. It has to be chemically and mechanically stable in both reducing and oxidising atmosphere and provide excellent electron conductivity in each of them.

Stainless steel, the first choice for other types of fuel cells, is problematic in SOFCs because of the high temperatures causing corrosion and unwanted reactions with other fuel cell parts. The ceramic material lanthanum chromite (LaCrO_3) has been widely discussed, usually doped with divalent ions like strontium, calcium or magnesium [25], providing p-type conductivity and chemical and mechanical stability at temperatures up to 1000 °C. High manufacturing costs and, compared to metal based interconnects, low electronic and thermal conductivities, however, are disadvantages of this material.

The development of SOFCs working at temperatures of 850 °C and lower allows the use of more cost effective metallic materials. Chromium iron alloys of different compositions are used as interconnect materials and as protective coatings for stainless steel [26], but on the downside, volatile chromium species are formed within these materials under the cathode working conditions poisoning the cathode material [27]. One approach to solve this problem is the development of new interconnect alloys with a lower level of chromium, which grow a chromium free e.g. (Fe,Co,Ni)₃O₄ spinel outer layer exhibiting sufficient electronic conductivity while avoiding the chromium migration observed from Cr₂O₃ layers [28].

1.7.2. Electrolyte materials

At working temperature the electrolyte of a SOFC should show high conductivity for oxide ions and negligible electron conductivity. It should be dense enough to prevent gaseous diffusion and provide some mechanical stability. Chemical compatibility and a similar thermal expansion coefficient to the other materials are necessary. Materials which are cheap and easy to fabricate and to process into thin dense films are desirable.

State of the art electrolyte material for SOFCs is yttria stabilised zirconia (YSZ). Pure zirconia ZrO₂ shows very low ionic conductivity and a phase transition from monoclinic to tetragonal at around 1000 °C, which is accompanied by a large change in volume, making it difficult to obtain stable sintered products. The addition of yttria (Y₂O₃) to zirconia replaces some of the Zr⁴⁺ ions with Y³⁺ ions in the cation lattice and produces oxygen vacancies in the anion lattice due to charge compensation. At around 8 mol% yttria substitution YSZ shows a cubic fluorite structure without any phase transformations between room

temperature and over 2000 °C. Also around this doping level the oxide ion conductivity provided by the oxygen vacancies reaches a maximum.

Ionic conductivity in solids can be explained by the hopping model referring to the hopping of interstitial ions or defects to adjacent equivalent sites. In a small external field a temperature dependence ($1/T$) is introduced into the pre-exponential factor of the Arrhenius equation [29]. The ionic conductivity of YSZ can be expressed by the modified Arrhenius equation [30].

$$\sigma = \frac{A}{T} \cdot e^{-\frac{\Delta E_A}{R \cdot T}}$$

σ ... ionic conductivity [Sm^{-1}]

A ... pre-exponential factor

T ... absolute temperature [K]

R ... universal gas constant (~ 8.31) [$\text{JK}^{-1}\text{mol}^{-1}$]

ΔE_A ... molar activation energy for the ionic conductivity [Jmol^{-1}]

Equation 1.7: Arrhenius equation for the ionic conductivity

When $\log(\sigma \cdot T)$ is plotted against $1/T$ a straight line can be expected where the slope can be used for the calculation of ΔE_A .

Alternative electrolyte materials to YSZ aim for higher ionic conductivity [31], suitable for operation in a SOFC at lower temperatures (700 °C and below). Cerium gadolinium oxide (CGO) [32] offers a substantially higher ionic conductivity than YSZ, but at higher temperatures and reducing conditions cerium is partly reduced from Ce^{4+} to Ce^{3+} , introducing electronic conductivity to

the material, which is intolerable for an electrolyte material. Lanthanum gallate doped with strontium and magnesium (LSGM) [33] exhibits an ionic conductivity nearly as good as CGO without electronic conductivity related problems at higher temperatures. Single phased LSGM materials of sufficient purity are, however, difficult to prepare and to retain during fuel cell operation. Because of the reactivity of LSGM with nickel it is necessary to place a buffer layer between LSGM electrolytes and conventional SOFC anodes to avoid unwanted secondary phases [34].

1.7.3. Electrode materials

Generally at the electrodes of fuel cells a gas is in contact with a solid surface, where it undergoes an electrochemical reaction. At the anode a fuel is oxidised and at the cathode oxygen is reduced to form oxide ions. The electrodes are porous and ideally provide a big surface area, where gas ionisation or deionisation reactions can occur. Good electronic and ionic conductivity is needed to transport the electrons and ions generated or used by the electrochemical reactions through the electrode material between the reaction sites and the electrolyte or interconnect. Catalytic activity for the reaction taking place at the electrode is also desirable.

1.7.3.1. Composite electrodes

Since these multiple requirements for electrode materials of SOFCs are hardly ever possible to meet by one single material, composite electrodes consisting of two or more materials are commonly used. One material can provide the ionic conductivity and mechanical stability and the chemical compatibility to the electrolyte. This material often is identical with the electrolyte material, YSZ, LSGM or CGO. Another material can be used to provide the electronic conductivity and catalytic activity for the oxidation of the fuel or the reduction of oxygen. Since the reaction zone is limited to the so called triple phase boundary (TPB), areas where both ions and electrons are in contact with the gaseous phase, the microstructure of composite electrodes is extremely important for their performance.

By using materials which are conductive for oxide ions for the scaffold of the composite electrode, it is possible to extend the reaction zone from the areas directly connecting to the electrolyte to the whole surface of the electrode. In figure 1.10 a) the anode does not exhibit any ionic conductivity, and so the electrochemically active areas are confined to the triple phase boundary between the pores, the electrolyte and the electrode. The electrochemically active area in figure 1.10 b) is increased beyond this area because one phase of the composite anode is conductive for oxide ions.

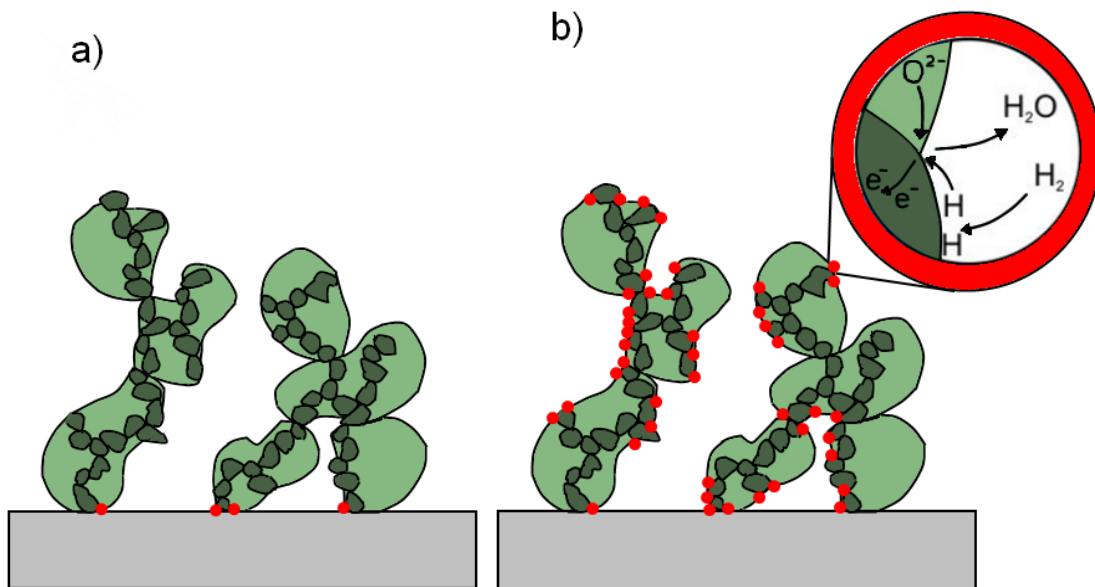


Figure 1.10: Schematic drawing of the microstructure of a SOFC composite electrode, the anode in this case. The electrolyte is coloured grey, the dark green phase is the anode compound responsible for the catalytic activity and electronic conductivity, the light green scaffold phase is responsible for stability in a) and for stability and ionic conductivity in b). The red dots mark the areas active for the electrochemical reaction

1.7.3.2. Microstructure of composite electrodes

Ideally the number of the electrochemical reaction zones and their overall area should be as big as possible, which is a matter of the microstructure of the electrode as well as of its chemical composition, making the microstructure of composite electrodes a key factor to achieve high performance.

Each of the different components of the composite electrode should consist of well connected grains providing pathways for the transport of electrons and oxide ions, and the whole electrode phase should be in good contact to the electrolyte without any delamination. The degree of porosity normally is a compromise between ensuring sufficient conductivity and mechanical stability and the access of the gases to all areas of the electrode. Microstructural stability during long term operation and interruptions of the operation by shut down and start up phases is desirable.

The microstructure of composite electrodes is intimately linked with the method of fabrication. Generally the co-firing of the anode and the electrolyte have to be carried out at high temperatures to fully densify the electrolyte. On the downside, high firing temperatures lead to coarsening of the microstructure of the electrode and to a reduction of the electrochemically active area. One way to avoid these problems connected with a high firing temperature, is the so called impregnation method [35]. .

1.7.3.3. Cathode materials

At the SOFC cathode oxygen is reduced to oxide ions using electrons provided through the interconnect. These ions subsequently enter the electrolyte. The place where these reactions occur must contain gaseous oxygen, electrons and a possible pathway for the oxide ions to move away. Cathode materials must be electronically conductive, highly porous to allow contact with oxygen, and should provide some catalytic activity for the reduction of oxygen. They should be chemically and mechanically stable at operation temperature and compatible to the other fuel cell materials.

State of the art SOFC cathodes are composites of the electrolyte material, mainly YSZ, and ceramic materials with perovskite structures like lanthanum strontium manganite (LSM), lanthanum strontium ferrite (LSF) or lanthanum strontium cobalt ferrite (LSCF). LSM is a good electronic conductor and reasonably compatible with YSZ, but unfortunately it is a poor ionic conductor. LSM/YSZ composite cathodes show good electrochemical performance at high temperatures over 800 °C [36]. At lower temperatures mixed ionic and electronic conductors (MIECs) like LSCF show better performances than LSM [37].

1.7.3.4. Anode materials

At the SOFC anode hydrogen or other fuels are oxidised and react with the oxide ions from the electrolyte to form water and other reaction products. The electrons generated in this oxidation process are removed via the interconnect. These reactions depend on the presence of gaseous fuels and possible pathways for the electrons and reaction products to move away. Anode materials must be electronically conductive, highly porous to allow contact with the fuel, and should provide some catalytic activity for the fuel oxidation. They should be chemically and mechanically stable at operation temperature at reducing conditions and compatible to the other fuel cell materials.

1.7.3.4.1. State of the art SOFC anodes

The state of the art anode for SOFCs is a composite of a ceramic and a metallic material, a so called cermet. The ceramic material is usually identical with the material of the electrolyte, YSZ, and improves the mechanical stability and conductivity for oxide ions as well as providing a better match of the thermal expansion between the electrolyte and the electrode. Metallic nickel particles alongside the YSZ provide electronically conductive pathways and catalytic activity for the fuel oxidation. Ni/YSZ anodes exhibit excellent electronic conductivity and catalytic performance for the oxidation of hydrogen and for reforming reactions of hydrocarbons.

However, next to these advantages, the system Ni/YSZ exhibits also some disadvantages when used as a SOFC anode. Firstly, metallic nickel is catalytically very active for the cracking of hydrocarbons, leading to a build up of carbon fibres if the fuel cell is fuelled by hydrocarbons. Carbon fibres can lead to a loss of nickel due to metal dusting, they can produce mechanical stress and fracture the electrode, or block some of the pores, all of which deteriorate the performance of the anode. Cracking can be avoided by adding steam to the fuel, but this also means fuel dilution and a lower overall performance [38] , or by replacing nickel with copper, which results in problems with the thermal stability of the anode [39].

At high temperature metallic nickel tends to agglomerate resulting in grain growth and reduction of the specific nickel surface [40]. Although the anode is exposed to a reducing atmosphere under working conditions, during start up and shut down periods it is also likely to be in contact with ambient atmosphere containing oxygen. Because of this some tolerance to redox cycling is desirable for SOFC anodes. The oxidation of nickel to nickel oxide causes a massive volume expansion, leading to volume instability upon redox cycling and a potential danger of damage to the Ni/YSZ cermet anode.

Lastly, nickel is intolerant to impurities in the fuel, especially sulphur, which poisons the catalyst and increases the polarisation of the fuel cell. The poisoning is recoverable at H₂S concentrations of 1-5 ppm, but irreversible at H₂S concentrations of 100 ppm and more [41]. Since fuels from organic sources always contain sulphur it is necessary to clean fuels in a desulphuriser before the use in SOFCs with Ni/YSZ anodes, adding to the costs of the process.

1.7.3.4.2. Alternative SOFC anodes

There has been a lot of research with the goal of finding alternative anode materials to overcome the disadvantages and retain the advantages of the Ni/YSZ anode.

In the first category of alternative anodes, the Ni/YSZ system was retained, but other components added. To suppress carbon deposition, earth alkaline oxides like CaO and SrO were added around a quantity of 2 wt% [42]. Preparing cermets with other metals (cobalt, iron and copper) additional to nickel by combustion synthesis [43] served the same purpose.

Changing the ceramic part from YSZ to CGO the nickel catalyst inside the cermet still showed good catalytic activity for the oxidation of hydrogen and methane [44], [45] and good electrochemical performance [46]. Partly or fully replacing nickel with copper within this system prevents the formation of carbon [39], [47], [48]. Adding a mixed ionic and electronic conductor as a third component to the anode further decreases the polarisation resistance [49].

1.7.3.4.3. Fully ceramic SOFC anodes

A different strategy for alternative anodes for SOFCs is to substitute nickel with a ceramic phase, eliminating all the problems a metallic phase brings to the performance of the anode. On the downside it is generally very difficult to find a ceramic which matches the electronic conductivity and the catalytic activity of nickel. In the literature predominantly two groups of oxides have been of interest, chromites and titanates.

Doped Lanthanum Chromites are well known for being good electronic conductors and chemically and mechanically stable at high temperatures. They can be used for interconnectors in SOFCs, but their electronic conductivity also makes them an interesting candidate for a component in a composite anode. Lanthanum chromite doped with strontium and manganese and cerium (LSCM and CeLSCM) exhibited good performance as single phase anodes [50] [51], and even better performance as a composite with YSZ [52] or CGO [53] [54]. The microstructure of the composite anodes turned out particularly important, especially the microstructural changes upon redox cycling [55] [56].

Lanthanum strontium titanate (LST) was investigated as an anode for SOFCs [57], but similar to the chromite materials the electrochemical performance was better when used in composites with YSZ [58]. Of particular interest was the manganese doped material (LSTM), which next to good electrochemical performance and compatibility to YSZ [59] [60] showed interesting microstructural behaviour upon redox cycling. After the impregnation in air LSTM forms a dense coating on the YSZ scaffold, reminiscent of the wetting behaviour of liquids on solid surfaces. Under fuel conditions the dense coating breaks into interconnected nanoparticles, providing an uniform distribution of the impregnated phase and a big surface area [55].

1.7.3.4.4. Catalysts for SOFC anodes

Generally catalysts accelerate the rate of a reaction by lowering the reactions activation energy but do not change the thermodynamic equilibrium. Catalysts play a key role in the electrochemical performance of fuel cells [61]. The relevant reactions in a solid oxide fuel cell can be the oxidation of hydrogen, direct oxidation of methane or the steam reforming of methane or higher hydrocarbons.

In the state of the art SOFC anode metallic nickel is the catalyst. Nickel is well known to have high catalytic activity for the oxidation of hydrogen and also for steam reforming and is industrially utilised for these reactions. As mentioned in chapter 1.7.4.1 nickel unfortunately also catalyses the cracking of hydrocarbons and formation of carbon fibres, which are unwanted reactions in the operation of solid oxide fuel cells and it is sensitive to poisoning by sulphur.

Precious metal catalysts like platinum, palladium and rhodium are well known oxidation catalysts as well and widely used in research [62]. However, their high price is a major drawback for commercial use and they suffer from similar poisoning problems as nickel.

Cerium oxide shows good electrochemical performance and good catalytic activity [61], especially for the oxidation of methane [63]. Mixed ionic and electronic conductive doped perovskite oxides can work as oxidation catalysts as well due to their ability to reversibly accommodate and release lattice oxygen at high temperatures [64].

Recent research work points out the benefits of so called “intelligent catalysts”, consisting of perovskite oxides, which, under reducing conditions, produce in

situ exsolutions of nanoparticles of the catalytically active metal [65] [66]. Thus the catalyst has a very high specific area and the anode shows better electrochemical performance.

1.7.3.5. Impregnation method

In the impregnation method for the fabrication of composite materials the scaffold phase is fired at high temperatures to form a porous skeleton, and subsequently an aqueous precursor of the second material is infiltrated into the pores of the skeleton, to form the desired material in situ after firing at lower temperatures.

This method offers big advantages if the two components of a composite have to be fired at different temperatures, either because one of the materials is instable at the temperature necessary for the formation of the other material, or because one of the materials needs to be distributed in small particles for optimal performance and shows unwanted coarsening if the temperature is too high.

The electrodes of solid oxide fuel cells can consist of a skeleton phase to provide ionic conductivity and contact to the electrolyte, a second phase for electronic conductivity and sometimes a third phase providing catalytic activity for the electrochemical reactions, as described in chapter 1.7.3. Using the impregnation method for the fabrication of composite electrodes allows the co-firing of the skeleton part of the electrode with the electrolyte at high temperatures of 1400 °C to 1500 °C provides a good bondage between these two phases, avoiding delamination and resulting in an ionic conduction path to all areas of the electrode, increasing the triple phase boundary. The lower firing temperature after the impregnation of the second electrode phase, typically

between 1000 °C and 1200 °C reduces the risk of unwanted solid state reactions between the different electrode materials during the fabrication process [67]. Generally lower firing temperatures at the fabrication also lead to a smaller grain size of the catalytic active phase, which increases the catalytically active area.

Cathodes prepared by impregnation of lanthanum strontium manganate (LSM) into a YSZ skeleton have been used successfully for a long time [68], and for composite anodes of YSZ and the mixed ionic and electronic conductors lanthanum strontium cobaltate (LSC) and lanthanum strontium ferrate (LSF), the impregnation method is even more important, because these perovskites show unwanted reactions with YSZ at temperatures larger than 1000 °C [69].

In anodes for SOFCs the impregnation method has been used to improve the performance of conventional nickel based anodes by the impregnation of YSZ and CGO nanoparticles, inhibiting nickel agglomeration and sintering [70]. The impregnation of precious metals like palladium or platinum improves the performance of anodes [71] and cathodes [72] by introducing a catalytic effect for the fuel oxidation, especially if the particles are very small, as provided by the low temperature firing after impregnation. A cheaper way of introducing a catalyst next to precious metals is the impregnation of cerium oxide into the anodes of solid oxide fuel cells [73]. Fully ceramic anodes based on YSZ and doped lanthanum strontium chromates [55] and lanthanum strontium titanates [55] [60] were successfully prepared using the impregnation method, and the importance of the microstructure for the performance of the anode in these compositions was investigated [55].

Recently a large area solid oxide fuel cell (5*5 cm) was fabricated using the impregnation method. The large area made it challenging to achieve a gas tight thin electrolyte between highly porous electrodes. The infiltration was a time consuming multiple step process [74].

1.7.4. Perovskite oxides for SOFCs

Perovskite oxides are mixed oxides with the general formula ABO_3 . The A-cations are relatively large, similar to the size of the oxide anions, and form a cubic closed packed structure together with the anions, containing one A-cation for every three oxide ions. One quarter of the octahedral holes of this cubic closed packing is filled with the significantly smaller B-cations. The unit cell of the ideal perovskite can be seen as a cube with the corners occupied by the B-cations, the centre by an A-cation and the middle of the edges by one oxide ion each. Every B-site cation is surrounded by 6 oxide anions forming an octahedron, while the A-site cations have a 12-fold cuboctahedral coordination.

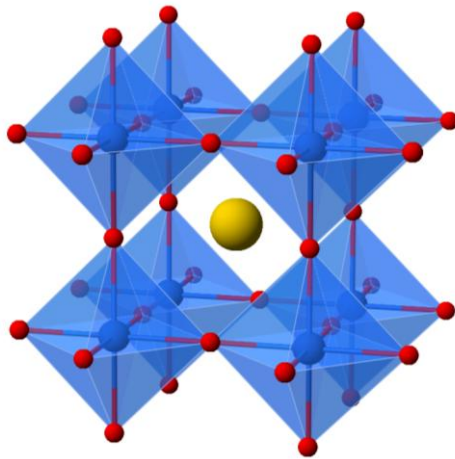


Figure 1.11: Schematic illustration of a perovskite oxide. The A-site cation is coloured yellow, the B-site cations blue and the oxide ions red. The size of the spheres in the drawing does not reflect the correct ratio of the ionic radii of the ions

For an ideal cubic single cell the sum of the radii of the B-site cation and the oxide ion has to be $\sqrt{2}$ times the sum of the radii of the A-site cation and the oxide ion. Most of the real perovskites do not have this ideal cubic structure, in fact, the perovskite system is known to be very flexible tolerating deviations from the ideal ratio of radii, leading to a big variety of possibilities for cations to occupy the A- and the B-site. The degree of deviation from the ideal radii ratio

and hence of the distortion of the unit cell can be expressed by the Goldschmidt factor.

$$t = \frac{r_A + r_O}{\sqrt{2} \cdot (r_B + r_O)}$$

t ... Goldschmidt tolerance factor

r_A ... ionic radius of the A-site cation [m]

r_B ... ionic radius of the B-site cation [m]

r_O ... ionic radius of the oxide ion [m]

Equation 1.8: Goldschmidt tolerance factor

In an ideal perovskite the tolerance factor would be one, however, stable perovskites are known in a range of tolerance factors from approximately 0.8 to 1.1. The tilting of the BO_6 octahedra in case of the tolerance factor being smaller than one can result in maintaining the cubic unit cell or a change to the orthorhombic system, depending how big the deviation is. If the tolerance factor is smaller than 0.8, the ilmenite structure will become more stable than the perovskite. A tolerance factor bigger than one can lead to hexagonal variants of the perovskite structure. The layers are stacked in a hexagonal close packed structure instead of cubic closed packed, and hence the BO_6 octahedra are sharing faces instead of corners.

The sum of the positive charges of the A- and B- cation in an ideal perovskite is +6, however, in real perovskites the B-cation often is multivalent, which, depending on the redox conditions in the environment, may lead to a sum different from +6. Doping of the A- or B-site with ions of a valence different from the original ions also leads to a deviation from the +6 charge of the cations in the perovskite, and not all of the A sites of the perovskites have to be filled with cations, some of them can be empty, a phenomenon known as A-site

deficiency. Whatever the reason for a cation charge different from +6, to retain charge neutrality, the amount of oxide ions has to change, leading to oxygen deficient perovskites in case of a cation charge sum smaller than +6, or oxygen excess perovskites in the case of a charge sum bigger than +6. Oxygen deficiencies as well as A-site deficiencies can be distributed randomly over the whole perovskite crystal, but also can be ordered, leading to superstructures and to layered perovskites.

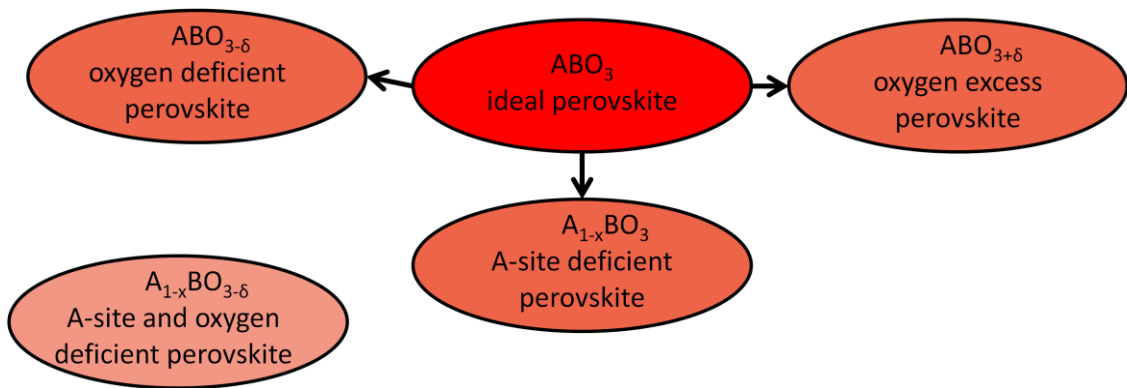


Figure 1.12: Examples for perovskite nonstoichiometry.

The accommodation of cations slightly smaller or bigger than the demands of the ideal structure, the possibility of doping A- and B-site, the tolerance for vacancies on the A-site and for excess or vacancies of oxygen with ordering and superstructures all lead to an exceptional variety of chemistry and structure in the perovskite family. This remarkable versatility of the perovskite oxides leads to a huge range of magnetic, optic, electrical and catalytic properties which often can be tailored for certain applications by doping.

Next to this chemical flexibility, perovskites generally show excellent thermal and mechanical stability even above 1000 °C and during temperature cycling, making them particularly interesting for the application in SOFCs. A lot of the

perovskite oxides also exhibit good chemical and mechanical compatibility with electrolyte materials like YSZ and CGO. Transition metal ions like titanium, niobium or vanadium on the B-site of the perovskite can adopt different oxidation states, thus generating free electrons and electronic conductivity under reducing conditions. Multivalent B-sites and doping by cations with a valence different from the original ions lead to oxygen excess or oxygen deficiency, both providing the possibility of ionic conductivity for oxide ions. Through doping it is possible to provide perovskite materials which show mixed ionic and electronic conductivity either at reducing or oxidising conditions, making them ideal materials for fuel cell anodes or cathodes, respectively.

In the past perovskite materials have been reported as electrolyte, anode, cathode and interconnect materials for SOFCs, making an “all perovskite” SOFC fuel cell at least a thinkable option. Perovskite materials of the composition $\text{La}_{0.8}\text{Sr}_{0.2}\text{Ga}_{0.8}\text{Mg}_{0.2-x}\text{Co}_x\text{O}_{3-\delta}$ (LSGMC) have been successfully tested as SOFC electrolytes at temperatures as low as 650 °C, with an oxide ion conductivity better than YSZ [75]. $\text{La}_{0.8}\text{Sr}_{0.2}\text{MnO}_3$ (LSM), a perovskite oxide as well, is the state of the art material for SOFC cathodes [76]. At lower temperatures, perovskites of the composition $\text{La}_{0.8}\text{Sr}_{0.2}\text{FeO}_3$ (LSF) [77], $\text{La}_{0.8}\text{Sr}_{0.2}\text{CoO}_3$ (LSC) [78], $\text{La}_{0.8}\text{Sr}_{0.2}\text{Co}_x\text{Fe}_{1-x}\text{O}_3$ (LSCF) [79] [77] and $\text{NdBa}_{1-x}\text{Sr}_x\text{Co}_2\text{O}_{5+\delta}$ (NBSCO) [80] showed even better electrochemical performance. Doped LaCrO_3 is the state of the art interconnect material for fuel cells operating at temperatures too high to allow steel [81] [25].

As an anode material, $\text{La}_{0.75}\text{Sr}_{0.25}\text{Cr}_{0.5}\text{Mn}_{0.5}\text{O}_3$ (LSCM) presents good electrochemical performance together with both YSZ electrolytes [50] [55] and LSGM electrolytes [82]. A-site deficient titanates like $\text{La}_{0.4}\text{Sr}_{0.4}\text{TiO}_3$ show excellent electronic conductivity and also some oxide ion conductivity under reducing conditions [83], making them very interesting materials for SOFC anodes. By doping the B-site of these titanates with gallium, iron or nickel the n-type conductivity and the mobility of the oxide ions in the lattice is greatly improved [84] [66]. Doping the B-site with manganese leads to an improvement

of the performance in composite anodes with YSZ, probably due to improved wetting of the YSZ scaffold during the production of the composite [55]. Another promising double perovskite anode material is $\text{Sr}_2\text{MgMoO}_{6-\delta}$, performing excellent when tested with hydrogen or methane fuels [85].

- [1] "Statistical Review of World Energy." *BP*, 2011.
- [2] "Key World Energy Statistics." *International Energy Agency*, 2010.
- [3] "Energy Use Per Capita." *World Bank, World Development Indicators*, 2012.
- [4] L. Maugeri, "Oil: Never Cry Wolf--Why the Petroleum Age Is Far from over," *Science*, **304**, 1114–1115, 2004.
- [5] N. A. Owen, O. R. Inderwildi, and D. A. King, "The status of conventional world oil reserves—Hype or cause for concern?," *Energy Policy*, **38**, 4743–4749, 2010.
- [6] J. Hansen, M. Sato, and R. Ruedy, "Perception of climate change," *PNAS*, 2012.
- [7] "Fourth Assessment Report, Summary for Policymakers." *UN Intergovernmental Panel on Climate Change (IPCC)*, 2007.
- [8] I. Dobrev, B. Mandadzhiev, R. Petranov, and B. J. Savilonis, "Implementation of Renewable Energy Sources in the State of California." *Worcester Polytechnic Institute*, 2007.
- [9] High Level Panel of Experts, "Price volatility and food security." *UN Committee on World Food Security*, 2011.
- [10] "The Scottish Energy Study Vol 1: Energy in Scotland: Supply & Demand." *The Scottish Government*, 2006.
- [11] J. Muth and E. Smith, "45% by 2030." *European Renewable Energy Council (EREC)*, 2011.
- [12] P. Simon and Y. Gogotsi, "Materials for electrochemical capacitors," *Nature Materials*, **7**, 845–854, 2008.
- [13] D. Rastler, "Electricity Energy Storage Technology Options." *Electric Power Research Institute (EPRI)*, 2010.
- [14] S. Succar and R. H. Williams, "Compressed Air Energy Storage: Theory, Resources, and Applications for Wind Power." *Princeton Environmental Institute*, 2008.
- [15] R. Hebner, J. Beno, and A. Walls, "Flywheel batteries come around again," *IEEE Spectrum*, **39**, 46–51, 2002.
- [16] N.-K. C. Nair and N. Garimella, "Battery energy storage systems: Assessment for small-scale renewable energy integration," *Energy and Buildings*, **42**, 2124–2130, 2010.
- [17] C. Ponce de León, A. Frías-Ferrer, J. González-García, D. A. Szánto, and F. C. Walsh, "Redox flow cells for energy conversion," *Journal of Power Sources*, **160**, 716–732, 2006.
- [18] P. P. Edwards, V. L. Kuznetsov, W. I. F. David, and N. P. Brandon, "Hydrogen and fuel cells: Towards a sustainable energy future," *Energy Policy*, **36**, 4356–4362, 2008.
- [19] S. H. Jensen, X. Sun, S. D. Ebbesen, R. Knibbe, and M. Mogensen, "Hydrogen and synthetic fuel production using pressurized solid oxide electrolysis cells," *International Journal of Hydrogen Energy*, **35**, 9544–9549, 2010.
- [20] R. Lan, J. T. S. Irvine, and S. Tao, "Ammonia and related chemicals as potential indirect hydrogen storage materials," *International Journal of Hydrogen Energy*, **37**, 1482–1494, 2012.
- [21] M. M. Mench, "Fuel Cell Engines", *John Wiley & Sons*, 2008.
- [22] EG&G Technical Services Inc., "Fuel Cell Handbook", 7th ed. *U.S. Department of Energy*, 2004.
- [23] "Fuel Cell Technologies Program." *U.S. Department of Energy*, 2011.

- [24] I. Frenzel, A. Loukou, D. Trimis, F. Schroeter, L. Mir, R. Marin, B. Egilegor, J. Manzanedo, G. Raju, M. de Bruijne, R. Wesseling, S. Fernandes, J. M. C. Pereira, G. Vourliotakis, M. Founti, and O. Posdziech, "Development of an SOFC based Micro-CHP System in the Framework of the European Project FC-DISTRICT," *Energy Procedia*, **28**, 170–181, 2012.
- [25] J. W. Fergus, "Lanthanum chromite-based materials for solid oxide fuel cell interconnects," *Solid State Ionics*, **171**, 1–15, 2004.
- [26] J. W. Fergus, "Metallic interconnects for solid oxide fuel cells," *Materials Science and Engineering*, **397**, 271–283, 2005.
- [27] C. Gindorf, L. Singheiser, and K. Hilpert, "Chromium vaporisation from Fe, Cr base alloys used as interconnect in fuel cells," *Steel research*, **72**, 528–533.
- [28] S. Geng, J. Zhu, M. P. Brady, H. U. Anderson, X.-D. Zhou, and Z. Yang, "A low-Cr metallic interconnect for intermediate-temperature solid oxide fuel cells," *Journal of Power Sources*, **172**, 775–781, 2007.
- [29] L. Smart and E. Moore, "Solid state chemistry: an introduction" *CRC Press*, 2012.
- [30] J. A. Kilner and B. C. H. Steele, "Mass transport in anion deficient fluorite oxides," *Non Stoichiometric Oxides*, 661–666, 1981.
- [31] V. Kharton, F. Marques, and A. Atkinson, "Transport properties of solid oxide electrolyte ceramics: a brief review," *Solid State Ionics*, **174**, 135–149, 2004.
- [32] B. C. H. Steele, "Appraisal of $Ce_{1-y}Gd_yO_{2-y/2}$ electrolytes for IT-SOFC operation at 500°C," *Solid State Ionics*, **129**, 95–110, 2000.
- [33] T. Ishihara, "Perovskite Oxide for Solid Oxide Fuel Cells," *Springer*, 65-89, 2009.
- [34] K. Huang and J. B. Goodenough, "A solid oxide fuel cell based on Sr- and Mg-doped LaGaO₃ electrolyte: the role of a rare-earth oxide buffer," *Journal of Alloys and Compounds*, **303–304**, 454–464, 2000.
- [35] G. Kim, G. Corre, J. T. S. Irvine, J. M. Vohs, and R. J. Gorte, "Engineering Composite Oxide SOFC Anodes for Efficient Oxidation of Methane," *Electrochem. Solid-State Lett.*, **11**, B16–B19, 2008.
- [36] J. M. Ralph, A. C. Schoeler, and M. Krumpelt, "Materials for lower temperature solid oxide fuel cells," *Journal of Materials Science*, **36**, 1161–1172, 2001.
- [37] F. Tietz, V. A. C. Haanappel, A. Mai, J. Mertens, and D. Stöver, "Performance of LSCF cathodes in cell tests," *Journal of Power Sources*, **156**, 20–22, 2006.
- [38] C. M. Finnerty and R. M. Ormerod, "Internal reforming over nickel/zirconia anodes in SOFCs operating on methane: influence of anode formulation, pre-treatment and operating conditions," *Journal of Power Sources*, **86**, 390–394, 2000.
- [39] T. Hibino, A. Hashimoto, K. Asano, M. Yano, M. Suzuki, and M. Sano, "An Intermediate-Temperature Solid Oxide Fuel Cell Providing Higher Performance With Hydrocarbons Than With Hydrogen," *Electrochemical and Solid-State Letters*, **5(11)**, A242–A244, 2002.
- [40] D. Simwonis, F. Tietz, and D. Stöver, "Nickel coarsening in annealed Ni/8YSZ anode substrates for solid oxide fuel cells," *Solid State Ionics*, **132**, 241–251, Jul. 2000.
- [41] Y. Matsuzaki and I. Yasuda, "The poisoning effect of sulfur-containing impurity gas on a SOFC anode: Part I. Dependence on temperature, time, and impurity concentration," *Solid State Ionics*, **132**, 261–269, 2000.

- [42] T. Takeguchi, Y. Kani, T. Yano, R. Kikuchi, K. Eguchi, K. Tsujimoto, Y. Uchida, A. Ueno, K. Omoshiki, and M. Aizawa, "Study on steam reforming of CH₄ and C₂ hydrocarbons and carbon deposition on Ni-YSZ cermets," *Journal of Power Sources*, **112**, 588–595, 2002.
- [43] A. Ringuedé, D. P. Fagg, and J. R. Frade, "Electrochemical behaviour and degradation of (Ni,M)/YSZ cermet electrodes (M=Co,Cu,Fe) for high temperature applications of solid electrolytes," *Journal of the European Ceramic Society*, **24**, 1355–1358, 2004.
- [44] M. B. Joerger and L. J. Gauckler, "Direct Oxidation Of Hydrocarbons At Catalytically Active Anodes," *Proceedings of the 7th International Symposium on Solid Oxide Fuel Cells (SOFC VII)*, 662, 2001.
- [45] B. Rösch, H. Tu, A. O. Störmer, A. C. Müller, and U. Stimming, "Electrochemical characterization of Ni-Ce_{0.9}Gd_{0.1}O_{2-δ} for SOFC anodes," *Solid State Ionics*, **175**, 113–117, 2004.
- [46] S. Primdahl and M. Mogensen, "Mixed conductor anodes: Ni as electrocatalyst for hydrogen conversion," *Solid State Ionics*, **152–153**, 597–608, 2002.
- [47] R. J. Gorte, J. M. Vohs, and S. McIntosh, "Recent developments on anodes for direct fuel utilization in SOFC," *Solid State Ionics*, **175**, 1–6, 2004.
- [48] R. J. Gorte, H. Kim, and J. M. Vohs, "Novel SOFC anodes for the direct electrochemical oxidation of hydrocarbon," *Journal of Power Sources*, **106**, 10–15, 2002.
- [49] J. C. Ruiz-Morales, J. Canales-Vázquez, D. Marrero-López, J. T. S. Irvine, and P. Núñez, "Improvement of the electrochemical properties of novel solid oxide fuel cell anodes, La_{0.75}Sr_{0.25}Cr_{0.5}Mn_{0.5}O_{3-δ} and La₄Sr₈Ti₁₁Mn_{0.5}Ga_{0.5}O_{37.5-δ}, using Cu-YSZ-based cermets," *Electrochimica Acta*, **52**, 7217–7225, 2007.
- [50] S. Tao and J. T. S. Irvine, "A redox-stable efficient anode for solid-oxide fuel cells," *Nature Materials*, **2**, 320–323, 2003.
- [51] E. Lay, G. Gauthier, S. Rosini, C. Savaniu, and J. T. S. Irvine, "Ce-substituted LSCM as new anode material for SOFC operating in dry methane," *Solid State Ionics*, **179**, 1562–1566, 2008.
- [52] S. P. Jiang, X. J. Chen, S. H. Chan, J. T. Kwok, and K. A. Khor, "(La_{0.75}Sr_{0.25})(Cr_{0.5}Mn_{0.5})O₃/YSZ composite anodes for methane oxidation reaction in solid oxide fuel cells," *Solid State Ionics*, **177**, 149–157, 2006.
- [53] J. C. Ruiz-Morales, J. Canales-Vázquez, B. Ballesteros-Pérez, J. Peña-Martínez, D. Marrero-López, J. T. S. Irvine, and P. Núñez, "LSCM-(YSZ-CGO) composites as improved symmetrical electrodes for solid oxide fuel cells," *Journal of the European Ceramic Society*, **27**, 4223–4227, 2007.
- [54] X. J. Chen, Q. L. Liu, K. A. Khor, and S. H. Chan, "High-performance (La,Sr)(Cr,Mn)O₃/(Gd,Ce)O_{2-δ} composite anode for direct oxidation of methane," *Journal of Power Sources*, **165**, 34–40, 2007.
- [55] G. Corre, G. Kim, M. Cassidy, J. M. Vohs, R. J. Gorte, and J. T. S. Irvine, "Activation and Ripening of Impregnated Manganese Containing Perovskite SOFC Electrodes under Redox Cycling," *Chem. Mater.*, **21**, 1077–1084, 2009.
- [56] G. Kim, S. Lee, J. Y. Shin, G. Corre, J. T. S. Irvine, J. M. Vohs, and R. J. Gorte, "Investigation of the Structural and Catalytic Requirements for High-Performance SOFC Anodes Formed by Infiltration of LSCM," *Electrochemical and Solid-State Letters*, **12**, B48, 2009.

- [57] J. Canales-Vázquez, S. . Tao, and J. T. . Irvine, "Electrical properties in $\text{La}_2\text{Sr}_4\text{Ti}_6\text{O}_{19-\delta}$: a potential anode for high temperature fuel cells," *Solid State Ionics*, **159**, 159–165, 2003.
- [58] R. Mukundan, E. L. Brosha, and F. H. Garzon, "Sulfur Tolerant Anodes for SOFCs," *Electrochem. Solid-State Lett.*, **7**, A5–A7, 2004.
- [59] A. Ovalle, J. C. Ruiz-Morales, J. Canales-Vázquez, D. Marrero-López, and J. T. S. Irvine, "Mn-substituted titanates as efficient anodes for direct methane SOFCs," *Solid State Ionics*, **177**, 1997–2003, 2006.
- [60] Q. X. Fu, F. Tietz, and D. Stöver, " $\text{La}_{0.4}\text{Sr}_{0.6}\text{Ti}_{1-x}\text{Mn}_x\text{O}_{3-\delta}$ Perovskites as Anode Materials for Solid Oxide Fuel Cells," *J. Electrochem. Soc.*, **153**, D74–D83, 2006.
- [61] J. H. Kim, H. Schlegl, and J. T. S. Irvine, "The catalytic effect of impregnated (La, Sr)(Ti, Mn) $\text{O}_{3\pm\delta}$ with CeO_2 and Pd as potential anode materials in high temperature solid oxide fuel cells," *International Journal of Hydrogen Energy*, **37**, 14511–14517, 2012.
- [62] S. McIntosh, J. M. Vohs, and R. J. Gorte, "Effect of Precious-Metal Dopants on SOFC Anodes for Direct Utilization of Hydrocarbons," *Electrochem. Solid-State Lett.*, **6**, A240–A243, 2003.
- [63] E. P. Murray, T. Tsai, and S. A. Barnett, "A direct-methane fuel cell with a ceria-based anode," *Nature*, **400**, 649–651, 1999.
- [64] H. Arai, T. Yamada, K. Eguchi, and T. Seiyama, "Catalytic combustion of methane over various perovskite-type oxides," *Applied Catalysis*, **26**, 265–276, 1986.
- [65] L. Adjianto, V. B. Padmanabhan, R. Küngas, R. J. Gorte, and J. M. Vohs, "Transition metal-doped rare earth vanadates: a regenerable catalytic material for SOFC anodes," *J. Mater. Chem.*, **22**, 11396–11402, 2012.
- [66] G. Tsekouras, D. Neagu, and J. T. S. Irvine, "Step-change in high temperature steam electrolysis performance of perovskite oxide cathodes with exsolution of B-site dopants," *Energy Environ. Sci.*, **6**, 256–266, 2012.
- [67] G. P. G. Corre, "Studies of Alternative Anodes and Ethanol Fuel for SOFCs," *Ph.D., University of St. Andrews*, 2009.
- [68] T. Z. Sholklipper, C. Lu, C. P. Jacobson, S. J. Visco, and L. C. D. Jonghe, "LSM-Infiltrated Solid Oxide Fuel Cell Cathodes," *Electrochem. Solid-State Lett.*, **9**, A376–A378, 2006.
- [69] Y. Huang, J. M. Vohs, and R. J. Gorte, "Fabrication of Sr-Doped LaFeO_3 YSZ Composite Cathodes," *J. Electrochem. Soc.*, **151**, A646–A651, 2004.
- [70] S. P. Jiang, S. Zhang, Y. D. Zhen, and W. Wang, "Fabrication and Performance of Impregnated Ni Anodes of Solid Oxide Fuel Cells," *Journal of the American Ceramic Society*, **88**, 1779–1785, 2005.
- [71] A. Babaei, S. P. Jiang, and J. Li, "Electrocatalytic Promotion of Palladium Nanoparticles on Hydrogen Oxidation on Ni/GDC Anodes of SOFCs via Spillover," *J. Electrochem. Soc.*, **156**, B1022–B1029, 2009.
- [72] H. Uchida, S. Arisaka, and M. Watanabe, "High Performance Electrode for Medium-Temperature Solid Oxide Fuel Cells: Control of Microstructure of $\text{La}(\text{Sr})\text{CoO}_3$ Cathodes with Highly Dispersed Pt Electrocatalysts," *J. Electrochem. Soc.*, **149**, A13–A18, 2002.

- [73] J. H. Kim, H. Schlegl, and J. T. S. Irvine, "The catalytic effect of impregnated (La, Sr)(Ti, Mn)O_{3±δ} with CeO₂ and Pd as potential anode materials in high temperature solid oxide fuel cells," *International Journal of Hydrogen Energy*, **37**, 14511–14517, 2012.
- [74] C. S. Ni, J. M. Vohs, R. J. Gorte, and J. T. S. Irvine, "Fabrication and characterisation of a large-area solid oxide fuel cell based on dual tape cast YSZ electrode skeleton supported YSZ electrolytes with vanadate and ferrite perovskite-impregnated anodes and cathodes," *J. Mater. Chem. A*, 2014.
- [75] K. Kuroda, I. Hashimoto, K. Adachi, J. Akikusa, Y. Tamou, N. Komada, T. Ishihara, and Y. Takita, "Characterization of solid oxide fuel cell using doped lanthanum gallate," *Solid State Ionics*, **132**, 199–208, 2000.
- [76] T. Tsai and S. A. Barnett, "Effect of LSM-YSZ cathode on thin-electrolyte solid oxide fuel cell performance," *Solid State Ionics*, **93**, 207–217, 1997.
- [77] J. M. Ralph, C. Rossignol, and R. Kumar, "Cathode Materials for Reduced-Temperature SOFCs," *J. Electrochem. Soc.*, **150**, A1518–A1522, 2003.
- [78] J. Januschewsky, M. Ahrens, A. Opitz, F. Kubel, and J. Fleig, "Optimized La_{0.6}Sr_{0.4}CoO_{3-δ} Thin-Film Electrodes with Extremely Fast Oxygen-Reduction Kinetics," *Advanced Functional Materials*, **19**, 3151–3156, 2009.
- [79] I. A. Raj, A. S. Nesaraj, M. Kumar, F. Tietz, H. P. Buchkremer, and D. Stoeber, "On the suitability of La_{0.60}Sr_{0.40}Co_{0.20}Fe_{0.80}O₃ cathode for the Intermediate Temperature Solid Oxide Fuel Cell (ITSOFC)," *Journal of New Materials for Electrochemical Systems*, **7**, 145–151, 2004.
- [80] J. H. Kim and J. T. S. Irvine, "Characterization of layered perovskite oxides NdBa_{1-x}Sr_xCo₂O_{5+δ} (x = 0 and 0.5) as cathode materials for IT-SOFC," *International Journal of Hydrogen Energy*, **37**, 5920–5929, 2012.
- [81] N. Sakai, H. Yokokawa, T. Horita, and K. Yamaji, "Lanthanum Chromite-Based Interconnects as Key Materials for SOFC Stack Development," *International Journal of Applied Ceramic Technology*, **1**, 23–30, 2004.
- [82] S. W. Tao, J. T. S. Irvine, and J. A. Kilner, "An Efficient Solid Oxide Fuel Cell Based upon Single-Phase Perovskites," *Advanced Materials*, **17**, 1734–1737, 2005.
- [83] D. Neagu and J. T. S. Irvine, "Structure and Properties of La_{0.4}Sr_{0.4}TiO₃ Ceramics for Use as Anode Materials in Solid Oxide Fuel Cells," *Chem. Mater.*, **22**, 5042–5053, 2011.
- [84] D. Neagu and J. T. S. Irvine, "Enhancing Electronic Conductivity in Strontium Titanates through Correlated A and B-Site Doping," *Chem. Mater.*, **23**, 1607–1617, 2011.
- [85] P. Zhang, Y.-H. Huang, J.-G. Cheng, Z.-Q. Mao, and J. B. Goodenough, "Sr₂CoMoO₆ anode for solid oxide fuel cell running on H₂ and CH₄ fuels," *Journal of Power Sources*, **196**, 1738–1743, 2011.

2. Experimental Methods and Techniques

The research necessary for this work was partly carried out using only the composite anodes, partly using complete fuel cells consisting of anode, electrolyte, cathode and current collection. For practical reason small button cells were used for all electrochemical testing.

This chapter describes the fabrication of the button cells as well as the techniques used for phase characterisation, investigation of the microstructure and for electrochemical testing. Where it was appropriate, an overview about the theoretical basics of the utilised method was prefixed.

2.1. Preparation of thin button cells

Circular button cells were used for the electrochemical testing of single fuel cells. The smaller anode is cylindrical shaped and sitting concentrically on the electrolyte and the cathode cylinder which has a bigger diameter. Depending on the firing temperature the diameter of cathode and electrolyte was between 14 mm and 18 mm, the diameter of the anode between 6.5 mm and 8 mm and the overall thickness of the single cell around 200 μm to 270 μm .

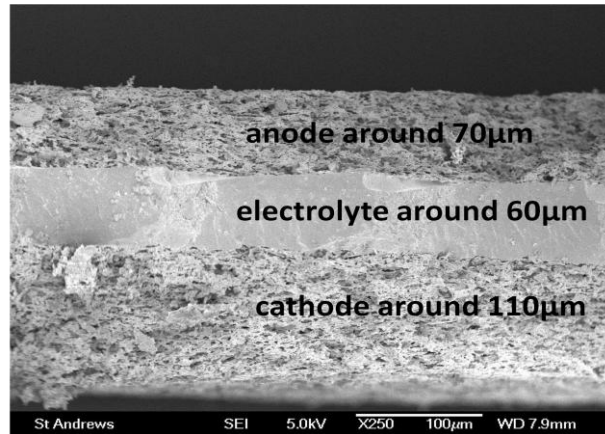


Figure 2.1: Photo of a single fuel cell from above and SEM picture of the cross section of a single cell, magnification 250-x, with the thickness of the layers of this specific single cell added.

2.1.1. Fabrication of the skeleton

Generally the single cells were fabricated by laminating three green tapes, which were produced by tape casting. Three different tapes were tape cast from slurries and combined to form the green cell [1] [2]. After the firing of the cells at temperatures between 1400 °C and 1500 °C, the porous parts of the skeletons, anode and cathode, were impregnated with aqueous precursors of another ceramic phase to achieve composite electrodes after another firing step between 1150 °C and 1250 °C. Catalysts were also added by the impregnation method. The advantage of this method is that the skeleton can be fired at very high temperatures to densify the electrolyte, bond the electrolyte and electrodes in a very intensive way and provide as much mechanical strength to the skeleton as possible, while the other components of the electrodes and the catalyst can be calcined at much lower temperatures avoiding problems like unwanted secondary phases, grain coarsening and particle agglomeration [3].

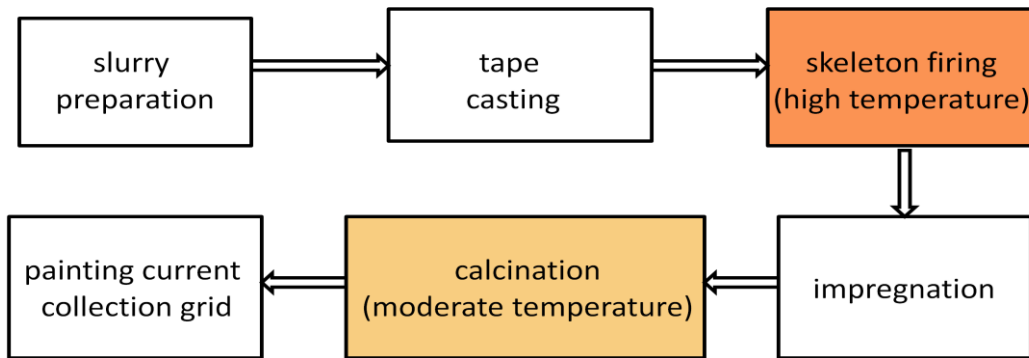


Figure 2.2: Flow diagram of the fabrication of thin single cells by tape casting and impregnation method

2.1.1.1. Slurry preparation for tape casting

In the first step of the slurry preparation the ceramic powders and the pore formers were dispersed in an organic solvent with the help of a dispersant. The ceramic powders used were 8 mol% yttria stabilised zirconia (8YSZ, Pi-Kem) and 10 mol% gadolinium doped ceria (CGO91, Praxair) for YSZ and CGO tapes respectively. The pore formers used in the green tapes used for porous layers were two different kinds of carbon, 80 wt% graphite flake, natural, 325 mesh (Alfa Aesar) and 20 wt% glassy carbon powder, 10-20 micron (Alfa Aesar). Dependent on the target porosity of the ceramic layer, the amount of pore formers in the mixture with the ceramic powder was between 30 wt% and 50 wt%. The solvent used for the slurries was a 3:2 mixture of methyl ethyl ketone (MEK) and ethanol with a small amount of phosphate ester (Triton QS44, Sigma Aldrich) as a dispersant. After dispersing the ceramic powder and the pore former in the solvent, the dispersions were ball milled for 18 hours at 160 rpm, using 36 zirconia balls (diameter 10 mm) in a 125 ml plastic container, which was placed horizontally on the metal rollers of a milling machine custom made by the University of St. Andrews.

In the second step of the slurry preparation a binder and two different kinds of plasticisers were added. The binder used to form a polymer matrix was poly(vinyl butyral) (Butvar B 98, Sigma Aldrich). Di butyl phthalate (DBP, Fisher Scientific) was used as a plasticiser to soften the polymer chains and poly(ethylene glycol) (PEG, Sigma Aldrich) as a different type of plasticiser to allow better mobility between the polymer chains. The slurry was put on a vibration mill for 20 minutes and afterwards ball milled for 4 hours at 100 rpm. To remove gas bubbles from the slurry, which is particularly important to cast a homogenous electrolyte tape without pin holes, the mixture was ball milled at a very low speed over night.

2.1.1.2. The tape casting process

The slurry was spread out on the surface of a silicone coated PET polymer film (single side silicone coated Mylar, Haiku Tech), and dried to form the green tape in a process called tape casting, which is described as follows. To apply the slurry onto the polymer film in a constant thickness, a stationary doctor blade is used on top of the moving polymer film carrier.

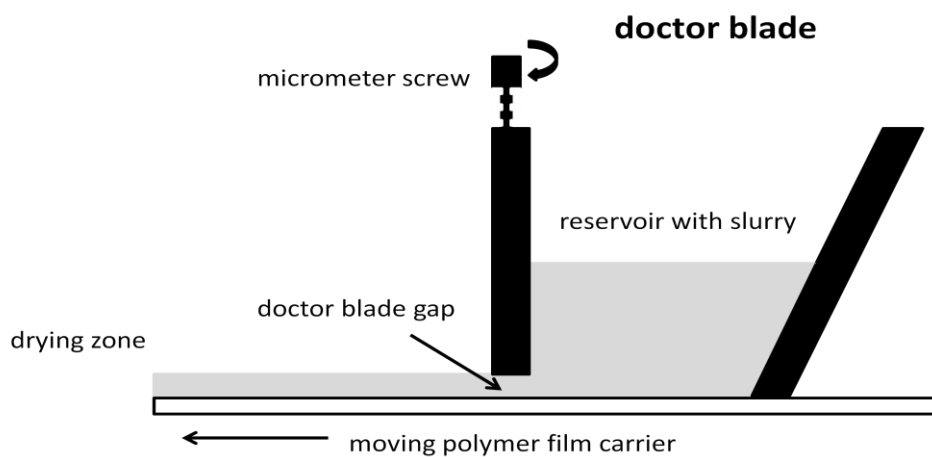


Figure 2.3: Schematic of the principle of tape casting with a doctor blade

The doctor blade consists of a reservoir for the slurry and a jig with a metal plate held in a very accurately defined distance from the carrier surface. This distance is called the blade gap and can be adjusted by micrometer screws. The polymer film carrier transports the slurry film to the drying zone where the organic solvent evaporates leaving the green tape.

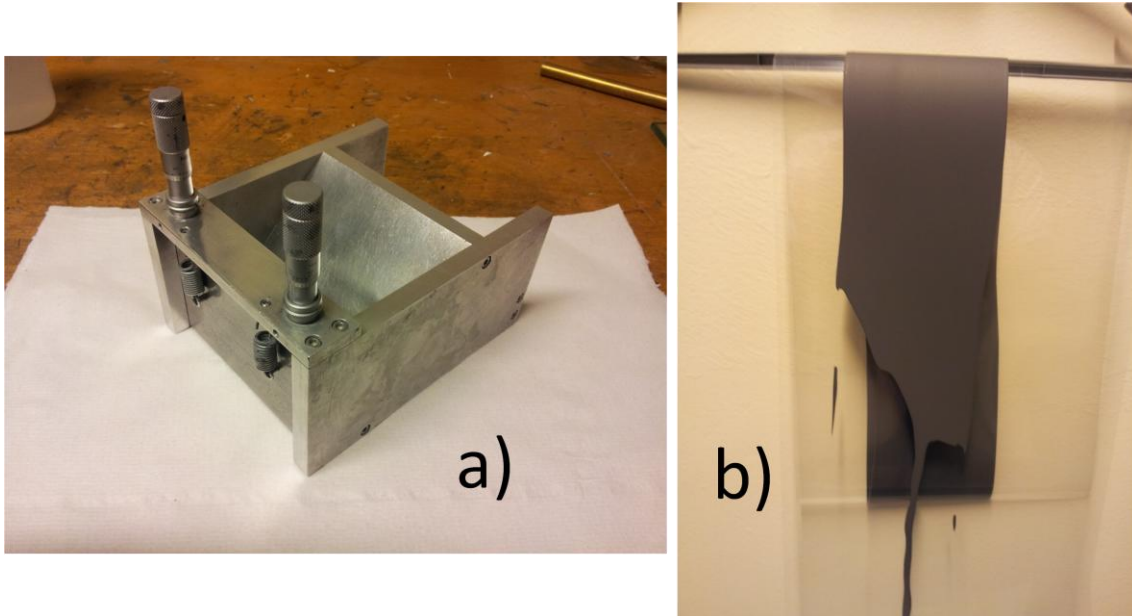


Figure 2.4: a) photo of the doctor blade and b) photo of a typical green tape on polymer film

The process parameters of tape casting, controlling the thickness and quality of the green tape, are: the composition of the slurry including its binder content and viscosity, the size of the doctor blade gap, the reservoir depth and the speed of the carrier tape movement. Very thin ceramic layers with a large area can be achieved by this technique.

2.1.1.3. Arrangement and lamination of the green tapes

The cathode green tape and the electrolyte green tape were laminated to each other using a common office laminator. Circular discs with a diameter of around 23 mm were punched out of these two layer stacks. Smaller discs with a diameter of around 11 mm were punched out of the anode green tape and placed centric on top of the electrolyte part of the two layer discs. In another lamination step the anode disc was connected to the electrolyte.

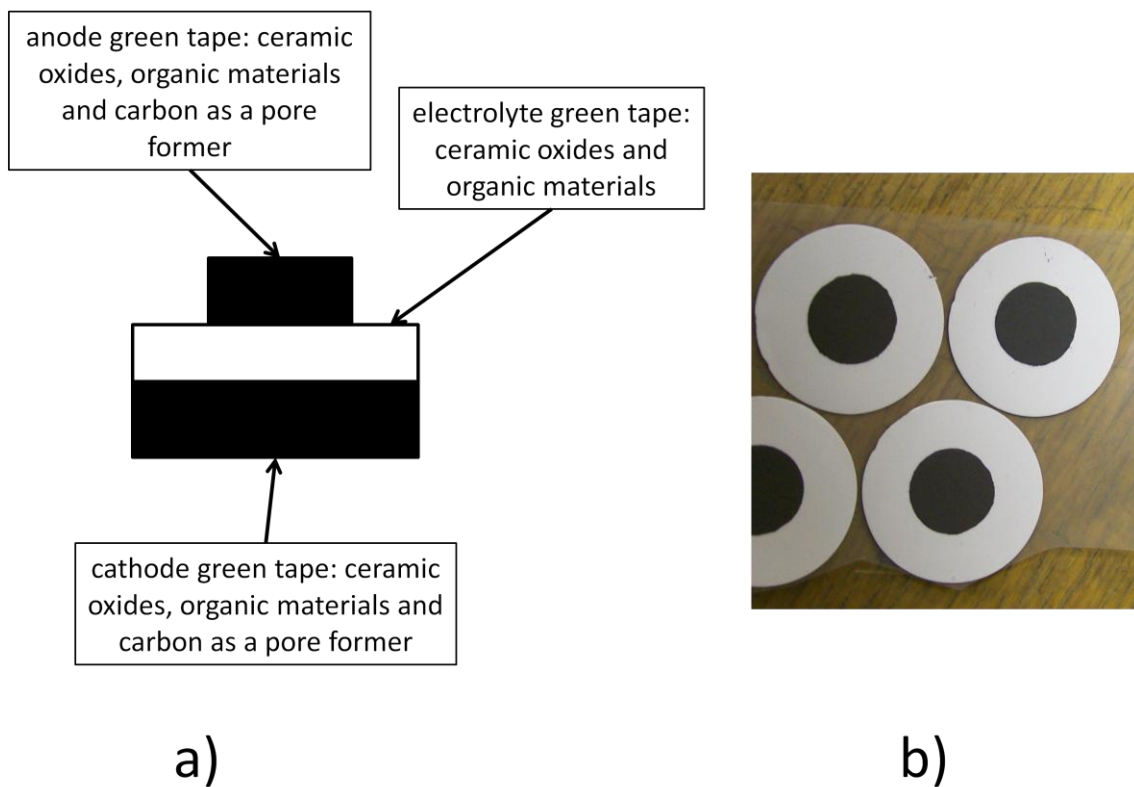


Figure 2.5: a) schematic of a typical green single cell, b) photo of green cells on PET film

2.1.1.4. Firing of the skeleton

For the firing process the single cells were placed on a dense alumina plate and covered with a porous alumina plate. Heat treatment for the single cells started with a 0.5 ° per minute ramping step up to 300 °C to burn out the organic binder and a second ramping step with a ramping rate of 0.3 ° per minute up to 600 °C to burn the carbon and any remaining binder and to form the pores in the electrodes. Subsequently another ramping step with a rate of 0.5 ° per minute to 1000 °C and then a final ramping step of 1 ° per minute temperature led to the desired sintering temperature. The sintering temperature varied for different experiments between 1400 °C and 1500 °C and was held for 5 hours leading to sintering and densification of the single cells resulting in an increase of the mechanical strength of the cells and their shrinkage from a diameter of 23 mm to 14-18 mm. The microstructure of the skeletons of the single cells, in particular the pore structure, was strongly influenced by the temperature profile of the sintering step. The overall quantity of heat applied during the firing cycle was monitored by process temperature control rings (Ferro electronic materials PTCR-MTH) to ensure a constant quality within different firing batches.

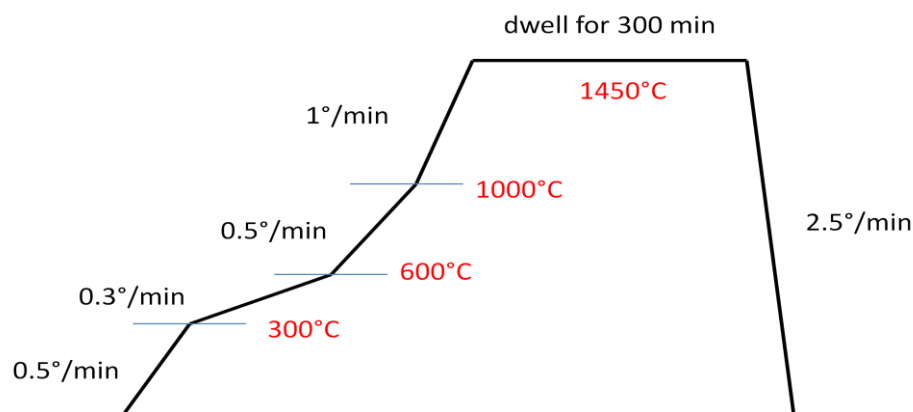


Figure 2.6: temperature profile of a typical skeleton firing

After this sintering step the scaffold of the single cells was complete and consisted of two porous layers separated by a dense layer. (Figure 2.1)

2.1.2. Impregnation of the skeleton

The skeleton of the single cells already provided a thermally and mechanically stable scaffold with a dense electrolyte and two porous electrodes exhibiting oxide ion conductivity. To work as a fuel cell both of the electrodes additionally need electronic conductivity, under oxidising conditions on the cathode side and under reducing conditions on the anode side. The pores of the anode and the cathode of the single cells were filled with aqueous precursors, which upon thermal treatment would produce in situ the oxides providing the electronic conductivity required under the working conditions of each electrode. Since the oxides used on the cathode side needed a lower calcination temperature than the oxides on the anode side [4] [5], the impregnation was carried out on the anode side first, and after firing the cell for the production of the anode composite, the impregnation process was carried out on the cathode side, followed by the cathode firing.

2.1.2.1. Preparation of the impregnation liquids

B-site doped lanthanum strontium titanates have been used to introduce electronic conductivity into the anode material under reducing conditions. The different compositions included $\text{La}_{0.4}\text{Sr}_{0.6}\text{Ti}_{0.4}\text{Mn}_{0.6}\text{O}_{3+\delta}$, $\text{La}_{0.4}\text{Sr}_{0.6}\text{Ti}_{0.8}\text{Mn}_{0.2}\text{O}_{3+\delta}$, $\text{La}_{0.4}\text{Sr}_{0.4}\text{Ti}_{0.94}\text{Mn}_{0.06}\text{O}_{3-\delta}$, $\text{La}_{0.4}\text{Sr}_{0.4}\text{Ti}_{0.94}\text{Fe}_{0.06}\text{O}_{3-\delta}$, $\text{La}_{0.4}\text{Sr}_{0.4}\text{Ti}_{0.94}\text{Ni}_{0.06}\text{O}_{3-\delta}$ and $\text{La}_{0.4}\text{Sr}_{0.4}\text{TiO}_3$, varying in A-site deficiency as well as in the materials used for the B-site doping and the dopant level. On the cathode side the perovskite oxides $\text{La}_{0.8}\text{Sr}_{0.2}\text{MnO}_{3-\delta}$ (LSM82) and $\text{La}_{0.8}\text{Sr}_{0.2}\text{FeO}_{3-\delta}$ (LSF82) provided electronic conductivity in air. Stoichiometric amounts of lanthanum(III) nitrate hexahydrate (Alfa Aesar), strontium nitrate (Sigma-Aldrich), titanium(IV) bis (ammonium lactato) dihydroxide (Sigma-Aldrich), manganese(II) nitrate hydrate (Alfa Aesar), iron(III) nitrate nonahydrate (Sigma-Aldrich), nickel(III) nitrate hexahydrate (Acros Organics) and cobalt(II) nitrate hexahydrate (Sigma-Aldrich) were dissolved in deionised water to form aqueous solutions of the molarity 0.5 mol/l.

For some of the cathode oxides the Pechini sol-gel method was used in the fabrication of the precursor solutions for a better distribution of the metal cations and small particle size of the perovskite oxide phase [6]. Citric acid monohydrate (Acros Organics) and ethylene glycol (Fisher Scientific) were used in the molar ratio 1:4 in addition to the precursors of LSM, LSC and LSF. All the impregnation liquids were stirred at room temperature for 30 minutes to achieve homogenous solutions.

2.1.2.2. The impregnation process

The impregnation solutions were applied on the surface of the electrode scaffolds with an adjustable micropipette or with a glass pipette. After one minute of contact between the surface of the skeleton and the impregnation solution the excess liquid was removed with a medical wipe. In some cases this was repeated before firing the cell at 450 °C for 40 minutes to decompose the nitrates. The whole process from the application of the impregnation liquid until the 450 °C firing was repeated 3 to 30 times, until the desired weight gain was reached.

Some of the impregnations were carried out in a vacuum vessel, applying an absolute pressure of 0.16 bar before the application of the impregnation solution. After the liquid was dropped on top of the electrode surface, the vessel was vented, providing ambient pressure on top of the impregnation liquid, while inside the smaller pores covered by the impregnation liquid a pressure of 0.16 bar was maintained. The idea of this process was that the comparably lower pressure inside the pores would suck the impregnation liquid into the pores providing a very uniform distribution of the impregnation liquid on the scaffold material. The liquid remaining on top of the electrode after the impregnation process was removed with a medical wipe.

2.1.2.3. Firing of the impregnated oxides

After the desired weight percentage of the impregnated phases was achieved, another firing step was necessary to form the final perovskites. Since the firing temperature required for the single phase forming of the perovskites used in the anodes was higher (1150 °C to 1250 °C) than the temperature required to form the cathode perovskites (around 1000 °C), the impregnation was started on the anode side of the cells. After finishing the anode impregnation, the cells were placed on a dense alumina plate and fired at a temperature between 1150 °C and 1250 °C for 5 hours. The total thermal energy applied was controlled by process temperature control rings (Ferro electronic materials PTCR-STH).

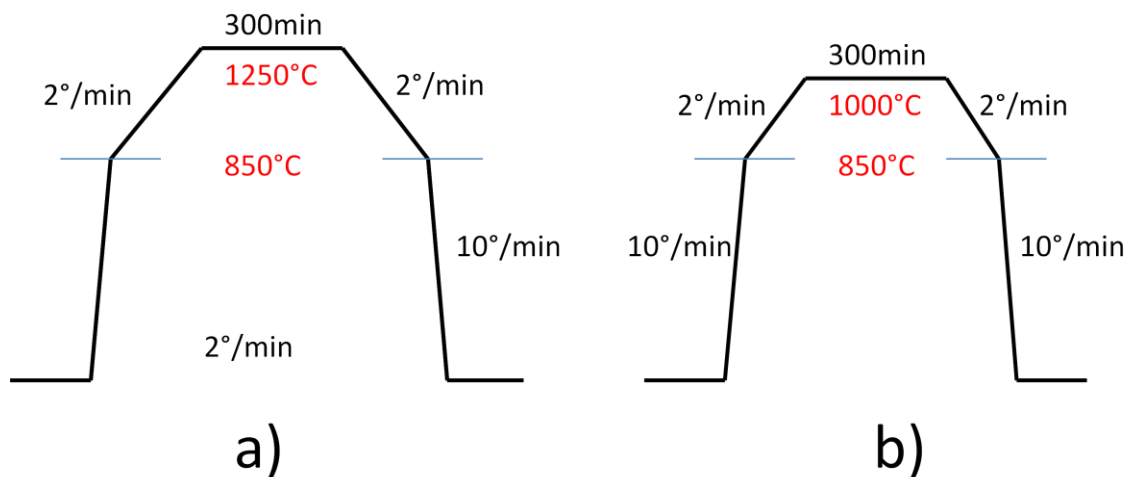


Figure 2.7: temperature profile of typical post impregnation firings: a) firing after the anode impregnation, b) firing after the cathode impregnation

The ramping rates were high compared to the firing of the skeletons, because the graphite pore former had been burnt out already before. The cathode side of the cells was impregnated in a similar manner followed by another heat treatment step at around 1000 °C.

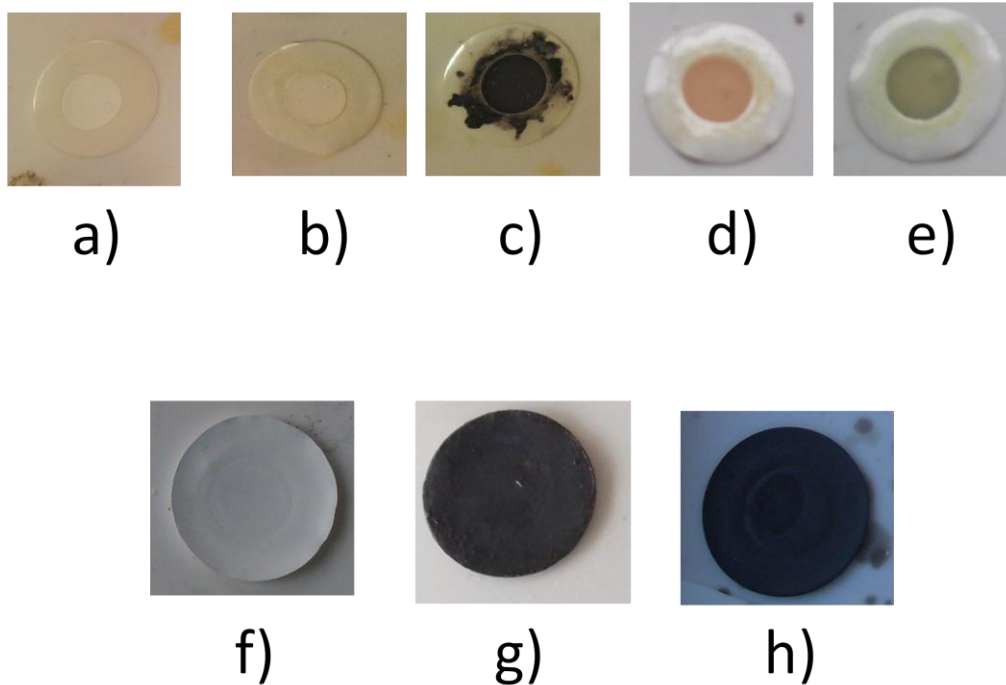


Figure 2.8: photos of the electrodes of the single cells before and after impregnation: a) un-impregnated anode, b) anode impregnated with LST, c) anode impregnated with LSTM, d) anode impregnated with LSTF, e) anode impregnated with LSTF, f) un-impregnated cathode, g) cathode impregnated with LSM, h) cathode impregnated with LSF

2.1.2. Impregnation with the catalyst

The anodes of a number of the cells prepared for electrochemical testing were impregnated with an additional catalyst for the oxidation of hydrogen. The catalyst precursor was an aqueous solution of 1 M palladium nitrate in a 10 wt% solution of nitric acid in water. This precursor was applied the same way as the precursors for the perovskite oxides and fired at 900 °C to form palladium oxide. At the highly reducing working conditions of the anode palladium oxide is reduced to metallic palladium, which has proved to be an excellent catalyst for the oxidation of hydrogen in titanate based fuel cell anodes [7].

2.1.3. Current collection

The cells which were used for electrochemical measurements were equipped with a current collection system. Using a small brush a current collection grid was painted directly onto the surface of the anode and the cathode with pastes containing silver or platinum particles. Subsequently silver or platinum wires were locally coated with the same paste and connected with the paste at the anode and the cathode side. The wire connected cells were fired for 40 minutes at 700 °C to ensure a good and mechanically stable contact between the electrodes, the paste and the wire, and also to make the wires softer and more flexible.

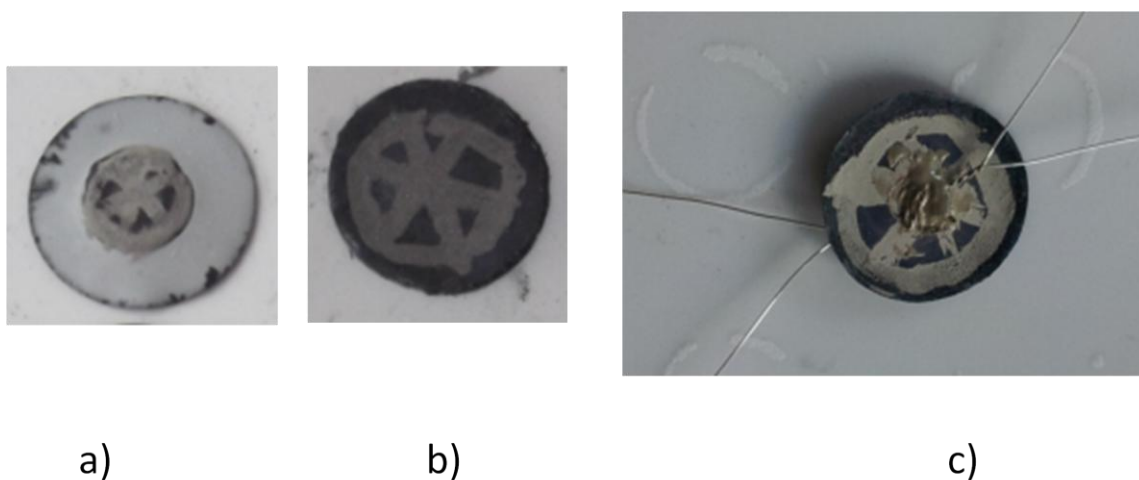


Figure 2.9: photos of the single cells with current collection. Metallic paste grid painted on the anode side (a), and on the cathode side (b). Metal wires attached to the metal paste (c).

The metal pastes used were a silver paste (ESL Europe, Conductive composition 9912-G) and a platinum paste (Gwent Advanced Material Systems Pt ink C2000904P3). The metal wires used for cell testing were silver wires or platinum wires with a diameter of 0.25 mm (Advent temper annealed silver wire).

2.2. Sample characterisation

2.2.1. X-ray diffraction (XRD)

Diffraction refers to a number of phenomena which occur whenever a group of waves encounters a group of obstacles, with the distance between the obstacles similar to the wavelength of the waves. Due to the interaction with the obstacles the waves might change their direction and their intensity. Since the distance between the atoms in a typical crystal are around 0.1 nm to 10 nm, in the same order of magnitude as the wavelength of typical X-rays, X-ray diffraction (XRD) can be used to examine the structure of crystalline solids [8].

It was used to prove the phase purity of skeleton and impregnated oxides, to identify secondary phases occurring after the firing, to observe the change of the crystal system and unit cell parameters during impregnation, and to investigate differences between the oxidised and the reduced form of the anode composites.

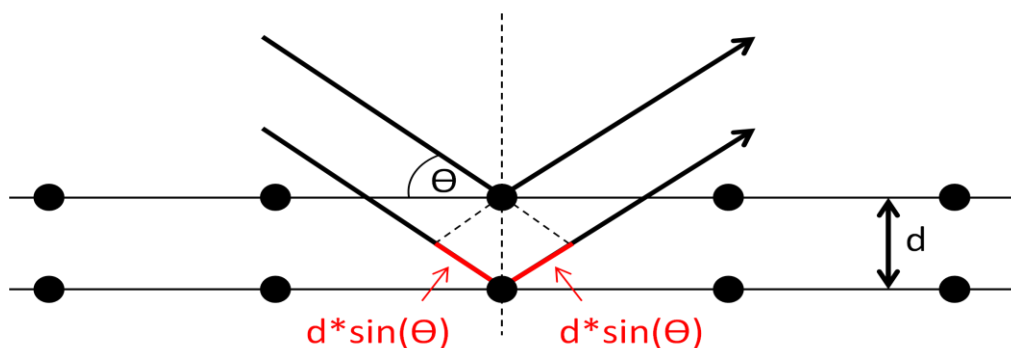


Figure 2.10: two adjacent layers of atoms in a crystal scattering parallel incoming waves. The difference in the length of the path of the waves is highlighted in red

The basic principle of XRD is the constructive interference of two X-ray waves scattered by two layers of atoms in a crystal. The difference of the lengths of the paths of the two scattered waves is highlighted in red in figure 2.10 and equals $2 \cdot d \cdot \sin(\theta)$. For constructive interference this path difference has to be an integer multiple of the wavelength, as stated in Bragg's law.

$$2 \cdot d \cdot \sin(\theta) = n \cdot \lambda$$

d ... interplanar space between the scattering planes [m]

θ ... angle between the incoming beam and the parallel planes [rad or °]

n ... any integer

λ ... wavelength of the used radiation [m]

Equation 2.1: Bragg's law for constructive interference of two scattered waves

In a crystal there are a very large number of sets of parallel planes with the possibility of interference between waves scattered from them. Each of these sets can be denoted by three integers h, k and l called Miller indices, which describe the inverse space intercepts of the plane with the lattice vectors of the unit cell [9]. The characteristic interplanar distance can be calculated for each set of Miller indices if the size and shape of the unit cell is known, the calculation is particularly easy if the unit cell is cubic, tetragonal or orthorhombic ($\alpha = \beta = \gamma = 90^\circ$) [9].

$$\frac{1}{d_{hkl}} = \frac{h^2}{a^2} + \frac{k^2}{b^2} + \frac{l^2}{c^2}$$

d_{hkl} ... interplanar distance in a set of planes

h, k, l ... Miller indices of the set of planes

a, b, c ... unit cell parameters of the crystal

Equation 2.2: distance between adjacent planes in a cubic, tetragonal or orthorhombic crystal

The characteristic interplanar distance in a set of planes results in a peak at a particular diffraction angle according to Bragg's law (equation 2.1). Structural information about the crystal can be obtained from the presence or absence of any of these peaks, from their shapes and from the exact position of their diffraction angles.

For the XRDs of powder samples investigated in capillary transmission mode a STOE Stadi P diffractometer was used in Debye-Scherrer geometry with a Thales MC61-10Cu tube and a germanium (111) monochromator providing a monochromatic Cu-K α_1 radiation. For reflection mode XRD studies either a Philips X'Pert diffractometer with a PW1730/10 goniometer, a copper tube and a graphite single crystal monochromator, or later a PANalytical EMPYREAN diffractometer with a germanium (111) monochromator were used, both using the Bragg-Brentano geometry and monochromatic Cu-K α_1 radiation with a wavelength of around 0.154 nm. Typical 2θ ranges were 10 to 90 degrees with overall collection times between 60 and 90 minutes.

Data visualisation and analysis were performed using the WinXPow software from STOE, including functions for the indexing of peaks, the generation of theoretical patterns and a basic refinement function.

2.2.2. Scanning electron microscopy (SEM)

Scanning electron microscopy is a technique used for analysing the morphology, topography and composition of the surface of a sample. Generally the sample is hit by an electron beam generated by a heated filament of lanthanum hexaboride or tungsten, or, in the case of a field emission microscope (FE-SEM), by a cold tip of tungsten in a huge electrical potential gradient.

Inside the high vacuum chamber the electrons are collected and focussed by electromagnetic lenses into a fine probe which is scanned across the surface of the sample by scan coils or plates.

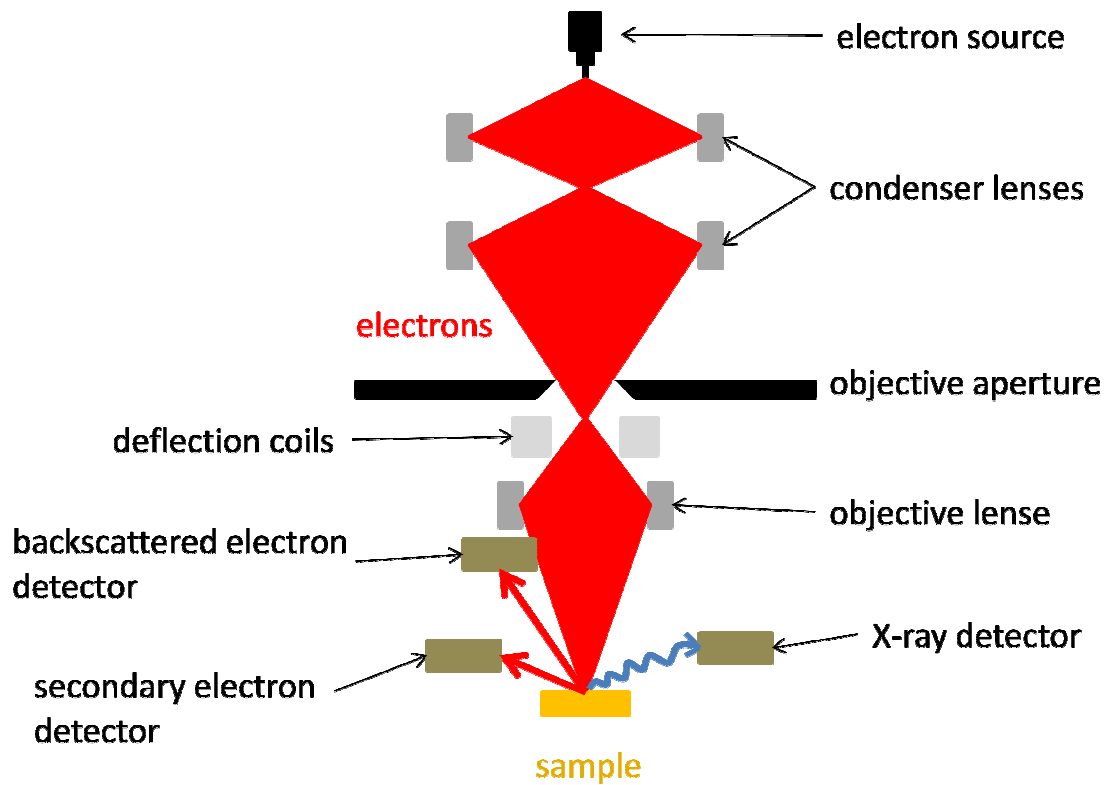


Figure 2.11: Schematic of a typical SEM.

As the electron beam traces over the surface, it interacts with the matter of the sample in many different ways causing secondary electrons, Auger electrons, backscattered electrons, characteristic X-rays and cathode luminescence, all carrying different kinds of information [10]. The volume of the sample which interacts with the electron beam is called interaction volume and depends in size and shape on the atomic numbers of the atoms in the sample, of the acceleration voltage and kinetic energy of the primary electrons and of the angle at which the electron beam strikes the sample surface.

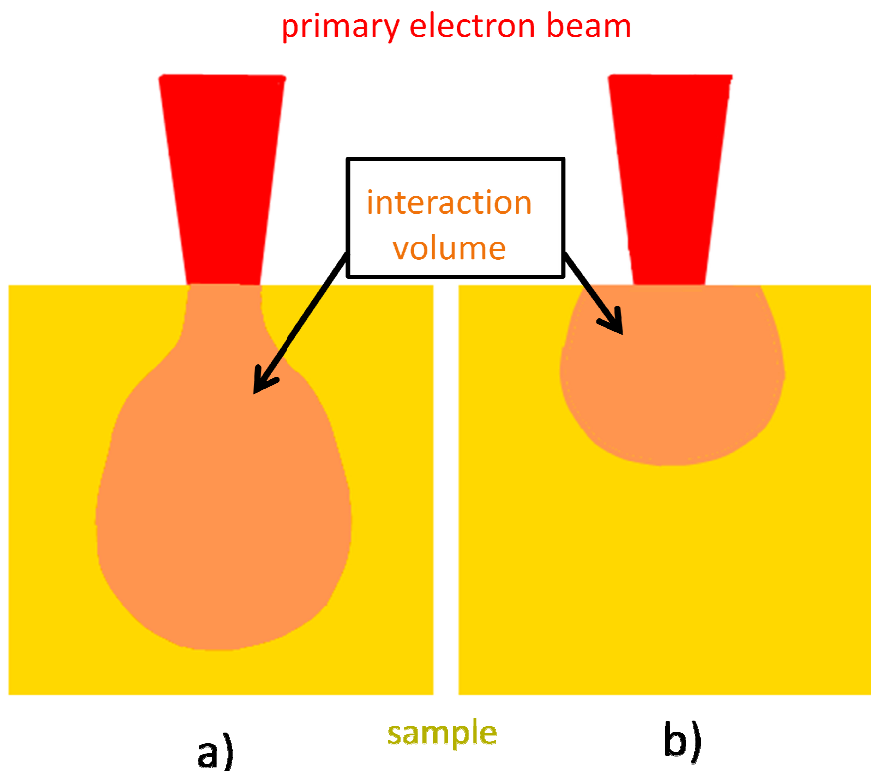


Figure 2.12: Schematic of the interaction volume of an electron beam hitting a sample. a) drop shaped interaction volume if the atoms inside the sample have relatively low atomic numbers b) if the atomic number of the sample atoms is higher, the interaction volume is semi-sphere shaped and smaller (using the same acceleration voltage)

Once an effect is produced, the electrons or the radiation has to get to the surface of the sample, leave the sample, and reach the detector. Since the amount of scattering and absorption is different for different signals, the fraction of the interaction volume, from which information can be obtained, is different for secondary electrons, backscattered electrons and characteristic X-ray radiation. The detected characteristic X-ray radiation comes from the whole interaction volume, the backscattered electrons from the top 40% of the interaction volume and the secondary electrons from the top 10-50 nm under the sample surface [10].

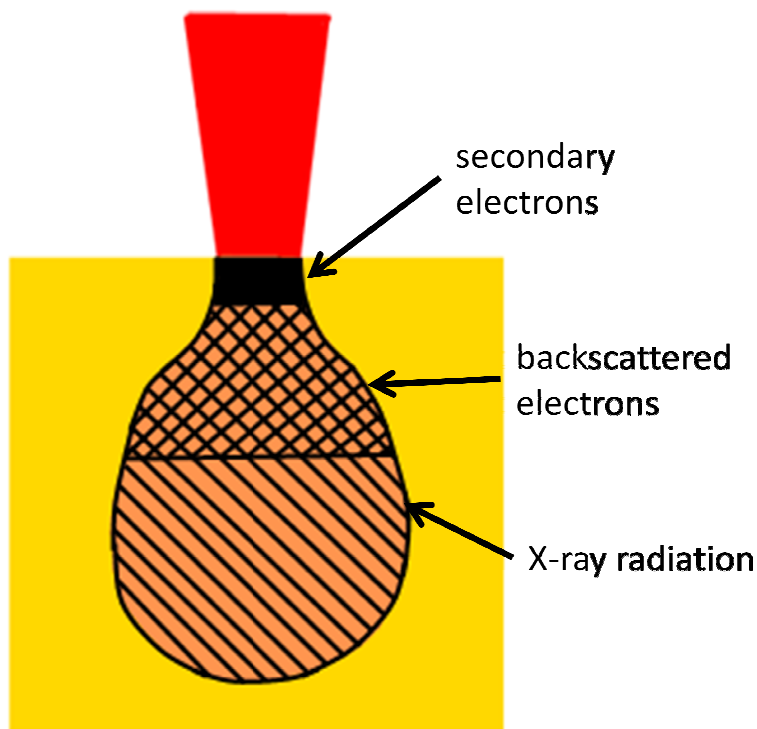


Figure 2.13: Interaction volume of an electron beam highlighting the areas of origin for the different signals detectable outside the sample [10].

2.2.2.1. Secondary electron imaging (SEI)

Secondary electrons are generated whenever an incident electron ejects the electron of a sample atom, passing a part of its energy to the secondary electron in a process called inelastic scattering. If the secondary electron has enough energy to exit the sample, it can be detected by a detector consisting of a scintillator and a photomultiplier. Typically the secondary electrons have a low energy of around 5-50 eV at the time of the ionisation, and can exit the sample only if their origin is not deeper than 10-50 nm below the sample surface [11].

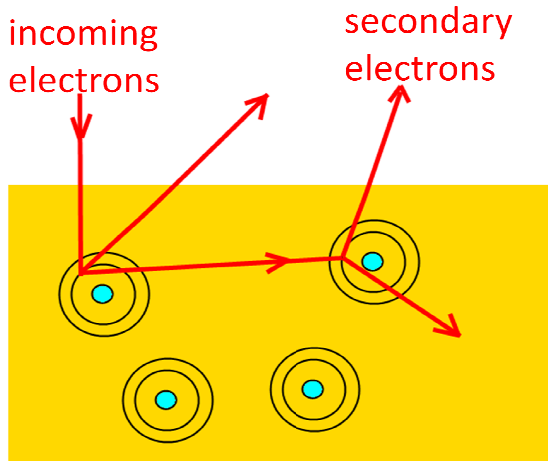


Figure 2.14: Schematic of the mechanism generating secondary electrons

The yield of secondary electrons is highly dependent on the topography of the sample surface and the resolution of the signal is only limited by the electron beam diameter resulting in high resolution pictures of details of the sample which are only a few nanometers across. Characteristic for secondary electron images of a SEM is also the large depth of field leading to a three dimensional appearance of the micrographs [10].

2.2.2.2. Backscattered electron spectroscopy (BES)

Whenever an electron of the incident electron beam passes the nucleus of a sample atom close enough, its path will be deflected by the attraction of the electron to the positive charge of the nucleus in a process called elastic scattering. The loss of kinetic energy of the electron during elastic scattering is only marginal compared to its original energy. A series of elastic scattering incidents might change the path of an electron close to 180 degrees and enable it to leave the sample, in which case it can be detected and is referred to as a backscattered electron.

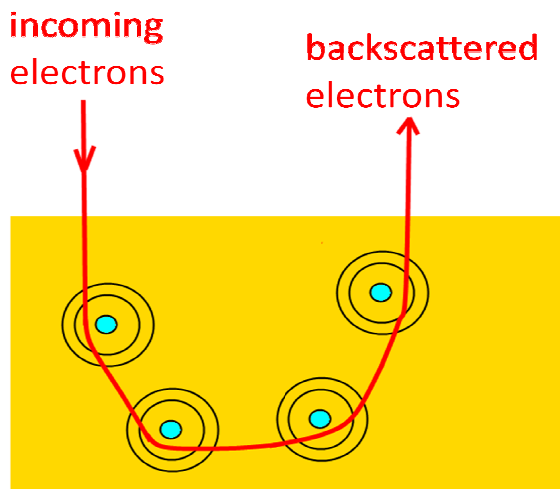


Figure 2.15: Schematic of the mechanism generating backscattered electrons

Backscattered electrons are detected at high angles, typically closed to 180 degrees from the incoming beam. The number of backscattered electrons is small compared to secondary electrons, and depends on the atomic number as well as on the surface morphology. Heavier atoms with higher charged nuclei deflect the incoming electrons to a higher angle making a backscatter more likely. Next to information about the surface topography the intensity of the signal of backscattered electrons thus carries information about the elemental composition of the sample [11].

2.2.2.3. Energy dispersive X-ray spectroscopy (EDS or EDX)

The incoming electrons sometimes remove electrons from the inner shells of sample atoms, ionising the atoms and leaving an empty space in the inner shell. The inner shell can be refilled by the transition of an electron from one of the outer shells to the inner shell, releasing the energy difference in the form of electromagnetic radiation in the X-ray region. The energy differences between different inner and outer shell combinations form a set of different wavelengths which is characteristic for one specific element.

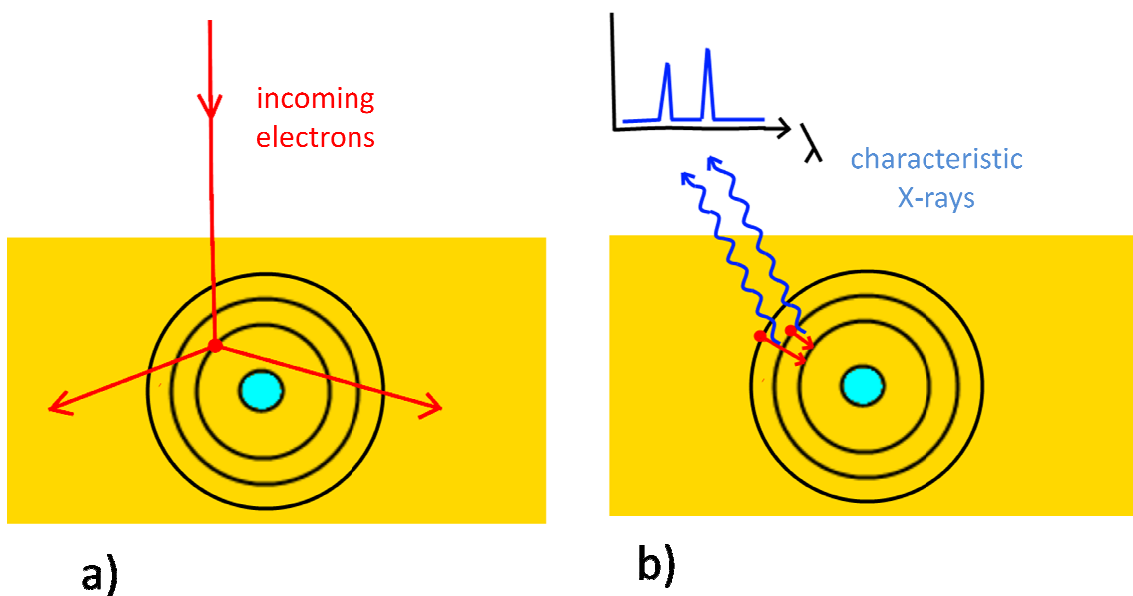


Figure 2.16: Schematic of the mechanism generating characteristic X-ray radiation. a) ionisation of an atom by the removal of an electron from the inner shell, b) the electron hole of the inner shell is filled with an electron from the outer shells, the energy difference is emitted as X-rays of characteristic wavelengths.

The EDS X-ray detector measures the amount of X-ray photons and their energy. One part of the detected radiation is the characteristic X-ray radiation from electron transitions, another part arises from interactions of incoming electrons with nuclei, the so called “Bremsstrahlung radiation”, forming a continuous background spectrum which underlies the characteristic EDS peaks.

Since X-ray radiation is not significantly diminished during the way to the surface, X-ray signals can be received from the whole interaction volume of the incoming electron beam, leading to lower resolution compared to SEI, but providing additional compositional information about the sample [11].

Next to the elemental composition of selected spots, techniques like line scan and mapping allow the measurement and visualisation of the distribution of elements along a line or inside a defined area of the sample surface.

2.2.2.4. Sample preparation

For the secondary electron images button cell samples were simply broken and stuck onto an adhesive carbon tape. The advantage of this technique compared to embedding the sample into a resin are a higher contrast and a better visibility of the three dimensional structure of the samples. To observe compositional effects in backscattered electron images or energy dispersive X-ray maps, however, it is important that the sample surface is as flat as possible. For these techniques the samples were embedded into a resin and ground and polished. The resin used was composed of a 5:1 mix of bisphenol-A-epichlorhydrin epoxy resin (molecular weight <700, Struer) and triethylenetetramine (Struers) as a hardener. To remove air bubbles from the resin, the sample was placed in a vacuum impregnation unit (Struers CitoVac) and exposed to an absolute pressure of 0.2 bar for 5 minutes. After curing the resin over night, the epoxy cylinders with the embedded samples were removed from the rubber mold and cut by a diamond saw (Struers Minitom). The cut surface was ground with SiC abrasive papers with median particle diameters of 25.8 and subsequently 15.3 μm (Buehler P600 and P1200 grit) under flowing water and polished on polishing clothes (MetPrep Plano Cloth) covered with diamond paste of average particle diameters of 6 μm and 3 μm with a water base lubricant (MetPrep Diamond Lubricant 15 50 02).

Both the samples on the adhesive carbon tape and the resin embedded samples were sputtered with a thin layer of gold to increase the surface conductivity and avoid charging upon exposition to the electron beam. A custom fabricated high vacuum gold evaporator of the University of St. Andrews was used as well as a rotary pumped sputter coater (Quorum Technologies Q150R ES).

2.2.2.4. Instrumentation

Two different kinds of electron microscopes were used. At the early stage of the PhD a Jeol JSM-5600 scanning electron microscope was used with an Oxford Instruments INCA Energy 200 EDS system and Oxford Instruments INCA software. For the main part of the work a newer field emission electron microscope, Jeol JSM-6700F, was used, equipped with detectors for backscattered electrons (Jeol SM-74071) and an Oxford Instruments INCA x-act EDS detector, which was used together with Oxford Instruments INCA software.

2.3. Electrochemical fuel cell testing

Electrochemical testing of the fabricated single cells was carried out by the measurement of IV curves and by AC electrical impedance spectroscopy (EIS). While the IV curves and the power density curves which are calculated from them serve as a quantitative evaluation of the fuel cell performance at different workloads, impedance spectroscopy provides a possibility to distinguish between ohmic losses and different kinds of polarisation losses.

2.3.1. IV curves

The anode and the cathode side of the fuel cell are connected to form an electrical circuit. A decrease of the external load resistance within this circuit leads to an increasing current to be drawn from the fuel cell, accompanied by a decrease of the cell voltage. The potential and the current within the circuit are measured by ammeters and voltmeters. A series of these measurements with decreasing load resistance values is carried out and the cell voltage plotted against the current to form the IV curve. For practical reasons the current is divided by the cell active area resulting in a current density (Acm^{-2}). The starting point of this curve is an open circuit with infinite resistance and no current drawn from the fuel cell, showing the characteristic open circuit voltage (OCV), which can be calculated theoretically by the Nernst equation (equation 1.6). The gradient at any point of the IV curve corresponds to the total resistance of the fuel cell at that point.

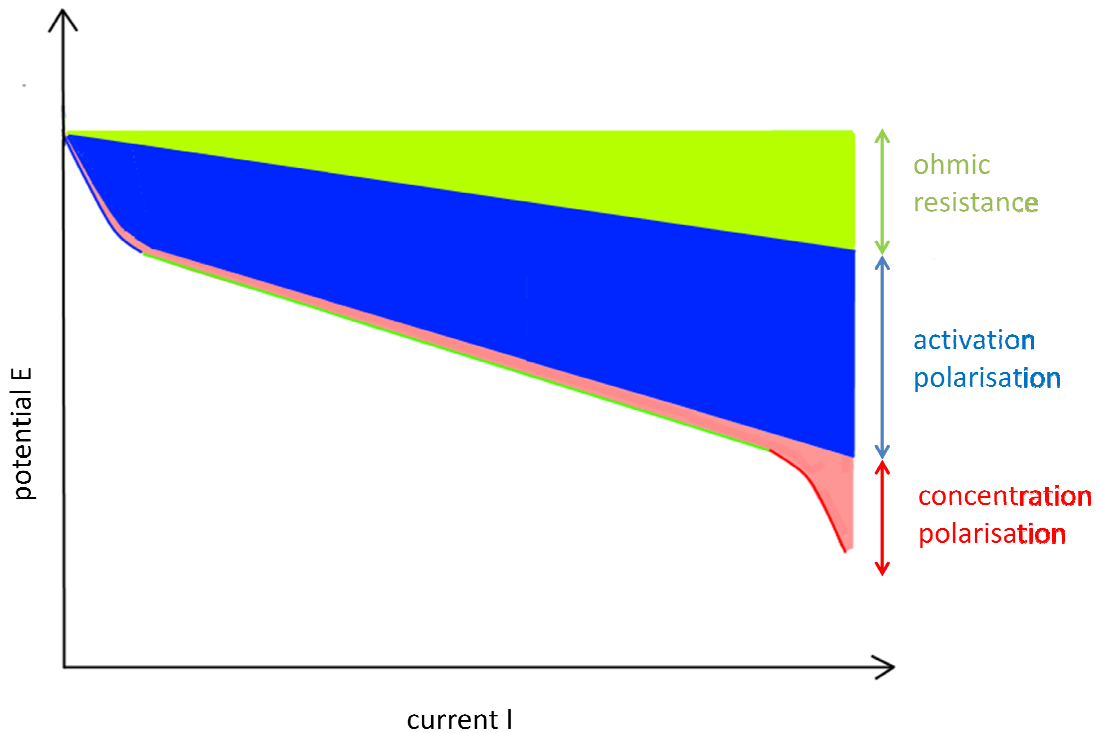


Figure 2.17: Schematic current potential curve of a fuel cell, displaying the influence of different resistances and polarisations

The resistances responsible for the decline of the IV curve can be classified into the activation polarisation, ohmic resistance and concentration polarisation [12]. Although all these polarisations are present at each of the points of the IV curve, figure 2.17 shows that different regions of the IV curve are dominated by different polarisation effects. At low current densities the majority of the losses are due to activation polarisation, at intermediate current densities the ohmic resistance of the cell and linear parts of its polarisation dominate the shape of the IV curve, and at high current densities mass transport losses become more influential.

2.3.1.1 Activation polarisation

The part of resistances in a fuel cell which are not proportional to the applied current and hence not following Ohm's law over the complete IV curve are summarised under the term polarisation. The polarisation dominating the total resistance of the fuel cell especially at low current densities is the activation polarisation.

Electrochemical reactions on the surface of electrodes include a charge transfer between an ionic conductor and an electronic conductor. A part of the potential is used to overcome the energy barrier related to this rate determining step and lost for power production. A common way to quantify the activation polarisation and its relationship with the current flowing through the electrodes is the Butler Volmer equation [12].

$$i = i_0 \cdot e^{\frac{\beta_A \cdot z \cdot F}{R \cdot T} \cdot \eta_A} - i_0 \cdot e^{-\frac{\beta_C \cdot z \cdot F}{R \cdot T} \cdot \eta_A}$$

i ... current density [Am^{-2}]

i_0 ... exchange current density [Am^{-2}]

η_A ... activation overpotential [V], $\eta_A = E - E_{\text{eq}}$

F ... Faraday constant (~ 96485) [Cmol^{-1}]

z ... number of electrons from one equivalent cell reaction

R ... universal gas constant (~ 8.31) [$\text{JK}^{-1}\text{mol}^{-1}$]

T ... absolute temperature [K]

β_A, β_B ... symmetry factors for the anode and the cathode, $\beta_A + \beta_B = 1$

Equation 2.3: Butler Volmer equation

Theoretically, this equation cannot be solved, because neither the symmetry factors β_A and β_B nor the exchange current density i_0 can be directly measured. If the overpotential is big enough, the contribution of either the anodic current or the cathodic current can be neglected, hence the relationship between the overpotential and the logarithm of the current is almost linear and can be expressed by the Tafel equation [12].

$$\eta_A = -\frac{R \cdot T}{\beta_A \cdot z \cdot F} \cdot \ln(i_0) + \frac{R \cdot T}{\beta_A \cdot z \cdot F} \cdot \ln(i)$$

Equation 2.4: Tafel equation, for explanation of the symbols see equation 2.3

The symmetry factor β_A can be calculated from the gradient of the corresponding line in a $\eta/\ln(i)$ diagram, the exchange current density from the point of intersection of this line with the y-axis of the diagram.

The current exchange density of an electrode describes the quality of its charge transfer kinetics, if i_0 is big, charge transfer happens easily and the activation losses at this electrode tend to be small. It can be enhanced by raising the cell temperature, using catalysts or by increasing the active surface of the electrode.

2.3.1.2. Ohmic resistance

One part of the voltage losses of a fuel cell is strictly proportional to the drawn current, behaving like an ohmic resistance in an electric circuit and obeying Ohm's law.

$$\Delta E = \Delta I \cdot R$$

ΔE ... potential difference [V]

ΔI ... difference in current [A]

R ... ohmic resistance [Ω]

Equation 2.5: Ohm's law

The origin of this ohmic losses in a fuel cell can be multiple, from the ionic resistance of the electrolyte to resistances in the electrodes or contact resistances between the parts of the fuel cell to ohmic resistances in the interconnect, the wires and the setup of the fuel cell test. However, in the case of fuel cells with solid electrolytes mostly the ionic resistance of the electrolyte is the dominating part of the ohmic resistances.

Employing highly ionic conductive materials for the electrolyte or keeping the electrolyte as thin as possible can be strategies to reduce this ohmic resistance part of a fuel cell.

2.3.1.3. Concentration polarisation

If a higher current is drawn from the fuel cell, more molecules of the fuel and of oxygen have to react at the electrodes in the same time. The performance of the fuel cell can in this case be limited by the depletion of the chemical reactants at certain areas of the electrode. The potential lost to overcome this kind of resistance is called diffusion polarisation or concentration polarisation. It can be expressed as:

$$\eta_D = \frac{R \cdot T}{z \cdot F} \cdot \ln \left(1 - \frac{i}{i_{lim}} \right)$$

η_D ... concentration polarisation [V]

F ... Faraday constant (~ 96485) [Cmol⁻¹]

z ... number of electrons from one equivalent cell reaction

R ... universal gas constant (~ 8.31) [JK⁻¹mol⁻¹]

T ... absolute temperature [K]

i ... current density [Am⁻²]

i_{lim} ... limiting current density [Am⁻²]

Equation 2.6: concentration polarisation [12]

Depending on conditions like gas flow rate, temperature, pressure or porosity of the electrodes only a certain number of reactants can be supplied to an area of the electrode per time. If hundred percent of this reactants react and create electrons this results in the limiting current density. The limiting current density cannot be exceeded unless the conditions are changed.

2.3.1.4. IV curves from experimental data

The sharp distinction between the areas of the IV curve dominated by different kinds of polarisation is often not possible from experimentally collected data of real fuel cells. The high operating temperatures in SOFCs mean that activation effects may be small, and in combination with high flow rates and low fuel utilisation reducing concentration polarisation, the whole IV curve basically appears as a straight line (see example figure 2.18). That means that the resistance of the fuel cell follows Ohm's law over the whole current range controlled by both ohmic resistance and the linear parts of the polarisation.

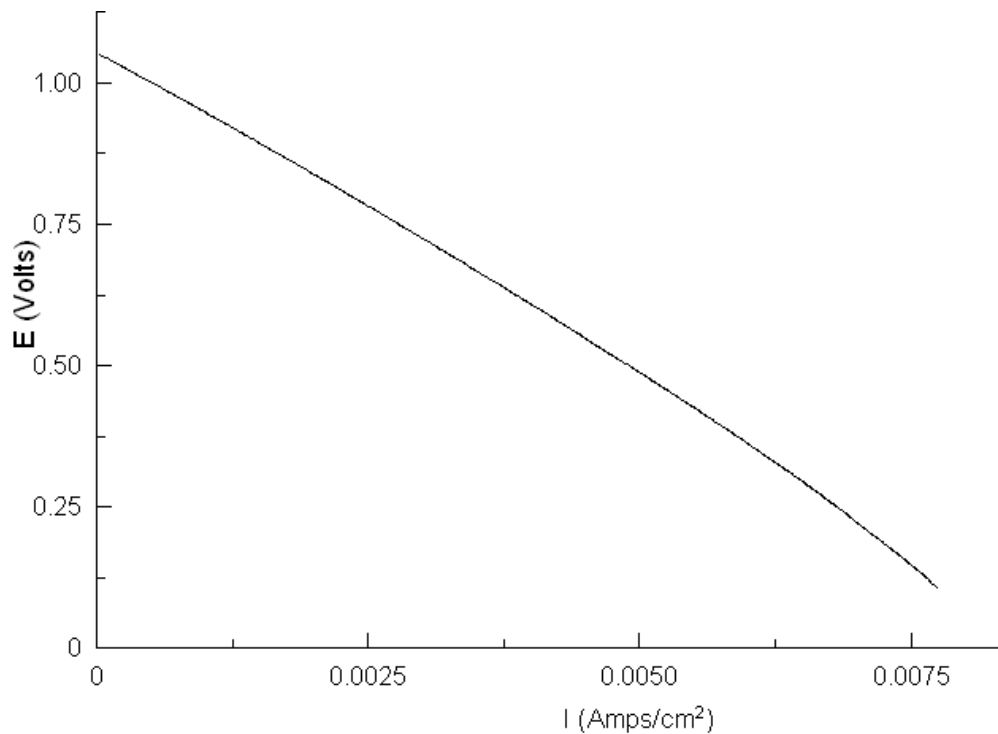


Figure 2.18: IV curve from experimental data

2.3.2. AC impedance spectroscopy (EIS)

2.3.2.1. Theory

Impedance is the resistance which an electrical circuit presents against the flow of electrons in alternating currents. Practically an excitation voltage with changing frequency is applied to perturb the electron flow in the circuit [13].

$$V = V_0 \cdot \sin(\omega \cdot t)$$

V ... potential [V]

V_0 ... amplitude of the potential [V]

ω ... angular frequency [rads^{-1}]

t ... time [s]

Equation 2.7: Potential perturbation in an AC circuit

The response current signal to this sinusoidal voltage is pseudo-linear if the perturbation voltage is very small compared to the cell voltage, which means it is of the same frequency as the perturbation signal, but with different amplitude and shifted phase [13].

$$I = I_0 \cdot \sin(\omega \cdot t + \varphi)$$

I ... current [A] or current density [Acm^{-2}]

I_0 ... amplitude of current [A] or current density [Acm^{-2}]

ω ... angular frequency [rads^{-1}]

t ... time [s]

φ ... phase shift between potential and current [rad]

Equation 2.8: Current or current density response to a circuit perturbed with the potential described in equation 2.7

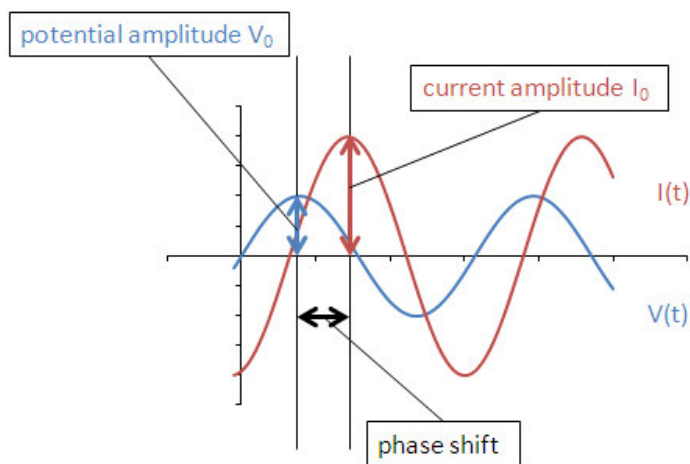


Figure 2.19: Schematic of a possible relation between potential and current in an AC circuit

The impedance, similar the resistance in DC circuits, can be calculated according to Ohm's law (equation 2.5) as the quotient of the potential and the current. In an AC circuit it is described by its magnitude Z_0 and the phase shift φ between potential and current [13].

$$Z = \frac{V(t)}{I(t)} = \frac{V_0 \cdot \sin(\omega \cdot t)}{I_0 \cdot \sin(\omega \cdot t + \varphi)}$$

Equation 2.9: Formula for the impedance in an AC circuit, for explanation of the symbols see equation 2.7. and 2.8.

The Euler formula establishes a relationship between trigonometric functions and complex exponential functions.

$$e^{j\alpha} = \cos(\alpha) - j \cdot \sin(\alpha)$$

e ... Euler constant and base of the natural logarithm

j ... imaginary unit square root of -1

α ... argument of sinus and cosinus [rad]

Equation 2.10: Euler's formula

Using Euler's formula, potential, current and impedance can be transformed from their trigonometric forms into their complex exponential forms [14].

$$V = V_0 \cdot \sin(\omega \cdot t) = V_0 \cdot e^{j \cdot \omega \cdot t}$$

$$I = I_0 \cdot \sin(\omega \cdot t + \varphi) = I_0 \cdot e^{j \cdot (\omega \cdot t - \varphi)}$$

$$Z = \frac{V}{I} = \frac{V_0 \cdot e^{j \cdot \omega \cdot t}}{I_0 \cdot e^{j \cdot (\omega \cdot t - \varphi)}} = Z_0 \cdot e^{-j \cdot \varphi}$$

Equation 2.11: Potential, current and impedance transformed into complex exponential form using Euler's formula, for explanation of the symbols see equations 2.7, 2.8 and 2.10

After retransformation back to the trigonometric form the impedance can be represented as a complex number, composed of a real and an imaginary part which can be displayed as a vector on the complex plane with the real part on the x-axis and the imaginary part on the y-axis [14].

$$Z = Z_0 \cdot e^{-j \cdot \varphi} = Z_0 \cdot (\cos(\varphi) + j \cdot \sin(\varphi))$$

Equation 2.12: Formula for the impedance in an AC circuit expressing the real and the imaginary part, for explanation of the symbols see equations 2.7, 2.8 and 2.10

The length of this vector represents the magnitude of the impedance Z_0 , and the projection of the vector on the x-axis or on the y-axis represent the real part or imaginary part of the impedance, respectively.

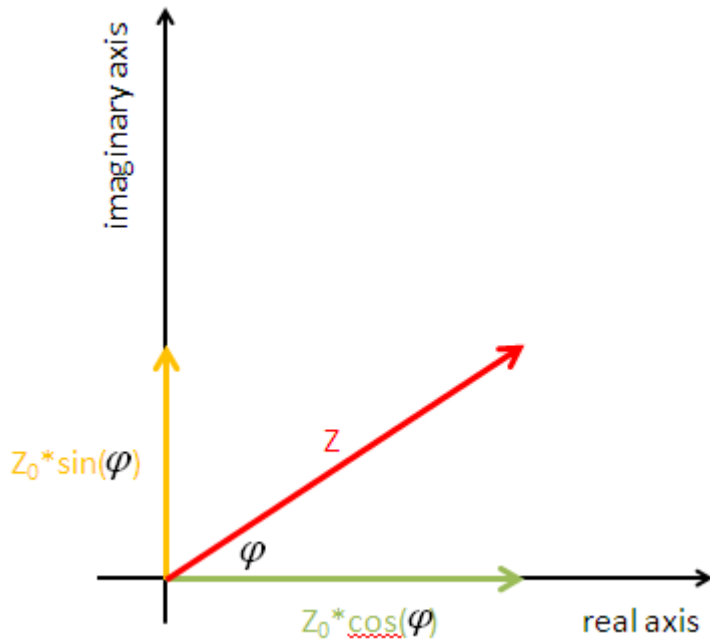


Figure 2.20: impedance displayed as a vector in a complex plane

An impedance spectrum consists of a series of impedance measurements at different frequencies, typically covering a range from 10^{-1} Hz to 10^6 Hz. If the magnitude of the impedance as well as the phase angle of each of these points is plotted against the logarithm of the frequency, the resulting two diagrams are called Bode plot. A diagram, in which the imaginary part is plotted against the real part of the impedance for every frequency point, is called Nyquist plot.

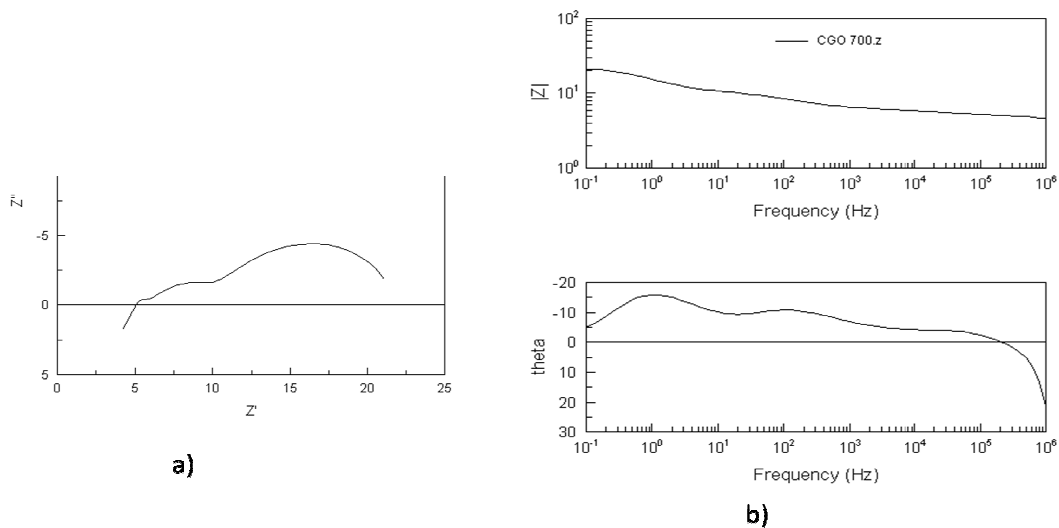


Figure 2.21: different ways of visualisation of the impedance spectra of a typical fuel cell. a) Nyquist plot, b) Bode plot

A negative imaginary value in the Nyquist plot means that changes in the current occur before changes in the potential, the current leads the potential, a behaviour typical for capacitors. Since the resistance in polycrystalline solid consists mainly resistive and capacitive elements, the negative imaginary part of the diagram is more interesting than the positive, and for that reason the y-axis in Nyquist plots shows the negative imaginary impedance part $-Z''$.

2.3.2.2. Utilisation of EIS in fuel cell testing

The resistance against the electron flow in the tested circuit is a sum of different resistances, originating from the electrolyte, the electrodes, the interconnects in the case of a stack test, the outer circuit, the testing device and the interfaces and connections between these components of the circuit. Some of the parts of the total resistance are due to limited conductivity of bulk and grain boundaries of metallic and ceramic materials used in the fuel cell test circuit, other parts are due to kinetics of electrochemical reactions or limitations to the mass transport

of the electrochemically active species to the electrodes. To the perturbation of the equilibrium applied by the sinusoidal potential change these different processes adapt with different frequency, making the impedance spectroscopy capable of separating and quantifying the different resistance parts.

Characteristic points of the Nyquist plot of an impedance spectrum of a fuel cell are its intercepts with the real axis. The intercept at the high frequency part shows the sum of all ohmic resistances and the intercept at the low frequency part shows the total circuit resistance consisting of all ohmic and non ohmic resistances [13]. The form of the curve of an impedance spectrum of a single cell in a Nyquist plot often consists of a series of depressed semi-circles, which are the arcs of circles with their centre below the x-axis. The frequency of the measuring point at the top of the arc makes it possible to connect each of the arcs with the resistance of one distinct process.

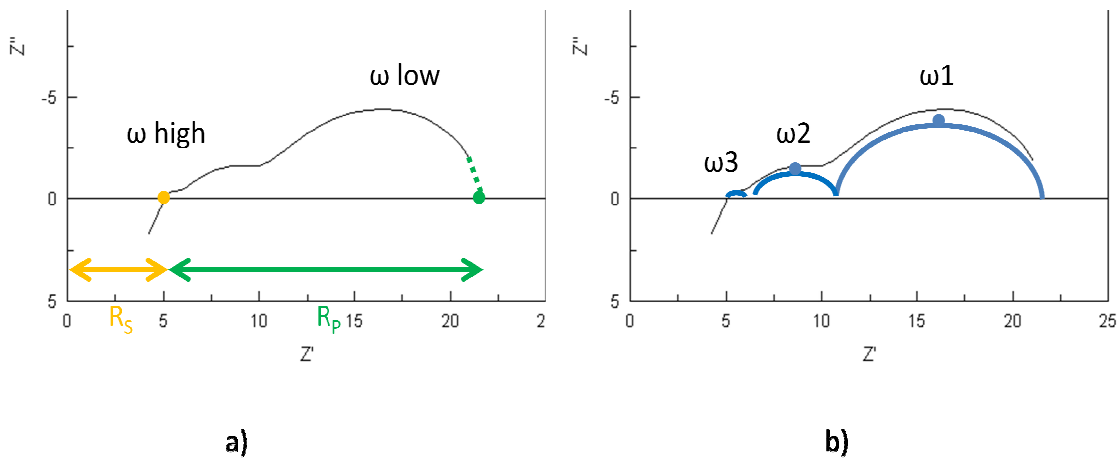


Figure 2.22: Nyquist plot of a typical impedance spectrum of a SOFC single cell. a) evaluation of the ohmic resistances R_S and the non ohmic resistances R_P from the interception points with the real axis. b) modelling of the graph of the Nyquist plot with depressed semi circles and their characteristic frequencies.

Another way of gaining information from the Nyquist plot of a fuel cell is to form an equivalent circuit from resistors, capacitors and inductors which exhibits the same behaviour upon the perturbations of different frequencies as the fuel cell. Generally a resistor and a capacitor placed in parallel form a semi-circle graph in the Nyquist plot, several of these RC elements put in series form a series of semi-circles in the Nyquist plot, similar to the Nyquist plot of a fuel cell [13].

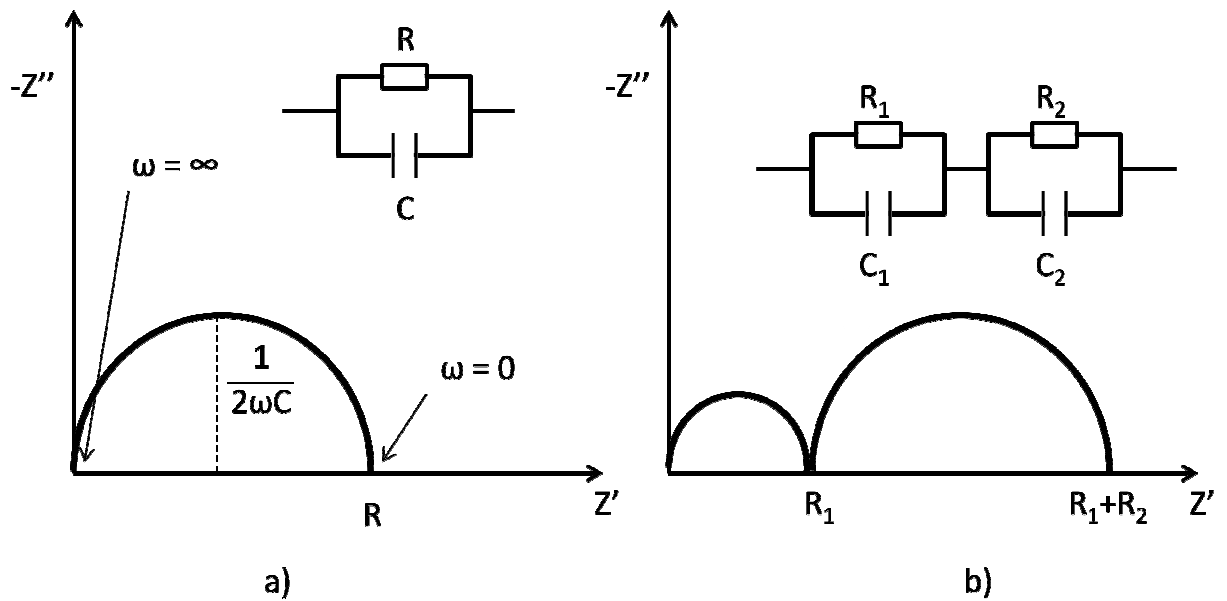


Figure 2.23: Nyquist plots of equivalent circuits. a) resistor and capacitor in parallel combination (RC element). b) two RC elements in series.

The Nyquist plot of RC elements crosses the real axis at an angle of 90° , which is different from the depressed semi-circles of real electrochemical cells. To model the behaviour of a double layer and form depressed semi-circles in the Nyquist plot a constant phase element (CPE) is used in the equivalent circuit instead of a capacitor [15]. The constant phase element is a non-ideal circuit element, invented to simulate real-world systems.

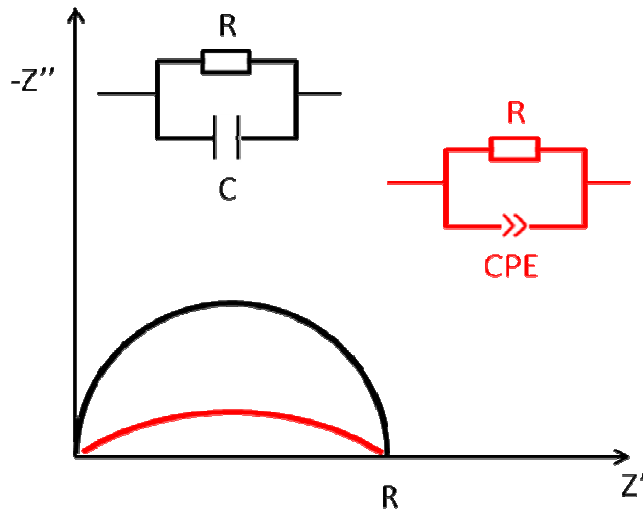


Figure 2.24: Nyquist plots of equivalent circuits with resistor and capacitor in parallel combination (black) and resistor and CPE in parallel combination (red).

$$\frac{1}{Z} = Q_0 \cdot (j \cdot \omega)^n$$

Z ... impedance [Ω]

Q_0 ... admittance [Ω^{-1}] at $\omega = 1 \text{ rads}^{-1}$

j ... imaginary unit square root of -1

ω ... angular frequency [rads^{-1}]

n ... constant between 0 and 1

Equation 2.13: Admittance of a constant phase element (CPE)

Mathematically the CPE's impedance can be expressed by equation 2.13. In the case of $n=1$ the CPE acts like an ideal capacitor, when $n=0$ the CPE acts like an ideal resistor. To create a depressed semi-circle in the Nyquist plot the CPE, with n value slightly less than 1, replaces a capacitor, resulting in a phase angle of less than 90° at all frequencies [15].

2.3.2.3. EIS setup and instrumentation

The single cells prepared and equipped with current collectors according to the procedures described in chapter 2.1. were attached to an alumina tube with an inner diameter of 15 mm and an outer diameter of 20 mm (Multilab 99.9%alumina tubes) and the edges were sealed with ceramic cement (Aremco Ceramabond 552 or Toku Ceramic inorganic adhesive P-24). The wires of the current collector were connected with the wires of the electrochemical measurement device to form a two terminal measurement system. The anode side was supplied with H_2 gas humidified by bubbling through water at room temperature while the cathode side was left open to air.

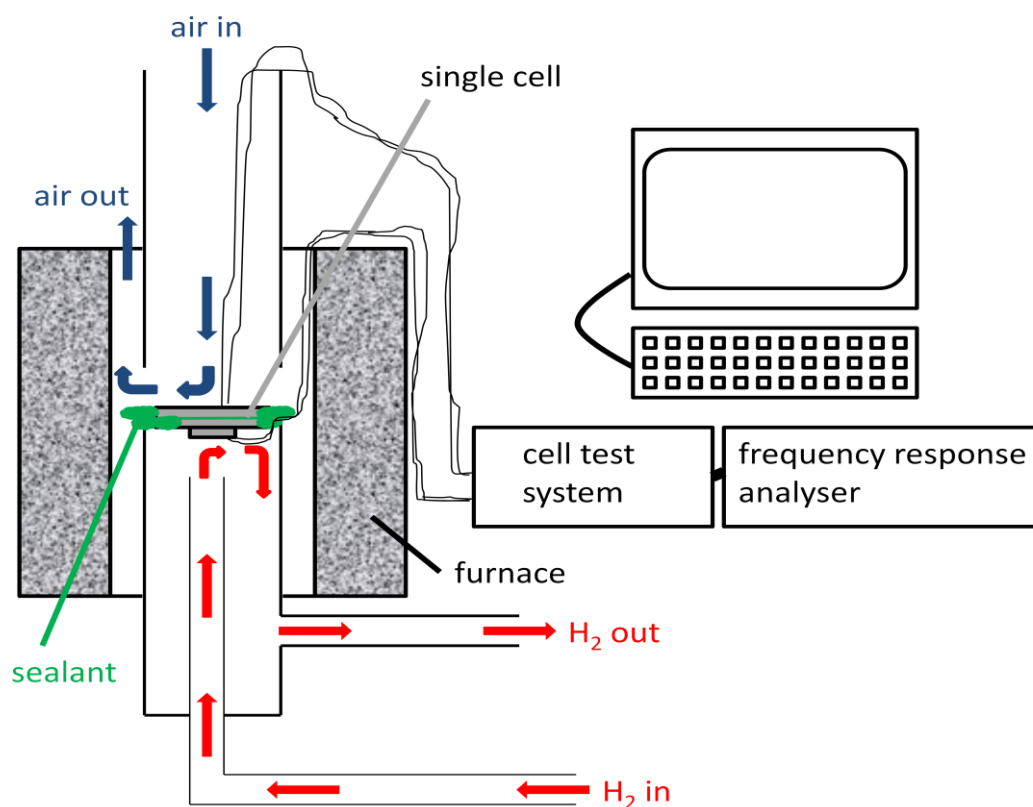


Figure 2.25: Schematic of the fuel cell electrochemical testing jig

IV curves were measured using a Solartron 1470E cell test system from OCV to OCV-0.7V taking 3 minutes at 1 measurement point per second. The same system combined with a Solartron 1252A frequency response analyzer was used for the EIS measurements. Frequency ranged from 200000 Hz to 0.1 Hz, 10 measurement points per decade were taken, the amplitude of the AC perturbation was 10 mV. Two impedance curves were taken at each temperature, one at OCV and one under a DC bias of -0.1 V compared to OCV. By applying a DC bias to the AC impedance, impedance spectra can be recorded of every point of the IV-curve instead just at OCV. This is important to distinguish the different resistance processes under the working conditions of the fuel cell. Current is flowing from the anode to the cathode of the fuel cell in the outer circuit at all times, while in an impedance spectrum at OCV the fuel cell is forced into electrolysis mode half of the measuring time, not necessarily reflecting the correct resistances of the working fuel cell.

- [1] C. B. Carter and M. G. Norton, "Ceramic Materials: Science and Engineering". *Springer*, 2007.
- [2] R. E. Mistler and E. R. Twinaime, "Tape casting: theory and practice". *Westerville, OH: American Ceramic Society*, 2000.
- [3] G. Corre, G. Kim, M. Cassidy, J. M. Vohs, R. J. Gorte, and J. T. S. Irvine, "Activation and Ripening of Impregnated Manganese Containing Perovskite SOFC Electrodes under Redox Cycling," *Chem. Mater.*, **21**, 1077–1084, 2009.
- [4] Q. X. Fu, F. Tietz, and D. Stöver, "La_{0.4}Sr_{0.6}Ti_{1-x}Mn_xO_{3-δ} Perovskites as Anode Materials for Solid Oxide Fuel Cells," *J. Electrochem. Soc.*, **153** (4), D74–D83, 2006.
- [5] T. Z. Sholklapper, C. Lu, C. P. Jacobson, S. J. Visco, and L. C. D. Jonghe, "LSM-Infiltrated Solid Oxide Fuel Cell Cathodes," *Electrochem. Solid-State Lett.*, **9**, (8), A376–A378, 2006.
- [6] L.-W. Tai and P. A. Lessing, "Modified resin–intermediate processing of perovskite powders: Part I. Optimization of polymeric precursors," *Journal of Materials Research*, **7**, 502–510, 1992.
- [7] J. H. Kim, H. Schlegl, and J. T. S. Irvine, "The catalytic effect of impregnated (La, Sr)(Ti, Mn)O_{3±δ} with CeO₂ and Pd as potential anode materials in high temperature solid oxide fuel cells," *International Journal of Hydrogen Energy*, **37**, 14511–14517, 2012.
- [8] B. D. Cullity, "Elements Of X Ray Diffraction". *Addison-Wesley Publishing Company, Inc.*, 1956.
- [9] A. R. West, "Basic solid state chemistry" . *Chichester u.a.: Wiley*, 1999.
- [10] I. M. Watt, "The Principles and Practice of Electron Microscopy", *Cambridge University Press*, 1997.
- [11] J. Goldstein, J. Newbury, D.E.Joy, C.E. Lyman, P. Echlin, E. Lifshin, L. Sawyer, J.R. Michael "Scanning Electron Microscopy and X-Ray Microanalysis", *Kluwer Academic/Plenum Publishers*, 2003.
- [12] C. H. Hamann and W. Vielstich, "Elektrochemie". *John Wiley & Sons Australia, Limited*, 2005.
- [13] X.-Z. Yuan, "Electrochemical impedance spectroscopy in PEM fuel cells fundamentals and applications". *London: Springer*, 2010.
- [14] P. Horowitz, "The art of electronics". *Cambridge University Press*, 1989.
- [15] V. F. Lvovich, "Impedance Spectroscopy: Applications to Electrochemical and Dielectric Phenomena". *John Wiley & Sons*, 2012.

3. Microstructure and performance of LSTM in skeletons of YSZ and CGO

The anode material for SOFCs has to be electronically conductive, with additional ionic conductivity for oxide ions being a big advantage. It has to show chemical and mechanical stability up to 1000 °C under reducing conditions, but also be tolerant to oxidising conditions and redox cycling. It should show good compatibility with the electrolyte material. As mentioned in chapter 1.7.3, so far no single material meeting all these conditions has been found, and the materials of the state of the art SOFC anodes are composites of two or more materials. Using the impregnation method, the skeleton of the anode is prepared from one material, and in a second step the precursor of a second material is infiltrated into the pores of the first material. The method and its advantages have been described in detail in chapter 1.7.3.

The skeleton material of the composite electrodes is often identical with the material of the electrolyte of the fuel cell. YSZ and CGO are frequently used as electrolytes in SOFCs, both commercially and in research. Perovskite oxides based on titanates with partial substitution on the B-site, like lanthanum strontium titanate manganate (LSTM), can add electronic conductivity and catalytic activity for the oxidation of the fuel to the composite anode.

3.1. Comparison of YSZ/LSTM and CGO/LSTM anodes

Three different kinds of thin button cells have been prepared using tape casting and the impregnation method as described in chapter 2.1. In the first type the whole skeleton was made of CGO91, with the pores of the anode impregnated with LSTM4646 and the pores of the cathode impregnated with LSM82. In the second type the whole skeleton was made of 8YSZ with the same materials impregnated as

in the first type. The third type of cells had a skeleton made of 8YSZ layers for cathode and electrolyte and a CGO91 layer for the anode. All the composite anodes contained of 55 wt% skeleton and 45 wt% perovskite and the cathodes of 50 wt% skeleton and 50 wt% LSM. The firing temperature for the skeleton was 1400 °C, the firing temperature after the impregnation of the anode 1150 °C and the firing temperature after the impregnation of the cathode 1000 °C. The procedure of the fabrication of the cells is described in detail in chapter 2.1. Unfortunately the thin button cells of type one (full CGO cells) lacked of mechanical stability and were neither characterized nor tested.

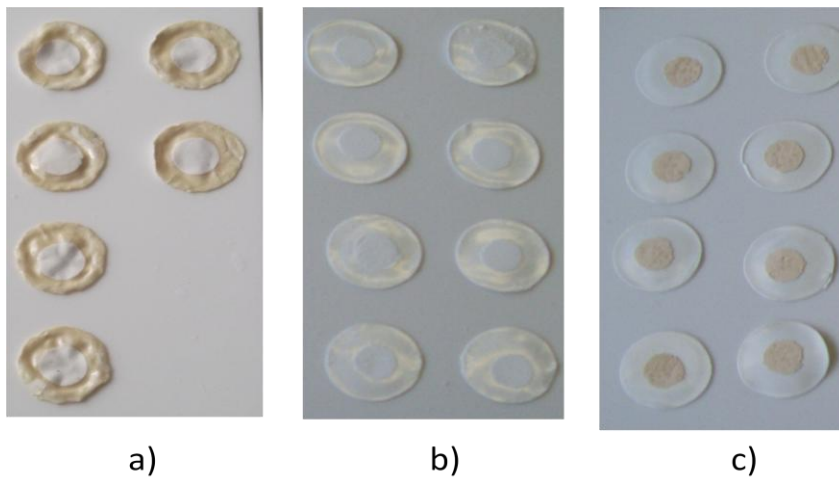


Figure 3.1: Skeletons of button cells: a) type1: full CGO skeleton, b) type2: full YSZ skeleton, c) type3: cathode and electrolyte made of YSZ, anode of CGO. Showing deformation and mechanical instability of the full CGO button cells

The anodes of the impregnated button cells of type two and of type three were characterized by XRD, electrochemically tested producing IV curves and AC impedance spectra and their microstructure was investigated by SEM.

3.1.1. XRD analysis of the composite anodes

XRD diagrams of anodes with skeletons of 8YSZ and CGO91 fired at 1400 °C, impregnated with a precursor of LSTM4646, and after impregnation fired at 1150 °C show the peaks of 8YSZ, CGO91 and LSTM4646, which could be indexed, and no significant signs of peaks of any secondary phases (see figure 3.2)

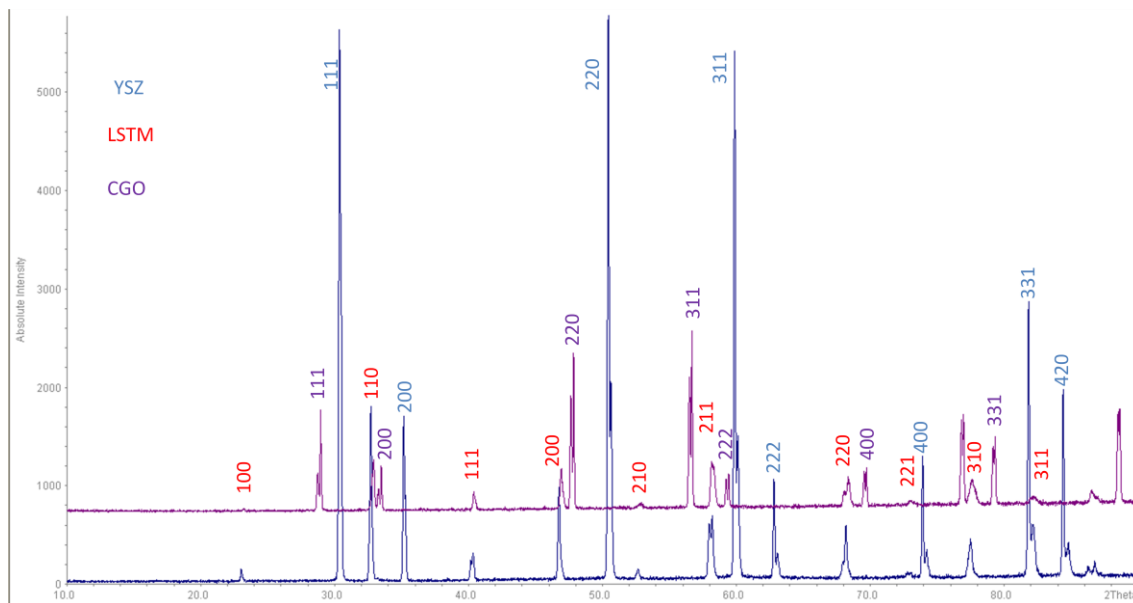


Figure 3.2: XRD diagrams of composite anodes 8YSZ/LSTM4646 (blue) and CGO91/LSTM4646 (purple). The peaks were indexed using the cubic space groups for 8YSZ and CGO91.

The position of the peaks in the XRD diagrams of composite 8YSZ/LSTM4646 and CGO91/LSTM4646 anodes are in good agreement with literature, which suggests cubic (Fm3m) or tetragonal (P42/nmc) phases for 8YSZ with lattice parameters of around 5.14 Å for the cubic phase [1] [2]. Similarly, a cubic fluorite structure with space group Fm3m is described for CGO91, having a cell parameter of around 5.42 Å [3]. The lattice of $\text{La}_{0.4}\text{Sr}_{0.6}\text{TiO}_{3.2}$ (LST46) changes from cubic (Pm3m) over tetragonal (I4/mcm) to rhombohedral (P6₃cm) with increasing level of manganese

doping of the B-site of the perovskite according to literature [4]. The lattice parameter of the cubic single cell is reported to be 3.8921 Å for LST46, however for manganese substituted LSTs a hexagonal or rhombohedral lattice is described with the hexagonal parameters $a = 5.4972 \text{ \AA}$ and $c = 13.4020 \text{ \AA}$ for LSTM4646 [4] [5].

A basic refinement of the spectra obtained from composite anodes YSZ/LSTM and CGO/LSTM carried out with the “Index&Refine” feature of the STOE WinXPOW software confirmed the literature cell parameters with 5.1392 Å and 5.1402 Å for cubic YSZ before and after the impregnation of LSTM and 5.4195 Å and 5.4224 Å for cubic CGO before and after the impregnation of LSTM. Literature suggests a hexagonal lattice with the parameters $a = 5.4972 \text{ \AA}$ and $c = 13.4020 \text{ \AA}$ for the hexagonal perovskite LSTM4646. The best results for the refinement of XRD spectra of all LSTM perovskites impregnated in a YSZ skeleton were achieved assuming a hexagonal unit cell resulting in pseudo-cubic lattice parameters of $a = 3.8894 \text{ \AA}$ for LSTM4646 and $a = 3.8914 \text{ \AA}$ for LSTM4682.

3.1.2. Comparison of the microstructure

The anodes of the button cells fabricated in the way described in chapter 3.1 were investigated in a secondary electron microscope (SEM) using secondary electron imaging (SEI) techniques. Anodes with skeletons of 8YSZ and CGO91 before and after the impregnation with LSTM4646 were examined under air and after simulating the working conditions of a SOFC anode by reducing them for 6 hours at 900 °C in a dry atmosphere of 5 % hydrogen in argon.

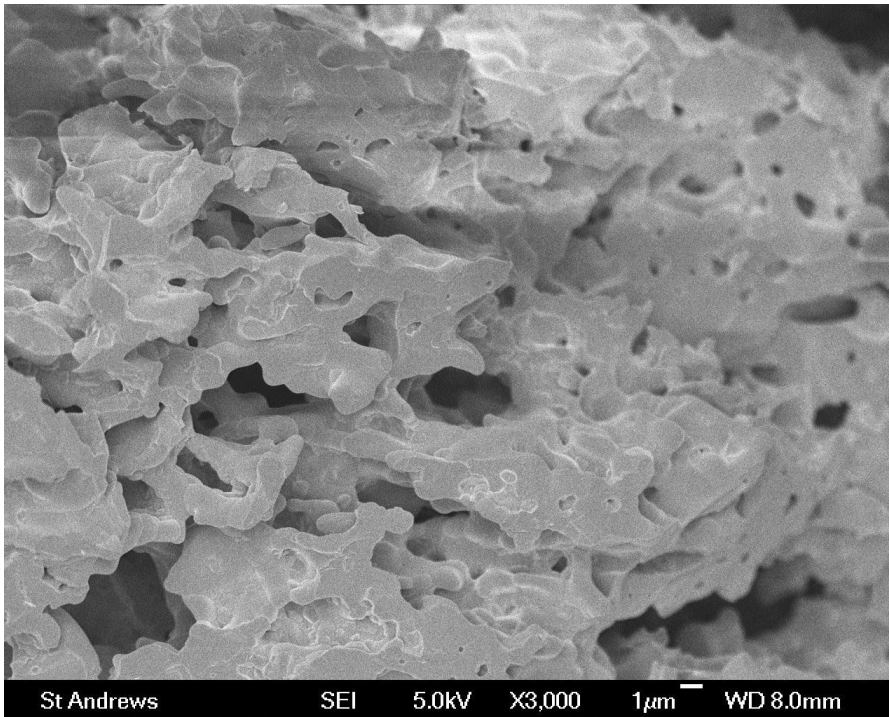


Figure 3.3: YSZ skeleton after impregnation with LSTM at 3000x magnification

Secondary electron imaging shows a very smooth coating of LSTM4646 on top of the YSZ skeleton after the impregnation with LSTM and firing of the cells under air atmosphere. (figure 3.3). The microstructure of the composite anodes is studied in more detail in the chapters 3.2.2 and 3.2.3.

The contact between electrolyte and anode is better in the cells with YSZ being the material of electrolyte and anode than in cells with a YSZ electrolyte and a CGO anode. Whenever splinters of the cells with CGO based anodes were used directly for the SEM investigation, the anode of the single cell separated from the electrolyte during the breaking of the cell. Even if the same kind of cells were embedded in resin and cut with a saw, a delamination phenomenon could be observed. Cells with a full YSZ skeleton could be broken without separation of the anode and did not show delamination, as shown in figure 3.4.

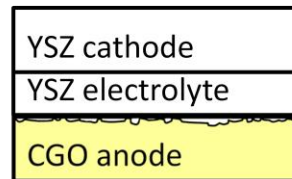
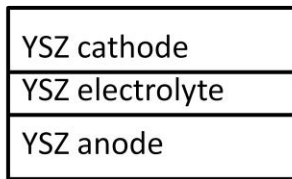
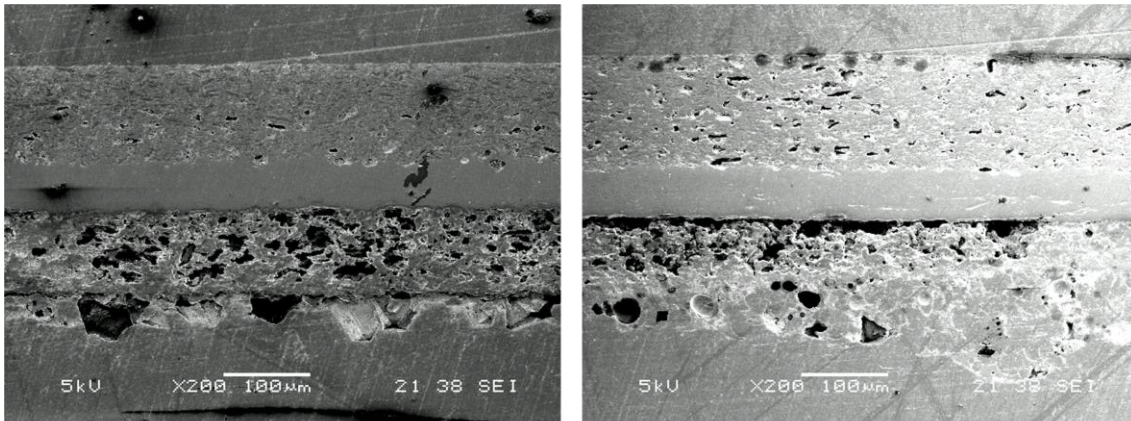


Figure 3.4: SEI images of single cells under low magnification showing delamination of the CGO anode from the YSZ electrolyte

3.1.3. Electrochemical performance of the single cells

Button cells fabricated in the way described in chapter 3.1 were electrochemically tested using a test jig, a Solartron cell test system and a frequency response analyser as described in chapter 2.3.2.3 and shown in figure 2.25. IV curves and EIS spectra were recorded in a temperature range from 600 °C to 800 °C in increments of 50 °C. The current collection grid was painted onto the button cells with a platinum containing paste, the fuel was humidified hydrogen gas at a flow rate of 30-40 ml/min.

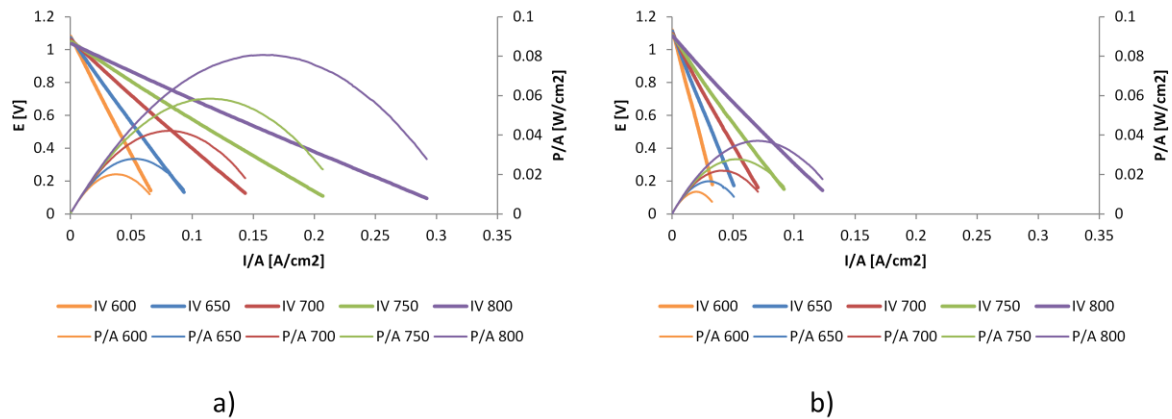


Figure 3.5: IV-curves and power density curves of single cells with composite anodes of YSZ/LSTM (a) and of CGO/LSTM (b) at different temperatures

The OCV values of the tested cells ranged from 1.05 V to 1.1 V, which is slightly lower than the theoretical. The shape of the IV-curves is almost linear over the whole range of current densities, without showing non-linear parts close to OCV or close to the maximal current density, indicating that ohmic resistances and linear polarisations dominate the resistance over the whole current density range.

The single cells with the YSZ/LSTM composite anodes generally showed better electrochemical performance than the cells with CGO/LSTM anodes, with a smaller gradient of the IV-curves and higher maximal power densities. The maximal power densities at 700 °C were around 0.042 W/cm² for the YSZ/LSTM cell and around 0.022 W/cm² for the CGO/LSTM cell, and at 800 °C around 0.081 W/cm² for the YSZ/LSTM cell and around 0.037 W/cm² for the CGO/LSTM cell. The power density of the cell with the YSZ/LSTM anode was double the power density of the cell with the CGO/LSTM anode at 750 °, below that temperature it was slightly less than double, above this temperature slightly more than double.

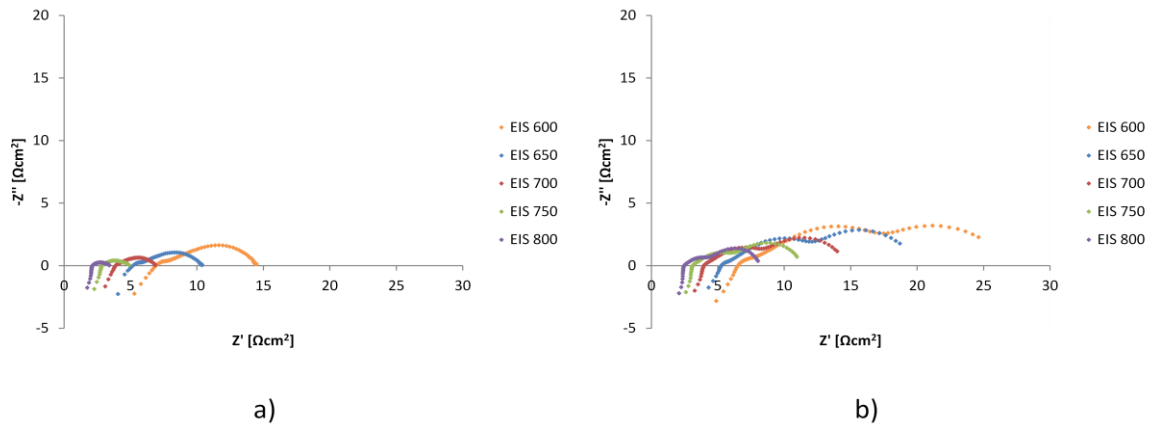


Figure 3.6: Nyquist plots of EIS spectra of single cells with composite anodes of YSZ/LSTM (a) and of CGO/LSTM (b) at different temperatures

Figure 3.6 shows the Nyquist plots of the impedance spectra of the two single cells with different composite anodes fabricated as described in chapter 3.1. The CGO/LSTM cell shows larger impedances than the YSZ/LSTM cell at all temperatures, as would have been expected from the IV curves of these cells shown in figure 3.5. The observed relation between the total resistance of the cells and the maximal power density shows good accordance with equation 3.1 for both cells at all temperatures tested.

Splitting the total resistance of the single cells into an ohmic part R_S and a non-ohmic polarisation R_P shows that all parts of the impedance are larger for the cells with the CGO/LSTM anodes, but while on average R_S of the CGO/LSTM anodes is only around 5 % larger than R_S of the YSZ/LSTM anodes, R_P is on average around 250 % larger. The better electrochemical performance of the YSZ/LSTM anodes seems predominantly caused by the lower polarisation of the YSZ/LSTM anodes compared to the CGO/LSTM anodes (see figure 3.7).

	YSZ/LSTM			CGO/LSTM		
T in °C	Rs	Rp	R total	Rs	Rp	R total
600	6.9	7.6	14.5	6.5	20.5	27
650	5.2	5.2	10.4	5.3	14.8	20.1
700	3.9	3	6.9	3.9	10.8	14.7
750	2.8	2.1	4.9	3.1	8.3	11.4
800	2.1	1.3	3.4	2.5	5.7	8.2

Figure 3.7: Table displaying ohmic parts and non ohmic polarisations of the impedance of single cells with YSZ/LSTM and CGO/LSTM composite anodes

The Nyquist plot of the CGO/LSTM cell shows two depressed semicircles at all temperatures and a third depressed semicircle, which is visible at temperatures of 600 °C to 700 °C, but not visible in the Nyquist plots at higher temperatures (see figure 3.8.b). The characteristic frequencies (the frequencies with a local maximum of imaginary resistances) of the low frequency arc range from 0.4 Hz (600 °C) to 1.3 Hz (800 °C), all corresponding to a capacitance of the capacitor of a Randle circuit of around 15 mF/cm², the polarisation causing this arc in the Nyquist plot is subsequently called R_{P3}. The characteristic frequencies of the medium frequency arc range from 25 Hz (600 °C) to 100 Hz (800 °C), all corresponding to a capacitance of the capacitor of a Randle circuit of around 0.25 mF/cm², the polarisation causing this arc in the Nyquist plot is called R_{P2}. The third, high frequency arc, which can only be observed in Nyquist plots at low temperatures, shows characteristic frequencies from 10 kHz (600 °C) to 20 kHz (650 °C), all corresponding to a capacitance of the capacitor of a Randle circuit of around 0.5 µF/cm², the polarisation causing this arc in the Nyquist plot is called R_{P1}.

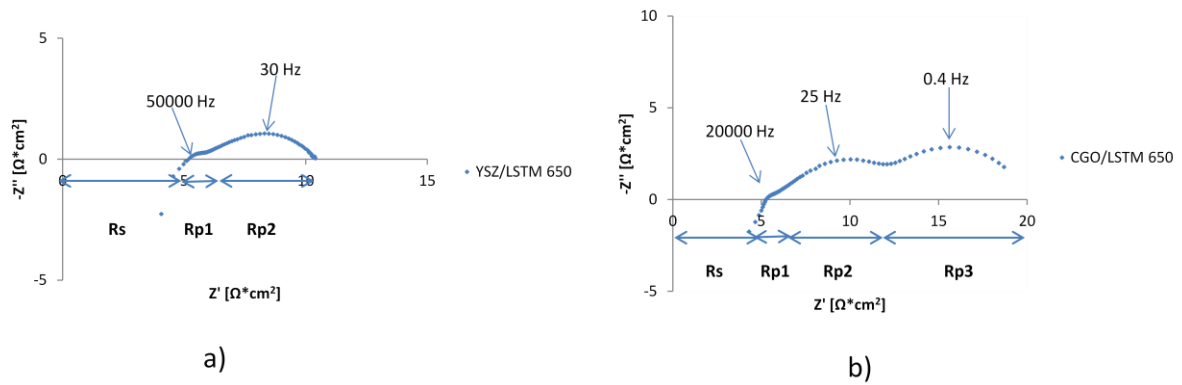


Figure 3.8: Nyquist plots of single cells with YSZ/LSTM composite anodes (a) and CGO/LSTM anodes (b) at 650 °C, showing the depressed semicircles and their characteristic frequencies

The Nyquist plot of the YSZ/LSTM cell shows only one depressed semicircle at frequencies under 1 kHz with characteristic frequencies from 20 Hz (600 °C) to 160 Hz (800 °C) (see figure 3.9 a). The similarities in the summit frequencies, in the shape of the arcs in the Nyquist plots and in the values of the activation energy of the mid-frequency arcs lead to the conclusion that R_{P2} in the cell with the YSZ/LSTM anode and the medium semi-arc R_{P2} in the cell with the CGO/LSTM anode are caused by the same process. Characteristic frequencies of 20 Hz to 160 Hz or capacitances of around 0.25 mF/cm^2 may relate R_{P2} in both cells to charge transfer from and to adsorbed species [11] or to the diffusion of the oxide ions [13]. The activation energy of the process is around 0.85 eV to 0.9 eV and only slightly smaller than the value of the activation energy for the oxide ion conductivity in 8YSZ pellets fabricated in a way similar to this work, which is 0.95 eV [14] [1]. Good performance of the LSTM network providing the electronic conductivity and the platinum paste providing the catalytic activity for the oxidation of hydrogen could lead to the transport of oxide ions to the triple phase boundary being the main factor of the impedance in the composite anode YSZ/LSTM and one of the two main factors in the composite anode CGO/LSTM.

At higher frequencies there is another small depressed semicircle visible only at temperatures up to 700 °C, both in the measurements of the CGO/LSTM cell and of the YSZ/LSTM cell, named R_{P1} . These small high frequency arcs with characteristic frequencies between 10^4 Hz and 10^5 Hz corresponding with capacitances of around $0.5 \mu\text{F}/\text{cm}^2$ can be associated with charge transfer processes to and from the oxide ions at the interface between the electrode and the electrolyte or in the case of a composite anode between the ion conductive and the electron conductive parts of the electrode [12] [11]. These arcs are significantly smaller than the other arcs and disappear at temperatures of 750 °C and above, so there seems to be a considerable thermal activation of the underlying process, even though because of the small size of the arc the activation energy could not be quantified.

The presence of an additional depressed semicircle in Nyquist plots of cells with CGO/LSTM anodes (R_{P3}) and its absence in comparable cells with YSZ/LSTM anodes was confirmed in all EIS measurements of over 20 different cells at all temperatures. The characteristic frequency of this additional semicircle ranged from below 0.1 Hz to 3 Hz at different temperatures and cells. This characteristic frequencies suggest a capacitance of around $15 \text{ mF}/\text{cm}^2$ of the Randle's circuit, which is normally caused by a mass transfer process [11]. The cells were identical apart from the skeleton material of the anodes, so the assumption is that the transport of the hydrogen fuel to the reaction sites is obstructed in the cells with CGO/LSTM composite anodes. This might be a result of the differences in the microstructure of the different anodes described in chapter 3.1.2.

The decrease of R_S and R_P with increasing temperature is displayed in an Arrhenius plot in figure 3.8 for the single cells with composite anodes of YSZ/LSTM and CGO/LSTM. From the gradient of the graphs in the Arrhenius plot the activation energy of the process responsible for the resistance can be calculated.

The series resistances R_S are caused by the ohmic resistance of the electrolyte and the electrodes and the contact resistance on the interfaces of the different parts of the single cells [11]. The fact that the ohmic resistance is similar in the YSZ/LSTM cells and the CGO/LSTM cells suggests either that the poor connection between the anode and the electrolyte caused by delamination of the CGO/LSTM cells (see figure 3.4) does not significantly affect the electrochemical performance of the cells, or that the major part of the severe delamination seen in figure 3.4 is caused by the mechanical stress during the sample preparation for SEM.

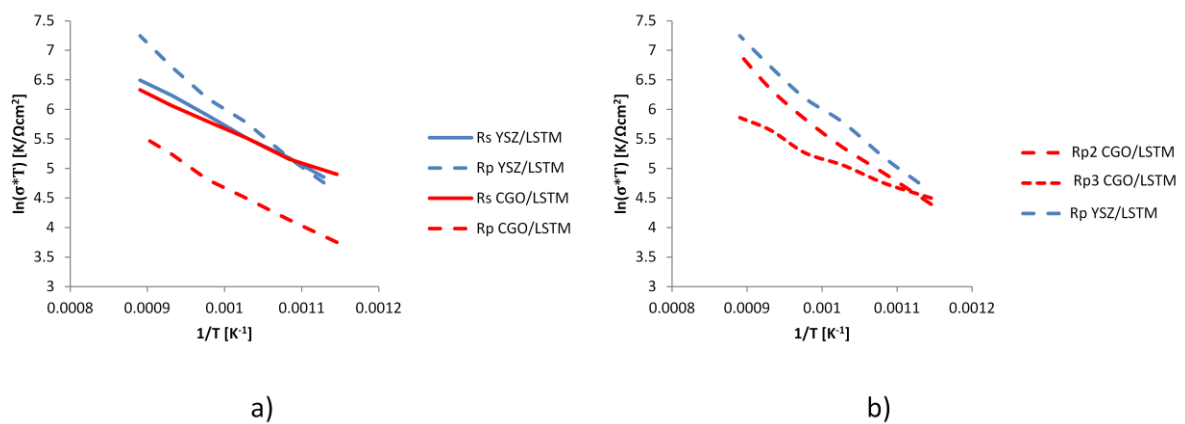


Figure 3.9: Arrhenius plots of the different parts of the impedance in single cells with YSZ/LSTM and CGO/LSTM composite anodes. In 3.8.b the different parts of the polarisation resistance visible in cells with CGO/LSTM anodes were plotted separately.

The activation energy of the ohmic processes calculated from the graphs displayed in figure 3.9. was similar for the cells with YSZ/LSTM and CGO/LSTM composite anodes with around 0.55 eV. The non ohmic polarisation processes had an activation energy of around 0.89 eV for the cell with the YSZ/LSTM anode, and an activation energy of around 0.83 eV for the cell with the CGO/LSTM anode. Since the R_P of the cells with CGO/LSTM consisted of two clearly distinctive arcs, it was obvious that the 0.83 eV was the average thermal activation energy of two different processes. Splitting up the polarisation resistance of the cell with the CGO/LSTM

anode into two different lines in the Arrhenius plot (figure 3.9.b) resulted in an activation energy of around 0.96 eV for R_{P2} (the polarisation with the higher characteristic frequency) and around around 0.76 eV for R_{P3} (the polarisation with the lower characteristic frequency).

Comparing of the values of R_{P2} in the YSZ/LSTM cell with the values of R_{P2} in the CGO/LSTM cell shows that although the activation energy for the processes is the same, the absolute value for the resistance in the YSZ/LSTM cell is lower. The lines in the Arrhenius plot are almost parallel, but the line for R_{P2} (YSZ/LSTM) is located half an order of magnitude above the line for R_{P2} (CGO/LSTM), as can be seen in figure 3.9.b. According to the theory of the interaction of manganese with YSZ as presented in chapter 3.1.4 the smooth LSTM coating of the YSZ skeleton would lead to a large number of small triple phase boundary reaction sites after reduction. The average pathway of oxide ions to reach the next triple phase boundary site would be shorter in YSZ/LSTM composite anodes compared to CGO/LSTM composite anodes, which could explain the lower values of R_{P2} .

In literature cells with LSTM anode materials of the composition $\text{La}_{0.6}\text{Sr}_{0.4}\text{Ti}_{1-x}\text{Mn}_x\text{O}_{3-\delta}$ ($x=0.2, 0.4, 0.6, 0.8$) achieved maximal power densities of 240 – 300 mW/cm² at 800 °C, with the composition with the highest manganese content $\text{La}_{0.6}\text{Sr}_{0.4}\text{Ti}_{0.2}\text{Mn}_{0.8}\text{O}_{3-\delta}$ showing the best performance [6]. The better performance compared with the cells in this study might be due to the CGO electrolyte material and to the fact that the anode of the cell was not a composite but pure porous LSTM. Other research in literature with LSTM4646/YSZ composite anodes could achieve R_S values of around 3 Ωcm^2 and R_P values between 0.8 and 0.9 Ωcm^2 at 820 °C [7]. The higher R_S values compared to the cells in this study can be ascribed to the thicker electrolyte (2 mm), the lower R_P values to higher firing temperatures (1500 °C) of the YSZ skeleton. Cells with dimensions and materials very similar to the cells in this study were fabricated in the same research group at the University of St. Andrews and achieved around 150 mW/cm² at 800 °C [8], the superiority of the electrochemical performance of these cells is the result of enhanced catalytic activity due to the impregnation of 10 wt.% CeO₂ next to 1 wt.% Pd.

3.1.4. Theory of the interaction of Mn with YSZ

One possible reason for the superiority in the electrochemical performance of the cells with composite anodes made of YSZ/LSTM over the cells with CGO/LSTM anodes is the interaction of manganese containing perovskites with YSZ, as also mentioned in chapter 1.7.4. After the impregnation of LSTM a thin and dense layer is formed on top of the YSZ skeleton, a behaviour similar to liquids wetting the surface of a solid, which can't be observed on top of a CGO skeleton (see figure 3.3) or if LST is impregnated instead of LSTM [9] [10]. Upon reduction the dense coating is broken up to form nanoparticles, providing a large area of triple phase boundary in the composite anode [9]. This behaviour is explained by the reduced solubility of Mn^{2+} in YSZ compared to Mn^{3+} or Mn^{4+} , depleting the surface of the perovskite of manganese under reducing conditions and thus weakening the interaction responsible for the wetting [9].

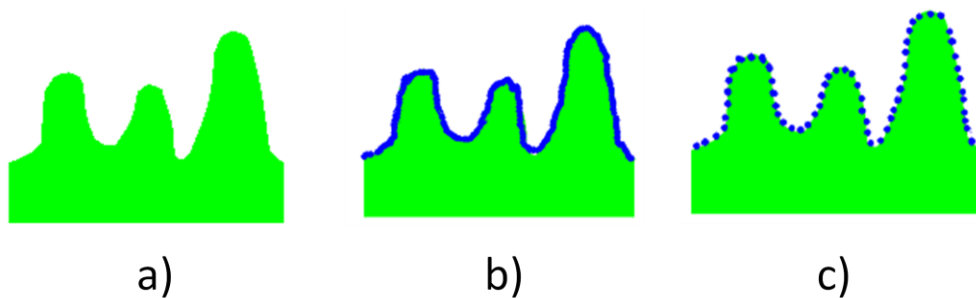


Figure 3.10: Schematic of a YSZ skeleton (a) impregnated with LSTM under oxidising conditions (b) and after reduction (c)

The microstructure of the system YSZ/LSTM according to this theory is schematized in figure 3.10, showing the dense coating under oxidising conditions (3.10.b) and the nanoparticles under reducing conditions (3.10.c).

3.1.5. Conclusions

XRD patterns of composite anodes of YSZ/LSTM4646 and CGO/LSTM4646 showed all the peaks expected for YSZ, CGO and LSTM4646, which could be indexed, and no distinctive secondary phase peaks. A basic refinement confirmed the cell parameters for 8YSZ, CGO91 and LSTM4646 found in literature.

SEM images of the cells with a YSZ skeleton for the cathode and electrolyte and a CGO skeleton of the anode show delamination between the electrolyte and anode which can't be found in cells with an all YSZ skeleton. LSTM4646 forms a smoother coating on top of a YSZ skeleton than on top of a CGO skeleton after impregnation and firing. This smooth coating of manganese containing perovskites on top of YSZ skeletons has been investigated in literature [9] and ascribed to a characteristic interaction between the two phases triggered by the solubility of Mn^{3+} and Mn^{4+} in YSZ.

Impedance spectroscopy showed similar ohmic resistance values for the YSZ/LSTM cell and the CGO/LSTM cell. The polarisation part of the spectra showed two depressed semi-arcs for the YSZ/LSTM cells and three depressed semi-arcs for the CGO/LSTM cells. The high frequency arc R_{P1} was small and only visible at low temperatures, it was ascribed to charge transfer processes. The characteristic frequencies and the thermal activation of the medium frequency arc R_{P2} indicate a relation to the surface movement and diffusion of oxide ions to the triple phase boundary of the electrodes. The low frequency arc R_{P3} can only be observed in spectra of CGO/LSTM cells and is related to a mass transport phenomenon, probably an obstruction of the movement of hydrogen fuel to the anode reaction sites caused by a different microstructure of the CGO/LSTM anode compared to the YSZ/LSTM anode.

3.2. Microstructural studies of composite anodes

Both literature [9] and own results (see chapter 3.1) show the importance of the microstructure for the electrochemical performance of composite anodes. The studies about the microstructure of the composite anodes were carried out using an electron microscope with an EDS and BSE facility as described in chapter 2.2.2.4.

3.2.1. Microstructure of the skeletons of the composite anodes

3.2.1.1. Skeletons of pure YSZ and CGO

The microstructure of the skeleton of composite anodes made of the materials 8YSZ and CGO91 prepared as described in chapters 2.1.1 and 3.1 is displayed in figure 3.11 in different magnifications.

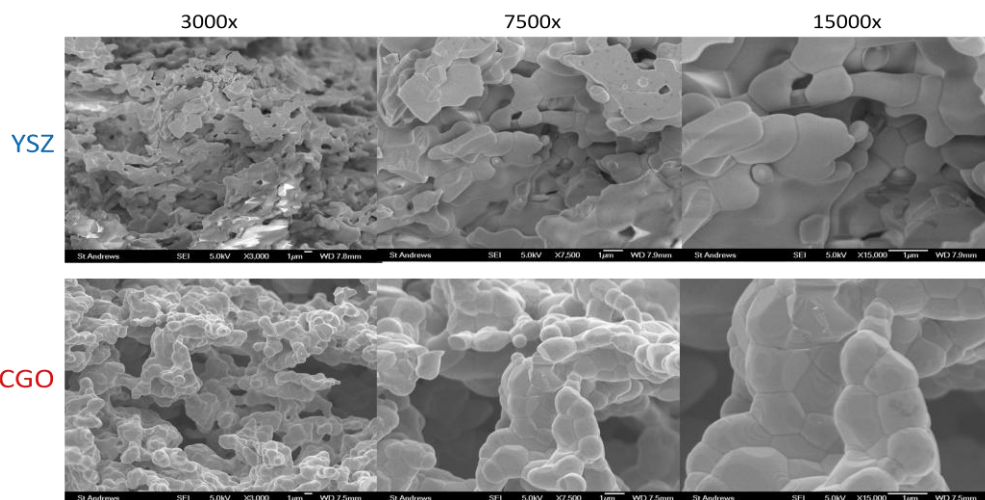


Figure 3.11: SEI images of a YSZ skeleton and a CGO skeleton under 3000x, 7500x and 15000x magnification

The grains of the CGO skeleton seem to be spherical and the size of the different grains similar to each other around 1 µm, while the grains in the YSZ skeleton are

irregular shaped with considerable differences in the size of the grains between 200 nm and 2 μm (see figure 3.11).

3.2.1.2. Skeletons of YSZ with impregnated CGO

A composite skeleton fabricated by impregnation of an 8YSZ skeleton with an aqueous precursor of CGO91 could improve the ionic conductivity of the skeleton while avoiding the delamination problems between a YSZ electrolyte and a CGO electrode described in chapter 3.1.2. According to literature CGO applied to a YSZ skeleton by the impregnation method can form a smooth and dense layer on top of the YSZ [15].

After the preparation of the YSZ skeleton as described in chapter 2.1.1 a precursor solution for CGO91 consisting of the stoichiometric amounts of cerium nitrate and gadolinium nitrate in deionised water was impregnated into the pores of the electrode skeleton. The impregnation was repeated until the weight of CGO inside the pores reached 10 % of the total electrode weight and the cells were fired at 1200 $^{\circ}\text{C}$ for 6 hours. The microstructure of the composite anodes was investigated by SEI, BS and EDS techniques with a FE-SEM electron microscope.

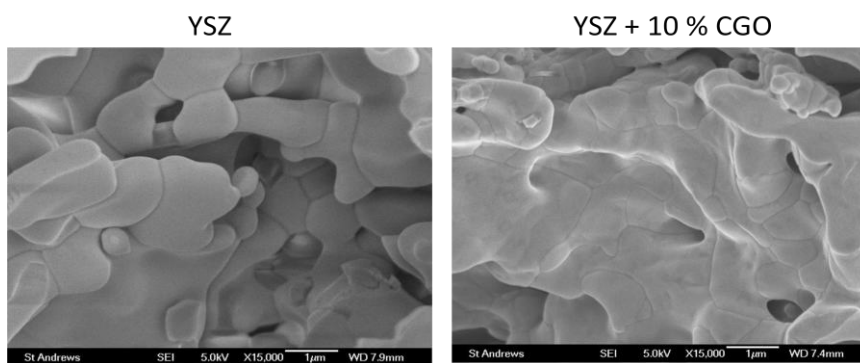


Figure 3.12: SEI images of a YSZ skeleton and a YSZ skeleton impregnated with 10 wt% CGO at 15000x magnification.

The SEI images of the skeleton reveal that the grain boundaries seem less visible after the YSZ skeleton is impregnated with 10 wt% CGO, the gaps between the grains seem less deep. This could support the theory of a thin and smooth coating of CGO over the YSZ skeleton as suggested in [15], reducing the depth of the gaps between the grains as schematized in figure 3.13.

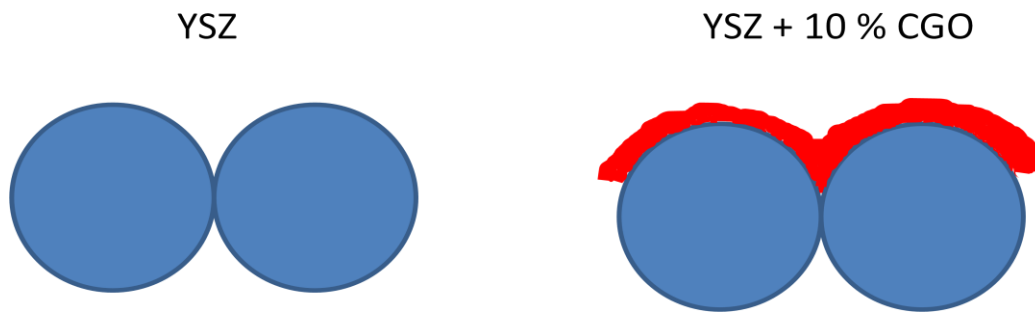


Figure 3.13: schematic of a YSZ skeleton and a YSZ skeleton covered with a thin cover of 10 wt% CGO explaining the reduction of depth of the grain boundaries

Further investigation of the microstructure of the composite skeleton fabricated by impregnation of CGO into the pores of a YSZ skeleton was carried out by X-ray mapping and backscattered electron images. The single cell was embedded into a resin, cut, ground and polished in the way described in chapter 2.2.2.4, and elemental maps of zirconium and cerium were created for the identification of the YSZ and the CGO phase.

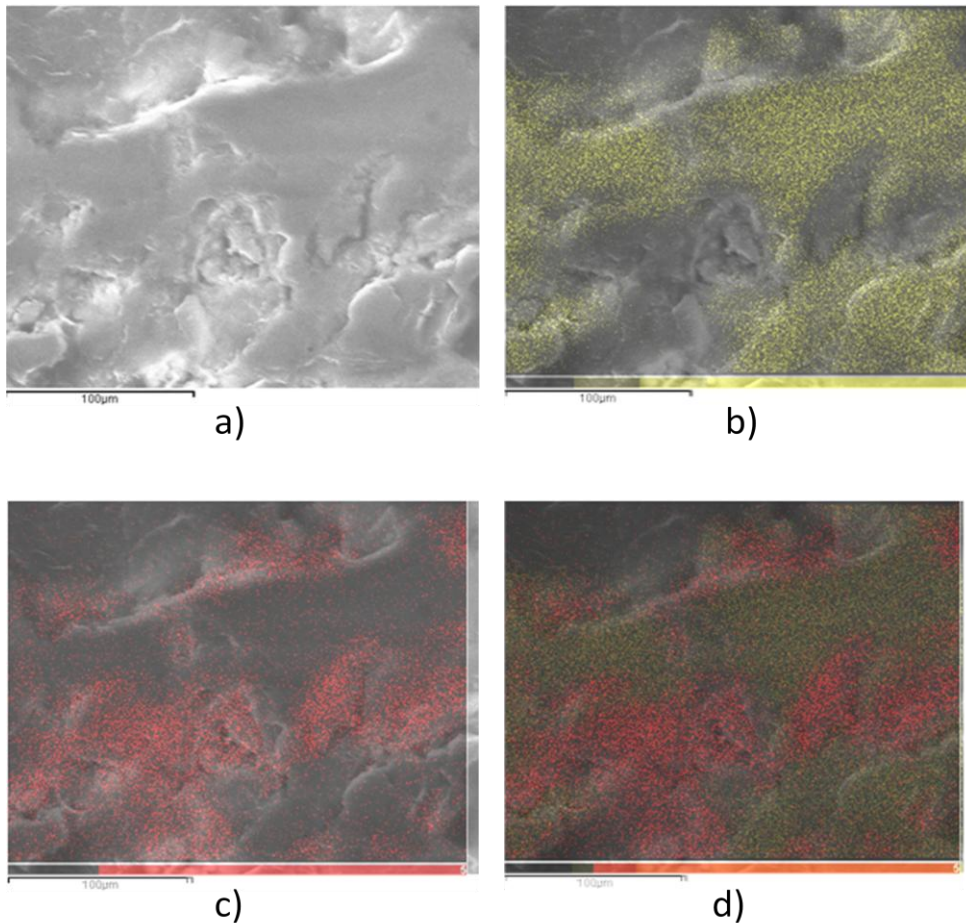


Figure 3.14: A SEI picture of the microstructure of the composite skeleton in 6000x magnification (picture a). The SEI image is superimposed by an EDS zirconium map (picture b), by an EDS cerium map (picture c), and by both a zirconium and a cerium map (picture d) of the same area

The EDS elemental maps seem to support the theory of CGO forming a coating and seem to suggest that the impregnated CGO layer is thicker at parts of the YSZ skeleton looking concave at the two-dimensional pictures, which would be cavities in the three-dimensional skeleton. It seems reasonable that the aqueous precursor applied to the YSZ skeleton during the impregnation fills cavities in the skeleton resulting in an accumulation of impregnated CGO at these parts of the skeleton after firing.

This impression is also supported by images of backscattered electrons, which allow to draw conclusions about the average atomic weight of the atoms building the different phases. Phases with higher average atomic weight deflect the incoming electrons to a higher angle making a backscatter more likely, resulting in a brighter picture. In a skeleton containing YSZ and CGO the CGO parts look brighter and the YSZ parts darker, due to the higher atomic numbers of the atoms in CGO.

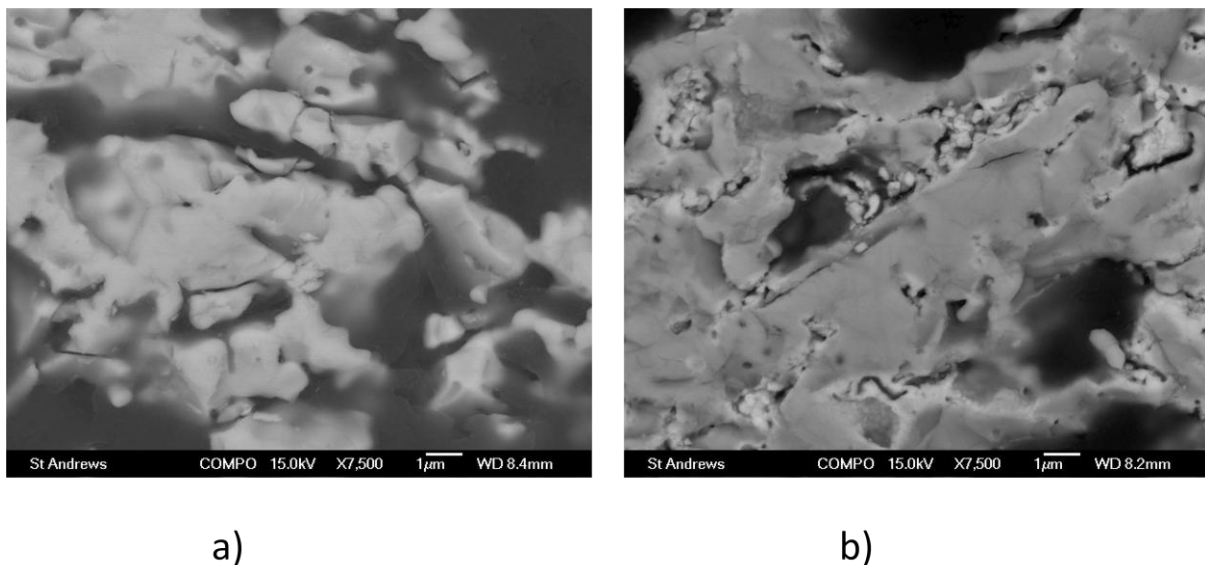


Figure 3.15: BS-SEM pictures of the microstructure of the composite skeleton in 7500x magnification of a YSZ skeleton (a) and by a skeleton of YSZ with 10wt% impregnated CGO (b)

The backscattered electron images show uniform brightness of the YSZ skeleton (figure 3.15 a) and brighter areas in a YSZ skeleton impregnated with CGO (figure 3.15 b), as expected. The bright areas do not make the impression of a smooth coating of CGO, but of a concentration of CGO in the cavities of the YSZ skeleton.

In skeletons of YSZ and 10wt% CGO applied by the impregnation method the CGO forms a layer on top of the YSZ grains, as shown by SEI images, EDS mapping and backscattered electron images. The assumption that this layer is smooth and dense [15] is supported by the SEI images, but not by EDS mapping or BS images. The

SEI images show high resolution pictures of the surface of the skeletons, without the destruction of this surface by cutting, grinding and polishing the sample. This SEI images show a dense and smooth coating on the surface, but as a pure surface investigation technique can't answer the question if the thickness of the layer is uniform. The images of EDS mapping and BS show a concentration of CGO in the cavities of the YSZ skeleton, which can be interpreted in two ways. Either CGO was concentrated in the cavities of the YSZ skeleton during the impregnation, or the CGO in the cavities was better protected against the mechanical forces applied during cutting, grinding and polishing the sample in the sample preparation for EDS and BS.

3.2.1.3. Skeletons of CGO with impregnated YSZ

Instead of impregnating a CGO precursor into a YSZ skeleton to form a composite skeleton combining the good properties of both materials, it is also possible to infiltrate an aqueous precursor of YSZ into a CGO skeleton. For the aqueous precursor solution of YSZ a stoichiometric amount of yttrium oxide was dissolved in concentrated nitric acid and the solution diluted with 10 times the original volume of deionised water to, after which a stoichiometric amount of zirconium acetylacetonate was added to form an aqueous precursor solution of 0.5 mol/l. A number of impregnation steps were carried out until the weight of YSZ added was 10 % of the anode. The composite skeleton was fired at 1200 °C for 6 hours. The microstructure of the composite anode was investigated by SEI technique with a FE-SEM electron microscope.

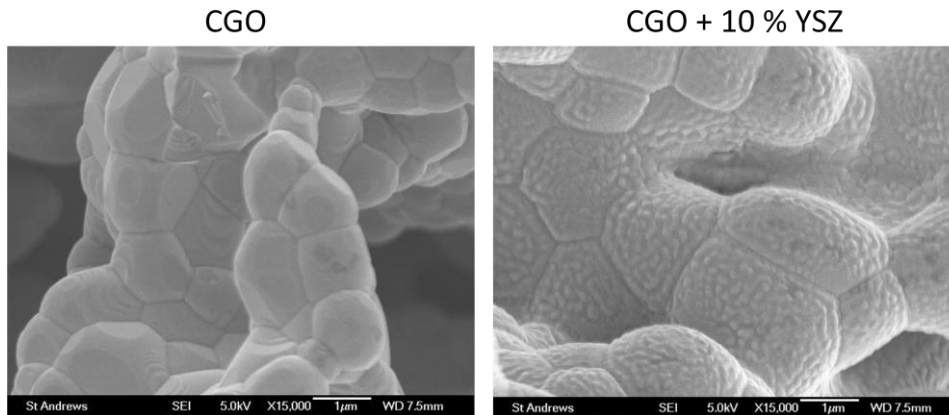


Figure 3.16: SEI images of a CGO skeleton and a CGO skeleton impregnated with 10 wt% YSZ at 15000x magnification.

The microstructure of the composite skeleton achieved by the impregnation of YSZ into CGO, as shown in figure 3.16, seems very different from the microstructure achieved by the impregnation of CGO into YSZ. Compared with the original CGO skeleton the grain boundaries still are visible very clearly in the skeleton impregnated with YSZ and the gaps between the grains seem of similar depth. The surface of the CGO grains, which seemed smooth before the impregnation appears rough and regularly covered with bumps of an average diameter of around 100 nm after the impregnation with 10 % YSZ.

3.2.2. Microstructure of composite SOFC anodes impregnated with titanates

The skeletons of the composite anodes, responsible for the mechanical stability of the anodes and their oxide ion conductivity, were impregnated with a second phase to provide electron conductivity. As mentioned above the microstructure of composite electrodes has a big influence on their triple phase boundary and the electrochemical performance.

LSTM4646 was impregnated into skeletons of YSZ and CGO as described in chapter 2.1.2, and the microstructure of the composite anodes investigated by SEM techniques.

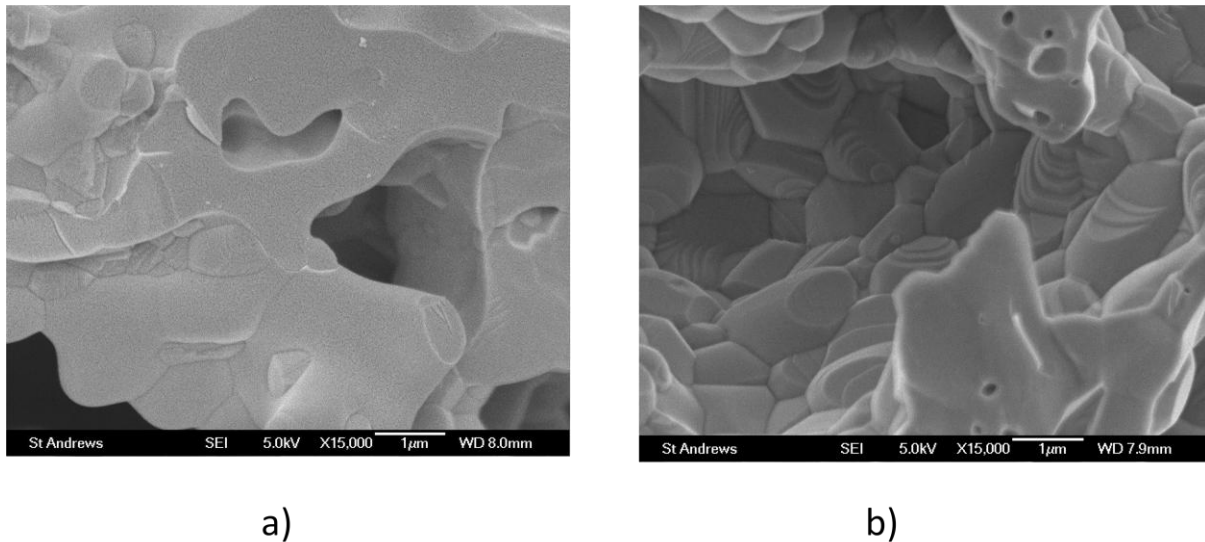
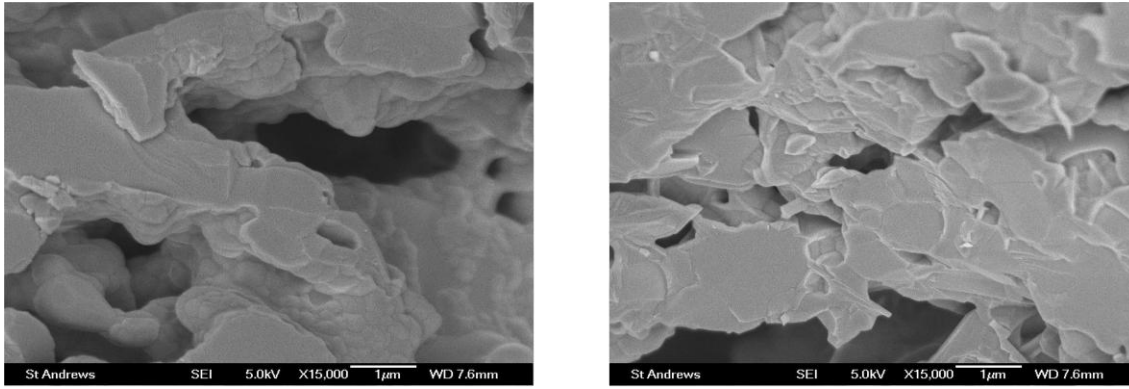


Figure 3.17: SEI images of a YSZ skeleton (a) and a CGO skeleton (b) each impregnated to a total content of 40 wt% LSTM4646 at 15000x magnification.

The SEI pictures show significant differences between the anodes with a YSZ skeleton and the anodes with a CGO skeleton. After the impregnation with LSTM and firing of the cells under air atmosphere the anodes with a YSZ skeleton show a much smoother coating than the anodes with a CGO skeleton (see figure 3.17). In literature [9] this smooth coating is explained by an interaction between manganese and YSZ. An anode with 45 wt% $\text{La}_{0.4}\text{Sr}_{0.6}\text{TiO}_{3.2}$ (LST46) was fabricated by the impregnation method as described in chapter 2.1 and investigated with a SEM using the secondary electron imaging (SEI) technique. Since the impregnated phase is manganese free, such an electrode is suitable to test the manganese dependency of the development of a smooth perovskite coating on a YSZ skeleton after impregnation and firing under oxidising conditions.



a)

b)

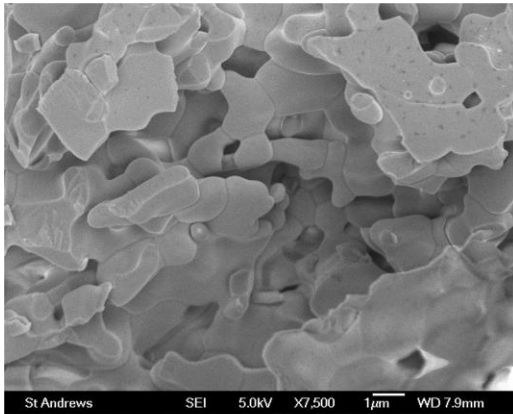
Figure 3.18: SEI images of a YSZ skeleton (a) and a CGO skeleton (b) each impregnated to a total content of 40 wt% LST46 at 15000x magnification.

Although the coating of the LST46 on top of the YSZ skeleton seems to produce a smoother surface than on top of the CGO skeleton, both of the coatings show a surface structure similar to LSTM4646 on top of a CGO skeleton, as shown in figure 3.18. The smooth surface structure shown in figure 3.17 a) is unique to the composite anode fabricated by the impregnation of LSTM4646 on a YSZ skeleton. This observation seems to support the theory that a specific interaction between YSZ and manganese provides this smooth coating, which will not be developed if manganese is absent in the impregnated phase.

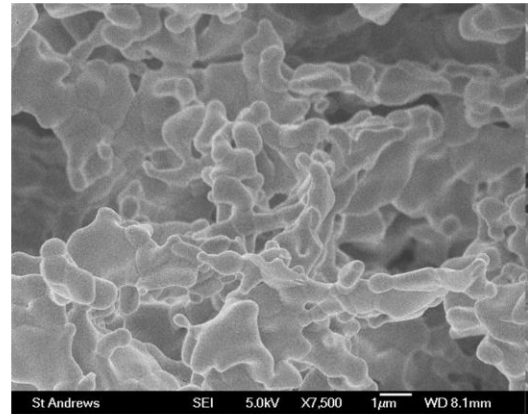
3.2.3. Changes of the microstructure of composite SOFC anodes upon reduction

Since the working conditions at a SOFC anode are highly reductive, the changes of the microstructure of the electrode under hydrogen atmosphere are significant. The changes of the microstructure were studied with the same SEM SEI techniques as the oxidised samples above, after reducing the samples at 900 °C for 6 hours in a dry atmosphere of 5 % hydrogen in argon.

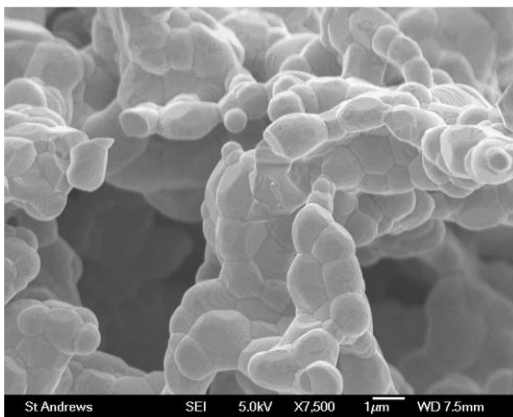
As a starting point the microstructure of the unimpregnated skeletons of CGO and YSZ were compared before and after reduction, as shown in figure 3.19.



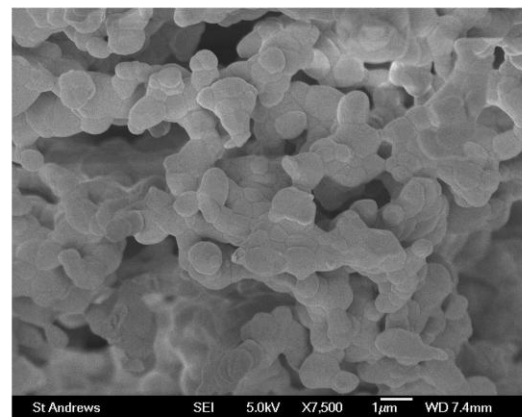
a) YSZ ox.



b) YSZ red.



c) CGO ox.

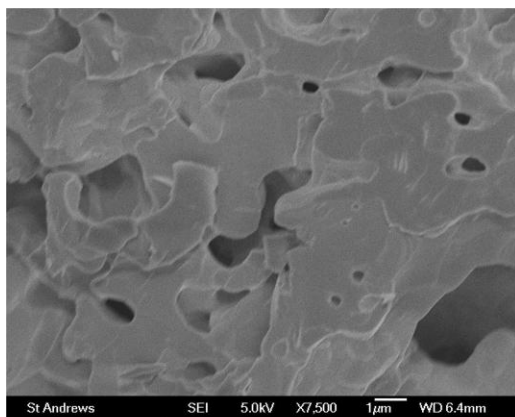


d) CGO red.

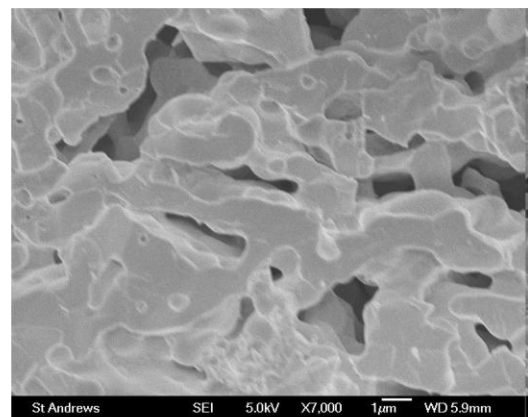
Figure 3.19: SEI images of a YSZ skeleton under oxidising conditions (a) and under reducing conditions (b) and a CGO skeleton under oxidising conditions (c) and under reducing conditions (d) at 7500x magnification.

As expected, the microstructures of the YSZ and CGO skeletons are hardly changing at all upon reduction, proving the stability of the skeleton materials at reducing conditions at 900°C.

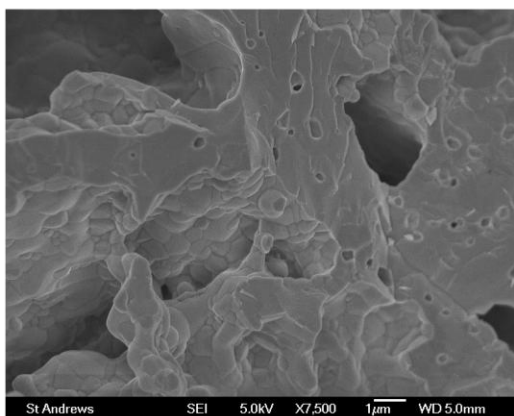
Composite anodes with skeletons of 8YSZ or CGO91 were fabricated by impregnation with LSTM4646 and reduced at 900 °C for 6 hours in a dry atmosphere of 5 % hydrogen in argon. The microstructure of the anode samples was investigated using a SEM SEI technique before and after reduction, as shown in figure 3.20.



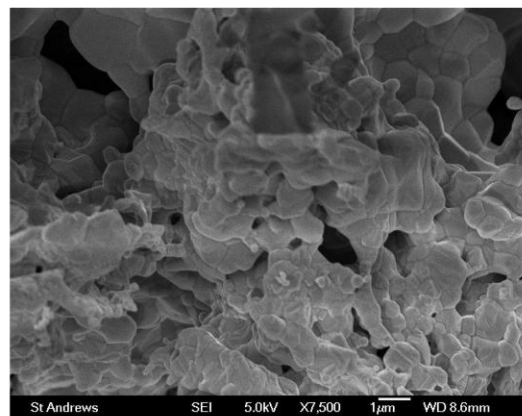
a) YSZ/LSTM ox.



b) YSZ/LSTM red.



c) CGO/LSTM ox.



d) CGO/LSTM red.

Figure 3.20: SEI images of a YSZ/LSTM composite anode under oxidising conditions (a) and under reducing conditions (b) and a CGO/LSTM composite anode under oxidising conditions (c) and under reducing conditions (d) at 7500x magnification.

The microstructure of the composite anodes after reduction at 900°C for 6 hours is very similar to the microstructure before the reduction. Especially the breakup of the smooth coating of LSTM on YSZ into nanoparticles, like described with similar materials in literature [6], could not be observed under the chosen reduction conditions.

To study the differences in the microstructure between composite anodes containing titanates with manganese and without manganese, YSZ skeletons were impregnated with $\text{La}_{0.4}\text{Sr}_{0.6}\text{Ti}_{0.4}\text{Mn}_{0.6}\text{O}_{3-\delta}$ (LSTM4646) and $\text{La}_{0.4}\text{Sr}_{0.6}\text{TiO}_{3.2}$ (LST46). After calcinations in air half of the samples were reduced at 900 °C for 12 hours in a dry atmosphere of 5 % hydrogen in argon. The microstructure of the composite anodes before and after reduction was investigated with a SEM microscope using the SEI imaging technique as shown in figure 3.21.

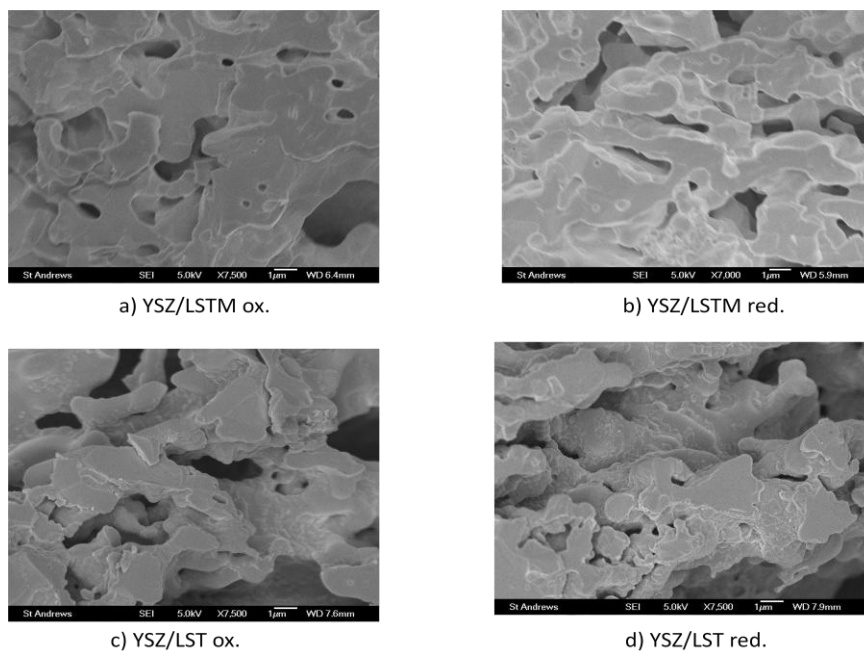


Figure 3.21: SEI images of a YSZ/LSTM composite anode under oxidising conditions (a) and under reducing conditions (b) and a YSZ/LST composite anode under oxidising conditions (c) and under reducing conditions (d) at 7500x magnification.

The difference between the composite anodes impregnated with LST and LSTM is very clear from this picture, YSZ/LST shows no sign of the smooth coating of the YSZ/LSTM composite, neither in the oxidised nor in the reduced form. Like the bare skeletons and the composite anodes impregnated with LSTM, also the composite anodes with LST do not show any obvious difference between their oxidised and their reduced form. Generally none of the observed samples showed significant differences between the oxidised and the reduced form.

3.2.4. Development of the microstructure of composite SOFC anodes

The development of the microstructure of composite anodes with increasing content of the impregnated phase from the pure skeleton to the fully developed composite anode was studied using the SEI technique of a SEM microscope. Several anode samples with 8YSZ and CGO91 skeletons and different amounts of impregnated LSTM4646 were prepared using the impregnation method and subsequent anode calcinations as described in chapter 2.1. The prepared cells had contents of 0 % LSTM (the pure skeleton), 10 wt % LSTM, 20 wt % LSTM, 30 wt % LSTM and 40-45 wt % LSTM (the fully impregnated composite anode).

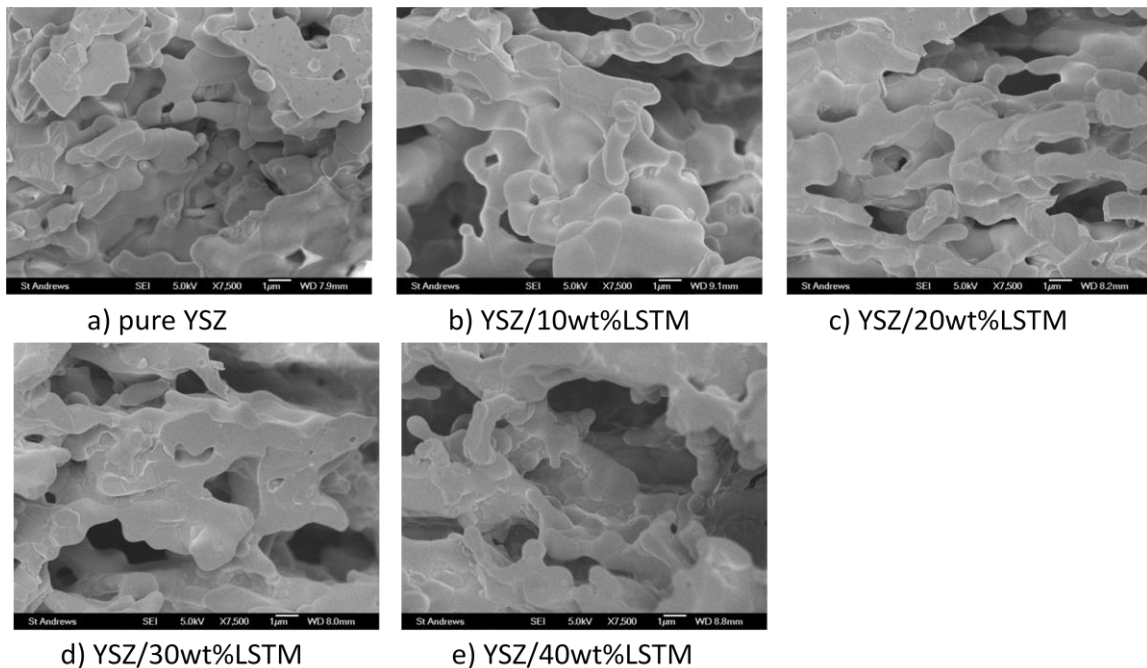


Figure 3.22: SEI images of the microstructural development a YSZ/LSTM composite anode with increasing amounts of impregnated LSTM at 7500x magnification.

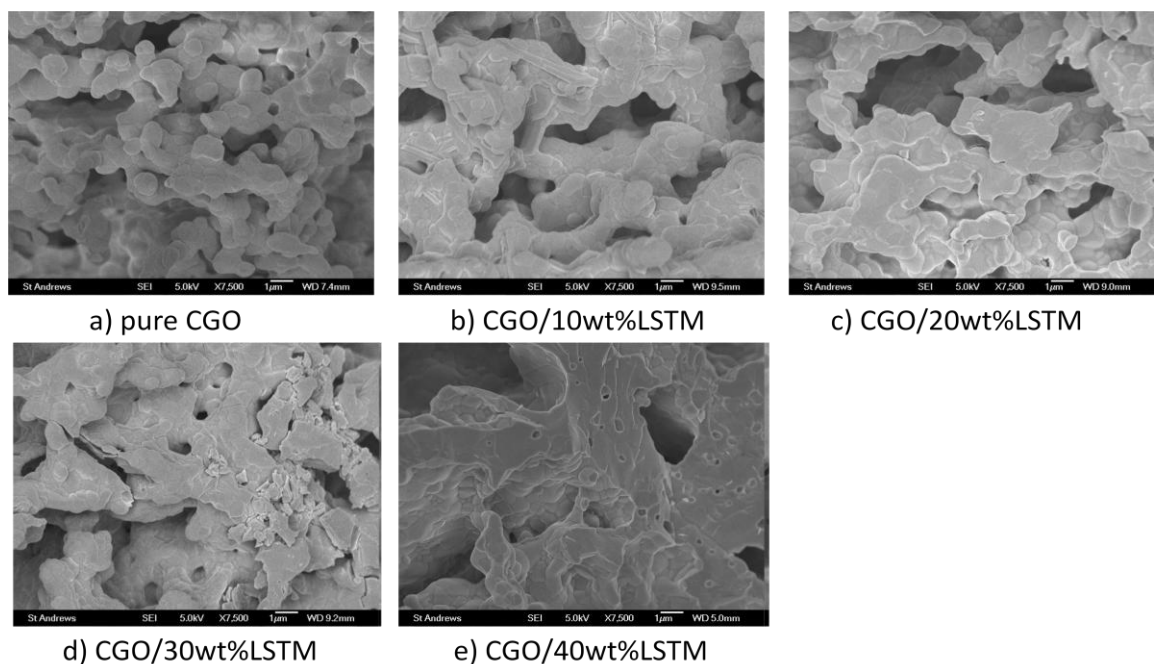


Figure 3.23: SEI images of the microstructure development a YSZ/LSTM composite anode with increasing amounts of impregnated LSTM at 7500x magnification.

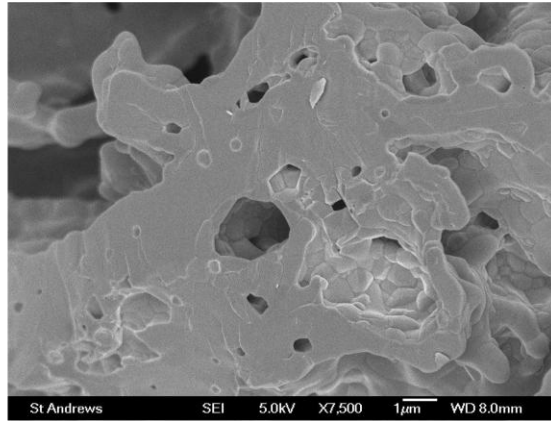
Comparing the microstructure development of composite anodes with YSZ and CGO skeletons, the YSZ based composites do not change their appearance from 10 wt % impregnated LSTM to 40 wt % LSTM. Compared to that, the difference between a CGO based composite with 10 wt % LSTM to a composite anode with 40 wt % LSTM is very obvious. The smaller pores of the skeleton seem increasingly blocked with the amount of impregnated phase increasing, and at the composition of an anode suitable for electrochemical testing, the surface appears as one big chunk of material without any small pores (see figures 3.22 and 3.23).

There were no visible differences between the composite anodes under oxidising and reducing conditions no matter how much of the perovskite phase had been impregnated.

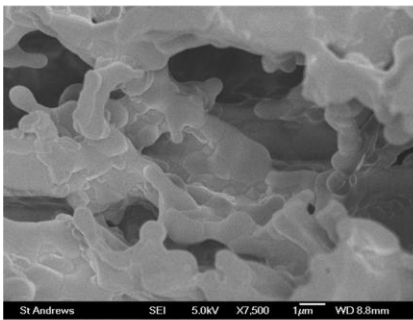
3.2.5. Microstructure of composite anodes with a mixed material skeleton of YSZ and CGO

As already mentioned in chapter 3.2.1.2, a composite skeleton fabricated by impregnation of an 8YSZ skeleton with an aqueous precursor of CGO91 could improve the ionic conductivity of the skeleton while avoiding the delamination problems between a YSZ electrolyte and a CGO electrode described in chapter 3.1.3. According to literature CGO applied to a YSZ skeleton by the impregnation method can form a smooth and dense layer on top of the YSZ [15].

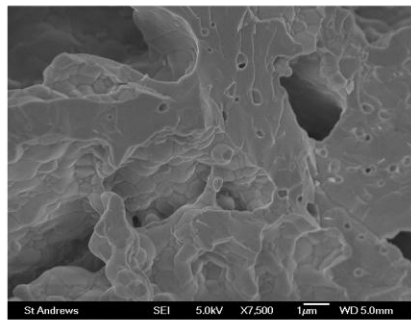
After fabricating a skeleton of 8YSZ with 10 wt % impregnated CGO91 in the way described in chapter 3.2.1.2 this skeleton was impregnated with the perovskite oxide $\text{La}_{0.4}\text{Sr}_{0.6}\text{Ti}_{0.4}\text{Mn}_{0.6}\text{O}_{3-\delta}$ (LSTM4646). The composite anode was sintered under ambient atmosphere at 1200 °C for 3 hours, and half of the samples were reduced at 900 °C for 12 hours in a dry atmosphere of 5 % hydrogen in argon. The microstructure of the calcinated and the reduced samples was investigated with a SEM microscope using the SEI technique.



a) YSZ/10wt%CGO/35wt%LSTM



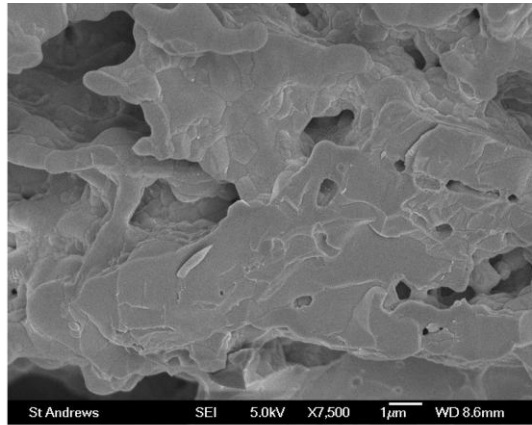
b) YSZ/40wt%LSTM



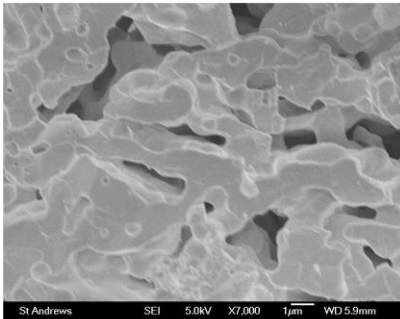
c) CGO/40wt%LSTM

Figure 3.24: SEI image of the microstructure of a composite anode with a skeleton of YSZ and 10% CGO impregnated with 35% LSTM at 7500x magnification (a). Composite anodes of 40 wt % LSTM impregnated into skeletons of pure YSZ (b) and CGO (c)

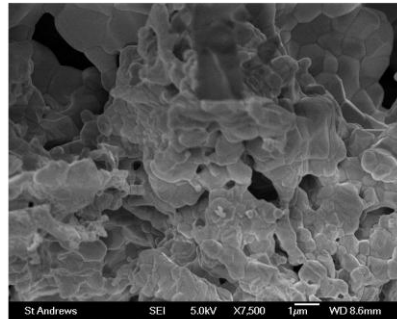
Figure 3.24 shows the microstructure of a composite anode prepared like this after the firing step. For comparison reasons SEI images of cells with similar perovskite loadings but skeletons of pure YSZ (figure 3.24 b) and CGO (figure 3.24 c) were added. The microstructure of the composite anode with a mixed material skeleton, even if it contains only 10 wt % CGO, looks very much like the microstructure of the anode with the CGO skeleton. One reason for that might be that the CGO is impregnated into the YSZ skeleton to form a dense coating layer [15], which means that the LSTM impregnated afterwards is in physical contact rather with the CGO than with the YSZ of the skeleton. Interactions between YSZ and manganese, which lead to the smooth coating typical for YSZ/LSTM composite materials, are thus inhibited in the anode with the mixed material skeleton.



a) YSZ/10wt%CGO/35wt%LSTM



b) YSZ/40wt%LSTM



c) CGO/40wt%LSTM

Figure 3.25: SEI image of the microstructure of a composite anode with a skeleton of YSZ and 10% CGO impregnated with 35% LSTM after reduction at 7500x magnification (a). Composite anodes of 40 wt % LSTM impregnated into skeletons of pure YSZ (b) and CGO (c), after reduction as well.

After reduction the images of the microstructure of the anode fabricated with YSZ and CGO as described above (figure 3.25 a) looked very similar to their appearance before the reduction, following the trend observed with composite anodes with pure YSZ or CGO skeletons in the figures 3.21 and 3.22.

3.2.6. Conclusions

Skeletons of CGO91 show grains of a regular round shape with a diameter of around 1 μm , while 8YSZ skeletons show irregular shaped grains with diameters between 200 nm and 2 μm . SEI images, BSE images and EDS mapping indicate that 10 wt.% CGO impregnated into the pores of a YSZ skeleton form a smooth dense coating layer. After impregnation of 10 wt.% YSZ into the pores of a CGO skeleton, the surface of the CGO grains seems to be covered in bumps of a size of around 100 nm.

After impregnation of 45 wt.% LSTM into the pores of skeletons into the pores of a YSZ skeleton and a CGO skeleton the composite YSZ/LSTM seems to have a much smoother coating than the CGO/LSTM composite, and the overall porosity seems bigger. A mixed skeleton of YSZ and 10 wt.% CGO impregnated with 35 wt.% LSTM4646 shows the same microstructure as the CGO/LSTM composite.

After reduction of the composite anodes in an atmosphere of 95 % argon and 5 % hydrogen at 900 °C for 5 hours the microstructure of the YSZ/LSTM and CGO/LSTM composite anodes doesn't show any distinctive changes compared to the microstructure in the oxidised state.

Once the sharp edges of the irregular shaped grains of the YSZ skeleton are covered with a smooth layer, the appearance of the YSZ/LSTM doesn't change much with increasing amount of impregnated LSTM, the composite anodes with 10 wt.% LSTM impregnated and 40 wt.% LSTM impregnated very much look alike. With increasing amount of LSTM impregnated into a CGO skeleton the smaller pores are increasingly blocked, and the microstructure continuously changes.

3.3. Improvement of the performance of cells with CGO/LSTM composite anodes

3.3.1. LSTM4646 and LSTM4682

Different doping levels at the B site of LST perovskite oxides result in different materials with different properties, in between LST with no manganese at the B-site and LSM, where all the titanium has been substituted by manganese. LST is well known as anode material with excellent stability and reasonably good electrical conductivity under reducing conditions [16]. Partly substituting the titanium with manganese can improve the electrical conductivity even further, and even more important, provide some electrocatalytic activity for the oxidation of hydrogen and other fuels [4]. However, if the level of manganese is too high, the stability of the material under reducing conditions is insufficient, traces of MnO and $(\text{La,Sr})_2\text{MnO}_4$ as secondary phases could be shown in XRDs of LSTM4646 after reduction in literature [4]. The lack of stability under reducing conditions explains why LSM is well known as a cathode material for SOFCs rather than as an anode material.

Electrochemical tests have been performed using button cells with composite anodes of CGO and different compositions of LSTM, hosting 20% manganese on the B-site (LSTM4682) or 60% manganese on the B-site (LSTM4646). The button cells were fabricated by tape casting and the impregnation method as described in detail in chapter 2.1. The skeleton materials were YSZ for cathode and electrolyte and CGO for the anode, with the amount of perovskite impregnated into the CGO skeleton being between 40 wt% and 45 wt%. The cathode was impregnated with LSM82. Firing temperatures were 1400 °C for the skeleton, 1100 °C after the impregnation of the anode and 1000 °C after the impregnation of the cathode. No additional catalyst was added to the electrodes, however, a platinum paste was used for current collection.

At the testing temperatures between 600 °C and 850 °C the OCV values were between 1.1 V and 1.04 V for the LSTM4646 cell and between 1.08 V and 1.02 V for the LSTM4682 cell. The different OCV values can be explained with unintentional differences in the fabrication of the different cells, for instance the quality of the sealing between the cell and the test tube might have lead to different pO_2 levels on the anode side. For both cells the IV curves were close to linear over the whole current density range, as shown in figure 3.26 a).

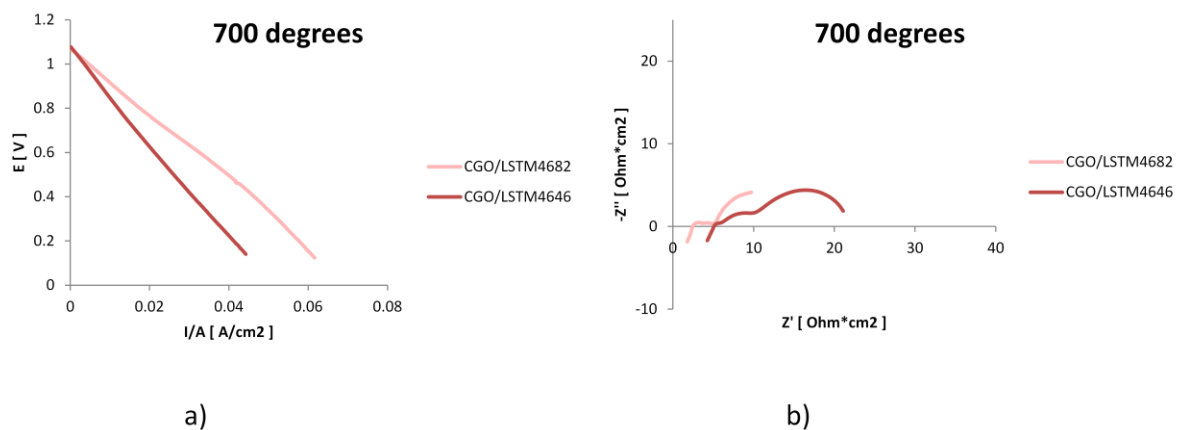


Figure 3.26: IV-curves (a) and Nyquist plots (b) of single cells with composite anodes of CGO/LSTM with different level of manganese in the LSTM at 700 °C.

Figure 3.26 a) already shows the better electrochemical performance of the cell with the LSTM4682 anode compared to the LSTM4646 anode expressed by the lower gradient of the IV curve at the same temperature, which is caused by a lower total cell resistance. The comparison of the Nyquist plots for EIS curves of the two cells at 700 °C is shown in figure 3.26 b).

There are distinctive differences in the shape of the EIS curves between these cells, which are identical apart from the composition of the LSTM impregnated into the skeleton on the anode side. The LSTM4646 cell shows the three distinctive semi arcs at lower temperatures of 600 °C, 650 °C and 700 °C, the high frequency arc disappears at higher temperatures. The characteristic frequencies range from 0.3 Hz

(600 °C) to 2 Hz (800 °C) for the low frequency arc, from 20 Hz (600 °C) to 200 Hz (800 °C) for the medium frequency arc, and from 15 kHz to 25 kHz for the high frequency arc which is only visible in the Nyquist plots of the EIS recorded between 600 °C and 700 °C. The high frequency arc can be associated with charge transfer processes, the medium frequency arc with the diffusion of oxide ions, and the low frequency arc with a mass transport process, as discussed in more detail in chapter 3.1.5.

The most distinctive difference in the appearance of the Nyquist plots of the LSTM4682 cell compared to the LSTM4646 cell is that the low frequency arc seems to be shifted to lower frequencies. Since the lowest frequency recorded is 0.1 Hz, this means that the lower temperature curves only show the onset of the low frequency arc, making it difficult to extrapolate the curves to estimate both their characteristic frequency and their intersection with the real axis marking the total resistance of the cells. The characteristic frequencies for the low frequency arcs range from somewhere below 0.1 Hz at 600 °C to 0.2 Hz at 800 °C, the calculated capacitance of the related Randles circuit is with around 0.1 F/cm² around 5 times as big as in the LSTM4646 cell. The characteristic frequencies of the medium frequency arcs range from 40 Hz to 2500 Hz at different temperatures and the high frequency arcs from 15 kHz to 30 kHz. Compared to the LSTM4646 cell this means a shift to higher frequencies for the medium frequency arc, and a reduction of the Randles circuit capacitance from around 0.1 mF/cm² to around 0.05 mF/cm², while the high frequency arcs stay in the same frequency and capacitance range for both cells.

The “fit circle” function of the EIS software ZView provides an extrapolation for an incomplete semi arc, however, if only a small onset of the arc is visible in the Nyquist plot, this extrapolation might be extremely inaccurate, as shown in figure 3.29.

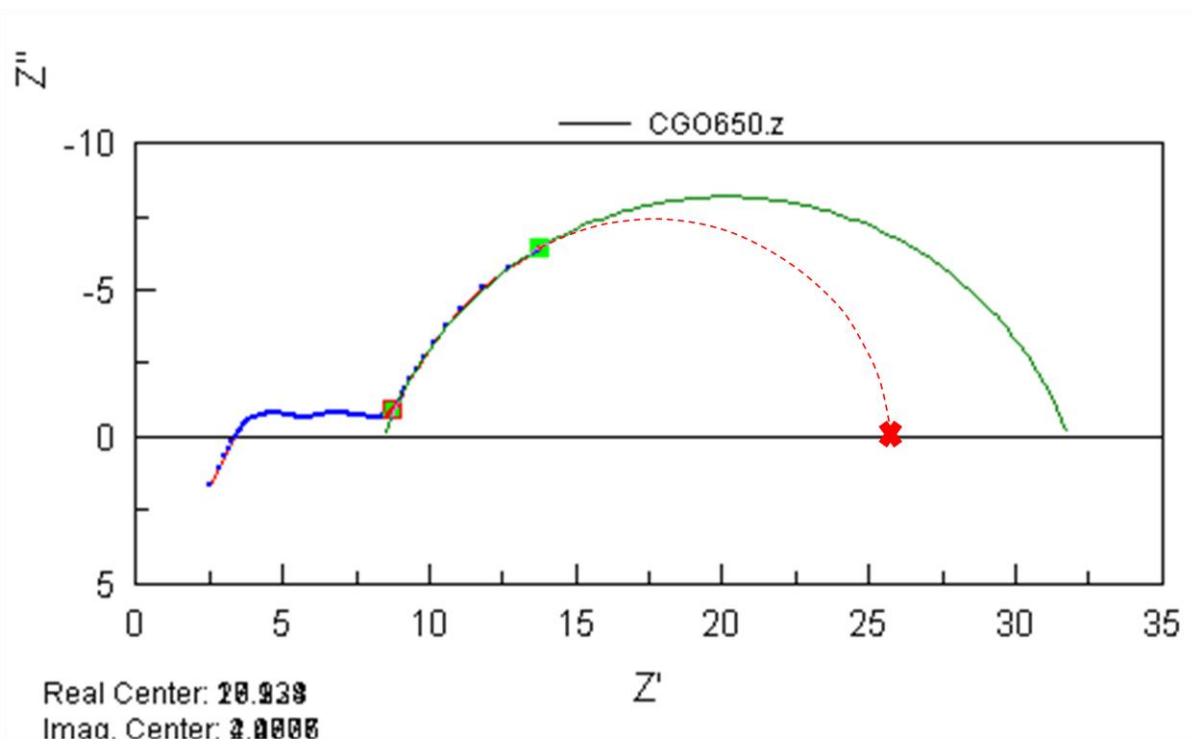


Figure 3.27: Nyquist plot with an incomplete low frequency arc, extrapolated by the “fit circle” function of ZView (green line) and this extrapolation corrected with the total resistance obtained from the gradient of the IV curve (red cross)

The extrapolation of the Nyquist plot of the EIS curve recorded at 650 °C from the LSTM4682 cell results in a total resistance of around 32.5 $\Omega \cdot \text{cm}^2$, if carried out by the “fit circle” function of the program ZView. However, the gradient of the relevant section of the IV curve shows a total resistance of 26 $\Omega \cdot \text{cm}^2$, which rather suggests a different extrapolation curve shown as the red dotted line in figure 3.27. The value for the total resistance calculated from the gradient of the IV curve seems to have a higher level of credibility than the extrapolation, based on the height of the semi-circle being around 7.5 $\Omega \cdot \text{cm}^2$, which suggests around 15 $\Omega \cdot \text{cm}^2$ for the diameter, a value achieved in a rough approximation by the red dotted curve in figure 3.27.

The way the non ohmic polarisation was roughly divided into different frequency areas is shown in figure 3.28.

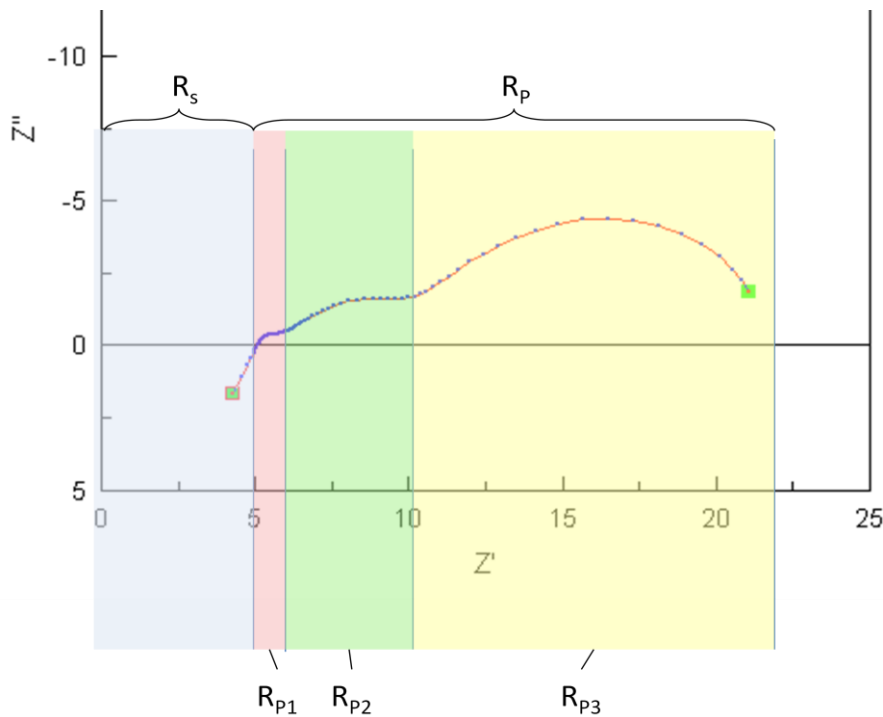


Figure 3.28: Differentiation of the different parts of the polarisation and resistance of the Nyquist plot of the EIS of the LSTM4646 cell at 700 °C.

Figure 3.29 shows the differences in polarisations between a cell with a composite CGO/LSTM4646 anode and a cell with a composite CGO/LSTM4682 anode.

	CGO/LSTM4646			CGO/LSTM4682		
T in °C	Rs	Rp	R total	Rs	Rp	R total
600	9.9	37.3	47.2	4.5	35.2	39.7
650	7.9	27.7	35.6	3.4	23.1	26.5
700	5.1	16.8	21.9	2.4	13.2	15.6
750				1.8	8.4	10.2
800	2.9	7.3	10.2	1.4	5.5	6.9
850	2.2	4.7	6.9	1	4.2	5.2

Figure 3.29: Table displaying ohmic parts and non ohmic polarisations of the impedance of single cells with CGO/LSTM4646 and CGO/LSTM4682 composite anodes

The ohmic parts of the polarisation are around double in the LSTM4646 cell compared to the LSTM4682 cell over the whole range of temperatures. This difference can't be explained by the different chemical behaviour of LSTM4646 and LSTM4682, but rather by a different microstructure of the composite anodes, leading to different levels of percolation. The non ohmic parts are similar for the two cells at low temperatures, at higher temperatures the LSTM4646 cell shows a non ohmic polarisation 20 % higher than those of the LSTM4682 cell. If the non ohmic polarisation is divided further into a low frequency part, a medium frequency part and a high frequency part, it turns out that the differences between the non ohmic polarisations of the two cells can be accounted to the medium frequency arcs of the Nyquist plots. Especially at high temperatures R_{P2} of the LSTM4646 cell is 2-3 times higher than in the LSTM4682 cell, while the low frequency part is similar and the high frequency part is so small that it hardly contributes to the total resistance.

3.3.2. Catalytic effects

Substances with a catalytic effect for the oxidation of the fuel inside the anode can have a positive effect on the performance of the fuel cell. Especially the effect of catalysts based on palladium and cerium oxide inside composite anodes with YSZ and LSTM has been studied in literature [17]. Apart from catalysts specifically added to enhance the performance of the cell also some metals used for current collection can have a catalytic effect on the oxidation of fuels, for example, cells with platinum paste used as a current collector show better performance than otherwise identical cells with a silver paste current collector [10].

To study the catalytic effects on the performance of button cells with composite anodes of CGO and LSTM, three different cells were prepared using the methods of tape casting and impregnation as described in chapter 2.1. The firing temperature after the preparation of the CGO/YSZ skeleton was 1400 °C, the amount of

impregnated LSTM4646 between 40 wt.% and 45 wt.%, and the calcination temperature 1100 °C to 1200 °C after the impregnation of the anode and 1000 °C after the impregnation of the cathode for all three cells. A platinum current collection grid was painted onto anode and cathode of cell1 and this cell additionally contained 1-2 % palladium oxide formed in situ inside the pores of the anode after impregnation of an aqueous solution of palladium nitrate, as described in chapter 2.1.2. Cell2 was fitted with the same platinum current collection grid, but without infiltrated palladium oxide, and cell3 had simply a current collection grid of silver painted on both electrodes, without palladium inside the anode.

The three different cells were electrochemically tested using a test jig, a Solartron cell test system and a frequency response analyser as described in chapter 2.3.2.3 and shown in figure 2.25. IV curves and EIS spectra were recorded in a temperature range from 600 °C to 850 °C in increments of 50 °C.

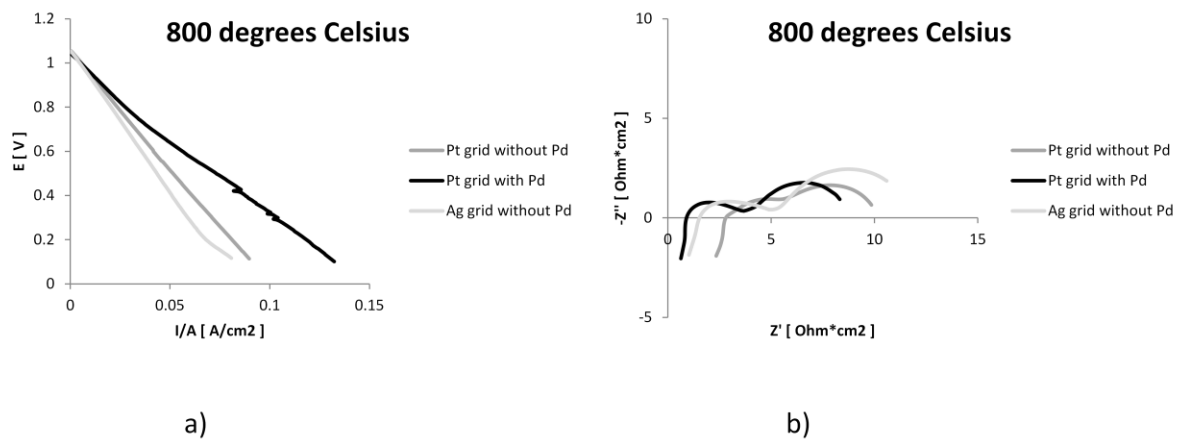


Figure 3.30: IV-curves (a) and Nyquist plots (b) of single cells with composite anodes of CGO/LSTM4646 with no catalysts at all, Pt current collection grid but no additional catalyst and Pt current collection grid with additional 1-2 wt.% PdO added as catalyst, recorded at 800 °C

Figure 3.30 a) shows almost linear shapes of the IV curves for all three cells over the whole range, even if the IV curve of the cell with the silver grid shows a lower gradient at high power densities, which means a decrease of the cell resistance under higher current density. This is presumably because of slow electrochemical kinetics which can be overcome by a higher driving force due to a higher overpotential at a higher load. From the gradients of the curves of the different cells it is obvious that the total cell resistance of the cell with the silver grid without any additional palladium shows the highest total resistance, which was expected because of the lack of any catalytic effect for the oxidation of hydrogen. The cell with the platinum current collection grid shows lower total cell resistance, confirming earlier observations in literature [10] about the catalytic effect of this kind of current collection grids. Not surprisingly, the best electrochemical behaviour with the lowest total cell resistance of the three tested cells is shown by the cell with additional palladium, which is well known for being a good catalyst for the oxidation of hydrogen.

The Nyquist plots in figure 3.30 b) show that the superiority of the cell with the additional palladium catalyst at the high temperature of 800 °C is only due to the reduced ohmic resistance, however, at lower temperatures R_S and R_P are both decreased by the impregnation of palladium, as can be seen in the table in figure 3.31. The effect of the catalysts platinum (from the painted current collection grid) and palladium (added to the composite anode) on the polarisation of the cells is shown in the Nyquist plots in figure 3.30 b) and in the table summarising the different kinds of cell resistances in figure 3.31.

T in °C	Ag grid no Pd cat			Pt grid no Pd cat			Pt grid Pd cat		
	R _s [Ω*cm ²]	R _p [Ω*cm ²]	R total	R _s [Ω*cm ²]	R _p [Ω*cm ²]	R total	R _s [Ω*cm ²]	R _p [Ω*cm ²]	R total
600	4.7	100.3	105	9.9	37.3	47.2	3.7	33.9	37.6
650	3.4	59.2	62.6	7.9	27.7	35.6	2.6	19.8	22.4
700				5.1	16.8	21.9	1.7	12.9	14.6
750	1.8	18.6	20.4				1.2	9.6	10.8
800	1.6	10.3	11.9	2.9	7.3	10.2	0.9	7.9	8.8
850	1.3	6.6	7.9	2.2	4.7	6.9	0.7	7.1	7.8

Figure 3.31: Table displaying ohmic parts and non ohmic polarisations of the impedance of single cells with different catalysts and current collection grids

Comparing the two cells with the platinum current collection grid, the cell with additional palladium unsurprisingly shows the better electrochemical performance with a lower total cell resistance at low temperatures. The ohmic parts (R_S) of the resistance are around 60-70 % lower over the whole temperature range, while the non ohmic parts (R_P) are around 25-30 % lower at 650 °C and 700 °C, but there is no reduction of R_P at higher temperatures, and R_P of the palladium infiltrated cell is even 50 % higher compared with the palladium free cell at 850 °C. Obviously the palladium catalyst has a positive effect on R_S over the whole temperature range, while a positive effect on R_P only takes place at relatively low temperatures.

Investigating the values of the polarisation of the palladium catalyst cell in more detail, it turns out that both the medium frequency part of the polarisation (R_{P2}) and the low frequency part of the polarisation (R_{P3}) are reduced by around 10-40 % compared to the cell without palladium at 600 °C and 650 °C while both are increased at higher temperatures like 800 °C and 850 °C, R_{P3} only by 7 %, but R_{P2} by 34 %.

Comparing the two cells without palladium but with different current collection grids, the cell with the platinum grid shows a lower total resistance than the cell with the silver grid over the whole temperature range, which was to be expected, because of the catalytic effect platinum has on the oxidation of hydrogen. It comes as a surprise that the ohmic parts of the resistance R_S are much lower for the cell with the silver grid than for the cell with the platinum grid. The R_S values are reduced by 40-55 % at all temperatures, as demonstrated in figure 3.31. Although silver has a slightly better electronic conductivity than platinum, both metals should be conducting so well that they shouldn't contribute to the total cell resistance at all. Considering the melting points of metallic silver (962 °C) and platinum (1768 °C) it seems logical that at electrochemical testing at temperatures up to 850 °C silver shows significant mobility inside the porous ceramic framework of both electrodes, intruding deeper into the pore structure than platinum.

The non ohmic polarisation R_P of the cell with the silver grid is around 170 % higher than R_P of the cell with the platinum grid at 600 °C and around 40 % higher at 850 °C. The increased polarisation R_P of the silver grid cell can be explained by the lack of catalytic activity compared to cells containing platinum or palladium. Another explanation could be that the enhanced distribution of silver within the pores of the ceramic electrodes, mentioned above to explain the better conductivity, covers and masks some of the active area of the triple phase boundary. This would increase both R_{P2} and also R_{P3} , because the reduced number of active sites might increase the length of pathways for gaseous reactants and products in anode and cathode.

The polarisation can be split into a medium frequency part of around 40 Hz to around 2500 Hz (R_{P2}) and a low frequency part of below 0.1 Hz to around 2 Hz (R_{P3}), like shown in figure 3.30. At the low temperature of 600 °C the cell with the silver grid has a higher polarisation mainly because R_{P3} is higher, in fact around 265 % higher than R_{P3} of the cell with the platinum grid. At the high temperature of 850 °C R_{P3} of the cell with the silver grid is only 15 % higher compared to the cell with the platinum grid, the main factor for the high polarisation of the silver grid cell now is R_{P2} , which is 110 % higher in the cell with the silver grid than it is in the cell with the platinum

grid. The activation energy of the processes causing R_{P3} is around 1.01 eV for the silver grid cell compared to 0.76 eV for the platinum grid cell, and the activation energy of the processes causing R_{P2} is around 0.60 eV for the silver grid cell compared to 0.96 eV for the platinum grid cell. The big difference in the thermal activation of R_{P2} and R_{P3} between the silver grid cell and the platinum grid cell strongly suggests that both R_{P2} and R_{P3} are caused by different processes or mechanisms in the different cells.

Maximal power densities of 21.8 mW/cm² for the Ag-grid cell and 36.9 mW/cm² for the cell with the Pd catalyst at 800 °C are comparable to former research conducted at the University of St. Andrews at similar button cells with LSTM4682/YSZ anodes with additional CeO₂ and Pd impregnated for additional catalytic activity. 30 mW/cm² maximal power density was achieved for a cell with similar thickness and materials apart for the anode skeleton was made of YSZ without additional catalyst, increasing to 100 mW/cm² with 10 wt.% CeO₂ and to 150 mW/cm² with 10 wt.% CeO₂ and 1 wt.% Pd [8] and even up to 197 mW/cm² with 20 wt.% CeO₂ and 1 wt.% Pd [18].

3.3.3. Effects of the cathode porosity

Higher porosity of the electrodes generally can improve the diffusion of gaseous products to and from electrochemically active sites, thus enhancing the cell performance, but also lead to a lower conductivity and mechanical stability, deteriorating the cell performance. To study the effect of different porosities of the cathode side on the electrochemical performance of the cell, two different cells were fabricated by the methods of tape casting and impregnation method as described in chapter 2.1. Preparing the tapes for the skeleton of the cathode, as described in chapter 2.1.1.1, the slurry for one tape contained 30 wt% carbon as a pore former, while the other tape contained 50 wt% carbon. The cells fabricated using these two tapes subsequently are referred to as 30 % carbon cell and 50 % carbon cell.

The skeleton of both cells was fabricated of YSZ for the cathode and electrolyte and CGO for the anode of the cell, with LSTM4646 impregnated into the anode and LSM82 into the cathode of the cell. No additional catalysts were used apart from the platinum current collection grid in both cells. The firing temperature after the preparation of the skeleton was 1400 °C, the amount of impregnated LSTM4646 between 40 wt.% and 45 wt.%, and the calcination temperature around 1100 °C after the impregnation of the anode. The amount of impregnated LSM82 was around 50 wt% for the cell with the higher porosity and around 40 wt% for the cell with the lower porosity, because the same amount of precursor was impregnated into the skeletons. The firing temperature after the cathode impregnation was 1000 °C for both cells.

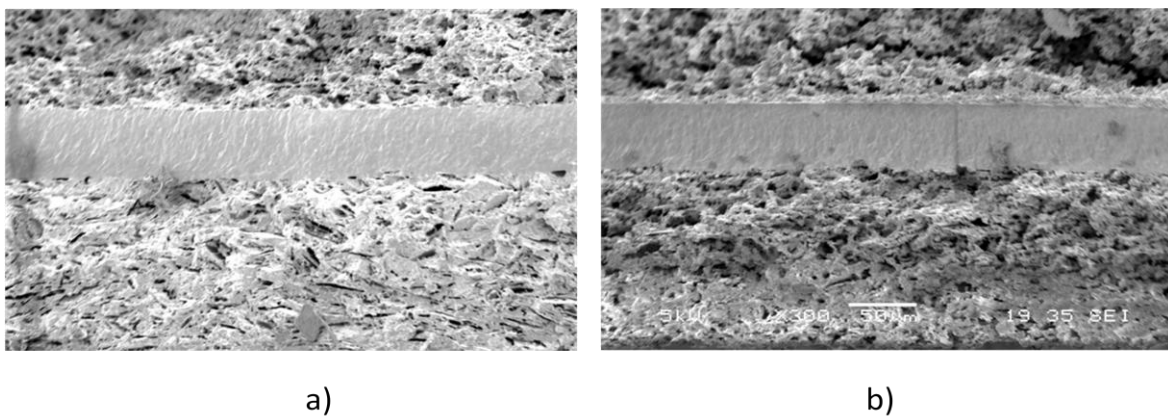


Figure 3.32: SEI images of the microstructure of different cells under 300x magnification. The bottom part is the cathode of YSZ and LSM82. The cathode skeleton slurry contained a) 30 wt% carbon pore former and b) 50 wt% carbon pore former.

The SEI pictures in figure 3.32 show a more porous cathode in the 50 % carbon cell in 3.32 b) compared to the 30 % carbon cell in 3.32 a), even after impregnation, as expected.

The cells were electrochemically tested using a test jig, a Solartron cell test system and a frequency response analyser as described in chapter 2.3.2.3 and shown in figure 2.25. IV curves and EIS spectra were recorded in a temperature range from 600 °C to 850 °C in increments of 50 °C.

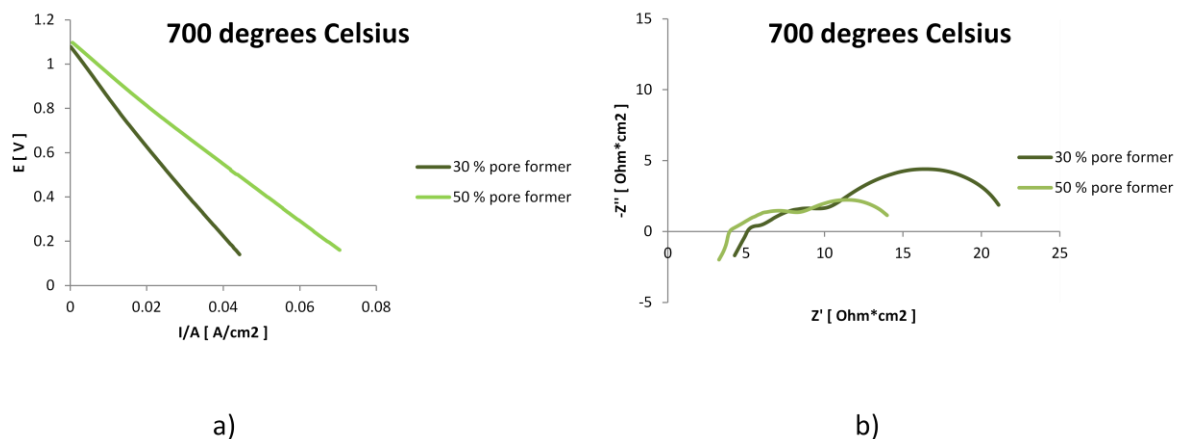


Figure 3.33: IV-curves (a) and Nyquist plots (b) of single cells with composite anodes of CGO/LSTM4646 and composite cathodes of YSZ/LSM82, recorded at 700 °C. The cathodes have different porosities because of the different amounts of pore formers in the slurries used for the cathode skeleton tapes.

Figure 3.33 a) shows almost linear shapes of the IV curves for both cells over the whole current density range, the open circuit voltages are between 1.03 (at 850 °C) and 1.08 V (at 600 °C) and slightly lower than the theoretical values calculated from the Nernst equation. From the gradients of the curves of the different cells it is obvious that the total cell resistance of the cell with the higher porosity shows less total resistance and the better electrochemical performance.

The Nyquist plots in figure 3.33 b) show that the 30 % carbon cell shows a higher total cell resistance due to higher ohmic resistance as well as higher non ohmic polarisation parts. Especially in the low temperature plots the low frequency part of the polarisation seems to be bigger at the 30 % carbon cell, which can be explained by mass transfer effects responsible for the low frequency arcs in the Nyquist plots.

In the cell with the lower porosity the gaseous reactants and products are partly blocked making their way to and from the electrochemically active sites resulting in a higher mass transport part of the resistance. Also the number of triple phase boundary sites is highly reduced because the perovskite can't be impregnated as deep into the skeleton. The different parts of the cell resistances are summarised in more detail in a table in figure 3.34.

	30 % pore former			50 % pore former		
T in °C	Rs	Rp	R total	Rs	Rp	R total
600	9.9	37.3	47.2	6.5	20.6	27.1
650	7.9	27.7	35.6	5.3	14.8	20.1
700	5.1	16.8	21.9	3.9	10.8	14.7
750				3.1	8.3	11.4
800	2.9	7.3	10.2	2.5	5.7	8.2
850	2.2	4.7	6.9	2	4.3	6.3

Figure 3.34: Table displaying ohmic parts and non ohmic polarisations of the impedance of single cells with different cathode porosity.

Analysis of the data displayed in figure 3.34 shows that the high porosity cell has an ohmic resistance reduced from around 10 % at high temperatures to around 35 % at low temperatures compared to the low porosity cell, and the non ohmic polarisation is reduced from around 10 % at high temperatures to around 45 % at low temperatures, due to a reduced low frequency part of the polarisation R_{P3} . While the reduced non ohmic polarisation can be explained by enhanced mass transport, the reduced ohmic resistance is a surprise, because the cell with higher porosity should theoretically show lower conductivity because of less material capable of conducting electrons present in the electrode. Obviously the enhanced porosity leads to an increase in electrochemically active triple phase boundary sites, which leads to a reduction of the length the average charge carrier has to travel through the material. A decreased pathway length for oxide ions travelling from the triple phase boundary of the cathode to the electrolyte and for electrons travelling from the current

collection grid to the next available triple phase boundary site clearly can reduce the ohmic resistance of the cell. The low frequency part of the polarisation is around 56 % lower in the high porosity cell than in the low porosity cell at 600 °C but only around 6 % lower at 850 °C.

3.3.4. Conclusions

Electrochemical tests were performed for button cells with composite anodes of CGO/LSTM4646 and CGO/LSTM4682. The CGO/LSTM4682 cell shows better performance with a maximal power density of around 20 mW/cm² at 700 °C. The values for the ohmic resistance R_S of the CGO/LSTM4682 cell are around half of the values for R_S of the CGO/LSTM4646 cell over the whole temperature range tested. Also the R_P values are comparatively smaller, particularly at high temperatures, because of smaller medium frequency arcs. R_{P2} with characteristic capacitances of 0.2 to 2 mF/cm² can be related to charge transfer processes to and from adsorbed species [11] or to the diffusion of oxide ions [13]. The characteristic frequencies for the low frequency part of the polarisation R_{P3} of the CGO/LSTM4682 cell are shifted to lower frequencies compared to the CGO/LSTM4646 cell.

Adding 1-2 wt.% of palladium oxide into the anode of the cell by impregnation improves the electrochemical performance by decreasing both the ohmic resistance R_S and the non ohmic polarisation R_P of the cell. While R_S is reduced over the whole temperature range, R_P is only reduced at lower temperatures, and shows similar values in the cells with palladium and without palladium at the higher temperature of 800 °C. Comparing cells with current collection grids painted with silver paint and platinum paint, R_P of the silver paint cell is much higher, especially at low temperatures, suggesting a catalytic effect of the platinum current collection grid paste. R_S of the silver grid cell is lower than R_S of the platinum grid cell, probably due to a better distribution of the silver paste inside the pores of the anode and cathode of the tested cell.

Increasing the porosity of the cathode of the tested button cell by increasing the amount of carbon pore former used in the green tape for the cathode from 30 wt.% to 50 wt.% has a positive influence on the electrochemical performance of the button cell. Unsurprisingly the low frequency part of the polarisation R_{P3} , related to mass transport phenomena, was reduced in the more porous cell, especially at low temperatures. Also R_S of the cells with higher porosity was reduced, probably because of an enhanced triple phase boundary in the porous cell reducing the average length of pathways for electrons and oxide ions from the current collection grid or to the electrolyte.

- [1] M. Ghatee and J. T. S. Irvine, "Investigation of electrical and mechanical properties of tetragonal/cubic zirconia composite electrolytes prepared through stabilizer coating method," *International Journal of Hydrogen Energy*, **35**, 9427–9433, 2010.
- [2] R. S. A. Paterson, "Phase analysis of sintered yttria–zirconia ceramics by X-ray diffraction," *Journal of Materials Research*, **1**, 295 – 299, 1986.
- [3] K. C. Anjaneya, G. P. Nayaka, J. Manjanna, G. Govindaraj, and K. N. Ganesha, "Preparation and characterization of $\text{Ce}_{1-x}\text{Gd}_x\text{O}_{2-\delta}$ ($x = 0.1\text{--}0.3$) as solid electrolyte for intermediate temperature SOFC," *Journal of Alloys and Compounds*, **578**, 53–59, 2013.
- [4] F. T. Q. X. Fu, "La_{0.4}Sr_{0.6}Ti_{1-x}Mn_xO_{3-d} Perovskites as New Anode Materials for Solid Oxide Fuel Cells." *J. Electrochem. Soc.*, **153**, D74-D83, 2006.
- [5] A. Smith, "Structural and Defect Chemistry of Strontium Titanate," *University College London*, 2011.
- [6] M. K. Rath, B.-G. Ahn, B.-H. Choi, M.-J. Ji, and K.-T. Lee, "Effects of manganese substitution at the B-site of lanthanum-rich strontium titanate anodes on fuel cell performance and catalytic activity," *Ceramics International*, **39**(6), 6343–6353, 2013.
- [7] Q. X. Fu, F. Tietz, and D. Stöver, "La_{0.4}Sr_{0.6}Ti_{1-x}Mn_xO_{3-δ} Perovskites as Anode Materials for Solid Oxide Fuel Cells," *J. Electrochem. Soc.*, **153**(4), D74–D83, 2006.
- [8] J. H. Kim, D. Miller, H. Schlegl, D. McGrouther, and J. T. S. Irvine, "Investigation of Microstructural and Electrochemical Properties of Impregnated (La,Sr)(Ti,Mn)O_{3±δ} as a Potential Anode Material in High-Temperature Solid Oxide Fuel Cells," *Chem. Mater.*, **23**(17), 3841–3847, 2011.
- [9] G. Corre, G. Kim, M. Cassidy, J. M. Vohs, R. J. Gorte, and J. T. S. Irvine, "Activation and Ripening of Impregnated Manganese Containing Perovskite SOFC Electrodes under Redox Cycling," *Chem. Mater.*, **21**, 1077–1084, 2009.
- [10] G. P. G. Corre, "Studies of Alternative Anodes and Ethanol Fuel for SOFCs," *Ph.D. thesis, University of St. Andrews*, 2009.
- [11] B. Boukamp, "Electrochemical Impedance Spectroscopy Part1," *presented at the Supergen Electrochemical Impedance Workshop, St. Andrews*, 2010.
- [12] J. T. S. Irvine, D. C. Sinclair, and A. R. West, "Electroceramics: Characterization by Impedance Spectroscopy," *Advanced Materials*, **2**, 132–138, 1990.
- [13] A. Leonide, V. Sonn, A. Weber, and E. Ivers-Tiffée, "Evaluation and Modeling of the Cell Resistance in Anode-Supported Solid Oxide Fuel Cells," *J. Electrochem. Soc.*, **155**, B36–B41, 2008.
- [14] U. G. Bossel and L. Dubal, "Facts & Figures: Final Report on SOFC Data". *Swiss Federal Office of Energy, Operating Agent Task II*, 1992.
- [15] R. Küngas, F. Bidrawn, J. Vohs, and R. Gorte, "Doped-Ceria Diffusion Barriers Prepared by Infiltration for Solid Oxide Fuel Cells," *Departmental Papers (CBE) University of Pennsylvania*, 2010.
- [16] O. A. Marina, N. L. Canfield, and J. W. Stevenson, "Thermal, electrical, and electrocatalytic properties of lanthanum-doped strontium titanate," *Solid State Ionics*, **149**, 21–28, 2002.
- [17] J. H. Kim, H. Schlegl, and J. T. S. Irvine, "The catalytic effect of impregnated (La, Sr)(Ti, Mn)O_{3±δ} with CeO₂ and Pd as potential anode materials in high temperature solid oxide fuel cells," *International Journal of Hydrogen Energy*, **37**, 14511–14517, 2012.

4. Composite SOFC anodes with YSZ and A-site deficient titanates

The theoretical formula for the ideal perovskite is ABO_3 , building a cubic unit cell as mentioned and described in more detail in chapter 1.7.4. One of the reasons why the perovskite oxide group is so interesting for material chemists, is the tolerance of perovskites to doping, vacancies and distortions and the variety of physical and chemical properties resulting from this. In A-site deficient perovskites the A-site cation lattice positions are not fully occupied by A-site cations, a certain part of this positions are vacant. The sum of positive charges within the crystal is reduced by cations missing, and overall charge neutrality demands a decrease of the oxygen anions, sometimes leading to a perovskite crystal structure which is both oxygen deficient and A-site deficient. The material $La_{0.4}Sr_{0.4}TiO_3$ (LST44) exhibits a perovskite structure with lanthanum and strontium occupying 80 % of the A sites and titanium all the B sites. The material is not oxygen deficient under oxidising conditions because the reduction of positive charges due to missing cations at the A site is compensated by doping of the A site with lanthanum cations of higher valence compared to strontium in strontium titanate.

Under the reducing working conditions of a SOFC anode a part of the titanium ions at the B-site of LST44 are reduced from the oxidation state +4 to +3, releasing electrons and, because the reduced positive charge has to be matched by reduction of oxide anions, oxygen deficiency. The free electrons make A-site deficient lanthanum strontium titanate (LST) an n-type electronic semiconductor under reducing conditions, the oxygen deficiency an oxide ion conductor, so the material is a mixed ionic and electronic conductor (MIEC). [1]

The anodes studied in this chapter are composite anodes comprised of an YSZ skeleton for mechanical stability, compatibility with the YSZ electrolyte and ionic conductivity, and an impregnated phase of A-site deficient LST for electronic conductivity and catalytic activity for the oxidation of hydrogen fuel.

4.1. Composite anodes with LST44

Button cells were fabricated by tape casting and impregnation method as described in chapter 2.1. The firing temperature after the preparation of the YSZ skeleton was 1400 °C and impregnation with an aqueous precursor of was carried out to an extent resulting in between 40 wt.% and 45 wt.% of $\text{La}_{0.4}\text{Sr}_{0.4}\text{TiO}_3$ (LST44) . For additional studies of the microstructure and composition a different set of button cells was fabricated with anodes impregnated only with 10-15 wt.% LST44, due the lack of percolation these cells were not used for electrochemical testing. The calcination temperatures were around 1150 °C after the impregnation of the anode and 850 °C after the impregnation of the cathode with an aqueous precursor for $\text{La}_{0.8}\text{Sr}_{0.2}\text{FeO}_{2.9}$ (LSF82). The anodes were impregnated with a precursor for palladium oxide as an additional catalyst for the oxidation to the extent of 1-2 wt.%, as described in chapter 2.1.2.

4.1.1. Microstructure of composite anodes with A-site deficient perovskites

The microstructure of the composite anodes fabricated in the way described above was studied using the SEI technique of a SEM microscope as described in chapter 2.2.2.1.

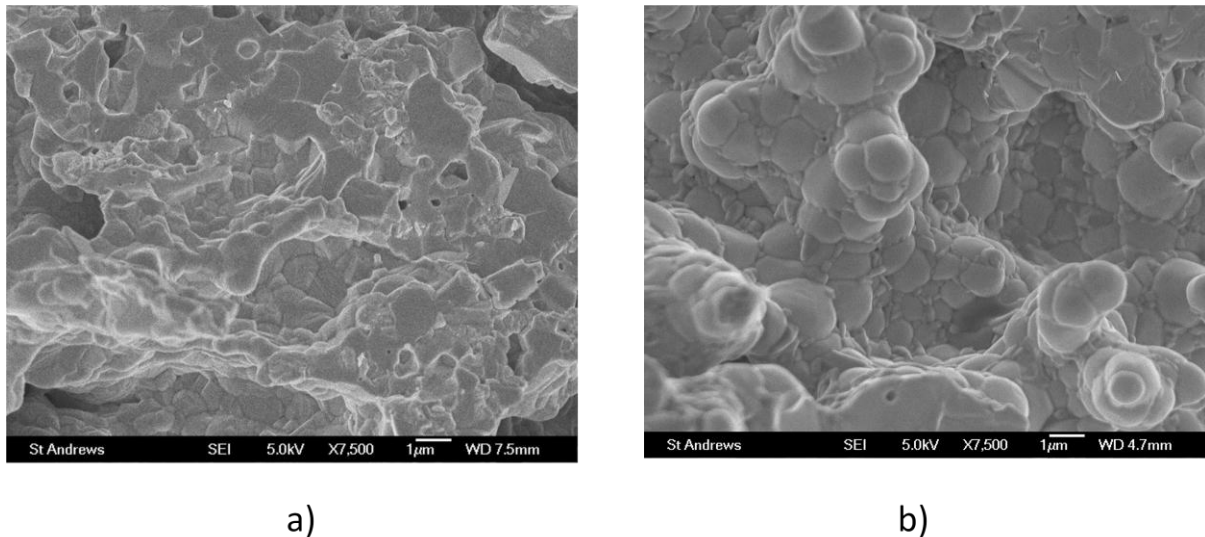


Figure 4.1: SEI image of the microstructure of composite anodes under 7500x magnification. The YSZ skeleton was impregnated with precursors for $\text{La}_{0.4}\text{Sr}_{0.4}\text{TiO}_3$ (LST44) up to 45 wt.% in image a) and up to 15 wt.% perovskite in image b).

As shown in figure 4.1.a) the composite anode with the perovskite phase impregnated up to 45 wt.%, as it would be used in a cell for electrochemical testing, has only a few small areas exhibiting grains. Also studying the differences between oxidised and reduced anodes does not show significant results, mainly because the impregnated phase at anodes with high percentages of impregnated perovskite forms a flat and uniform blanket layer over the visible grains. In composite anodes with the perovskite phase impregnated up to only 15 wt.% as shown in figure 4.1.b) the structure of the grains can be studied in more detail because the flat and uniform blanket layer is missing.

The development of the composite anode with an increasing amount of A-site deficient perovskite into the YSZ skeleton is shown in figure 4.2, from the unimpregnated skeleton in a) over the 10-15 wt.% perovskite composite in b) to the 45 wt.% composite in c), which is the composite anode composition used in test cells, clearly showing the flat and uniform blanket layer partly hiding the grain structure.

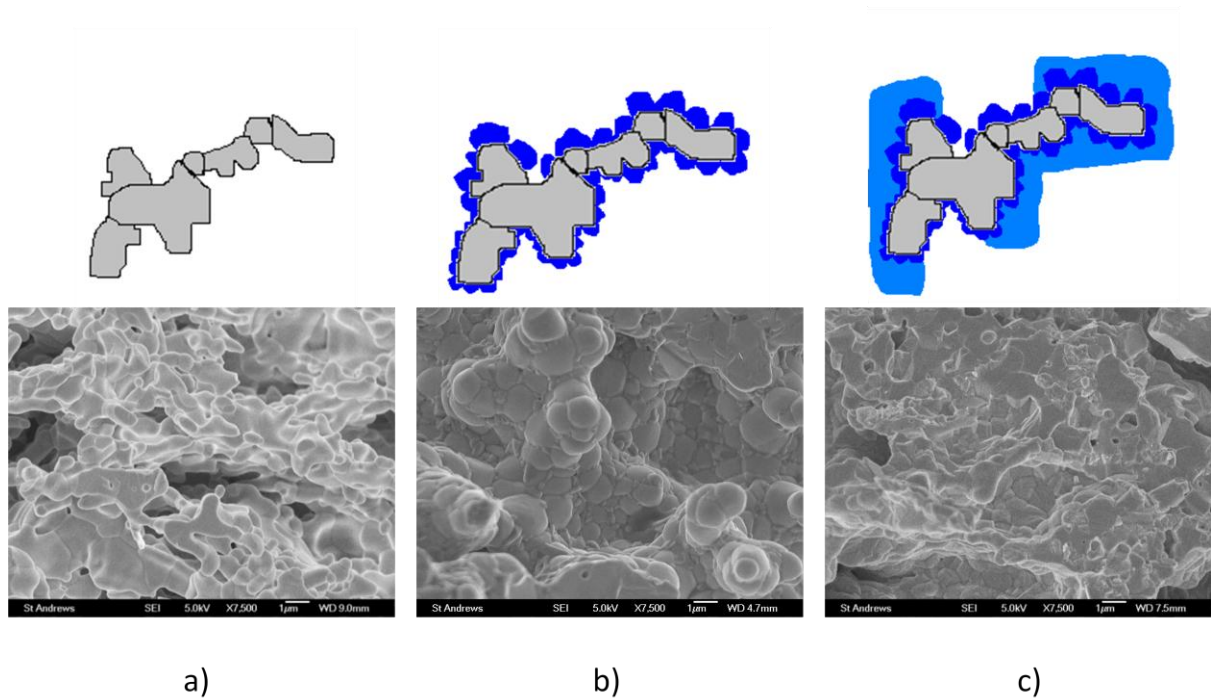


Figure 4.2: Schematics and SEI images of the microstructure of composite anodes with A-site deficient perovskites under 7500x magnification. Image and schematic a) show the unimpregnated skeleton, image and schematic b) the skeleton impregnated with 10-15 wt.% LST44 and figure and image and schematic c) impregnated with 45 wt.% LST44.

4.1.2. Oxidized and reduced forms of composite anodes with A-site deficient perovskites

Further investigation of the composite anodes consisting of 85-90 wt.% YSZ skeleton and 10-15 wt.% LST44 exhibits under oxidising conditions a bimodal grain size distribution with big grains of sizes between 500 and 2000 nm which are spherical and regular shaped, and small grains of irregular shapes and a size of 100 nm to 300 nm. After reduction in a tube furnace at 900 °C in a dry atmosphere of 5 % hydrogen in argon for 5 hours the small grains disappeared, while the big grains remained of similar size and shape.

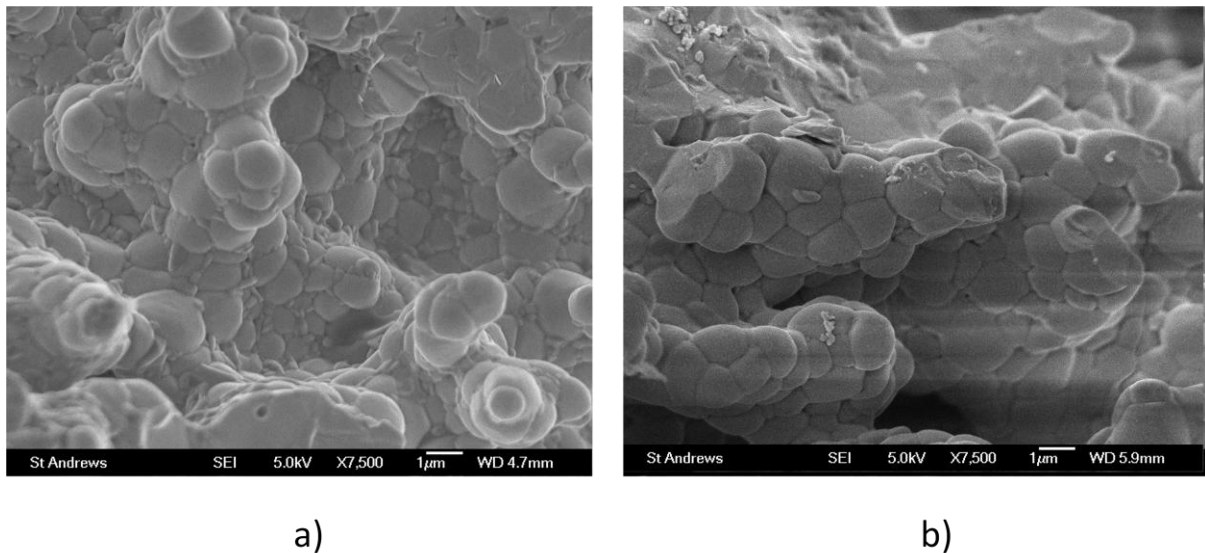


Figure 4.3: SEI images of the microstructure of composite anodes of YSZ and 10-15 wt.% $La_{0.4}Sr_{0.4}TiO_3$ (LST44) at 7500x magnification, recorded a) before and b) after reduction at 900 °C for 5 hours.

Phase characterisation of the LST44 impregnated anode was carried out by X-ray diffraction of a composite anode with 45 wt.% perovskite in reflection mode using a PANalytical EMPYREAN diffractometer as described in chapter 2.2.1.

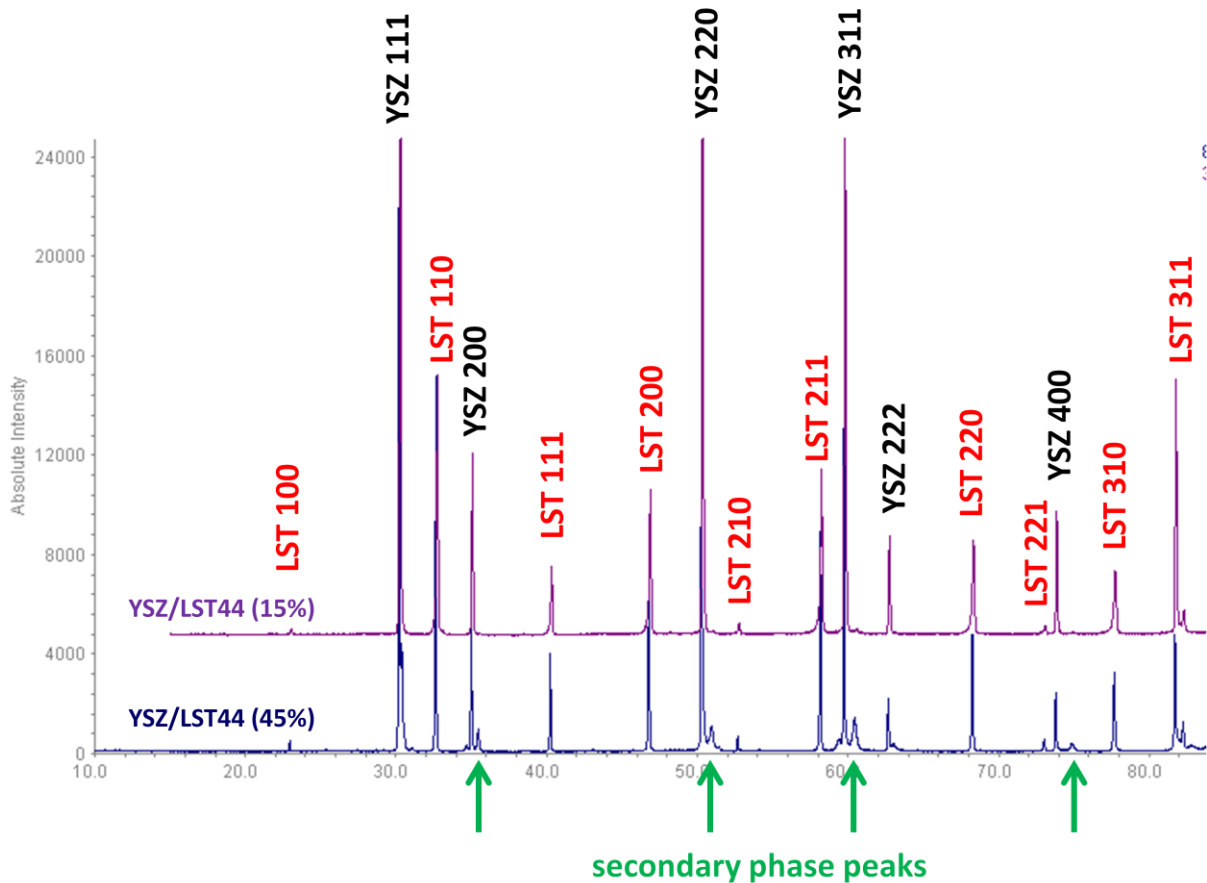


Figure 4.4: XRD diagrams of composite anodes of YSZ and LST44 with 45 wt.% LST44 (blue line) and 15 wt.% LST44 (purple line).

The main peaks of the diagram can easily be assigned to and indexed for cubic YSZ of the space group $Fm\bar{3}m$ and cubic perovskite of the space group $Pm\bar{3}m$, as shown in figure 4.4. There are no significant secondary phase peaks in the XRD diagram of the composite anode with 10-15 wt.% perovskite, however, the diagram of the anode with 45 wt.% perovskite does show some secondary phase peaks, the most significant at 2θ angles of around 35.5° , 51.0° , 60.5° and 74.9° , highlighted by green arrows in figure 4.4.

It is obvious that the major secondary phase peaks are all located at the right side of YSZ peaks, but interestingly no secondary phase peak can be found at the right side of the [1 1 1] peak of YSZ. The distance between the YSZ peaks and the secondary phase peaks ranges from 2θ angles of 0.45° to 1.05° . The pattern of the secondary phase peaks suggests peak splitting, which occurs if the ideal cubic unit cells are distorted. The absence of a split at the [1 1 1] peak suggests a tetragonal distortion of the cubic YSZ unit cell. A slight shoulder at the right side of the cubic [1 1 1] peak suggests a mix of cubic and tetragonally distorted YSZ with the [1 0 1] peak of the tetragonal phase and the [1 1 1] peak of the cubic phase too close to be resolved in the XRD spectrum. Comparison of the peak positions of the above spectrum with peak positions obtained from a tetragonal YSZ of similar composition obtained from the ICDD library [2], as shown in figure 4.5. results in a good match of the peak positions and of the distance between the split peaks. The tetragonal distortion of the YSZ lattice takes place after firing the composite anode at 1150°C , which is 100°C lower than the temperature suggested to be critical for the occurrence of a tetragonal phase in literature [3].

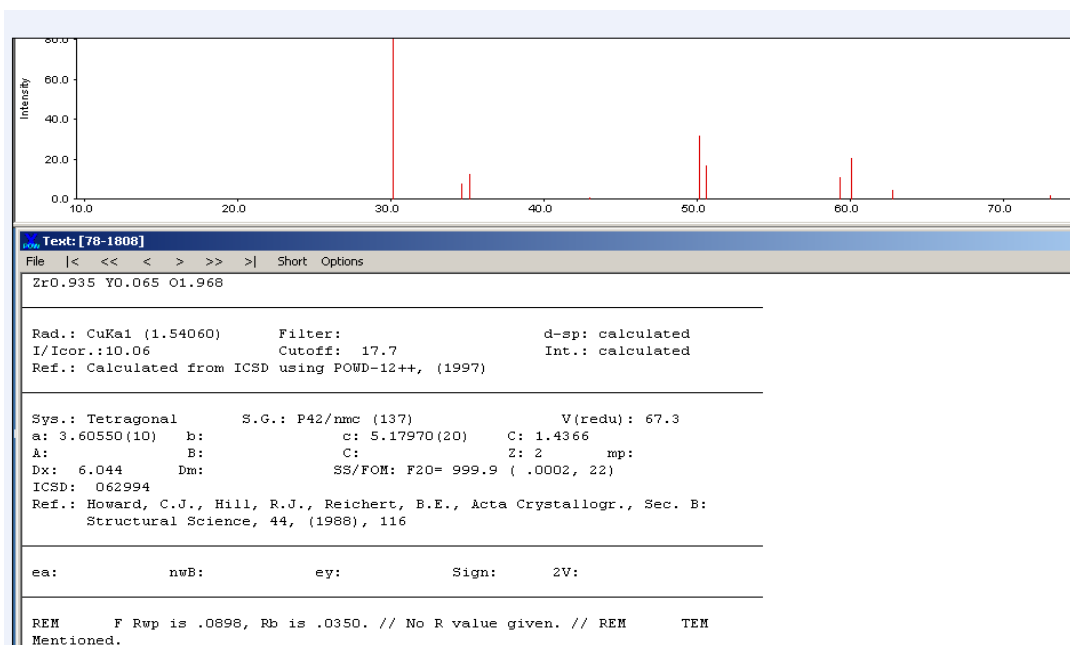


Figure 4.5: Screenshot of a card of the ICDD library [2] showing the peak positions and additional information about the XRD diagram of a tetragonal distorted YSZ of a composition similar to the one used in the experiment.

The chemical interaction between YSZ and A-site deficient titanates resulting in a tetragonal distortion of the cubic YSZ unit cell is also described in literature [3]. The reason for the tetragonal distortion of the unit cell of YSZ might be the migration of ions from the impregnated perovskite phase into the YSZ phase of the composite anode and their integration into the YSZ lattice.

A basic refinement carried out with the "Index&Refine" feature of the STOE WinXPOW software results in a cell parameter of the fitted cubic unit cell of YSZ of between 5.1389 and 5.1404 Å in both composite anodes with 10-15 wt.% and 45 wt.% perovskite content respectively. This results in a reduction of the cell parameter of around 0.001 Å on average compared to the 5.1395 to 5.1419 Å refined with the same program for YSZ in an unimpregnated skeleton. The refinement of the cell parameter of the perovskite unit cell resulted in pseudo-cubic cell parameters of 3.8890 Å in the 45 wt.% composite anode and in 3.8912 Å in the 10-15 wt.% composite anode.

After reduction in a tube furnace at 900 °C in a dry atmosphere of 5 % hydrogen in argon for 5 hours all the peaks observed in the XRD diagram of the oxidised sample remain present and at roughly the same position, including the secondary phase peaks observed in the spectrum of the 45 wt.% composition, and no additional peaks emerge. The peaks assigned to the perovskite phase are slightly broadened in both compositions, and show a distinctive shoulder at their left side in the XRD diagram of the composite anode with 10-15 wt.% perovskite, as shown in figure 4.6.

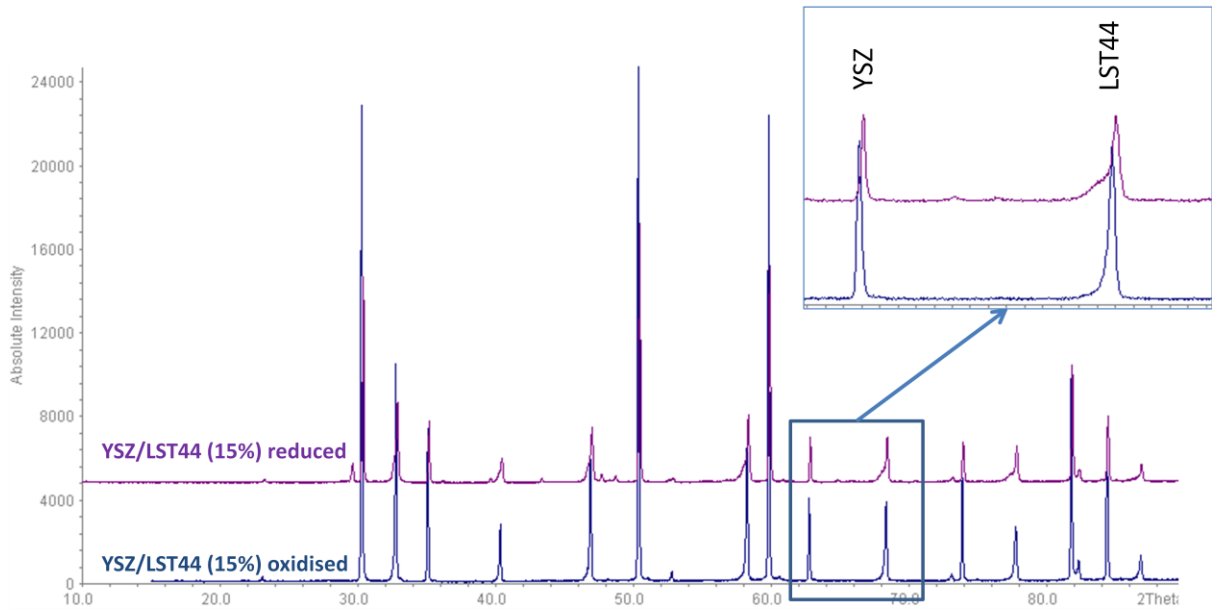


Figure 4.6: XRD diagrams of composite anodes of YSZ and LST44 with 15 wt.% LST44 in oxidised state (blue line) and reduced state (purple line), showing the distinctive shoulders at the left side of the perovskite peaks after reduction.

The main change during the reduction of the LST44 concerns the titanium ions at the B-sites of the perovskite, part of which are reduced from a charge of +4 to a charge of +3 and release some free electrons introducing n-type electronic conductivity. To maintain charge neutrality, some oxide ions are removed from the lattice, leaving oxygen vacancies. The ionic radius according to Shannon [4] is 0.605 Å for Ti^{4+} and 0.67 Å for Ti^{3+} , and the space occupied by an oxygen vacancy is bigger than the space occupied by an oxide ion in the perovskite lattice, so the cell parameter of LST44 is expected to increase upon reduction. This could explain a second peak at the left side of the original perovskite peaks, or a series of overlapping peaks forming a shoulder, probably indicating crystals with different amounts of Ti^{3+} or grains with a reduced shell and an oxidised core.

While the refined cell parameter of YSZ stayed almost the same after reduction with 5.140 Å compared to 5.139 Å before the reduction, the refined cell parameter of the perovskite increased by 0.005 Å from 3.889 Å to 3.894 Å during the reduction.

4.1.3. Electrochemical performance

A button cell fabricated as described at the very start of chapter was electrochemically tested using a test jig, a Solartron cell test system and a frequency response analyser as described in chapter 2.3.2.3 and shown in figure 2.25. IV curves and EIS spectra were recorded in a temperature range from 650 °C to 850 °C in increments of 50 °C.

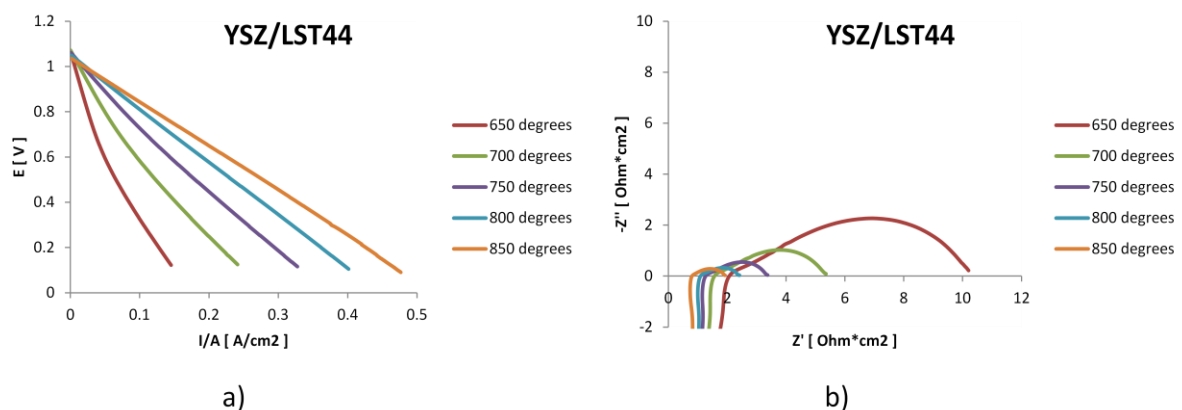


Figure 4.7: IV-curves and Nyquist plots of the EIS of a single cells with a composite anode of YSZ/LST44 and additional 1-2 wt.% PdO added as catalyst at different temperatures.

Figure 4.7 shows almost linear shapes of the IV curves for over the whole temperature range, even if the IV curve at 650 °C shows a lower gradient at high power densities, which theoretically means a decrease of the cell resistance under a stronger current. The reason can be slow electrochemical kinetics which are overcome either by higher temperatures or by increasing the driving force of the reaction by increasing the overpotential. The Nyquist plots show total resistances between around 1.9 Ωcm^2 at 850 °C and around 10.3 Ωcm^2 at 650 °C, with the ohmic part between around 0.8 Ωcm^2 at 850 °C and around 2.1 Ωcm^2 at 650 °C. The non ohmic polarisation does not show a clear distinction between two or three depressed arcs like this was the case with the cells with a CGO skeleton in chapter 3, in the cells with a YSZ skeleton a clear separation between R_{P1} and R_{P2} is not possible,

even if especially the arc at 650 °C indicates a smaller arc at higher frequencies and a bigger arc at lower frequencies.

4.1.4. Conclusions

In a composite anode with 45 wt.% LST44 with YSZ, like used for electrochemical testing, changes of the microstructure are hard to observe, because an uniform blanket layer covers big parts of the grain structure. Microstructural changes of composite anodes are better observed in a composite anode with only 10-15 wt.% of the perovskite phase.

The bimodal grain size distribution observed in the oxidised form of the YSZ/LST44 composite anode, changes upon reduction, because the smaller sized and irregular shaped grains disappear.

The XRD diagrams of composite anodes of YSZ and LST44 show some distinctive secondary phase peaks, which can be explained by a tetragonal distortion of the cubic YSZ unit cell, probably caused by migration of ions from the perovskite into the YSZ lattice.

Upon reduction the peaks of the XRD diagram assigned to the peaks of LST44 show distinctive shoulders on their left side, which can be explained by an increase of the cell parameter due to the reduction from Ti^{4+} to Ti^{3+} .

Button cells with composite anodes of YSZ and LST44 show good electrochemical performance, with a total cell resistance down to $1.9 \Omega cm^2$ at 850 °C.

4.2. B-site substitution of A-site deficient titanates

To improve the catalytic activity for fuel oxidation and the conductivity under reducing conditions the B-site of LST44 can be doped with elements like manganese [5], iron [5][6] or nickel [6]. The compositions studied in this chapter were $\text{La}_{0.4}\text{Sr}_{0.4}\text{TiO}_3$ (LST44), with an undoped B-site of titanium as a starting point, $\text{La}_{0.4}\text{Sr}_{0.4}\text{Mn}_{0.06}\text{Ti}_{0.94}\text{O}_{3-y}$ (LST44Mn6), $\text{La}_{0.4}\text{Sr}_{0.4}\text{Fe}_{0.06}\text{Ti}_{0.94}\text{O}_{3-y}$ (LST44Fe6) and $\text{La}_{0.4}\text{Sr}_{0.4}\text{Ni}_{0.06}\text{Ti}_{0.94}\text{O}_{3-y}$ (LST44Ni6).

Button cells were fabricated by tape casting and impregnation method as described in chapter 2.1. The firing temperature after the preparation of the YSZ skeleton was 1400 °C and impregnation with an aqueous precursor of the perovskites was carried out to an extent resulting in between 40 wt.% and 45 wt.% of $\text{La}_{0.4}\text{Sr}_{0.4}\text{TiO}_3$ (LST44), and in 10-15 wt.% LST44 for additional microstructure studies. The calcination temperatures were around 1150 °C after the impregnation of the anode and 850 °C after the impregnation of the cathode with an aqueous precursor for $\text{La}_{0.8}\text{Sr}_{0.2}\text{FeO}_{2.9}$ (LSF82). The anodes were impregnated with a precursor for palladium oxide as an additional catalyst for the oxidation to the extent of 1-2 wt.%, as described in chapter 2.1.2.

4.2.1. Microstructure of B-site substituted perovskites

As explained in chapter 4.1.1. it is easier to spot changes of the microstructure in composite anodes with only 10-15wt.% perovskite impregnated into a YSZ skeleton. Investigation of the microstructure was carried out using the SEI technique of a SEM microscope as described in chapter 2.2.2.1.

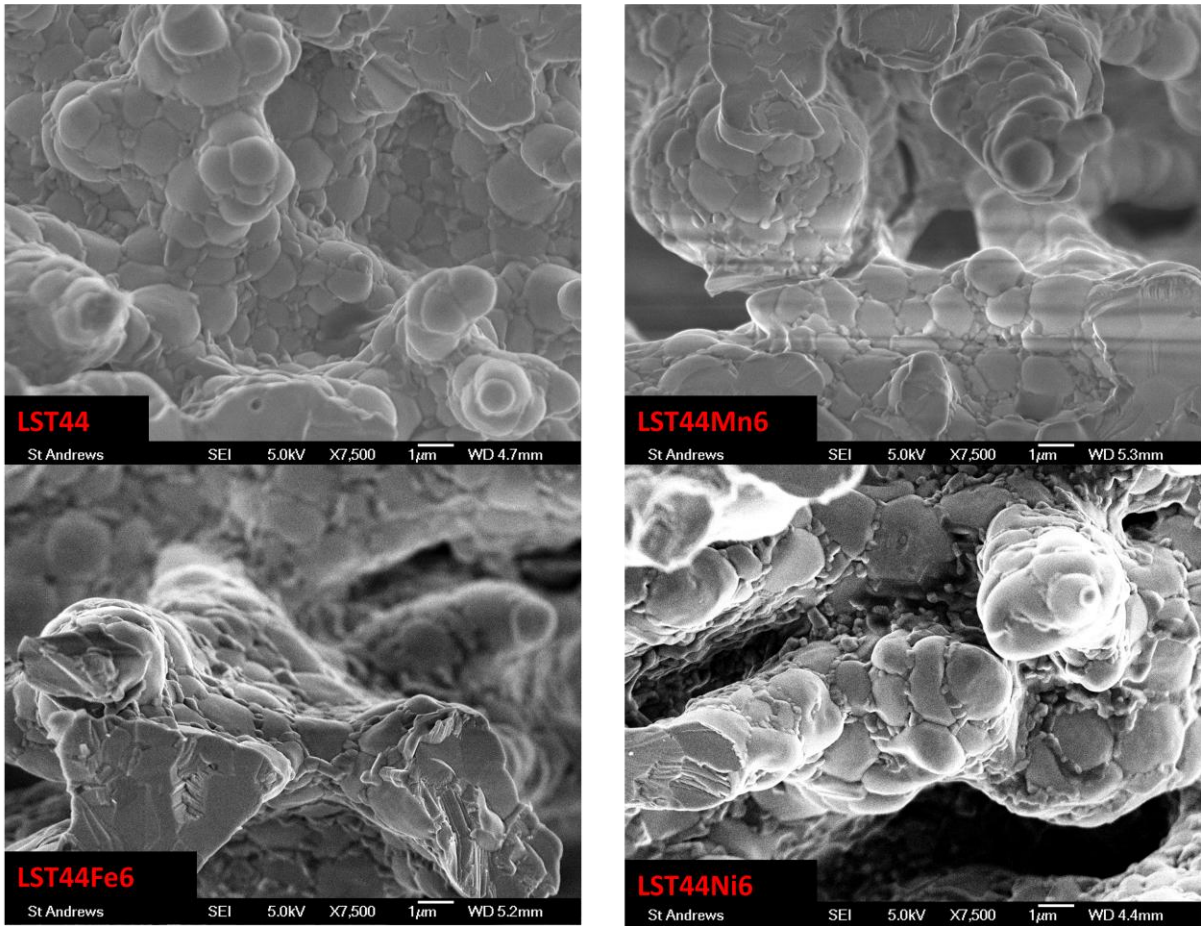


Figure 4.8: SEI images of the microstructure of composite anodes of YSZ and 10-15 wt.% of the different perovskites $\text{La}_{0.4}\text{Sr}_{0.4}\text{TiO}_3$ (LST44), $\text{La}_{0.4}\text{Sr}_{0.4}\text{Mn}_{0.06}\text{Ti}_{0.94}\text{O}_{3-\gamma}$ (LST44Mn6), $\text{La}_{0.4}\text{Sr}_{0.4}\text{Fe}_{0.06}\text{Ti}_{0.94}\text{O}_{3-\gamma}$ (LST44Fe6) and $\text{La}_{0.4}\text{Sr}_{0.4}\text{Ni}_{0.06}\text{Ti}_{0.94}\text{O}_{3-\gamma}$ (LST44Ni6) at 7500x magnification under ambient conditions.

As shown in figure 4.8. the microstructure of the oxidised samples of composite anodes containing YSZ and 10-15 wt.% B-site substituted A-site deficient titanates are hardly any different from the unsubstituted compound $\text{La}_{0.4}\text{Sr}_{0.4}\text{TiO}_3$ (LST44). The bimodal grain size distribution mentioned for LST44 in chapter 4.1.1 can be observed even better in LST44Mn6, LST44Fe6 and LST44Ni6, as shown in figure 4.8.

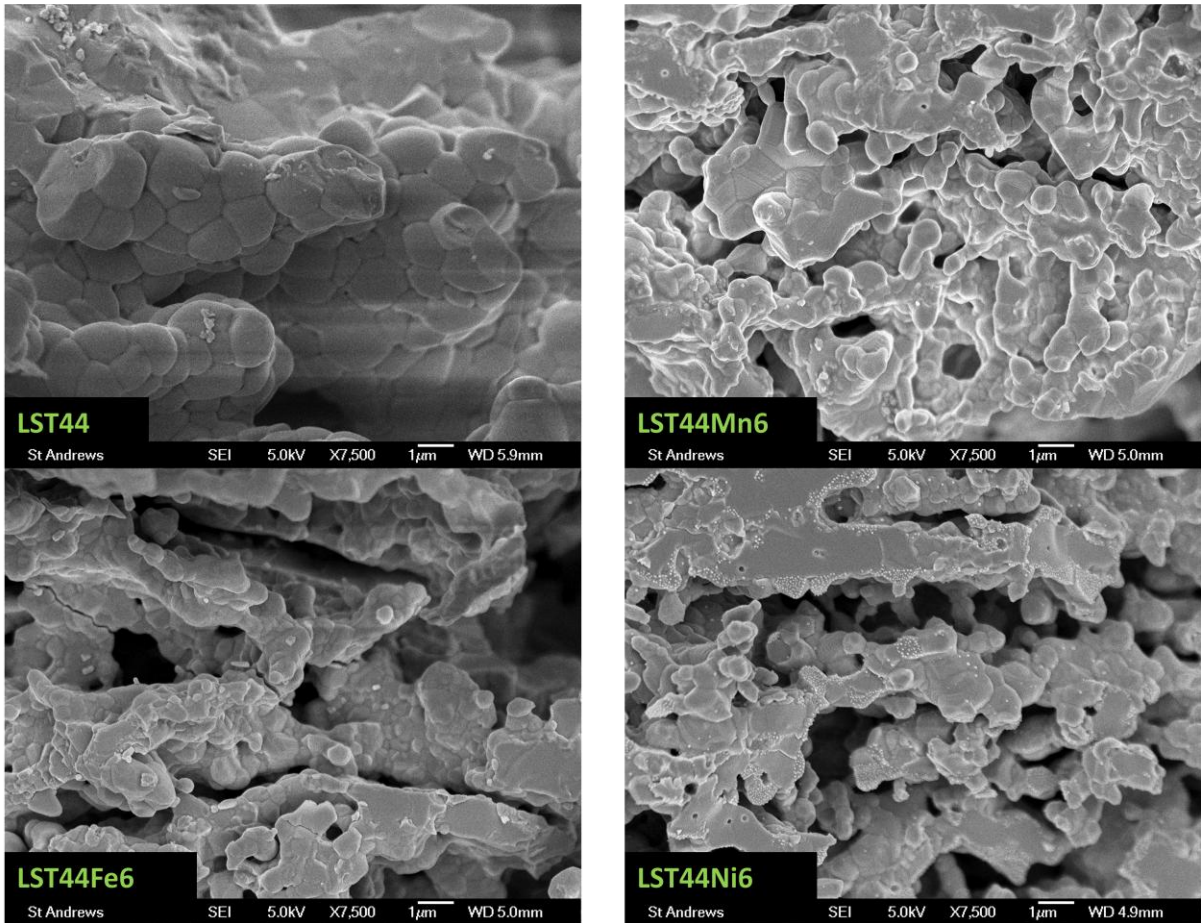


Figure 4.9: SEI images of the microstructure of composite anodes of YSZ and 10-15 wt.% of the different perovskites $La_{0.4}Sr_{0.4}TiO_3$ (LST44), $La_{0.4}Sr_{0.4}Mn_{0.06}Ti_{0.94}O_{3-y}$ (LST44Mn6), $La_{0.4}Sr_{0.4}Fe_{0.06}Ti_{0.94}O_{3-y}$ (LST44Fe6) and $La_{0.4}Sr_{0.4}Ni_{0.06}Ti_{0.94}O_{3-y}$ (LST44Ni6) at 7500x magnification after reduction.

The substitution on the B-site of the perovskite changes the microstructure much more clearly after reduction in a tube furnace at 900 °C in a dry atmosphere of 5 % hydrogen in argon for 5 hours, as shown in figure 4.9. As mentioned in chapter 4.1.1 the only change to the microstructure of the composite anode with undoped LST44 upon reduction is that the small irregular shaped grains disappear. The situation is different for all three B-site doped samples, which completely change the appearance of their microstructure upon reduction, no matter if the B-site is doped to a level of 6% with manganese, iron or nickel, as apparent from figure 4.9. Under oxidising conditions the microstructure shows a bimodal grain size distribution with large grains of regular round shape with a diameter between 500 nm and 2000 nm

and small irregular shaped grains with diameters of 100 nm to 300 nm located at some of the grain boundaries of the large grains, as can be seen in figure 4.8. After reduction the anodes with B-site substituted perovskites show an irregular shaped mass with much smaller pores and hardly any visible grain boundaries, similar to undoped YSZ, making an estimate for the grain size difficult, but certainly smaller than in the oxidised sample, as can be seen in the three of the four pictures in figure 4.9 showing anodes containing B-site substituted perovskites.

Another difference in the microstructure of the reduced samples with B-site substituted perovskites compared to samples with unsubstituted LST44 is the forming of terraces, which can be observed even under a magnification of 7500x in the LST44Mn6 sample of figure 4.9. These terraces are visible in all reduced B-site substituted samples at a magnification of 30000x, but not at the reduced sample with unsubstituted LST44 under the described reducing conditions. The extent of the terraces is largest in the $\text{La}_{0.4}\text{Sr}_{0.4}\text{Mn}_{0.06}\text{Ti}_{0.94}\text{O}_{3-y}$ composite, second in the $\text{La}_{0.4}\text{Sr}_{0.4}\text{Ni}_{0.06}\text{Ti}_{0.94}\text{O}_{3-y}$ composite and hardly visible in the $\text{La}_{0.4}\text{Sr}_{0.4}\text{Fe}_{0.06}\text{Ti}_{0.94}\text{O}_{3-y}$ composite, as can be seen in figure 4.10. The forming of these terraces is a result of restructuring of the crystals during sintering. A decrease in the lattice energy results in a lower melting temperature and a start of sintering at lower temperatures. Reduced samples show decreased lattice energy, because some of the oxide ions in the perovskite lattice are removed and substituted by vacancies. Substitution of titanium(IV) ions at the B-site of the perovskite with cations of a lower valence has the same effect.

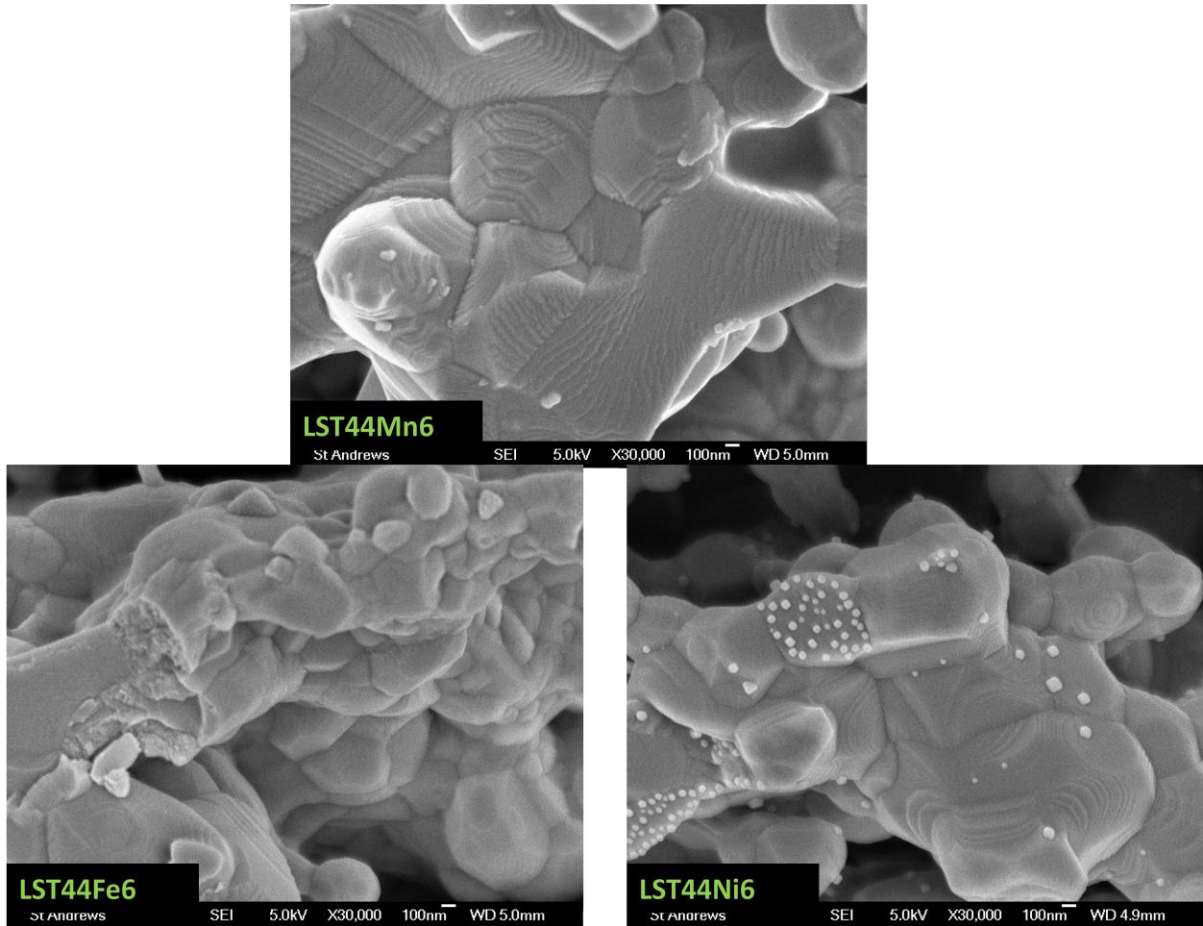


Figure 4.10: SEI images of the microstructure of composite anodes of YSZ and 10-15 wt.% of the different perovskites $La_{0.4}Sr_{0.4}Mn_{0.06}Ti_{0.94}O_{3-y}$ (LST44Mn6), $La_{0.4}Sr_{0.4}Fe_{0.06}Ti_{0.94}O_{3-y}$ (LST44Fe6) and $La_{0.4}Sr_{0.4}Ni_{0.06}Ti_{0.94}O_{3-y}$ (LST44Ni6) at 30000x magnification after reduction.

Another phenomenon, which under the chosen reduction conditions can only be observed in the nickel doped reduced sample, is the exsolution of a secondary phase, forming small regular square and triangular shaped crystals of sizes between 10 nm and 50 nm.

In oxidised state LST44 is an A-site deficient oxygen stoichiometric perovskite [7], while the B-site doped compounds are A-site deficient and also slightly oxygen deficient because the charge neutrality demands the compensation of the charge difference between Ti^{4+} and the manganese, iron and nickel ions with charges lower

than +4 [6] [7]. Upon reduction the titanium and the doped ions are reduced and oxide ions are removed from the lattice leading to A-site deficient and oxygen deficient perovskites, no matter if the B-site is doped or not [7]. If the reducing conditions are strong enough, the ions on the B-site can be exsolved from the lattice and be reduced to the metal, this way making the perovskite lattice less A-site and oxygen deficient and forming metal exsolution nanoparticles on top of the perovskite [6] [7] [8].

Reducing the composite anodes in a dry atmosphere of 95 % argon and 5 % hydrogen at 900 °C for 5 hours obviously was sufficient to exsolve nickel from the LST44Ni6 lattice, but not manganese or iron from the other doped perovskites or titanium from the undoped LST44. The position in the electrochemical series results in a standard potential of -0.25 V for the redox couple Ni^{2+}/Ni , compared to lower potentials for Ti^{2+}/Ti (-1.63 V), Fe^{2+}/Fe (-0.44 V) and Mn^{2+}/Mn (-1.18 V), which explains why nickel ions are easiest to reduce to metal [9]. If the reduction is carried out at an increased temperature of 1050 °C in the same atmosphere for 5 hours, LST44Mn6 and even undoped LST44 show exsolution of nanoparticles as well, as can be seen in figure 4.11 and will be discussed in more detail in chapter 4.4.1.

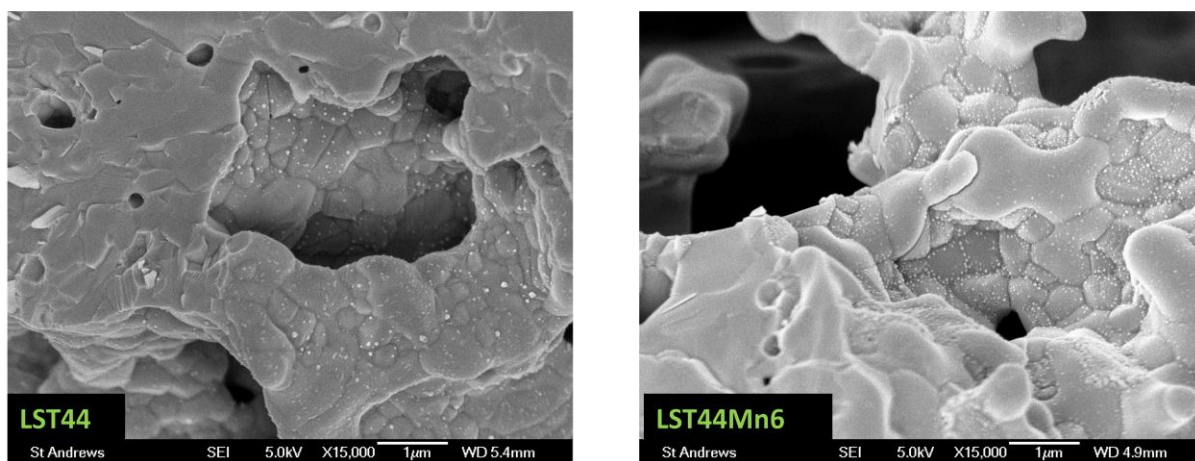


Figure 4.11: SEI images of the microstructure of composite anodes of YSZ and 45 wt.% of $\text{La}_{0.4}\text{Sr}_{0.4}\text{TiO}_3$ (LST44) and $\text{La}_{0.4}\text{Sr}_{0.4}\text{Mn}_{0.06}\text{Ti}_{0.94}\text{O}_{3-y}$ (LST44Mn6) at 15000x magnification after reduction at 1050 °C.

4.2.2. Phase investigation of B-site substituted titanates

Phase investigation of the composite anodes fabricated of YSZ and $\text{La}_{0.4}\text{Sr}_{0.4}\text{TiO}_3$ (LST44), $\text{La}_{0.4}\text{Sr}_{0.4}\text{Mn}_{0.06}\text{Ti}_{0.94}\text{O}_{3-y}$ (LST44Mn6), $\text{La}_{0.4}\text{Sr}_{0.4}\text{Fe}_{0.06}\text{Ti}_{0.94}\text{O}_{3-y}$ (LST44Fe6) and $\text{La}_{0.4}\text{Sr}_{0.4}\text{Ni}_{0.06}\text{Ti}_{0.94}\text{O}_{3-y}$ (LST44Ni6) the way described at the start of chapter 4.2, was carried out using XRD.

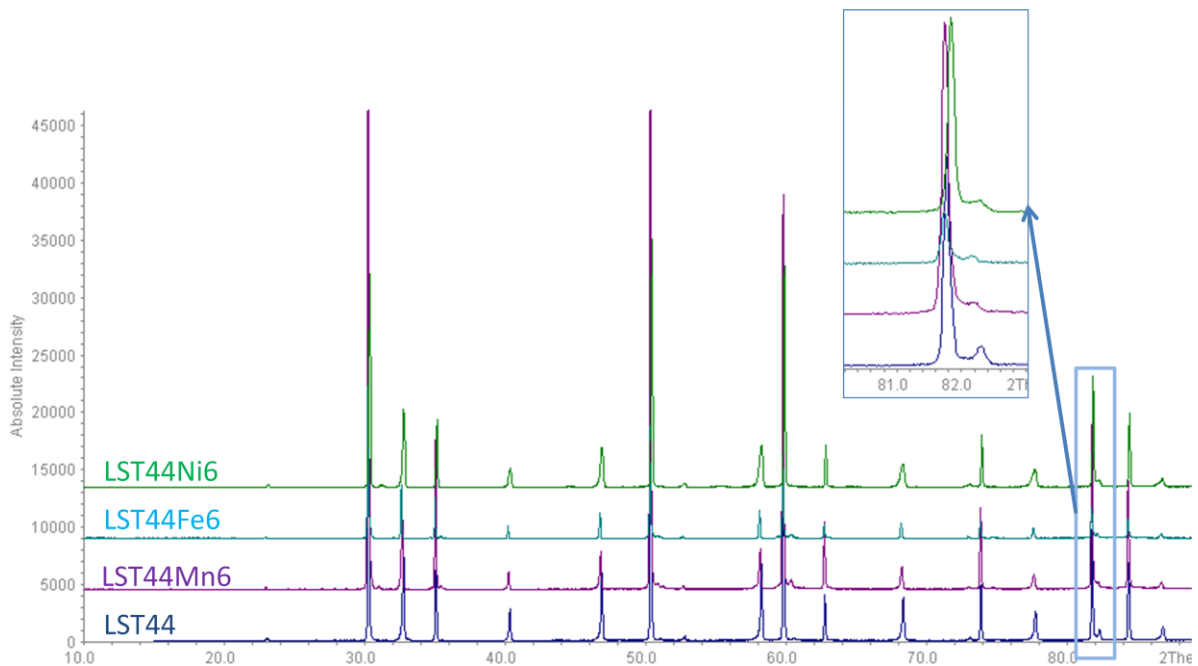


Figure 4.12: XRD diagrams of composite anodes of YSZ and A-site deficient perovskites, most of them B-site substituted, under oxidising conditions.

All the peaks which could be assigned to YSZ and the perovskite phase and indexed for the anode containing unsubstituted LST44, as shown in figure 4.4, are also visible in the XRD of the anodes containing the B-site substituted perovskites LST44Mn6, LST44Fe6 and LST44Ni6, as shown in figure 4.12. That includes the secondary phase peaks at the right side of some of the YSZ peaks, for instance at the right side of the [3 3 1] peak of cubic YSZ at 2θ angles of approximately 81.8° , which was magnified displayed in a separate figure inside figure 4.12. These

secondary phase peaks, which are clearly visible in the XRDs of all anodes with B-site substituted and unsubstituted perovskites, have been ascribed to a tetragonal distortion of the cubic YSZ unit cell due to an interaction with the perovskite phase in chapter 4.1.2.

A refinement carried out with the STOE WinXPOW software resulted in cell parameters of the fitted cubic unit cells of YSZ between 5.1389 Å and 5.1404 Å for all investigated cells, which means that the cell parameter of YSZ remains relatively unchanged, no matter if it is impregnated with LST44 or B-site substituted perovskites. The pseudo-cubic cell parameter fitted to the perovskite unit cell resulted in 3.8912 Å for LST44, 3.8921 Å for LST44Mn6, 3.8937 Å for LST44Fe6 and 3.8965 Å for LST44Ni6. The ionic radii according to Shannon and Prewitt are 0.605 Å for Ti^{4+} in 6-fold coordination, 0.645 Å for Mn^{3+} and Fe^{3+} and 0.69 Å for Ni^{2+} [4], so the size of the ionic radii for the B-site substituting ions forms the same sequence as the size of the perovskite titanates doped with these ions.

After reduction in an atmosphere consisting of 5% hydrogen and 95 % argon at 900 °C for 5 hours the XRDs of the composite anodes show all the peaks observed in the XRDs of the oxidised samples, and no additional distinctive secondary phase peaks emerge after reduction. The additional peaks marked with an “*” in figure 4.13 were assigned to blue tac, which was used to glue the samples into their position on top of the XRD sample holders. The reason for the visibility of these “blue tac peaks” predominantly in the reduced samples is the lack of mechanical stability of the anodes after reduction. Most of the reduced samples showed cracks after the sample preparation for XRD, making the blue tac under the samples a target for the X-rays.

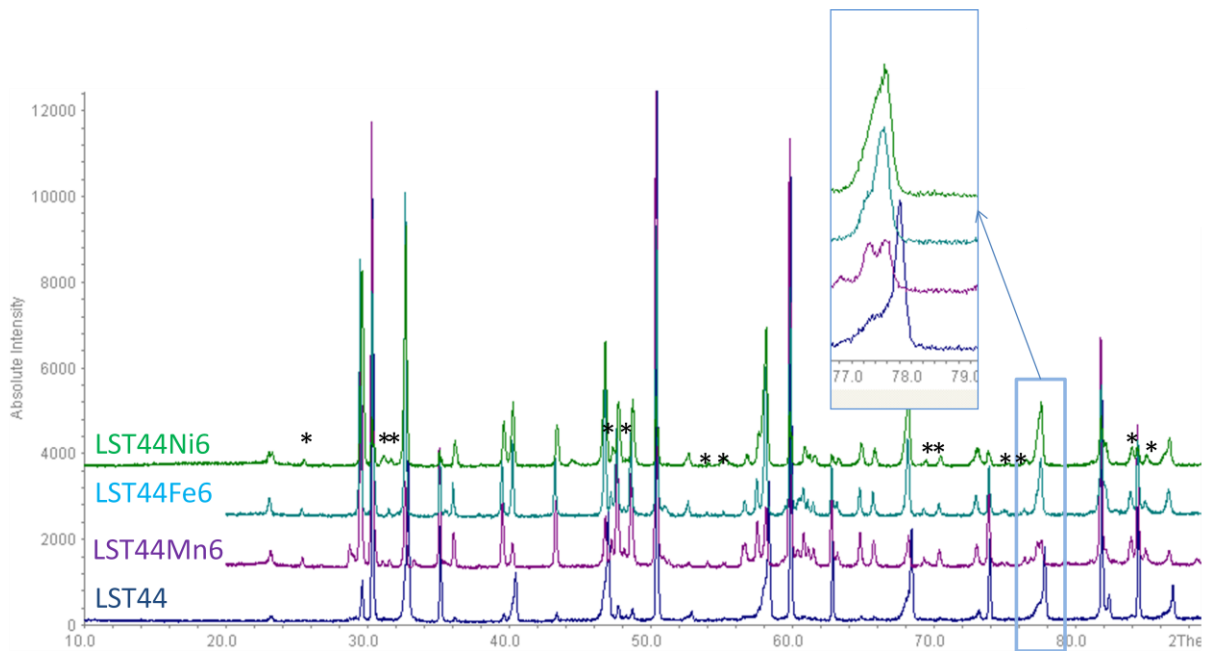


Figure 4.13: XRD diagrams of composite anodes of YSZ and A-site deficient perovskites, most of them B-site substituted, after reduction. The secondary phase peaks marked with a “*” result from blue tac.

The perovskite peaks of the B-site substituted samples show shoulders on their left sides after reduction in the same way as the samples with unsubstituted LST44 already described in chapter 4.1.2. This fact was shown in a magnified additional window for the [3 1 0] peak of the cubic perovskite at a 2θ angle of around 77.5° in figure 4.13. In the LST44Mn6 sample the shoulder of this peak is resolved into two peaks.

The cell parameter of the reduced perovskites was refined to be 3.8952 Å for LST44 and around 3.8996 Å for LST44Ni6, which is around 0.004 Å bigger than the cell parameter of the perovskites in oxidised state. The increase of the cell parameter can be explained by the fact that the ions at the B site of the perovskites all have bigger ionic radii in the lower charge states they have in their reduced forms.

The exsolution of particles upon reduction unique to the LST44Ni6 sample under a reduction temperature of 900 °C was described in chapter 4.2.1. These particles are believed to be metallic nickel [6] [7], however, the XRD showed none of the peaks expected for this compound from the ICDD database, probably because the amount of this secondary phase is too little to be detected by XRD.

4.2.3. Electrochemical performance

The electrochemical performance of button cells fabricated by tape casting and the impregnation method as described in chapter 2.1 with composite anodes made of YSZ and LST44, LST44Mn6 or LST44Ni6 was tested using a test jig, a Solartron cell test system and a frequency response analyser as described in chapter 2.3.2.3 and shown in figure 2.25. IV curves and EIS spectra were recorded in a temperature range from 650 °C to 850 °C in increments of 50 °C. The anodes of the cells tested in this chapter all have 1-2 wt.% palladium oxide added as a catalyst for the oxidation of hydrogen.

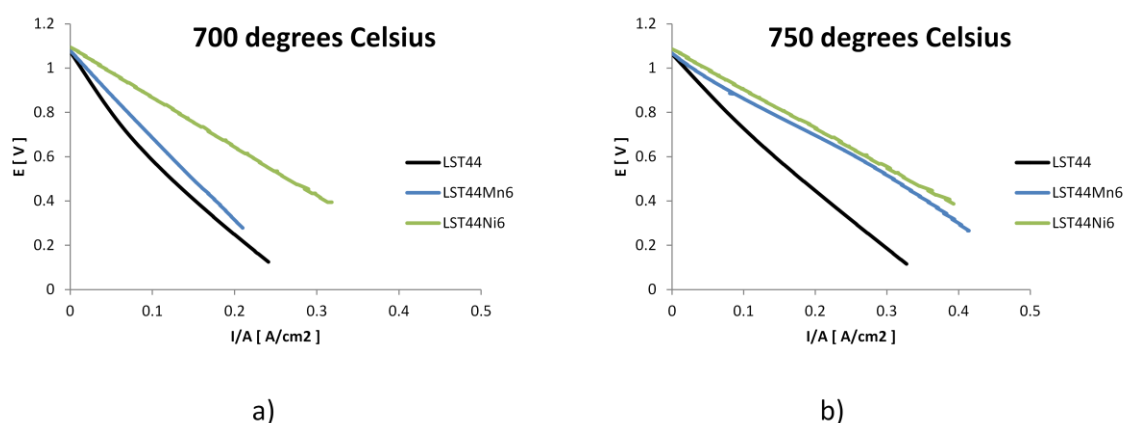


Figure 4.14: IV curves of cells with composite anodes of YSZ and different A-site deficient perovskites, some of them B-site substituted.

Figure 4.14 shows almost linear shapes of the IV curves for all three cells over the whole range, even if the cell containing unsubstituted LST44 shows a lower gradient at high power densities, especially at lower temperatures, as mentioned in chapter 4.1.3. The gradient of the IV curves indicates an enhanced electrochemical performance for the cell with the anode containing LST44Ni6 at 700 °C, resulting in a maximal power density of 134.7 mW/cm², while the cells with LST44 and LST44Mn6 only show maximal power densities of 61.9 mW/cm² and 74.7 mW/cm², respectively. At a slightly higher temperature of 750 °C, as expected, the electrochemical performance of all three cells improves, expressed by lower gradients of the IV curves because of lower cell resistances of the cells and by higher maximal power densities. The maximal power density for the cell with LST44 reached 90.1 mW/cm² and the maximal power density for the cell with LST44Ni6 166.7 mW/cm² at 750 °C, both increasing by around 30 mW/cm² compared to the same cell at 700 °C, but the cell with LST44Mn6 more than doubled its maximal power density from 74.7 mW/cm² to 156.2 mW/cm². As a result, at 700 °C, the cell with LST44Mn6 showed an electrochemical performance similar to the cell with LST44, but at 750 °C, its performance was much better, nearly reaching the level of the cell with LST44Ni6. It seems obvious that a higher temperature improves the electrochemical performance of the cell with the manganese substituted perovskite in a more impressive way than it improves the cell with the nickel substituted perovskite.

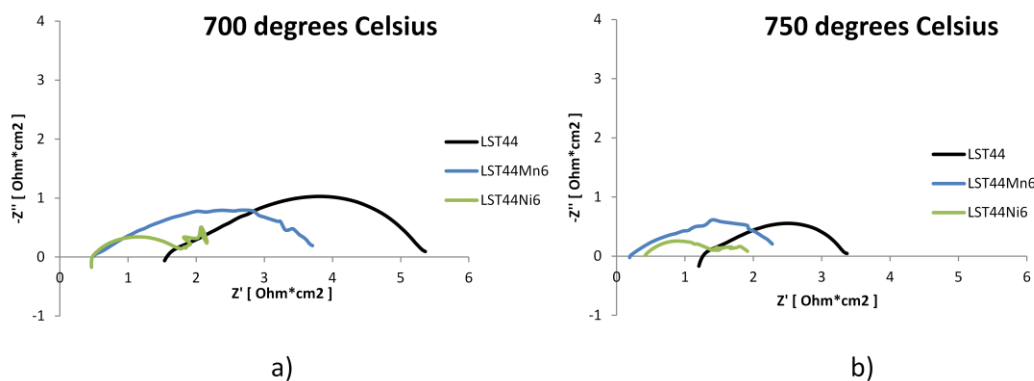


Figure 4.15: Nyquist plots of EIS curves of cells with composite anodes of YSZ and different A-site deficient perovskites, some of them B-site substituted.

Figure 4.15 shows that the superiority of the electrochemical performance of the cell with LST44Ni6 at 700 °C is predominantly caused by a non ohmic polarisation R_p of this cell of around $1.8 \Omega \cdot \text{cm}^2$, which is much lower than the non ohmic polarisations of the LST44 cell with $3.8 \Omega \cdot \text{cm}^2$ and the LST44Mn6 cell with $3.4 \Omega \cdot \text{cm}^2$. The ohmic resistance R_s is very similar in the cells with LST44Mn6 and LST44Ni6 with both around $0.5 \Omega \cdot \text{cm}^2$, while R_s of the cell with unsubstituted LST44 is much higher, around $1.6 \Omega \cdot \text{cm}^2$. The non ohmic polarisation R_p of the cell with LST44Ni6 at 750 °C is with around $1.5 \Omega \cdot \text{cm}^2$ still considerably lower than R_p of the cells with LST44 and LST44Mn6, both with values of $2.1 \Omega \cdot \text{cm}^2$, but this is partly compensated by a decrease of the ohmic resistance of the LST44Mn6 cell down to around $0.2 \Omega \cdot \text{cm}^2$, compared to an R_s value of around $0.4 \Omega \cdot \text{cm}^2$ for the LST44Ni6 cell and $1.3 \Omega \cdot \text{cm}^2$ for the cell containing undoped LST44.

Generally the doping of the B-site of the perovskite seems to reduce R_s of the cell. Manganese as a dopant seems to reduce R_s even further, but this effect seems to take effect only at temperatures of 750 °C and higher. The reduction of R_s can be explained by the change of microstructure resulting in a higher degree of percolation and an increase in triple phase boundary area, reducing the length of the pathways of electrons and oxide ions.

4.2.4. Conclusions

The microstructure of composite anodes with an YSZ skeleton and 10-15 wt.% A-site deficient perovskites is similar under oxidising conditions, no matter if the B-site is undoped titanium or titanium doped to 6 % with manganese, iron or nickel. The grain size distribution is bimodal with large regular round grains with a diameter of 500 to 2000 nm and smaller grains with a diameter between 100 and 300 nm located at the grain boundaries of the big grains.

After reduction in a dry atmosphere of 5% hydrogen in argon at 900 °C the sample with the undoped LST44 remains unchanged apart from the disappearance of the smaller grains. The samples with impregnated perovskites with doped B-sites LST44Mn6, LST44Fe6 and LST44Ni6 change their microstructure upon reduction to an irregular shaped mass with much smaller pores and the grain boundaries of the grains harder to see. The grains seem irregular shaped and smaller than in the oxidised samples.

If the reduction is carried out at 900 °C the nickel doped sample is the only sample that shows exsolution of nanoparticles upon reduction, while the samples with undoped LST44, and the other doped samples LST44Mn6 and LST44Fe6 do not show any exsolutions. However, if the reduction is carried out at 1050 °C the surfaces of the reduced LST44 and LST44Mn6 samples are decorated with nanoparticles as well.

The microstructures of the samples with B-site doped perovskites show terrace structures after reduction, this phenomenon most clearly visible at the LST44Mn6 sample. The terraces are neither visible in any of the oxidised samples nor in the reduced sample with undoped LST44.

XRD diagrams of the anodes made of YSZ and B-site doped A-site deficient perovskites show the same peaks of YSZ, perovskites and secondary phases as the anodes of YSZ and undoped LST44 reported in chapter 4.1. Refinement results for cell parameters of the substituted perovskites in the oxidised samples are slightly increased compared to the sample with undoped LST44, with the cell parameter biggest in LST44Ni6, followed by LST44Fe6, LST44Mn6 and the undoped LST44. This sequence is in good accordance with the sequence of sizes of the Shannon radii of the doped ions of nickel, iron and manganese and of the original B-site ion titanium.

After reduction of the anodes with B-site substituted perovskites the perovskite peaks in the XRD diagrams show shoulders on their left sides similar to the perovskite peaks in the sample with undoped LST44. The cell parameters of the reduced perovskites are increased by around 0.004 Å compared to the oxidised perovskites, no matter if the B-site of the cells are undoped or doped.

The electrochemical performance of the cell with a composite anode of YSZ and LST44Ni6 is far better than the performance of the LST44Mn6 cell and of the LST44 cell at 700 °C, which is due to a reduced non ohmic polarisation. At 750 °C both cells with doped perovskites, LST44Mn6 and LST44Ni6, show a performance similar to each other and much better than the performance of the cell with undoped LST44. The non ohmic polarisation of the nickel doped cell is still superior at this temperature, but the LST44Mn6 cell shows a unique reduction of the ohmic cell resistance at this higher temperature which compensates the still higher polarisation and makes the overall cell resistance of the LST44Mn6 cell similar to the LST44Ni6 cell.

4.3. Comparison with stoichiometric titanates

The fabrication and the composition of the cell with the composite anode made of YSZ and LST44Mn6, which was investigated in chapter 4.2, is similar to that of one of the cells investigated in chapter 3, apart from the fact, that in this case a different perovskite was impregnated. Instead of the A-site deficient perovskite titanate with 6 % of the B-site titanium substituted by manganese, the impregnated perovskite LSTM4646 in chapter 3 was not A-site deficient and 60 % of the B sites were occupied by manganese.

The skeletons of both cells, the impregnation of the cathodes, the percentage of the impregnated phases, the firing temperature of the skeleton, the calcination temperatures after the impregnation of the anode and the cathode and the material and application of the additional catalyst for the oxidation of hydrogen were the same or very similar in both cells, so comparing the two cells could help to provide insight into the difference between composite anodes of YSZ and A-site deficient titanates on the one side and non A-site deficient titanates on the other side.

4.3.1. Differences in the microstructure

The YSZ/LSTM4646 composite anode shows a very smooth coating of the perovskite over the YSZ skeleton, neither the irregular grains of the YSZ nor any other grain structures are visible. On 10-15 wt.% LST44Mn6 impregnated into the YSZ skeleton the irregular shaped YSZ grains are changed to round and more regular grains, and this new microstructure is covered by a flat blanket layer if the level of the impregnated perovskite is increased to the 45 wt.% necessary for the percolation in the anode of a working fuel cell. The development of the microstructure of this composite anode is described in chapter 4.1.1 and in figure 4.2. The differences between the microstructure of the composite anodes YSZ/LSTM4646 and YSZ/LST44Mn6 are shown in SEM micrographs and schematics in figure 4.16.

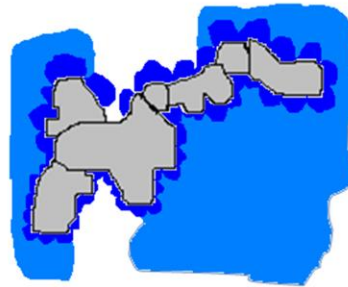
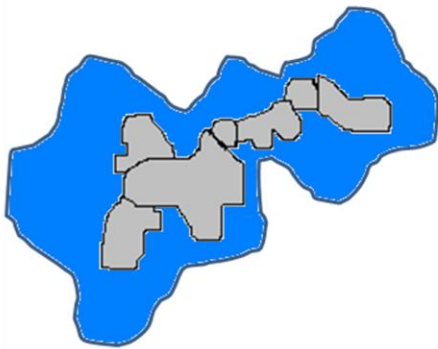
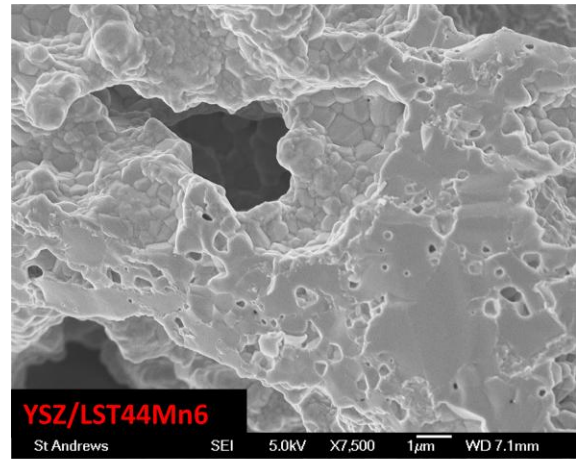
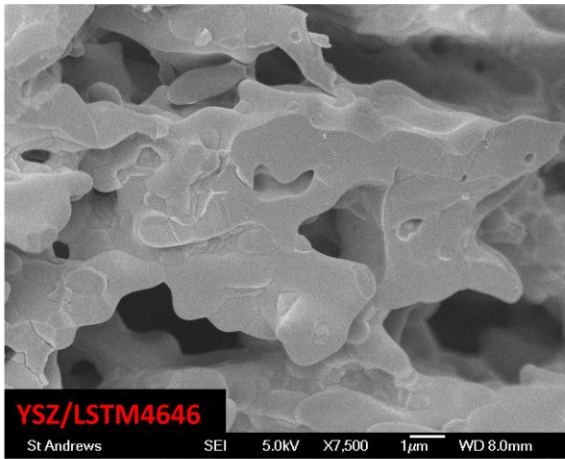


Figure 4.16: SEI images of the microstructure of composite anodes of YSZ and 45 wt.% of $\text{La}_{0.4}\text{Sr}_{0.6}\text{Ti}_{0.4}\text{Mn}_{0.6}\text{O}_3$ (LSTM4646) and $\text{La}_{0.4}\text{Sr}_{0.4}\text{Mn}_{0.06}\text{Ti}_{0.94}\text{O}_{3-y}$ (LST44Mn6) at 7500x magnification and corresponding schematic.

After 6 hours reduction at 900 °C in an atmosphere of 5 % hydrogen and 95 % argon the YSZ/LSTM4646 composite showed no changes of the microstructure. The composite anode of YSZ/LST44Mn6 showed an increase of the size of the grains visible below the blanket layer, and the formation of terraces on the surface of these grains, as shown in figure 4.17.

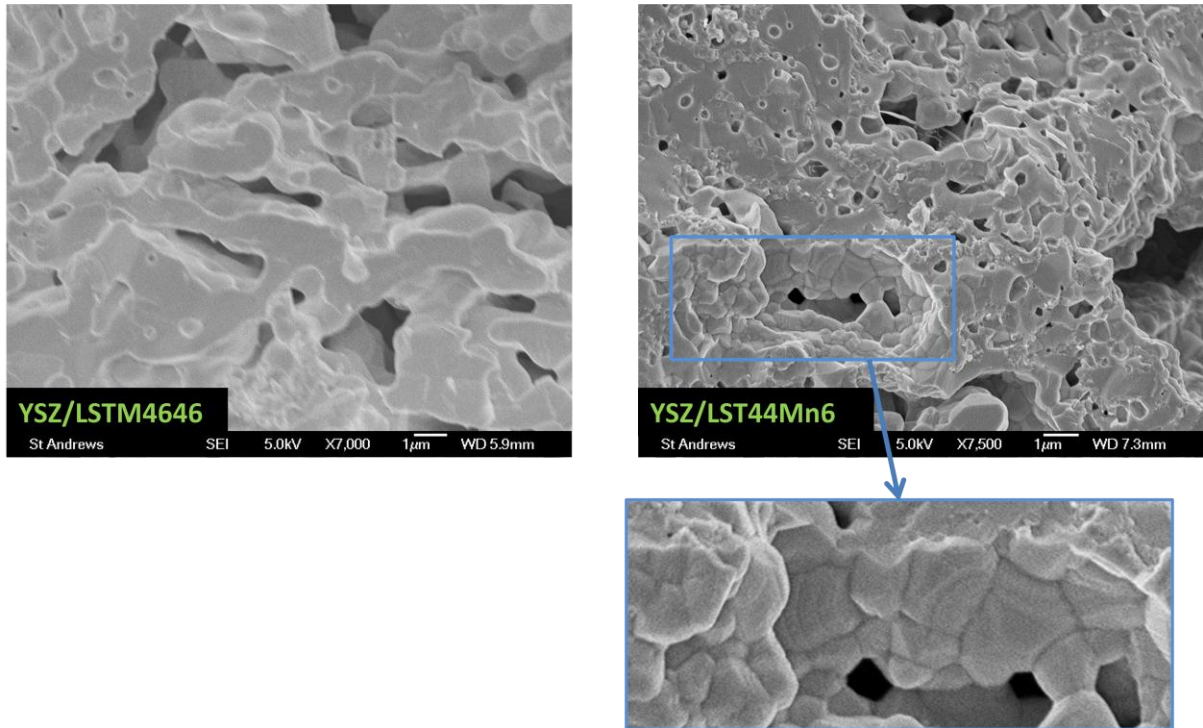


Figure 4.17: SEI images of the microstructure of composite anodes of YSZ and 45 wt.% of $\text{La}_{0.4}\text{Sr}_{0.6}\text{Ti}_{0.4}\text{Mn}_{0.6}\text{O}_3$ (LSTM4646) and $\text{La}_{0.4}\text{Sr}_{0.4}\text{Mn}_{0.06}\text{Ti}_{0.94}\text{O}_{3-\gamma}$ (LST44Mn6) after reduction at 7500x magnification.

4.3.2. Differences in the electrochemical performance

The IV curves of the two tested cells with composite anodes of YSZ and LSTM4646 and of YSZ and LST44Mn6 show almost linear shape over the whole range of current density. The IV curve of the cell containing LST44Mn6 shows a lower gradient, which indicates a lower total resistance and better electrochemical performance.

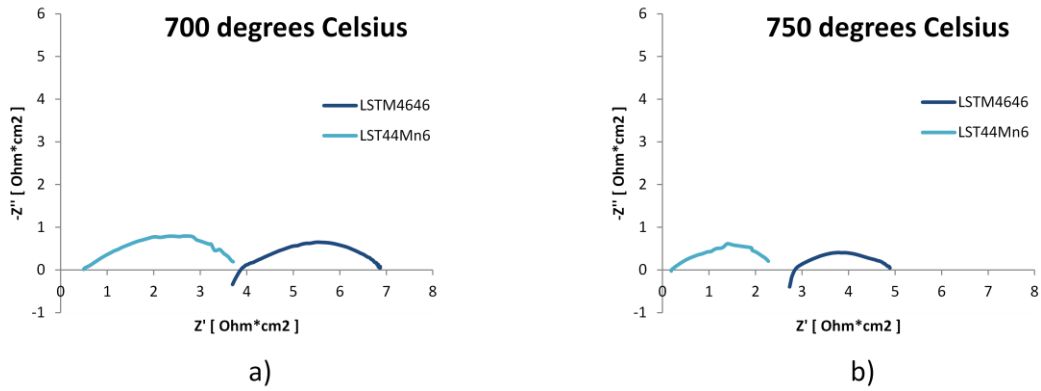


Figure 4.18: Nyquist plots of EIS curves of cells with composite anodes of YSZ and LSTM4646 and of YSZ and LST44Mn6.

The Nyquist plots of the EIS curves of the two cells at 700 °C and 750 °C show that the superiority of the cell with the A-site deficient perovskite is due to a reduced ohmic resistance part of the total resistance. While the non ohmic polarisation is very similar with around $3.0 \Omega \cdot \text{cm}^2$ for the LSTM4646 cell and around $3.4 \Omega \cdot \text{cm}^2$ for the LST44Mn6 cell at 700 °C and around $2.1 \Omega \cdot \text{cm}^2$ for both cells at 750 °C, the linear resistance of the cell with the A-site deficient LST44Mn6 is only around $0.5 \Omega \cdot \text{cm}^2$ compared to around $3.9 \Omega \cdot \text{cm}^2$ for the LSTM4646 cell at 700 °C.

4.3.3. Conclusions

The microstructure of the composite anode composed of YSZ and the A-site deficient perovskite $\text{La}_{0.4}\text{Sr}_{0.4}\text{Mn}_{0.06}\text{Ti}_{0.94}\text{O}_{3-y}$ (LST44Mn6) does not show the smooth coating observed in the microstructure of the composite anode made of YSZ and $\text{La}_{0.4}\text{Sr}_{0.6}\text{Ti}_{0.4}\text{Mn}_{0.6}\text{O}_3$ (LSTM4646). Since this smooth coating can be ascribed to an interaction between manganese in the coating perovskite and the YSZ skeleton [10], the reason for this coating missing in the YSZ/LST44Mn6 composite, could be that the B-sites in LST44Mn6 are only doped with manganese to a level of 6 %, compared to 60 % of the B-sites occupied with manganese in LSTM4646.

While reduction at 900 °C does not change the appearance of the microstructure of the composite anode YSZ/LSTM4646, the grains partly visible under the blanket layer of the YSZ/LST44Mn6 anode seem to increase their size upon reduction and develop a terrace structure.

While the non ohmic polarisation of cells with composite anodes of YSZ/LSTM4646 and of YSZ/LST44Mn6 are very similar, the ohmic resistance of the cell with the A-site deficient perovskite is with around $0.5 \Omega \cdot \text{cm}^2$ at 700 °C only a fraction of the ohmic resistance measured in the YSZ/LSTM4646 cell, resulting in a much lower total resistance and better electrochemical performance. These results seem to indicate that the ohmic resistance in the anode dominates over the ohmic resistance in the cathode and the electrolyte, and that the electrochemical performance of test cells can be greatly enhanced by using a better conductive composite anode. The higher conductivity in A-site deficient perovskites compared to non A-site deficient perovskites has been described in literature [1] [7] [11], and this higher conductivity seems to improve the conductivity of the composite anode with YSZ considerably.

4.4. The influence of a CGO coating on the YSZ skeleton

YSZ and CGO both are materials frequently used as electrolyte and electrode skeleton material in solid oxide fuel cells. Using a combination of these materials could combine the mechanical strength of YSZ [12] with the better oxide ion conductivity of CGO especially at low temperatures [13]. Literature states that 10 wt.% of CGO impregnated into the pores of a YSZ skeleton forms a dense and smooth layer on top of the YSZ [14], this theory seems to be supported by the experimental results in chapter 3.6.1.2 of this work.

After impregnating the YSZ skeleton with an aqueous precursor for CGO91 and firing it at 1200 °C, an aqueous precursor for $\text{La}_{0.4}\text{Sr}_{0.4}\text{Ti}_{0.94}\text{Mn}_{0.06}\text{O}_{3-\gamma}$ (LST44Mn6) was impregnated into the pores of the mixed skeleton and calcinated at 1150 °C. The final composite anode consisted of around 54 wt.% YSZ, 6 wt.% CGO and around 40 wt.% LST44Mn6. For the investigation of the microstructure a part of the cells were reduced in a tube furnace for 6 hours at 1050 °C in an atmosphere of 5 % hydrogen and 95 % argon.

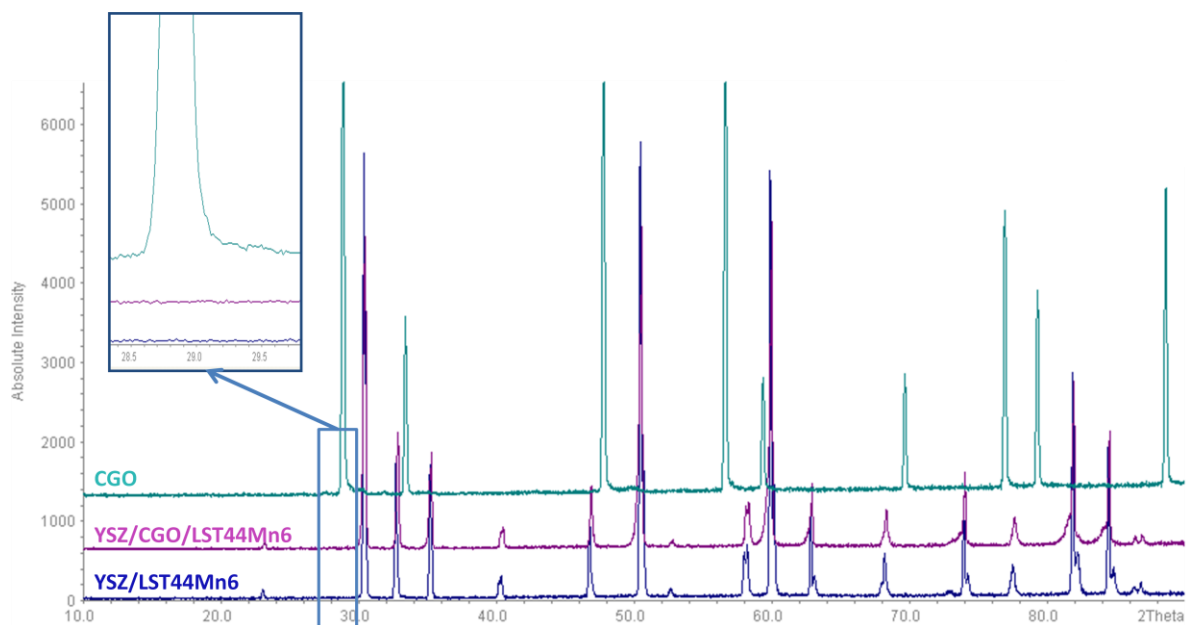


Figure 4.19: XRD diagram of a composite anode of YSZ, CGO and LST44Mn6 (purple), in comparison with a composite anode without CGO (blue). Magnified area around the [1 1 1] CGO peak.

As shown in figure 4.19 the XRD diagram of the composite anode composed of YSZ, CGO and LST44Mn6 shows the same peaks as the composite without CGO, which can be assigned to either YSZ or to the perovskite. The YSZ peaks of the composite with CGO, represented by the purple line in figure 4.19 seem broader than the YSZ peaks in the composite without CGO, especially on their left side.

Ce^{4+} ions have an ionic radius of 0.87 Å compared to 0.72 Å for Zr^{4+} ions, both in 6-fold coordination [4]. Substitution of Zr^{4+} by Ce^{4+} would lead to an increased lattice parameter of the cubic fluorite cell. Different crystals with different amounts of substituted zirconium could lead to the observed shoulders on the left side of the YSZ peaks in the XRD diagram.

Another sign for additional doping of the YSZ with cerium is the absence of secondary phase peaks at the right side of the YSZ peaks. These peaks indicate a tetragonal distortion of the YSZ unit cell as discussed in chapter 4.1.2 and shown in figure 4.4. The tetragonal distortion takes place after impregnation of YSZ with perovskites and calcination at temperatures of at least 1150 °C. After additional doping of 8YSZ with cerium the doping level might have been high enough to avoid the tetragonal area in the phase diagram shown in figure 4.20.

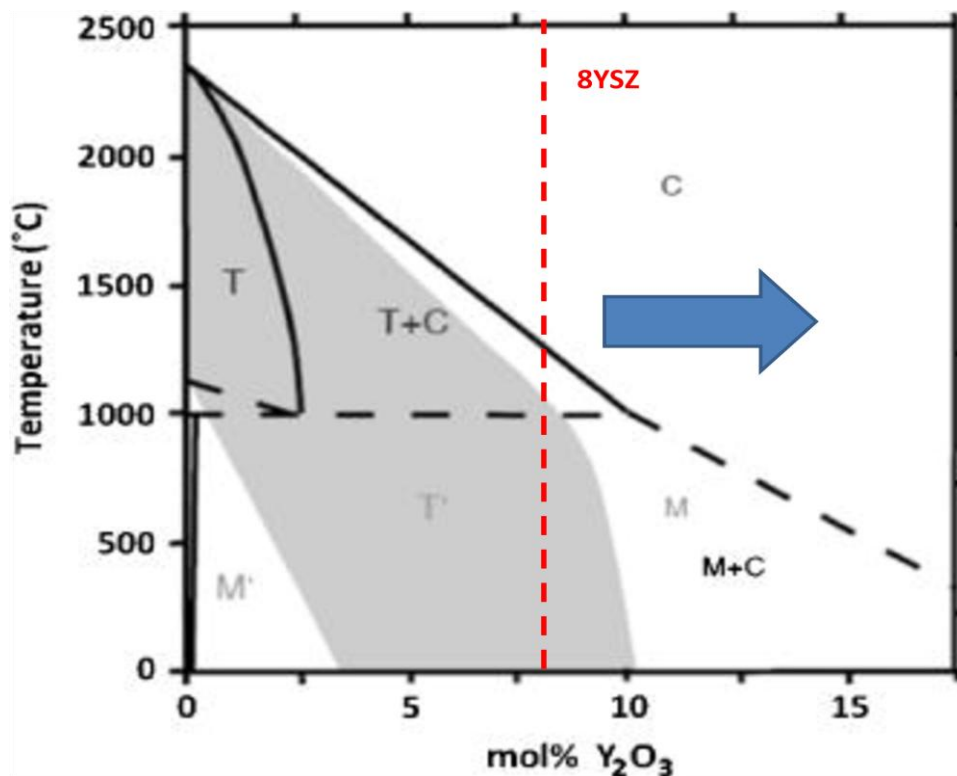


Figure 4.20: Phase diagram of zirconia with different yttria doping levels [15]. The broken red line shows the doping level of 8YSZ, the blue arrow the direction of additional doped compositions.

The composite anode YSZ/CGO/LST44Mn6, even if it contains 6 wt.% CGO, shows no sign of CGO peaks in the XRD diagram in figure 4.19, even if the 2θ area around 29° , where the CGO [1 1 1] peak is supposed to be, is magnified.

4.4.1. Microstructure of composite anodes with a CGO layer

The microstructure of the composite anode made of YSZ, CGO and LST44Mn6 in the way described above was studied using the SEI technique of a SEM microscope and compared with a similar anode of YSZ and LST44Mn6 but without CGO.

The top pictures in figure 4.21 show the microstructure of two skeletons made of YSZ and of YSZ with 10 wt.% CGO. These skeletons were impregnated with the A-site deficient perovskite LST44Mn6 to around 40 wt.%, so the composite anode without CGO was composed of 60 wt.% YSZ and 40 wt.% LST44Mn6 and the composite anode with CGO was composed of 54 wt.% YSZ, 6 wt.% CGO and 40 wt.% LST44Mn6. These composite anodes are also shown in figure 4.21 under oxidising conditions and after reduction at 1050°C .

The microstructure of an YSZ skeleton covered with a CGO layer has been investigated and described in detail in chapter 3.2.1.2. The composite anodes YSZ/LST44Mn6 and YSZ/CGO/LST44Mn6 appear very similar to each other under oxidising conditions with grains of around 500 nm covered by a flat blanket layer, as shown in figure 4.21.

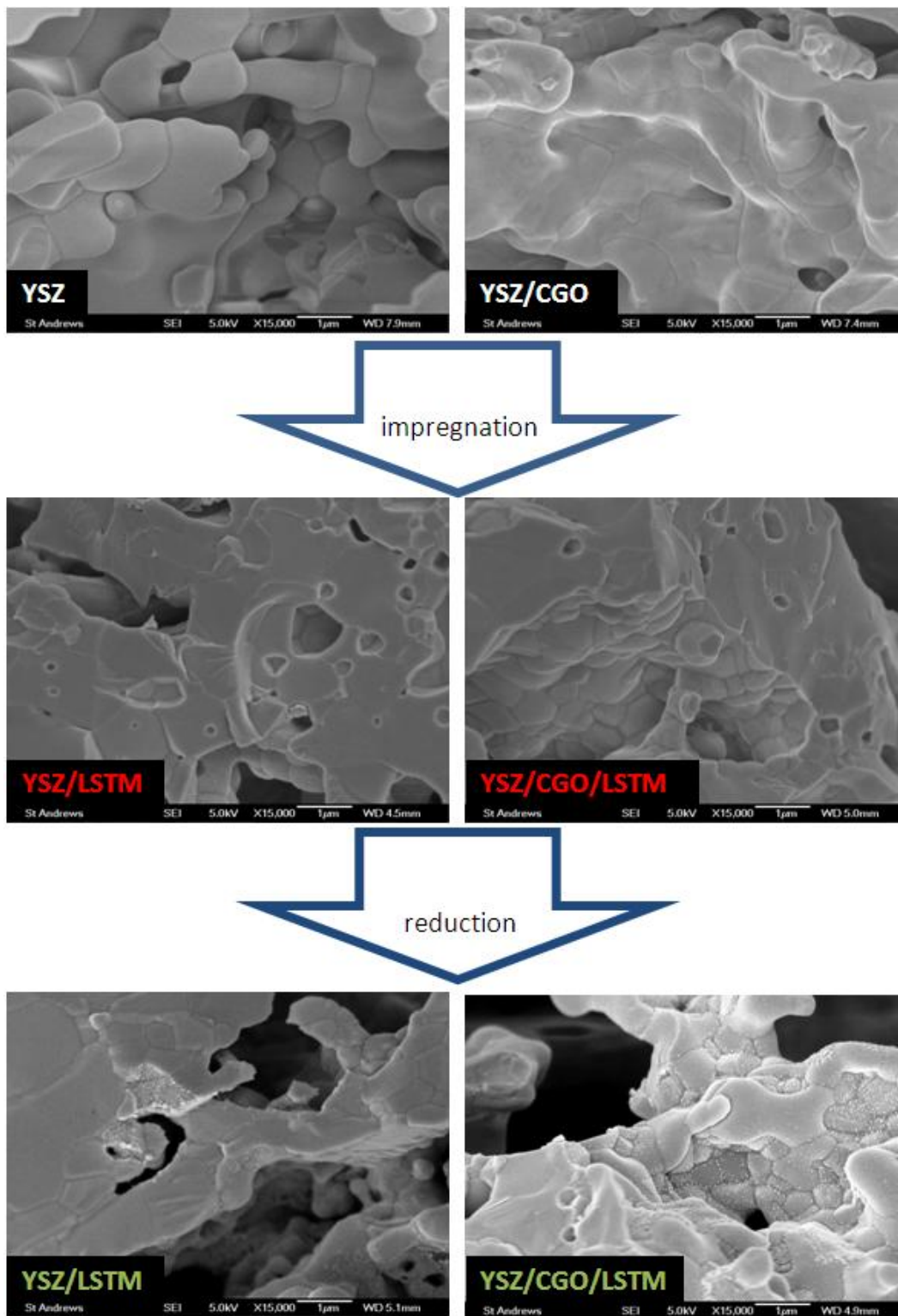


Figure 4.21: SEI images of the microstructure of skeletons of YSZ and YSZ with 10 wt.% CGO, of composite anodes of these skeletons and 40 wt.% of LST44Mn6 before and after reduction at 15000x magnification.

After reduction at 1050 °C both composites show nanoparticles from exsolution, but while the surface of the grains in the YSZ/CGO/LST44Mn6 composite is evenly decorated with few nanoparticles of a round shape and a size between 10 nm and 30 nm, the nanoparticles in the composite without CGO are concentrated at a small area and next to the majority of them between 10 nm and 30 nm there are also some particles up to around 80 nm diameter, as shown in figure 4.22 under higher magnification.

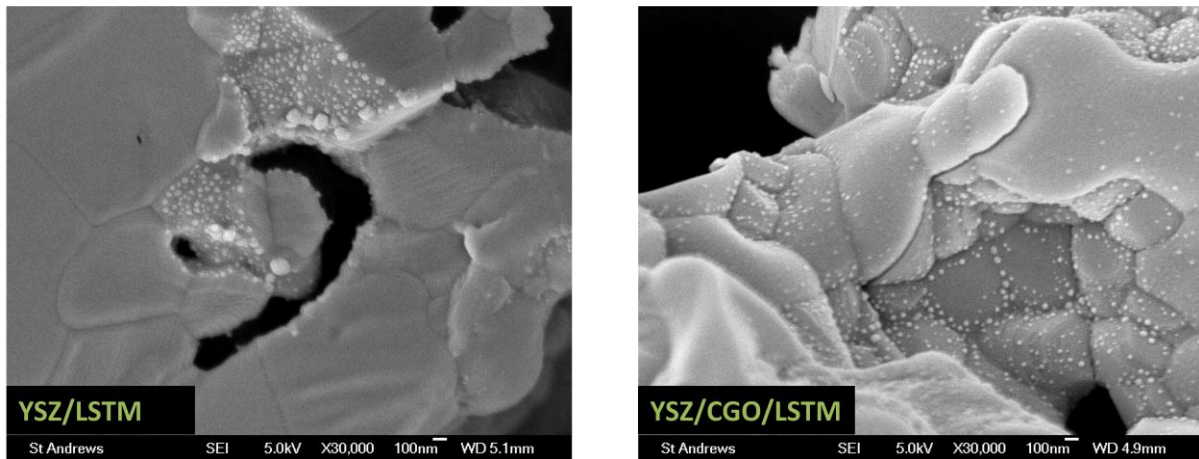


Figure 4.22: SEI images of the microstructure of skeletons of YSZ and YSZ with 10 wt.% CGO, each impregnated with 40 wt.% of LST44Mn6 after reduction at 30000x magnification.

The exsolution of nanoparticles is not dependent on the presence of manganese, the phenomenon can also be observed in composite anodes of YSZ and YSZ/CGO and impregnated $\text{La}_{0.4}\text{Sr}_{0.4}\text{TiO}_3$ (LST44) after reduction at 1050 °C, as shown in figure 4.23. The surface of the composite YSZ/CGO/LST44 is evenly decorated with particles of a size of between 20 nm and 50 nm, the concentration of the exsolved nanoparticles is lower than in the corresponding manganese containing composite YSZ/CGO/LST44Mn6 in figure 4.22. The nanoparticles in reduced YSZ/LST44 are concentrated at certain areas, just like they are in reduced YSZ/LST44Mn6, but there are more nanoparticles, they are partly connected and of a bigger size, up to 150 nm, as shown in figure 4.23.

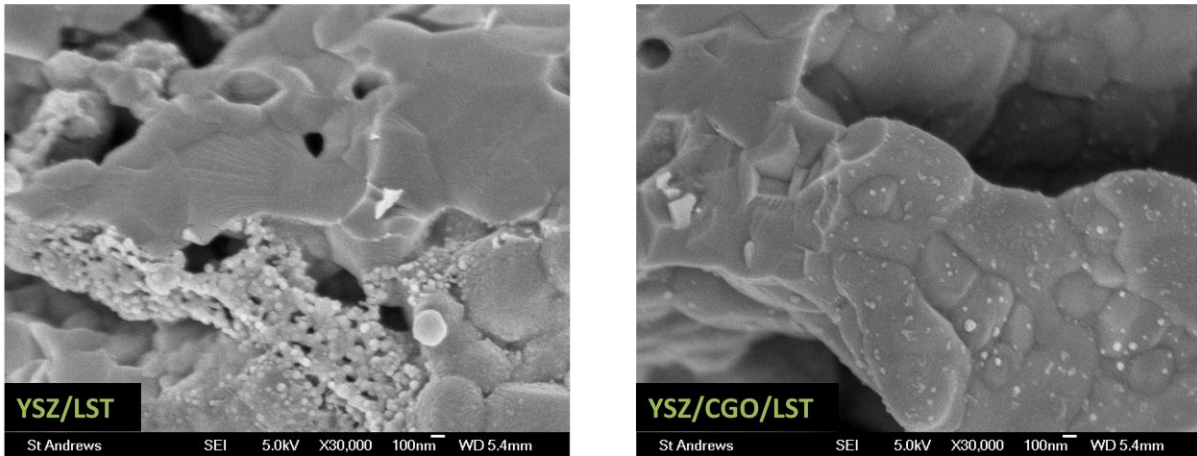


Figure 4.23: SEI images of the microstructure of skeletons of YSZ and YSZ with 10 wt.% CGO, each impregnated with 40 wt.% of LST44 without manganese doped at the B-site of the perovskite after reduction at 30000x magnification.

4.4.2. Electrochemical performance of composite anodes with a CGO layer

A set of button cells was prepared by tape casting and impregnation method like described in chapter 2.1 with a skeleton of YSZ fired at 1400 °C. The anode skeleton of a part of the cells was impregnated with CGO and all of them with an A-site deficient perovskite, either LST44 or LST44Mn6. The cathode was impregnated with $\text{La}_{0.8}\text{Sr}_{0.2}\text{FeO}_{3-\delta}$ (LSF82) and a palladium catalyst was added to the anode side. The four cells with four different composite anodes YSZ/LST44, YSZ/CGO/LST44, YSZ/LST44Mn6 and YSZ/CGO/LST44Mn6 were electrochemically tested using a test jig, a Solartron cell test system and a frequency response analyser, recording IV curves and EIS spectra.

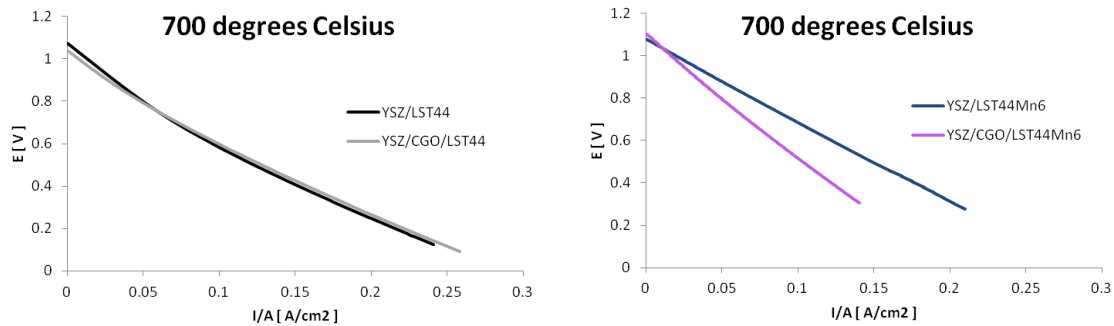


Figure 4.24: IV curves of cells with composite anodes of YSZ/LST44, YSZ/CGO/LST44, YSZ/LST44Mn6 and YSZ/CGO/LST44Mn6.

The IV curves of all four cells are close to linear over the whole range of current density, as shown in figure 4.24. The superiority in the electrochemical performance of the YSZ/LST44Mn6 cell over the YSZ/LST44 cell has been discussed in chapter 4.2.3. The gradient of the IV curves show hardly any difference between the electrochemical performance of the YSZ/LST44 cell and the YSZ/CGO/LST44 cell with their maximal power densities at 750 °C being 90.1 mW/cm² and 88.5 mW/cm², respectively. The electrochemical performance of the YSZ/LST44Mn6 cell, with a maximal power density at 750 °C of 156.2 mW/cm², deteriorates with an additional layer of CGO, the maximal power density of the YSZ/CGO/LST44Mn6 cell is only 90.6 mW/cm².

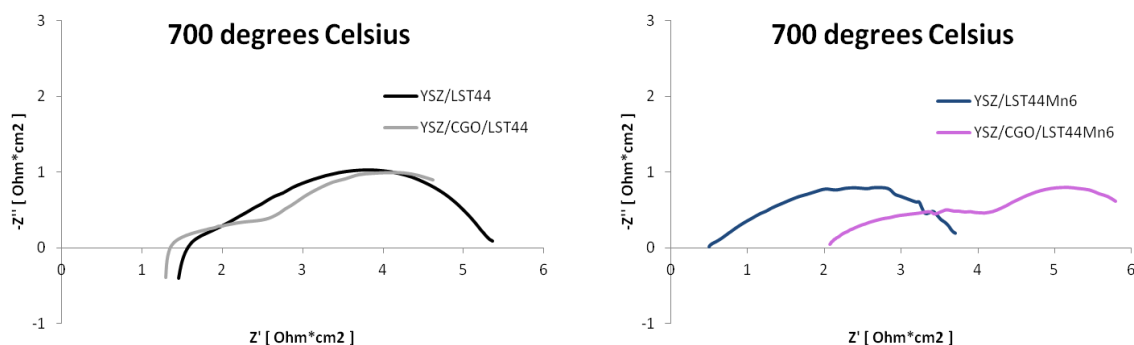


Figure 4.25: Nyquist plots of the EIS curves of cells with composite anodes of YSZ/LST44, YSZ/CGO/LST44, YSZ/LST44Mn6 and YSZ/CGO/LST44Mn6.

Both the ohmic resistance R_S and the non ohmic polarisation R_P of the cells with composite anodes of YSZ/LST44 and of YSZ/CGO/LST44 have similar values of around 1.4 to 1.6 $\Omega\cdot\text{cm}^2$ for R_S and around 3.8 to 4.3 $\Omega\cdot\text{cm}^2$ for R_P at 700 °C. The CGO layer over the skeleton seems not to be of great influence on the impedance of the YSZ/LST44 anode, but, as figure 4.25 shows, does enlarge both the ohmic resistance and the non ohmic polarisation of the cell with the YSZ/LST44Mn6 anode. The value for R_S is around 0.51 $\Omega\cdot\text{cm}^2$ for the YSZ/LST44Mn6 cell and around 2.1 $\Omega\cdot\text{cm}^2$ for the YSZ/CGO/LST44Mn6 cell at 700 °C, and at the same temperature R_P is 3.4 $\Omega\cdot\text{cm}^2$ for the YSZ/LST44Mn6 cell and 5.1 $\Omega\cdot\text{cm}^2$ for the YSZ/CGO/LST44Mn6 cell.

In the Nyquist plots of both cells with a CGO layer the shapes of the curves show two clearly separated depressed semicircle arcs, making it clearly possible to distinguish a low frequency polarisation R_{P2} with a characteristic frequency of around 0.2 Hz and a medium frequency polarisation R_{P1} with a characteristic frequency of 10-20 Hz at 700 °C. These two separated arcs can't be observed in the cells without CGO layer, YSZ/LST44 and YSZ/LST44Mn6. The shape of the Nyquist curves with two arcs for R_{P1} and R_{P2} resembles the shapes of Nyquist plots of cells with CGO/LSTM anodes, as described in chapter 3.4.

4.4.3. Conclusions

YSZ skeletons were covered with CGO by impregnation with an aqueous precursor and firing before impregnating them with an additional phase of the A-site deficient perovskites LST44 and LST44Mn6, in a way that the composition of the final composite anode was around 54 wt.% YSZ, 6 wt.% CGO and 40 wt.% perovskite.

Even if the composite anodes consisted around 6 wt.% CGO, no CGO peaks showed in the XRD, the diagram of the composite anode YSZ/CGO/LST44Mn6 shows exactly the same peaks as the diagram of the composite anode YSZ/LST44Mn6, but the peaks assigned to YSZ are broader and show shoulders on their left sides, which probably are caused by diffusion of Ce^{4+} into the YSZ lattice as described in literature [16]. The additional doping with Ce^{4+} also inhibits the formation of a secondary phase of tetragonally distorted YSZ after impregnation and calcination.

The microstructure under oxidizing conditions is very similar in the composite anodes YSZ/LST44Mn6 and YSZ/CGO/LST44Mn6. After reduction at 1050 °C both composite anodes show exsolution of nanoparticles, but while the surface of the grains are evenly decorated with nanoparticles in the YSZ/CGO/LST44Mn6 anode, the nanoparticles are concentrated on certain areas in the YSZ/LST44Mn6 anode. The exsolution of nanoparticles under the same reduction conditions can also be observed in composite anodes with perovskites not doped with manganese, YSZ/LST44 and YSZ/CGO/LST44, so it is not dependent on a doped B-site of the perovskite. As stated in literature the exsolved nanoparticles are MnO in case of the reduction of the manganese containing perovskite LST44Mn6 and Ti_2O_3 after the reduction of LST44 [7].

The CGO layer did not improve the electrochemical performance of the cells. There was hardly any difference in R_S or R_P between the YSZ/LST44 cell and the YSZ/CGO/LST44 cell, and the performance of the YSZ/CGO/LST44Mn6 had considerably higher R_S and R_P values than the YSZ/LST44Mn6 cell, probably because the electrochemical performance of the YSZ/LST44Mn6 cell was extraordinarily good without CGO layer.

The shape of the Nyquist plots of the cells with CGO the containing anodes YSZ/CGO/LST44 and YSZ/CGO/LST44Mn6 showed two depressed semi arcs unlike both cells without CGO, YSZ/LST44 and YSZ/LST44Mn6, which both only show one arc. This way the shape of the Nyquist plots resemble the shape of the cells with a CGO skeleton in chapter 3, even if the anodes of these cells only contained 6 wt.% CGO.

4.5. The influence of the calcination temperature on the composite anodes

The composition, microstructure and electrochemical performance of composite anodes fabricated by the impregnation method as described in chapter 2.1 is influenced by many parameters, one of which is the firing temperature of the composites after the impregnation of the perovskite phase [10] [17].

To study the influence of this calcinations temperature, a set of button cells was fabricated as described in chapter 2.1. The material of the skeleton was YSZ, which was fired after tapecasting at a temperature of around 1400 °C. The pores of the anode skeleton were impregnated with aqueous precursors of $\text{La}_{0.4}\text{Sr}_{0.4}\text{TiO}_3$ (LST44) or $\text{La}_{0.4}\text{Sr}_{0.4}\text{Ti}_{0.94}\text{Mn}_{0.06}\text{O}_{3-\gamma}$ (LST44Mn6) to around 40 wt.% and subsequently fired at temperatures of 1009 °C, 1059 °C, 1100 °C, 1159 °C or 1209 °C. Reduction was carried out at 900 °C for 6 hours in an atmosphere of 5 % hydrogen and 95 % argon.

4.5.1. Temperature related differences in the XRDs

The position of the peaks in XRDs of composite anodes with YSZ and LST44 have been discussed in chapter 4.1.2, the XRDs recorded after fabrication under oxidising conditions show, next to the peaks of YSZ and the perovskite, secondary phase peaks at the right side of some YSZ peaks, assigned to a tetragonal distortion of the cubic YSZ unit cell.

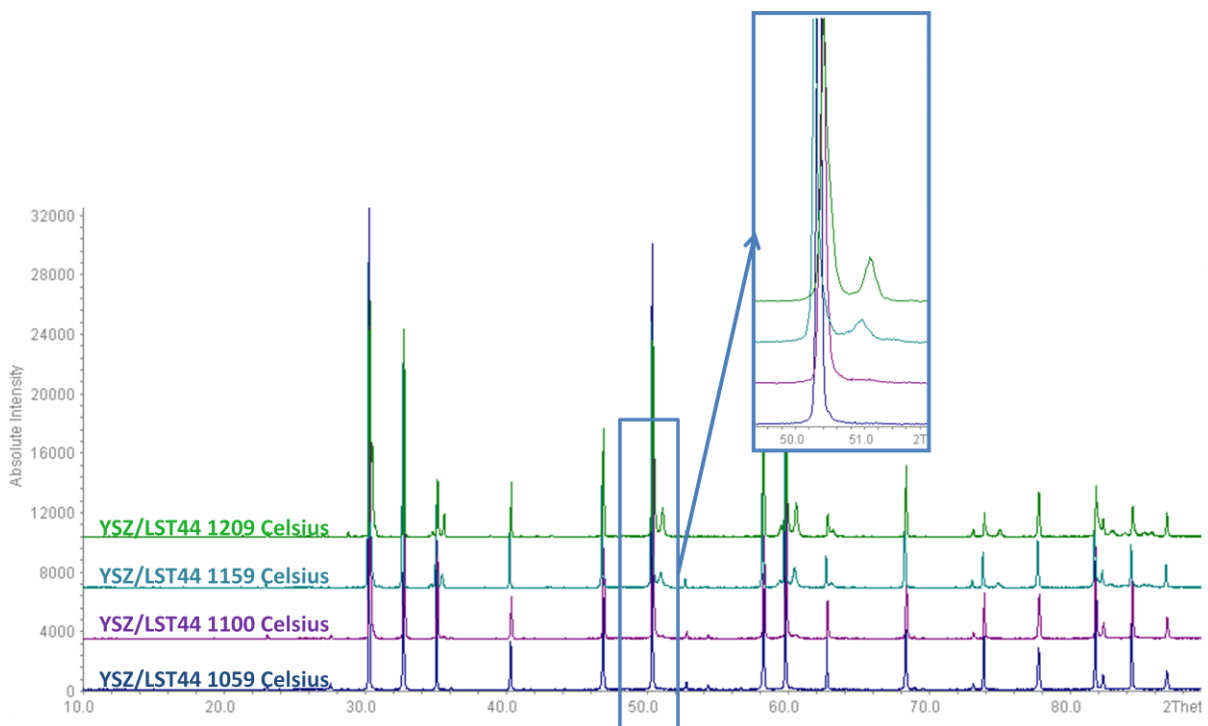


Figure 4.26: XRD diagram of composite anodes of YSZ and LST44 calcinated at different temperatures under oxidising conditions.

Figure 4.26 and especially the magnified area around the [2 2 0] peak of the cubic YSZ at a 2θ angle of around 50° show that the satellite peaks at the right side of the YSZ peaks, assigned to tetragonal distortion, are not visible at XRDs of composites calcinated at low temperatures, but slightly visible at a firing temperature of 1100°C , and well visible at 1159°C and 1209°C , growing with increasing firing temperature.

Comparing the XRDs of composite anodes of YSZ/LST44 and YSZ/LST44Mn6, the same YSZ peaks and perovskite peaks are visible including the secondary phase peaks related to the tetragonal distortion of YSZ. The satellite peaks on the right side of the YSZ peaks are clearly visible from a firing temperature of 1059 °C in the XRDs of the YSZ/LST44Mn6 composite anode. This is a lower temperature compared to the firing temperature 1159 °C, which is necessary to observe the same secondary phase peaks in the XRDs of the YSZ/LST44 anode. From a firing temperature of 1059 °C on, two additional secondary peaks are visible in the XRDs of composite anodes of YSZ/LST44Mn6, which are not visible in the XRDs of the YSZ/LST44 anodes, as shown in figure 4.27.

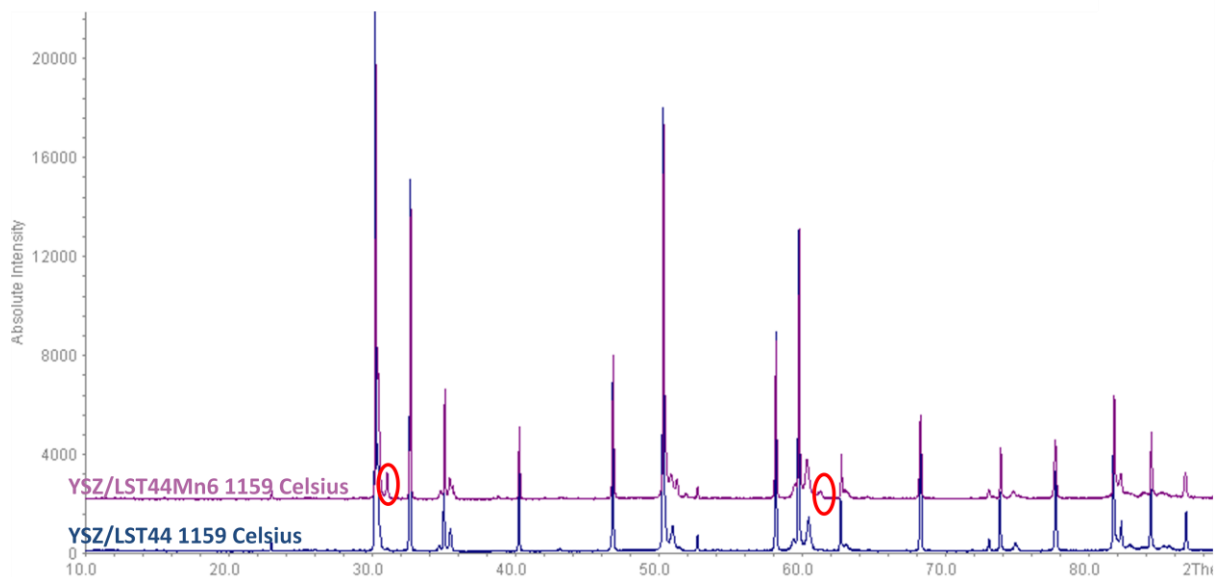


Figure 4.27: XRD diagram of composite anodes of YSZ and LST44 calcinated at different temperatures under oxidising conditions.

The peaks at 2θ angles of around 31.1° and around 60.4° , marked with red ovals in figure 4.27, are growing with increasing firing temperature and remain visible in the XRDs of the reduced samples. Comparing the position of these peaks with XRD peak positions of metallic manganese, manganese oxides, titanium oxides and manganese and titanium zirconates from the ICDD library, they could not be assigned to any of these substances.

A basic refinement was carried out with the “Index&Refine” feature of the STOE WinXPOW software investigating the cell parameters of the cubic unit cells of YSZ and the perovskites LST44 and LST44Mn6 fired at different temperatures.

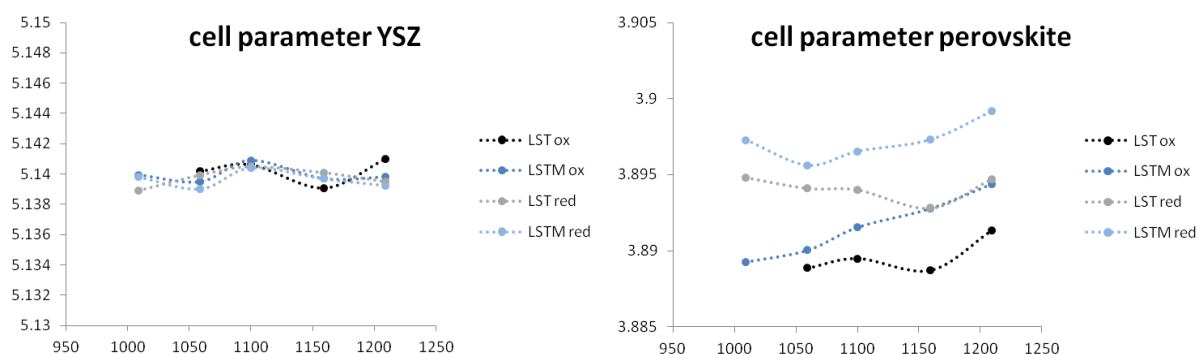


Figure 4.28: Cell parameters of cubic YSZ and cubic perovskites in oxidised and reduced states, refined from XRDs of composite anodes of YSZ and LST44 or LST44Mn6 calcinated at different temperatures.

Figure 4.28 shows an overview over the results of the cell parameter refinements of YSZ and the impregnated perovskites. While the cell parameter of cubic YSZ seems to remain within an area between 5.139 Å and 5.141 Å, no matter if the skeleton had been impregnated with LST44 or LST44Mn6 and if it was in oxidised or reduced state, the cell parameters of the perovskites showed more diversity allowing to draw some conclusions. As already mentioned in chapter 4.2.2 the cell parameter of the perovskites in the reduced cells seem to be larger than in the oxidised state, and the cell parameter of LST44Mn6 seems larger than the cell parameter of LST44. In the relationship between the firing temperature and the cell parameter of the perovskites the cell parameters show a local minimum at a firing temperature of 1159 °C for YSZ/LST44 in the oxidised and reduced state, and a local minimum at a firing temperature of 1059 °C in the reduced state of YSZ/LST44Mn6.

4.5.2. Influence on the microstructure

The microstructure of the composite anodes composed of YSZ and LST44 or LST44Mn6 and calcinated at different temperatures was investigated with the SEI technique of a SEM microscope like described in chapter 2.2.2.

As described in chapter 4.1.1 and illustrated in figure 4.2 the YSZ skeleton is covered in a way forming regular shaped grains at a level of 10 wt.% A-site deficient perovskite impregnated, and this structure is partly covered by a flat blanket layer without visible grain structure if the amount of impregnated perovskite is increased to 40 wt.%.

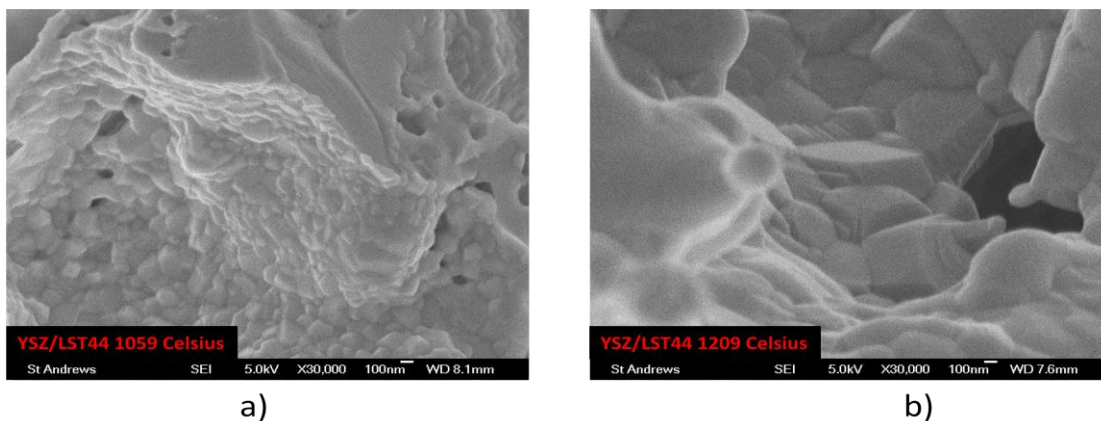


Figure 4.29: SEI images of a SEM microscope of composite anodes of YSZ and 40 wt.% LST44 fired after impregnation at temperatures of 1059 °C (a) and 1209 °C (b) under oxidising conditions and 30000x magnification.

Figure 4.29 shows that the size of the grains in the composite anode is a function of the firing temperature, in an YSZ/LST44 anode fired at 1059 °C the grains have a diameter of 100-150 nm, while they have a diameter of over 500 nm in an anode of the same composition fired at 1209 °C. Figure 4.30 shows a schematic of the development of composite anodes with increasing firing temperature on the one side and of increasing amount of impregnated perovskite on the other side.

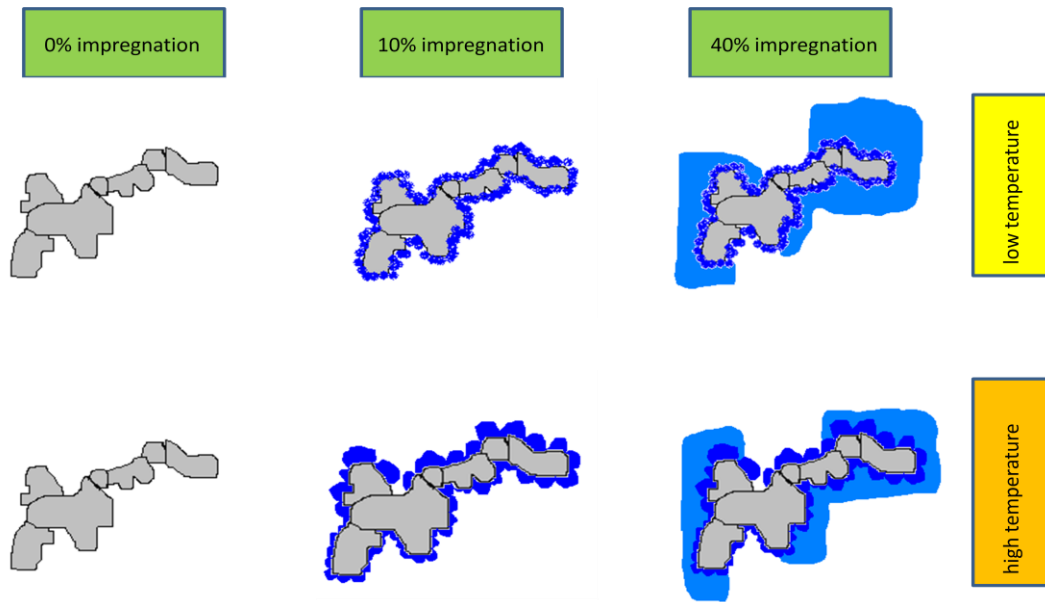


Figure 4.30: schematic of composite anodes with a YSZ skeleton and different amounts of impregnated perovskite phase subsequently fired at different temperatures.

In composite anodes with YSZ and LST44Mn6 the development of the size of the grains from small grains of around 100 nm to big grains of around 500 nm with increasing firing temperature happens in the same way as in anodes of YSZ and LST44, but generally at temperatures around 50 °C lower. In a composite anode of YSZ/LST44 fired at 1100 °C the size of the grains is around 100 nm or smaller, fired at 1159 °C they show an intermediate size of around 200 nm and fired at 1209 °C the average size is around 500 nm or larger. The intermediate grain size of around 200 nm is reached at a firing temperature of 1100 °C in a composite anode of YSZ/LST44Mn6, and a grain size of 500 nm is reached at a firing temperature of 1159 °C, as shown in figure 4.31. Theoretically substitution of 6% of the titanium at the B-site of the perovskite by manganese reduces the lattice energy because oxide ions are removed from the lattice to maintain charge neutrality, and because the bonding energy between manganese and oxygen is lower than the bonding energy between titanium and oxygen [18]. The resulting decrease of sintering temperature is consistent with the more advanced development of the microstructure for LST44Mn6 compared with LST44 at the same firing temperature, as found in the experiments in this chapter shown in figure 4.31.

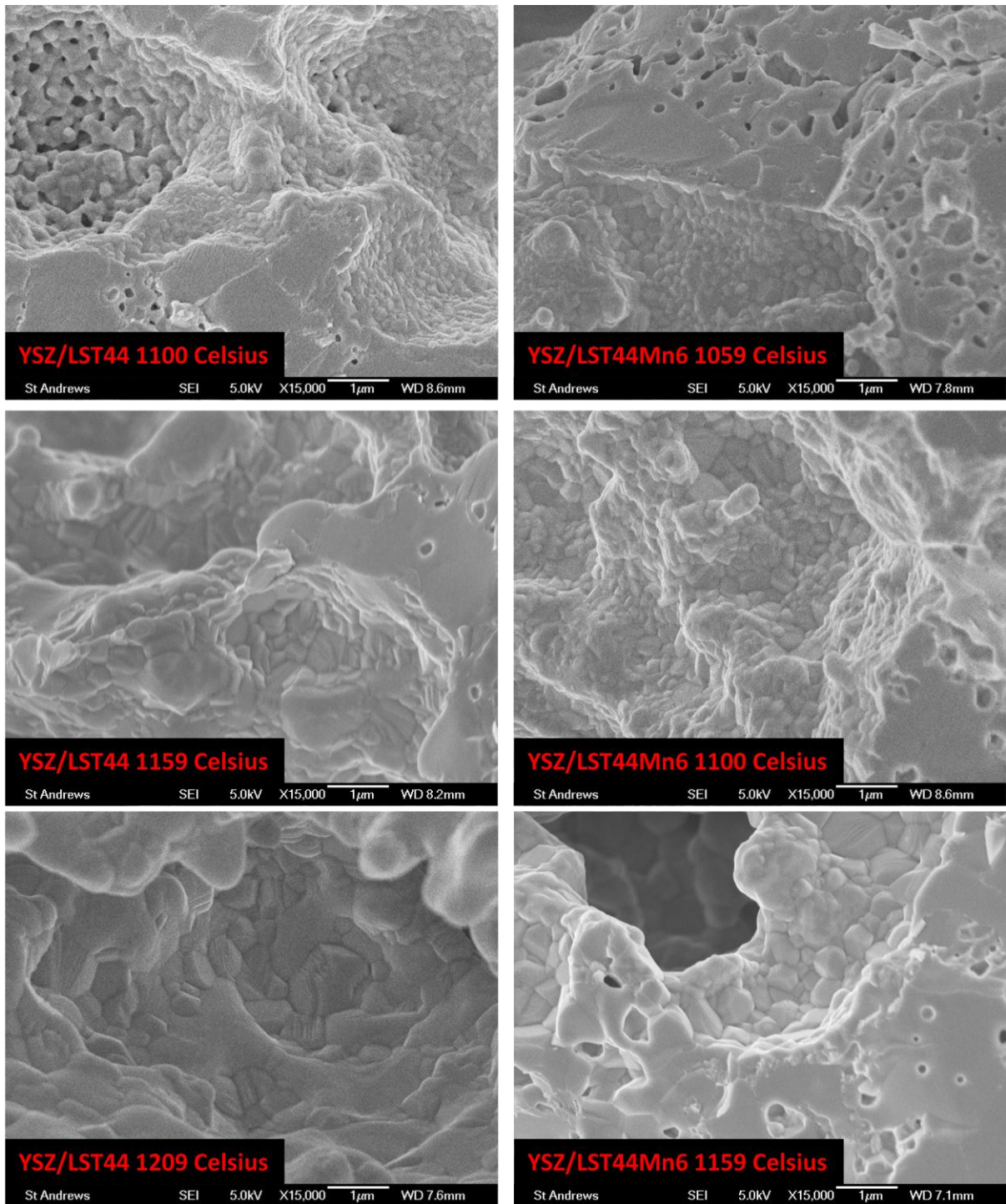


Figure 4.31: SEI images at 15000x magnification of composite anodes of YSZ/LST44 (left column) and YSZ/LST44Mn6 (right column) calcinated at different temperatures showing the different stages of grain development from small grains at the top over grains of an intermediate size in the middle to large grains in the bottom images.

The microstructure of the composite anodes looks very similar after reduction at 900 °C for 6 hours in an atmosphere of 5 % hydrogen and 95 % argon. As shown in figure 4.32 the size of the grains after reduction is a little bit bigger and the terrace structure of the grains is more distinctive. This might be related to the lower lattice energy in the reduced state, caused by the larger number of oxygen vacancies, causing stronger sintering effects at the same temperature.

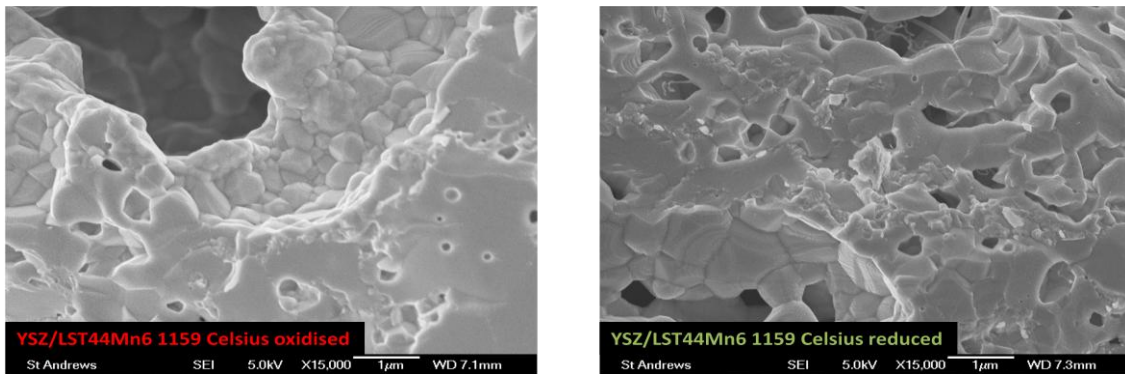


Figure 4.32: SEI images of composite anodes of YSZ/LST44Mn6 calcinated at 1159 °C before and after reduction at 900 °C at 15000x magnification.

4.5.3. Conclusions

Button cells with composite anodes of YSZ/LST44 and YSZ/LST44Mn6 were fired after impregnation at temperatures of 1009 °C, 1059 °C, 1100 °C, 1159 °C or 1209 °C. Their composition was investigated by XRD and their microstructure by SEI.

The secondary phase peaks in the XRDs assigned to the tetragonal distortion of YSZ upon impregnation of LST44 do not occur below a firing temperature of 1100 °C and are larger if the firing temperature is higher. Since the tetragonal distortion of the YSZ unit cell has been related to the migration of ions from the impregnated perovskite phase into the YSZ phase of the composite anode and their integration into the YSZ lattice [3], a higher temperature might help this migration and integration to happen faster and into deeper layers of the YSZ grains.

Basic refinement of the cell parameters of YSZ and the perovskites seem to indicate that the cell parameter of YSZ is neither influenced by the firing temperature, nor by the kind of titanate perovskite impregnated into the skeleton or by reduction at 900 °C. The cell parameters of LST44Mn6 are around 0.002 to 0.005 Å larger than the cell parameters of undoped LST44 depending on the firing temperature. The reduced state of both perovskites show cell parameters around 0.005 Å larger than their oxidised states. That was to be expected because the manganese ions in valence 2 and 3 have larger ionic radii than the titanium (IV) ion, and the ions of lower positive charge have bigger ionic radii.

The microstructure of the composite anodes generally shows grains covered by a flat blanket layer. The size of the grains is small at low firing temperatures and increases with increasing firing temperature. A certain size of the grains can be observed at temperatures around 50 °C lower if the impregnated perovskite is LST44Mn6 instead of undoped LST44, which is related to a lower lattice energy in LST44Mn6. The grain size in reduced composite anodes is larger than the same composites fired at the same temperature under oxidising conditions.

4.6. Cell fabrication using the vacuum impregnation method

The impregnation of a perovskite into a YSZ skeleton is a multiple step process with repeated infiltration of the aqueous precursor and firing until the percentage required for percolation, usually around 40 wt.% perovskite, is achieved. Depending on the kind of perovskite used the fabrication can take up to 25 cycles and be very time consuming.

In the vacuum impregnation technique a vacuum is applied before the infiltration and maintained during the application of the aqueous precursor on top of the surface of the porous anode. Upon venting the vessel the ambient pressure should ideally force the precursor deeper into the pores of the electrode because the pressure inside this pores is low compared to ambient pressure. In that way theoretically more substance can be impregnated into the skeleton reducing the number of cycles necessary for a 40 wt.% loading. The vacuum impregnation technique has been applied to produce cathodes [19] and anodes [20] for SOFCs in literature.

In each cycle 1 drop of the impregnation solution (nitrates stoichiometric for $\text{La}_{0.4}\text{Sr}_{0.4}\text{Ti}_{0.94}\text{Mn}_{0.06}\text{O}_{3-y}$ in water, 0.5mol/l) was applied on the anode of one of the cells, another drop on top of another cell under a reduced pressure of 0.16 bar, using a vessel custom made at the mechanical workshop of the university, after 5 seconds the vacuum chamber was vented and both cells were wiped with a tissue. This infiltration was repeated once before firing it for 40 minutes at 450 °C, and every third firing was carried out at a higher temperature of 800 °C. This procedure was repeated until a weight gain of around 6.1 mg was achieved, providing a 40-45 wt.% perovskite content in the composite anode.

4.6.1. Evaluation of the weight gain per cycle

The weight gain of the impregnated anodes was measured by weighing the cells before impregnation, after 4 cycles, 8 cycles, 9 cycles, 12 cycles, 13 cycles and 15 cycles. The weight gain of the anode impregnated by vacuum impregnation was compared to the weight gain of an anode impregnated without the application of reduced pressure.

number of cycles	number of drops	weight gain vacuum(mg)	weight gain normal(mg)
0	0	0	0
4	8	2.45	2.05
8	16	4.6	4.15
9	18	4.95	4.25
12	24	6.05	5.3
13	26	6.3	5.55
15	30		6.3

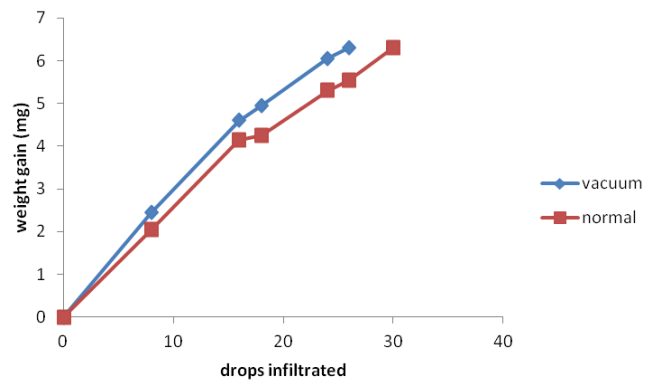


Figure 4.33: Table and diagram illustrating the weight gain during the process of impregnation comparing vacuum impregnation and normal impregnation.

Figure 4.33 shows that a larger weight gain can be achieved by vacuum impregnation, however, the weight gain after 13 cycles is only around 12 % higher than the weight gain of a cell impregnated under ambient pressure. To reach the required 40 wt.% or around 6.1 mg perovskite weight gain 13 cycles were needed using vacuum impregnation compared to 15 cycles using normal impregnation.

4.6.2. Comparison of the microstructure

The microstructure of two composite anodes of YSZ/LST44Mn6, one of which had been fabricated by vacuum impregnation, were compared using SEI imaging of an electron microscope.

As shown in figure 4.34 there are no significant differences between the microstructure of composite anodes fabricated by vacuum impregnation and normal impregnation.

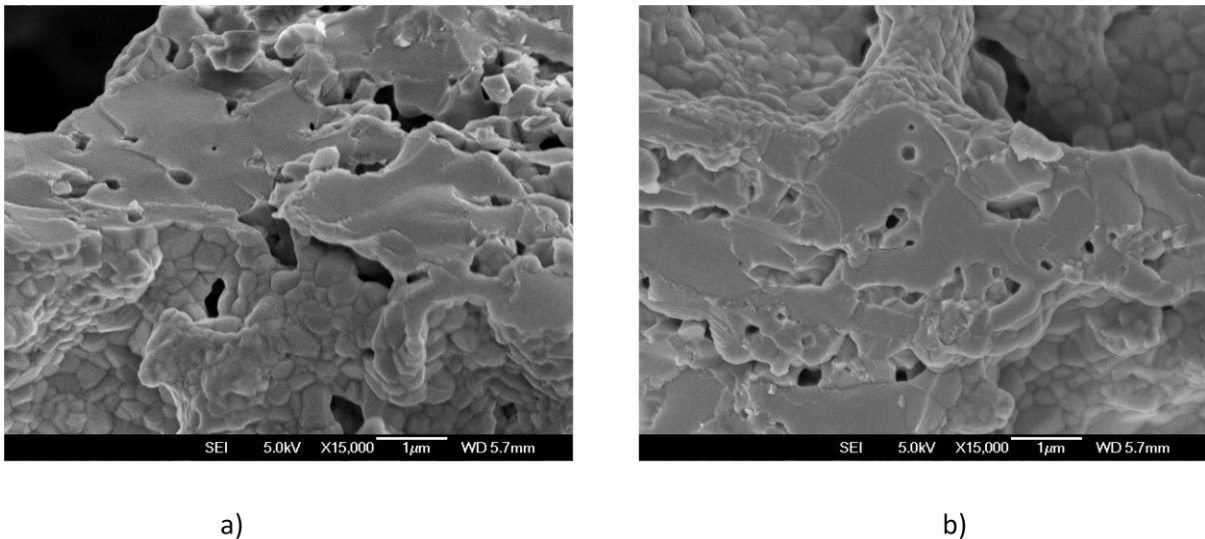


Figure 4.34: SEI images of composite anodes of YSZ/LST44Mn6 fabricated by vacuum impregnation (a) and normal impregnation (b).

To answer the question if the perovskite phase is brought deeper into the pores of the skeleton EDAX technique of the electron microscope was employed and a line scan for the distribution of the elements titanium and zirconium along a cross section of the electrode, as can be seen in figure 4.35.

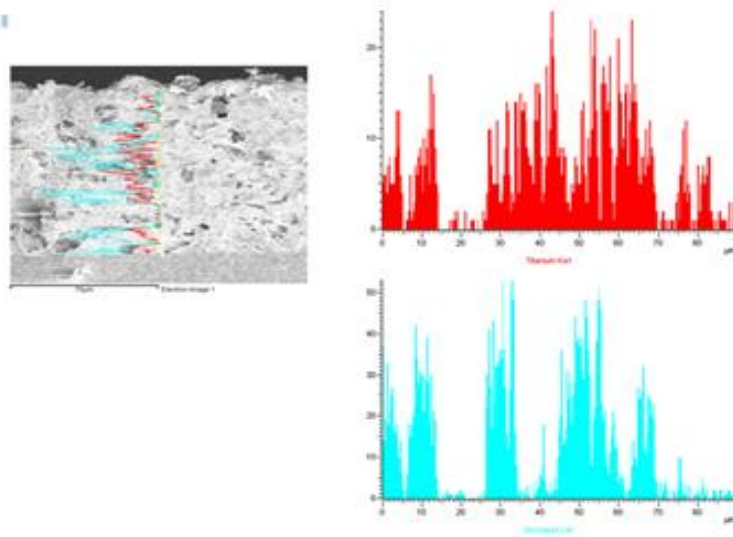


Figure 4.35: EDAX linescan for the elements zirconium (turquoise) and titanium (red) along a cross section of a composite anode of YSZ/LST44Mn6 .

Unfortunately the EDAX technique didn't appear to be the right tool for the investigation of the porous electrode and the question could not be answered.

4.6.3. Comparison of the electrochemical performance

After impregnation of the anode and firing at 1150 °C, the cathode was impregnated with LSF82 and fired at 850 °C. No additional catalyst was used, and the current collection grid was painted with a silver paste. IV curves were measured using a Solartron 1470E cell test system and the same system combined with a Solartron 1252A frequency response analyzer was used for the EIS measurements.

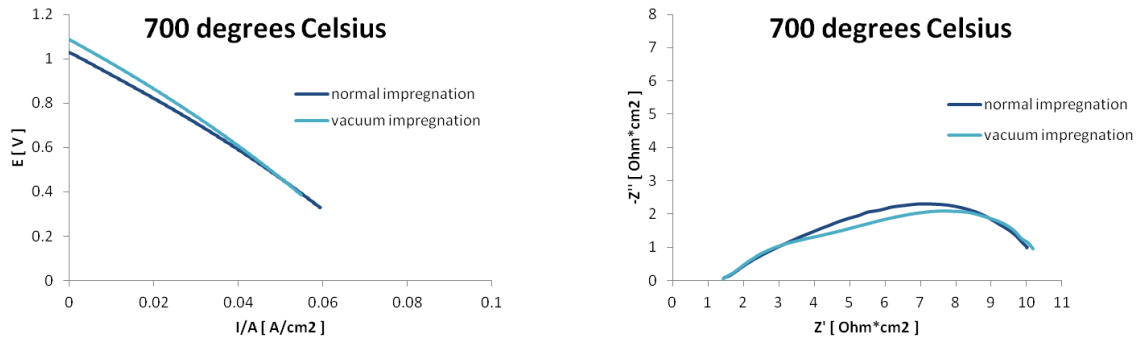


Figure 4.36: IV curves and Nyquist plots of cells with composite anodes of YSZ/LST44Mn6 fabricated by normal impregnation and vacuum impregnation.

The IV curves in figure 4.36 show a linear shape over the whole range of current densities and suggest a very similar electrochemical performance of cells fabricated by vacuum impregnation and normal impregnation, with the slightly higher OCV of the vacuum cell probably caused by a better quality of the sealing between the cell and the test tube. The maximal power density calculated from the IV curves is around 23.9 mW/cm^2 for the cell impregnated in the conventional way and around 23.9 mW/cm^2 for the vacuum impregnated cell.

The Nyquist plots of the two cells only slightly differ in their shape, but the values of their ohmic resistance R_S and non ohmic polarisation R_P are almost identical with around $1.3 \Omega \cdot \text{cm}^2$ for R_S and around $9.3 \Omega \cdot \text{cm}^2$ for R_P .

4.6.4. Conclusions

Cells with composite anodes of YSZ and LST44Mn6 have been fabricated by normal impregnation and vacuum impregnation. The vacuum impregnation shows an increased amount of perovskite impregnated per impregnation cycle, but only by around 12%.

The microstructure of the composite anodes was investigated by SEI and seems to be the same no matter if the composite anode was impregnated by conventional impregnation or vacuum impregnation. The question if the perovskite phase is impregnated into deeper areas of the pores by vacuum impregnation could not be answered by the EDAX technique.

The electrochemical performance of a cell with an anode fabricated by vacuum impregnation is very similar to a cell of the same composition fabricated by conventional impregnation. The values for the ohmic resistance R_S and the non ohmic polarisation R_P are almost identical.

4.7. Different cell fabrication with a higher skeleton firing temperature

Two cells with composite anodes of YSZ/LST44 and YSZ/CGO/LST44 were fabricated at the University of Pennsylvania by techniques of tape casting and impregnation using the chemicals and fabrication parameters traditionally used in the research group of Professor Raymond Gorte [10], and their microstructure and electrochemical performance were compared to the microstructure and electrochemical performance of cells fabricated at the University of St. Andrews in the research group of Professor John Irvine, as described in chapter 2.1.

4.7.1. Differences in the fabrication

In the first step of the slurry preparation 8 mol% yttria stabilised zirconia (8YSZ, TOSOH) was dispersed in an organic solvent containing ethanol and xylenes (Fisher Scientific) with the help of Blown Menhaden Fish Oil as a dispersant. The pore former used in the green tapes used for porous layers was crystalline graphite powder 300 mesh (Alfa Aesar). Two different kind of poly(vinylbutyral) binders were used for the tapes for electrolyte (BUTVAR B-98, Solutia) and for the tapes for electrodes (BUTVAR B-79, Solutia). After ball milling the slurry over night in a second step of the slurry preparation benzyl butyl phthalate (BBP, Fisher Scientific) and poly(ethylene glycol) (PEG, Sigma Aldrich) were added as plasticisers.

Circular discs of the diameter of 3/4 " for the electrolyte and 3/8 " for the electrodes were punched out, arranged and the green cells consisting of two electrode discs separated by an electrolyte disc were fired at 1500 °C for 6 hours resulting in the skeleton. The impregnation into the pores of the skeleton was carried out in exactly the same way as in St. Andrews and as described in chapter 2.1.2.

The anode of one of the cells was impregnated with an additional skeleton layer of CGO and subsequently fired at 1200 °C, and then the anodes of both cells were impregnated with the aqueous precursor for $\text{La}_{0.4}\text{Sr}_{0.4}\text{TiO}_3$ (LST44) and fired at 1100 °C. The cathodes were impregnated with $\text{La}_{0.8}\text{Sr}_{0.2}\text{FeO}_{3-\gamma}$ (LSF82) and fired at 850 °C. An additional palladium catalyst was added into the anodes also by impregnation. The composition of the anodes after the last calcination was 61.3 wt.% YSZ, 37.4 wt.% LST44 and 1.3 wt.% palladium oxide for the YSZ/LST44 anode and 52.0 wt.% YSZ, 15.3 wt.% CGO, 31.6 wt.% LST44 and 1.1 wt.% palladium oxide for the YSZ/CGO/LST44 anode.

4.7.2. Differences in the microstructure

SEI images of the composite anodes fabricated in St. Andrews and Philadelphia under relatively low 1000x magnification reveal a much higher porosity in the Philadelphia composite which might seem strange considering that the ratio between YSZ powder and graphite pore former was 1:1 in St. Andrews and 4:3 in Philadelphia, but can be explained by the different pore former utilized and by the different slurry recipe in general. A possible explanation for the finer pores of the St. Andrews cells is that the carbon pore former was added in the first step of the slurry preparation, adding an additional milling step. Smaller carbon particles could have led to a finer pore structure after the firing of the skeleton.

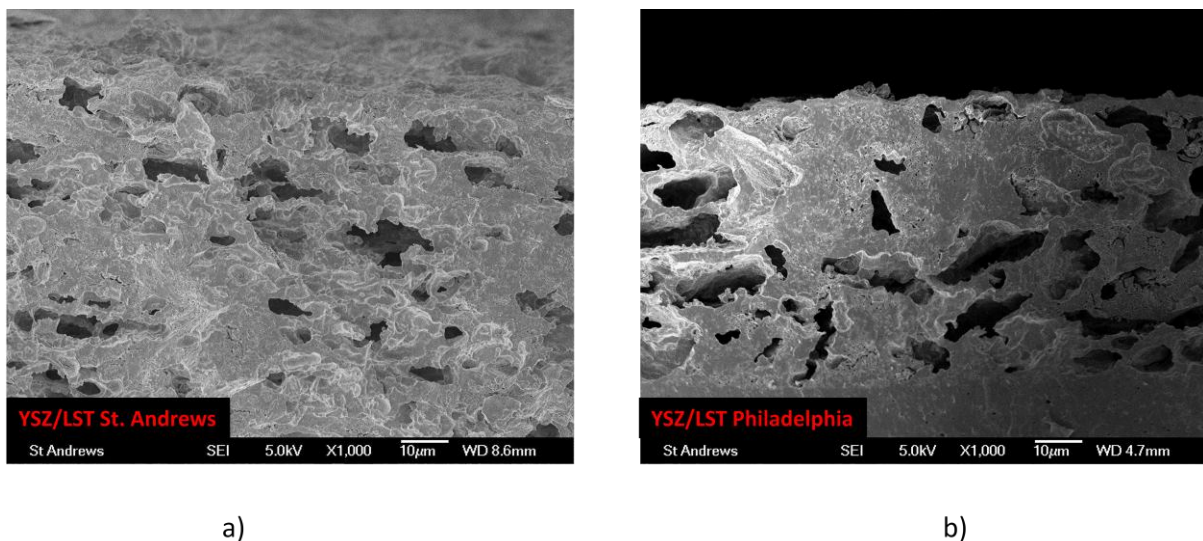
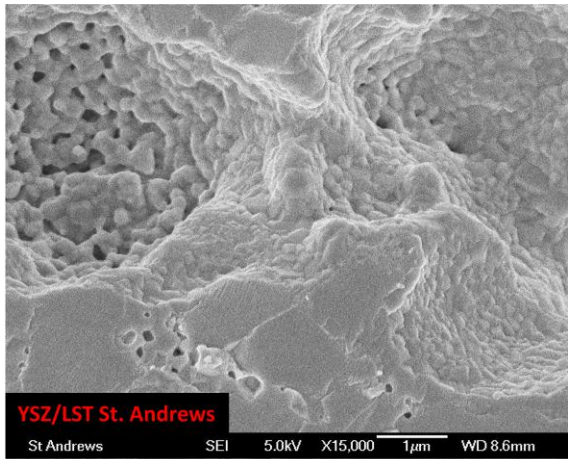
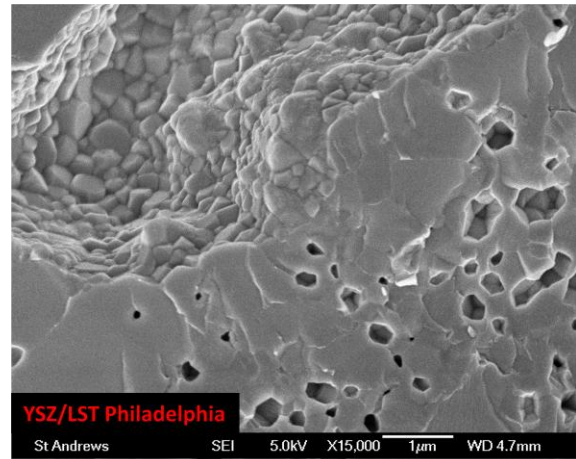


Figure 4.37: SEI images of composite anodes made of YSZ/LST44 fabricated in St. Andrews (a) and Philadelphia (b) under 1000x magnification.

Comparing the microstructure of the two composite anodes under higher magnification of 15000x, the grains seem a little bigger in the Philadelphia composite anode, but the general structure with grains partly covered with a flat layer is similar in both composites, as can be seen in figure 4.37.



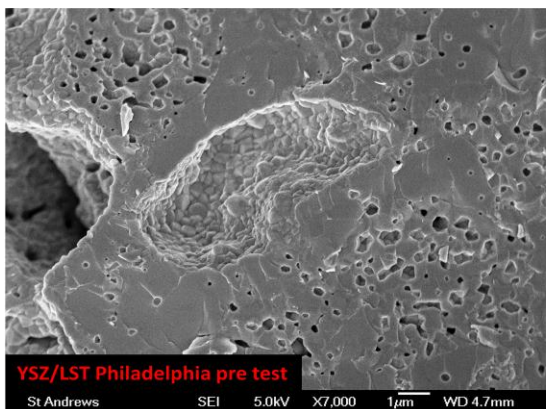
a)



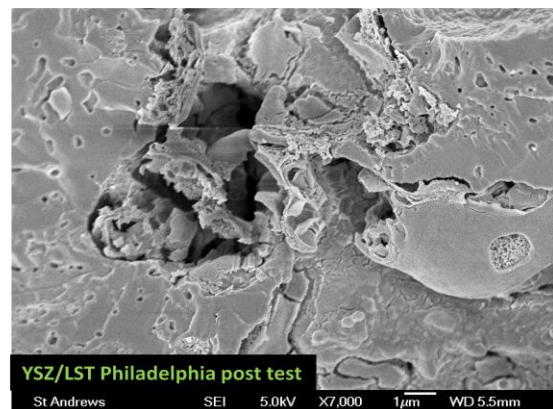
b)

Figure 4.38: SEI images of composite anodes made of YSZ/LST44 fabricated in St. Andrews (a) and Philadelphia (b) under 15000x magnification.

After electrochemical testing at temperatures up to 850 °C in hydrogen atmosphere the appearance of the microstructure has changed, as shown in figure 4.38. The regular shaped round grains building a grain structure visible below the blanket layer before the testing are not visible any more, instead the structure visible below the blanket layer after testing appears to consist of irregular shaped splinters which are separated by cracks from the blanket layer.



a)



b)

Figure 4.39: SEI images of composite anodes made of YSZ/LST44 fabricated in Philadelphia before (a) and after (b) electrochemical testing under hydrogen atmosphere.

4.7.3. Differences in the electrochemical performance

The two button cells fabricated as described at the very start of the chapter were electrochemically tested using a test jig, a Solartron cell test system and a frequency response analyser in Philadelphia. IV curves and EIS spectra were recorded in a temperature range from 650 °C to 850 °C in increments of 50 °C, and compared with two cells having anodes of a similar composition YSZ/LST44 and YSZ/CGO/LST44 prepared and tested in St. Andrews.

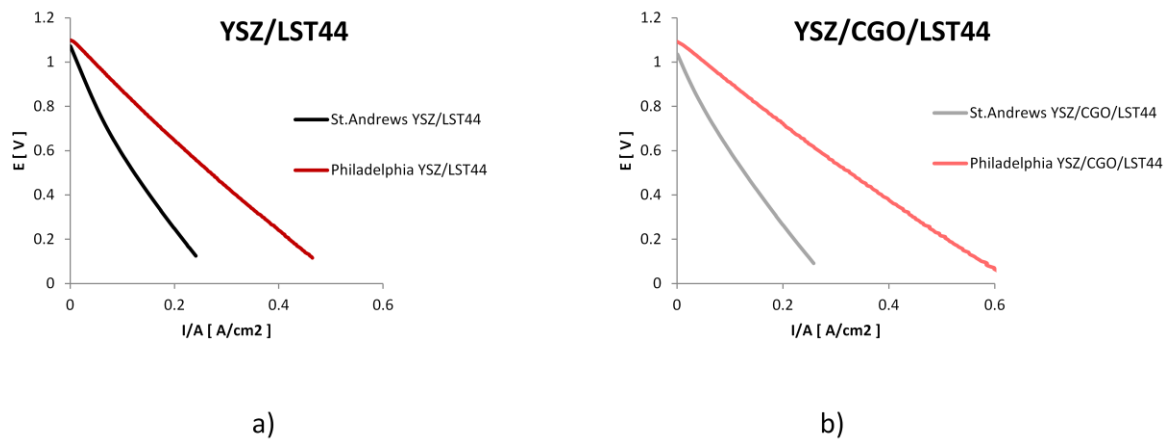


Figure 4.40: IV curves of cells with composite anodes made of YSZ/LST44 and YSZ/CGO/LST44 fabricated in St. Andrews and Philadelphia.

The IV curves are close to linear over the whole range of power density and their gradient suggests that the electrochemical performance of the cells fabricated in Philadelphia is superior to the electrochemical performance of cells with similar anodes fabricated in St. Andrews. The maximum power density of the cells calculated from the IV curves shows values of around 61.9 mW/cm² for the YSZ/LST44 cell fabricated in St. Andrews, around 135.4 mW/cm² for the YSZ/LST44 cell fabricated in Philadelphia, around 64.3 mW/cm² for the YSZ/CGO/LST44 cell

fabricated in St. Andrews and around 164.7 mW/cm^2 for the YSZ/CGO/LST44 cell fabricated in Philadelphia, all at $700 \text{ }^\circ\text{C}$. The additional CGO layer makes hardly any difference to the electrochemical performance of the St. Andrews cells with undoped LST44 perovskite, as already discussed in chapter 4.4, but seems to improve the electrochemical performance in the cells fabricated in Philadelphia.

The EIS curves used for the Nyquist plots shown in figure 4.41 were recorded at OCV conditions in St. Andrews and under a bias of -0.1 V in Philadelphia. Although both the ohmic resistance R_S and the non ohmic polarisation R_P are lower in the cells fabricated in Philadelphia, the main reason for the superiority of the Philadelphia cells seems to be the reduction of R_P .

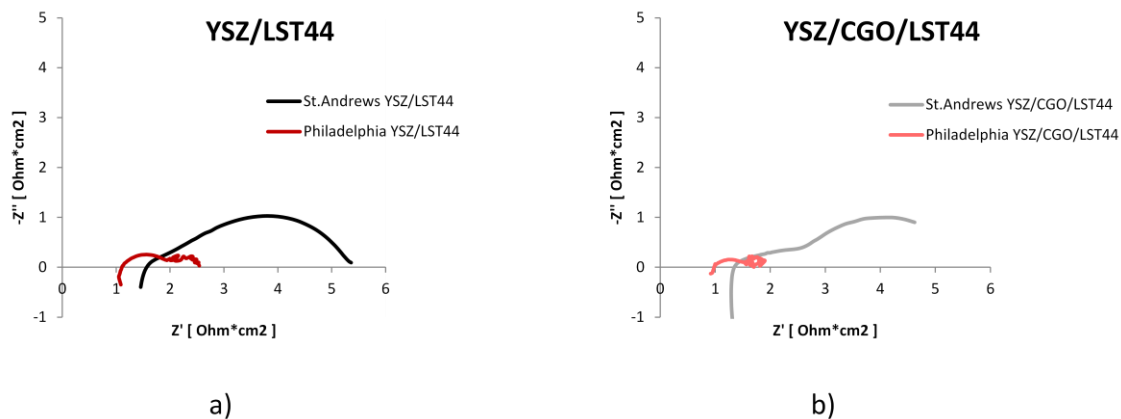


Figure 4.41: Nyquist plots of EIS curves of cells with composite anodes made of YSZ/LST44 and YSZ/CGO/LST44 fabricated in St. Andrews and Philadelphia.

The values for R_S of cells tested at $700 \text{ }^\circ\text{C}$ are around $1.6 \text{ } \Omega \cdot \text{cm}^2$ in the YSZ/LST44 cell and around $1.4 \text{ } \Omega \cdot \text{cm}^2$ in the YSZ/CGO/LST44 cell fabricated in St. Andrews, and around $1.1 \text{ } \Omega \cdot \text{cm}^2$ in the YSZ/LST44 cell and around $1.0 \text{ } \Omega \cdot \text{cm}^2$ in the YSZ/CGO/LST44 cell fabricated in Philadelphia. The CGO layer seems to have very little influence in R_S of the cells fabricated in St. Andrews or Philadelphia, and generally the R_S values of cells fabricated according to the methods in Philadelphia are around $0.5 \text{ } \Omega \cdot \text{cm}^2$ lower than to the corresponding St. Andrews cells. The

reduced ohmic resistance can be related to the higher firing temperature of the skeleton, providing bigger YSZ grains with fewer grain boundaries, resulting in better ionic conductivity of the material.

R_p values of cells tested at 700 °C are around 3.8 $\Omega\cdot\text{cm}^2$ in the YSZ/LST44 cell and around 4.3 $\Omega\cdot\text{cm}^2$ in the YSZ/CGO/LST44 cell fabricated in St. Andrews, and around 1.4 $\Omega\cdot\text{cm}^2$ in the YSZ/LST44 cell and around 0.9 $\Omega\cdot\text{cm}^2$ in the YSZ/CGO/LST44 cell fabricated in Philadelphia. Strangely the CGO layer seems to increase R_p of the cells fabricated in St. Andrews, but to decrease R_p of the cells fabricated in Philadelphia.

Considering the shape of the Nyquist plots, the two separated arcs visible in the YSZ/CGO/LST44 cell fabricated in St. Andrews, which are a distinctive feature of all cells containing CGO in their anode skeleton ever tested in this work in St. Andrews, are not visible in the YSZ/CGO/LST44 cell fabricated in Philadelphia.

Thin cells with anodes of $\text{La}_{0.2}\text{Sr}_{0.7}\text{TiO}_3$ fabricated by tape casting in literature exhibited maximum power densities of over 500 mW/cm^2 at 750 °C with an ohmic resistance R_s of around 0.5 Ωcm^2 and a polarisation R_p of around 0.5 Ωcm^2 [1]. Both the ohmic resistance and the polarisation are lower than observed in this study, probably due to the anode not being a composite and the utilisation of lanthanum strontium cobaltite at the cathode side. Maximal power densities of 520 mW/cm^2 at 700 °C were achieved by splitting the anode into a functional layer of YSZ/CeO₂/Pd and a conduction layer of $\text{La}_{0.3}\text{Sr}_{0.7}\text{TiO}_{3.15}$ [21]. Cells with A-site deficient yttrium doped strontium titanate in a composite anode with YSZ infiltrated with ruthenium and ceria exhibited a maximal power density of 470 mW/cm^2 at 800 °C even in the presence of 10 ppm H₂S in the hydrogen fuel [22].

4.7.4. Conclusions

Two cells with composite anodes consisting of YSZ/LST44 and YSZ/CGO/LST44 were fabricated in Philadelphia using tape casting according to the recipe used in the group of Professor Raymond Gorte at the University of Pennsylvania. Compared to the recipe used in the group of Professor John Irvine at the University of St. Andrews different solvent and dispersant substances were used for the tape slurries, the sequence was different (the binder was added in the first step of the slurry preparation and the graphite poreformer in the second step, unlike in St. Andrews) and most importantly the firing of the skeleton was carried out at a maximum temperature of 1500 °C instead of 1400 °C.

The microstructure of the anode fabricated in Philadelphia showed increased porosity under low magnification, the general structure of the composite however was similar in both anodes with a grain structure partly covered with a flat layer.

The electrochemical performance of the cells fabricated in Philadelphia is superior to cells with a similar anode composition fabricated in St. Andrews, mainly due to a considerably reduced non ohmic polarisation. While an additional skeleton layer of CGO in cells fabricated in St. Andrews reduces R_S and increases R_P by around the same value, the cell fabricated in Philadelphia with additional CGO has got reduced R_S and R_P values and accordingly shows a better electrochemical performance than the cell without CGO. The distinctive two arc shape in Nyquist plots, which is characteristic for cells with CGO present in the anode of cells in St. Andrews, can't be observed for the YSZ/CGO/LST44 cell fabricated in Philadelphia.

- [1] C.-D. Savaniu and J. T. S. Irvine, "Reduction studies and evaluation of surface modified A-site deficient La-doped SrTiO₃ as anode material for IT-SOFCs," *J. Mater. Chem.*, **19**, 8119–8128, 2009.
- [2] C. J. Howard, R. J. Hill, and B. E. Reichert, "Structures of ZrO₂ polymorphs at room temperature by high-resolution neutron powder diffraction," *Acta Crystallographica Section B Structural Science*, **44**, 116–120, 1988.
- [3] A. H. Dariusz Burnat, "On the chemical interaction of nanoscale lanthanum doped strontium titanates with common scandium and yttrium stabilized electrolyte materials," *International Journal of Hydrogen Energy*, **37**, 18326–18341, 2012.
- [4] R. D. Shannon and C. T. Prewitt, "Effective ionic radii in oxides and fluorides," *Acta Crystallographica Section B Structural Crystallography and Crystal Chemistry*, **25**, 925–946, 1969.
- [5] D. N. Miller and J. T. S. Irvine, "B-site doping of lanthanum strontium titanate for solid oxide fuel cell anodes," *Journal of Power Sources*, **196**, 7323–7327, 2011.
- [6] G. Tsekouras, D. Neagu, and J. T. S. Irvine, "Step-change in high temperature steam electrolysis performance of perovskite oxide cathodes with exsolution of B-site dopants," *Energy Environ. Sci.*, **6**, 256–266, 2012.
- [7] D. Neagu, "Materials and Microstructures for High Temperature Electrochemical Devices through Control of Perovskite Defect Chemistry," *PhD University of St. Andrews*, 2012.
- [8] D. Neagu, G. Tsekouras, D. N. Miller, H. Ménard, and J. T. S. Irvine, "In situ growth of nanoparticles through control of non-stoichiometry," *Nat Chem*, **5**, 916–923, 2013.
- [9] C. H. Hamann and W. Vielstich, "Elektrochemie". *John Wiley & Sons Australia, Limited*, 2005.
- [10] G. Corre, G. Kim, M. Cassidy, J. M. Vohs, R. J. Gorte, and J. T. S. Irvine, "Activation and Ripening of Impregnated Manganese Containing Perovskite SOFC Electrodes under Redox Cycling," *Chem. Mater.*, **21**, 1077–1084, 2009.
- [11] P. R. Slater, D. P. Fagg, and J. T. S. Irvine, "Synthesis and electrical characterisation of doped perovskite titanates as potential anode materials for solid oxide fuel cells," *J. Mater. Chem.*, **7**, 2495–2498, 1997.
- [12] S. P. Jiang and Y. Yan, "Materials for High-Temperature Fuel Cells". *John Wiley & Sons*, 2013.
- [13] B. C. H. Steele, "Appraisal of Ce_{1-y}Gd_yO_{2-y/2} electrolytes for IT-SOFC operation at 500°C," *Solid State Ionics*, **129**, 95–110, 2000.
- [14] R. Küngas, F. Bidrawn, J. Vohs, and R. Gorte, "Doped-Ceria Diffusion Barriers Prepared by Infiltration for Solid Oxide Fuel Cells," *Departmental Papers (CBE) University of Pennsylvania*, 2010.
- [15] C. N. Ginestra, R. Sreenivasan, A. Karthikeyan, S. Ramanathan, and P. C. McIntyre, "Atomic Layer Deposition of Y₂O₃/ZrO₂ Nanolaminates" *Electrochem. Solid-State Lett.*, **10**(10), B161–B165, 2007.
- [16] X.-D. Zhou, B. Scarfino, and H. U. Anderson, "Electrical conductivity and stability of Gd-doped ceria/Y-doped zirconia ceramics and thin films," *Solid State Ionics*, **175**, 19–22, 2004.
- [17] F. T. Q. X. Fu, "La_{0.4}Sr_{0.6}Ti_{1-x}Mn_xO_{3-d} Perovskites as New Anode Materials for Solid Oxide Fuel Cells." *J. Electrochem. Soc.*, **153**, D74-D83, 2006.
- [18] D. R. Lide, "Handbook of Chemistry and Physics, 81st Edition", *Norwich, N.Y.: CRC Press*, 2000.
- [19] T. Z. Sholklapper, C. Lu, C. P. Jacobson, S. J. Visco, and L. C. D. Jonghe, "LSM-Infiltrated Solid Oxide Fuel Cell Cathodes," *Electrochem. Solid-State Lett.*, **9**, A376–A378, 2006.

- [20] J. Qiao, K. Sun, N. Zhang, B. Sun, J. Kong, and D. Zhou, "Ni/YSZ and Ni-CeO₂/YSZ anodes prepared by impregnation for solid oxide fuel cells," *Journal of Power Sources*, **169**, 253–258, 2007.
- [21] K. Ahn, S. Jung, J. M. Vohs, and R. J. Gorte, "A support layer for solid oxide fuel cells," *Ceramics International*, **33**(6), 1065–1070, 2007.
- [22] H. Kurokawa, L. Yang, C. P. Jacobson, L. C. De Jonghe, and S. J. Visco, "Y-doped SrTiO₃ based sulfur tolerant anode for solid oxide fuel cells," *Journal of Power Sources*, **164**(2), 510–518, 2007.

5. Conclusions

The thesis presented has provided some interesting results which seem to be encouraging enough to justify more research both on topics of the fabrication of fuel cell electrodes by the impregnation method and on the utilisation of doped lanthanum strontium titanates (LSTs), especially the A-site deficient species, as materials for solid oxide fuel cells.

The composition, microstructure and electrochemical performance of composite anodes fabricated by the impregnation method have been explored. The investigated composite anodes consist of a skeleton of YSZ or CGO and an impregnated phase of doped LST of different compositions.

The impregnation method proved to be a useful technique for the fabrication of electrodes for solid oxide fuel cells. The method allows two different firing temperatures, a high one for the skeleton and a lower one after the impregnation, allowing the optimisation of the microstructure of the composite anode. The strong connection between the chemistry of the materials of electrodes, their microstructure and their chemical performance has been confirmed.

Composite anodes of YSZ and LSTs showed a smooth coating of the skeleton by the impregnated phase, different from composite anodes with a skeleton made of CGO instead of YSZ. The fact that the YSZ based electrodes showed a better electrochemical performance even though CGO is the better ionic conductor at temperatures between 650 °C and 850 °C can be explained by this smooth layer. The smooth layer and improved electrochemical performance of the YSZ composite was even more distinctive if the B site of the perovskite was doped with manganese, indicating a specific interaction between manganese and YSZ.

A CGO interlayer between the YSZ skeleton and the LSTM inhibited this interaction and deteriorated the electrochemical performance of the cell by increasing the ohmic resistance from $0.51 \Omega \cdot \text{cm}^2$ to $2.1 \Omega \cdot \text{cm}^2$ and the non ohmic polarisation from $3.4 \Omega \cdot \text{cm}^2$ to $5.1 \Omega \cdot \text{cm}^2$, even though the anode contained less than 10 wt.% CGO. This observation confirms the importance of the direct contact between YSZ and the perovskite phase for a good electrochemical performance of the anode.

A-site deficient perovskites impregnated into a YSZ skeleton showed an interesting change of microstructure upon reduction. The surface of the composite anode was covered with nanoparticles, which were exsolved from the B-site of the perovskite. The exsolution of B-site ions from the perovskite lattice can be explained as the stabilisation of a crystal, which, under reducing conditions is both A-site deficient and oxygen deficient. The electrochemical performance of cells with composite anodes containing A-site deficient perovskites was significantly better than the performance of cells with A-site stoichiometric perovskites. Since the better performance is mainly caused by a reduction of the ohmic resistance from $3.9 \Omega \cdot \text{cm}^2$ to $0.5 \Omega \cdot \text{cm}^2$, the better electronic conductivity of the A-site deficient perovskites seems more important than a catalytic effect for the reduction of hydrogen of the exsolved nanoparticles.

The electrochemical performance of the cells with fully ceramic electrodes fabricated during this work could not match the electrochemical performance of cells with conventional Ni/YSZ anodes, because the catalytic effect for the reduction of hydrogen and the electronic conductivity of metallic nickel are unrivalled by any ceramic materials used in this thesis.

However, the versatility of the perovskite system for doping and defect chemistry is impressive and the research about the optimisation of A-site deficient perovskites for fuel cell electrodes is quite a young discipline, so there is plenty of room for improvement by trying different doping strategies in the future. To evaluate the

advantages of fully ceramic anodes over Ni/YSZ anodes it would be desirable to expand the range of fuels used from hydrogen to methane or higher hydrocarbons, and compare the cell performances. For the same reason, long term studies about the degradation of cells with Ni/YSZ anodes compared to cells with ceramic composite anodes will be necessary.

The impregnation method was successfully used for the fabrication of button cells with enhanced triple phase boundary. Room for improvement with this method lies in the reduction of steps necessary for a specified loading of impregnated phase and in the improvement of consistency of the distribution of the impregnated phase inside the skeleton. Impregnation in the way carried out during this thesis was a time consuming multi step process, and unfortunately the number of steps couldn't be reduced in a significant way by the use of reduced pressure.